frontiers | Research Topics

Spotlighting the interaction network of hub genes, molecules, and cells in the tumor immune microenvironment (TIME) and their contribution to malignant progression

Edited by
Xuanbin Wang, Yongqian Shu and Xiaoqiang Qi

Coordinated by
Run Shi

Published in
Frontiers in Immunology

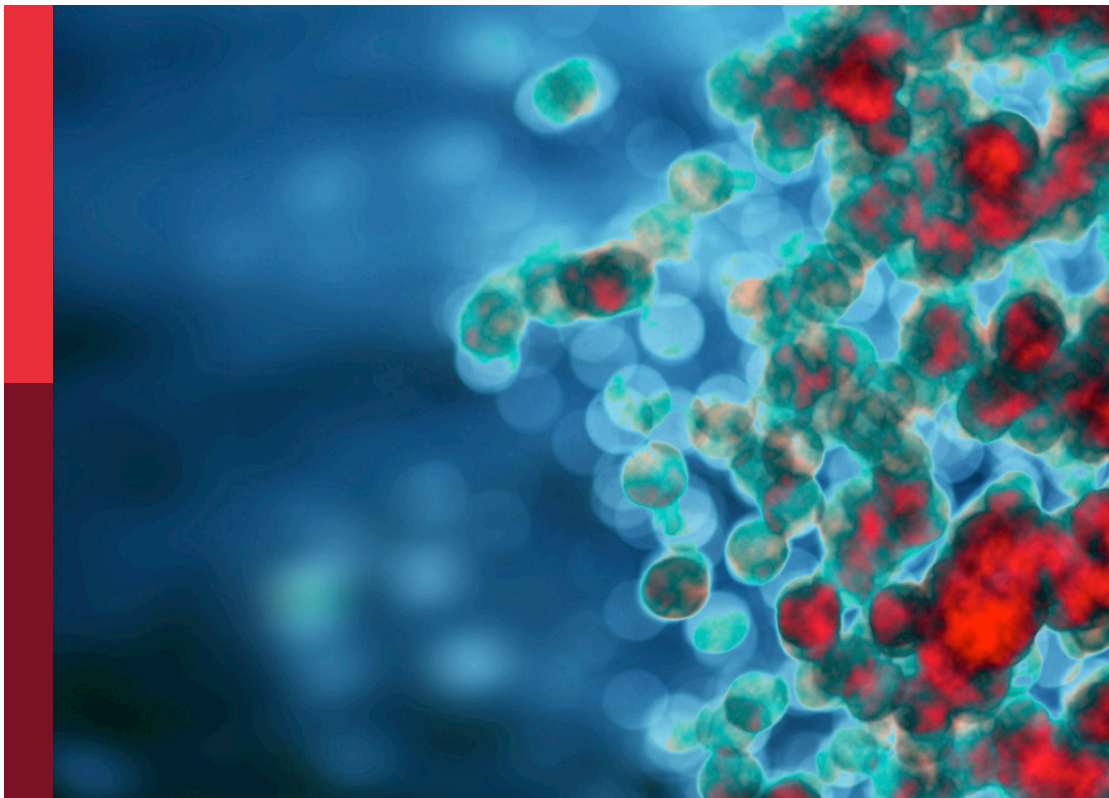

ISSN 1664-8714
ISBN 978-2-8325-5832-4
DOI 10.3389/978-2-8325-5832-4

About Frontiers

Frontiers is more than just an open access publisher of scholarly articles: it is a pioneering approach to the world of academia, radically improving the way scholarly research is managed. The grand vision of Frontiers is a world where all people have an equal opportunity to seek, share and generate knowledge. Frontiers provides immediate and permanent online open access to all its publications, but this alone is not enough to realize our grand goals.

Frontiers journal series

The Frontiers journal series is a multi-tier and interdisciplinary set of open-access, online journals, promising a paradigm shift from the current review, selection and dissemination processes in academic publishing. All Frontiers journals are driven by researchers for researchers; therefore, they constitute a service to the scholarly community. At the same time, the *Frontiers journal series* operates on a revolutionary invention, the tiered publishing system, initially addressing specific communities of scholars, and gradually climbing up to broader public understanding, thus serving the interests of the lay society, too.

Dedication to quality

Each Frontiers article is a landmark of the highest quality, thanks to genuinely collaborative interactions between authors and review editors, who include some of the world's best academicians. Research must be certified by peers before entering a stream of knowledge that may eventually reach the public - and shape society; therefore, Frontiers only applies the most rigorous and unbiased reviews. Frontiers revolutionizes research publishing by freely delivering the most outstanding research, evaluated with no bias from both the academic and social point of view. By applying the most advanced information technologies, Frontiers is catapulting scholarly publishing into a new generation.

What are Frontiers Research Topics?

Frontiers Research Topics are very popular trademarks of the *Frontiers journals series*: they are collections of at least ten articles, all centered on a particular subject. With their unique mix of varied contributions from Original Research to Review Articles, Frontiers Research Topics unify the most influential researchers, the latest key findings and historical advances in a hot research area.

Find out more on how to host your own Frontiers Research Topic or contribute to one as an author by contacting the Frontiers editorial office: frontiersin.org/about/contact

Spotlighting the interaction network of hub genes, molecules, and cells in the tumor immune microenvironment (TIME) and their contribution to malignant progression

Topic editors
Xuanbin Wang — Hubei University of Medicine, China
Yongqian Shu — Nanjing Medical University, China
Xiaoqiang Qi — University of Missouri, United States

Topic coordinator
Run Shi — Ludwig Maximilian University of Munich, Germany

Citation
Wang, X., Shu, Y., Qi, X., Shi, R., eds. (2024). *Spotlighting the interaction network of hub genes, molecules, and cells in the tumor immune microenvironment (TIME) and their contribution to malignant progression*. Lausanne: Frontiers Media SA.
doi: 10.3389/978-2-8325-5832-4

Table of contents

frontiers | Frontiers in Immunology

TYPE Editorial
PUBLISHED 11 December 2024
DOI 10.3389/fimmu.2024.1533290

OPEN ACCESS

EDITED AND REVIEWED BY
Peter Brossart,
University of Bonn, Germany

*CORRESPONDENCE
Run Shi
shirun0122@gmail.com

RECEIVED 23 November 2024
ACCEPTED 29 November 2024
PUBLISHED 11 December 2024

CITATION
Li J, Wang X and Shi R (2024) Editorial: Spotlighting the interaction network of hub genes, molecules, and cells in the tumor immune microenvironment (TIME) and their contribution to malignant progression.
Front. Immunol. 15:1533290.
doi: 10.3389/fimmu.2024.1533290

Editorial: Spotlighting the interaction network of hub genes, molecules, and cells in the tumor immune microenvironment (TIME) and their contribution to malignant progression

Jianpeng Li[1], Xuanbin Wang[2] and Run Shi[3]*

[1]Department of Cardiology, Taizhou Second People's Hospital, The Affiliated Taizhou Second People's Hospital of Yangzhou University, Taizhou, China, [2]Laboratory of Chinese Herbal Pharmacology, Department of Pharmacy, Renmin Hospital, Hubei University of Medicine, Shiyan, China, [3]Department of Oncology, The First Affiliated Hospital of Nanjing Medical University, Nanjing, China

KEYWORDS

tumor microenvionment, molecular subtyping, machine learning, precise medicine, cancer progression

Editorial on the Research Topic

Spotlighting the interaction network of hub genes, molecules, and cells in the tumor immune microenvironment (TIME) and their contribution to malignant progression

The tumor immune microenvironment (TIME) is a complex and dynamic network that comprises diverse elements, including various cell types, extracellular matrix components, and secreted molecules. These components interact with each other and deeply influence malignant phenotypes and therapeutic responses (1). For example, cancer cells can evade each step of the cancer immunity cycle by interacting with various immune cells (2). They can induce the recruitment of immunosuppressive cells, such as regulatory T cells (Tregs) and myeloid-derived suppressor cells (MDSCs), which could inhibit the activation and function of cytotoxic cells like T cells and natural killer (NK) cells (3). Furthermore, some tumor-associated macrophages (TAMs) can develop into a pro-tumor and immunosuppressive phenotype in response to tumor-derived signals (4). Besides, TIME has an impact on genomic instability and angiogenesis, and these alterations can jointly attenuate the therapeutic efficacy, especially immunotherapy for cancer (5). Therefore, we established the Research Topic to encourage researchers to focus on and further investigate the complex interactions within the TIME and their implications for cancer progression and treatments.

The Research Topic includes seven original articles and three reviews with a wide range of diverse cancer types. Three original articles focused on the tumor microenvironment (TME) and relevant molecules in hepatocellular carcinoma (HCC) from different perspectives. Gong et al. identified distinct molecular subtypes associated with

neutrophils in HCC, exhibiting significant differences in prognosis, clinical pathological characteristics, inflammation-related pathways, and immune-related features. Furthermore, the authors constructed a neutrophil-derived signature (NDS) to predict overall survival and efficacy of immunotherapy and chemotherapy for HCC patients using machine learning approaches. Additionally, Xu et al. reported two distinct m^6A modification patterns based on the 23 m^6A regulators, and the two m^6A subtypes correlate with different clinical outcomes and biological features. Subsequently, they developed an m^6A risk score model to improve survival prediction and estimation of drug responses for HCC patients. Moreover, Ouyang et al. conducted a comprehensive bioinformatics analysis to evaluate both the expression and mutation patterns of PANoptosis-related genes (PRGs) in HCC, and a PANoptosis risk model was constructed to offer a precise prediction of clinical outcomes and therapeutic sensitivity for HCC patients. The authors then performed experiments to validate the expression profiles and biological functions of their identified hub genes involved in the PANoptosis-related gene signature.

Despite different malignancies (osteosarcoma and chronic myeloid leukemia), the studies of Wu et al. and Zhong et al. shared similar ideas in investigating TME and implications for cancer treatment. They focused on differentially expressed genes (DEGs) and then identified different clusters with distinct immunological properties based on their expression profiles. They also commonly performed LASSO regression analysis to screen for key biomarkers of diagnosis or prognosis. Furthermore, sensitive drugs for specific subtypes or high-risk populations were investigated for precise treatment.

As regards immunosuppression, Bi et al. found that high expression of CDKL3 in esophageal cancer (ESCA) was not only associated with poor prognosis but also negatively correlated with the abundance of tumor-infiltrating immune cells and anti-tumor immune response. These findings suggest CDKL3 as an immunosuppressive molecule in the TME of ESCA. The authors also reported that the knockdown of CDKL3 in ESCA cells could inhibit autophagy induction and M2 macrophage polarization. Hypoxic TME is also a critical factor in the progression and outcome of solid cancers (6). To explore its influence on tumor progression and therapy outcome, Zhang et al. utilized Lasso regression to analyze transcriptomic data of patients with colorectal cancer (CRC) and identified seven robust hypoxia-associated genes. Based on these genes, the authors further established a novel prognostic score for CRC called the hypoxia-related prognosis score (HPS), and they found that HPS is significantly related to different extracellular matrix compositions, various immune cell infiltration, and suppressive immune response. The two articles suggest that some immunosuppressive factors involved in TME play important roles in shaping tumor progression, therapeutic resistance, and patient outcomes in solid cancers. These findings highlight the complexity of the TME in modulating immune responses and reveal the potential of targeting these factors to improve the therapy efficacy.

Overall, all the above-mentioned seven original articles regarding the identification of distinct molecular subtypes, immune-regulatory genes or molecules, and prognostic biomarkers in diverse cancer types or subtypes offer valuable insights into tumor progression and therapeutic sensitivity, which shows a promising way for personalized treatment strategies for cancer patients.

Li et al. focused on plasmablastic lymphoma (PBL), a rare but aggressive non-Hodgkin lymphoma. They comprehensively summarized the current knowledge on the epidemiology, molecular profiles, clinical and pathological features, differential diagnosis, treatment strategies, prognostic factors, and potential novel therapeutic approaches in PBL patients. This review highlights the fact that, despite developments in treatment strategies such as intensive chemotherapy, targeted therapies, and immunotherapy, the prognosis of PBL remains poor. Therefore, there is an urgent need for further exploration of PBL's biological characteristics and the development of more effective targeted therapeutic approaches. Another review from Guo et al. summarized five cellular composition modules by integrating the cellular (sub)types, phenotypes, and functions in the TME of pancreatic ductal adenocarcinoma (PDAC). Furthermore, the authors pointed out that cross-module regulations are determinants of the immunosuppressive TME in PDAC, and highlighted TME-targeted strategies that potentially improve PDAC therapy. In addition, Gunes et al. reviewed the current knowledge of the expression of signaling lymphocytic activation molecule family (SLAMF) receptors in solid tumors and tumor-infiltrating immune cells and summarized their associations with patient outcomes. The authors also discussed the therapeutic potential of targeting SLAMF receptors to improve outcomes of cancer therapy in solid tumors. Thus, a better understanding of the interactions between SLAMF receptors and TME components may contribute to the development of interventions that can reprogram the TME into a more favorable environment to enhance the efficacy of cancer therapy such as immunotherapy.

In summary, these studies contributed by diverse authors in this Research Topic highlight the important roles of TIME in cancer progression and therapeutic resistance. We believe these findings could show a promising way for personalized strategy to reprogram the TIME for improving cancer management.

Author contributions

JL: Writing – original draft. XW: Writing – review & editing. RS: Writing – review & editing.

Acknowledgments

We sincerely thank all the authors who contributed to this Research Topic.

Conflict of interest

The authors declare that the research was conducted in the absence of any commercial or financial relationships that could be construed as a potential conflict of interest.

Publisher's note

References

1. Baghban R, Roshangar L, Jahanban-Esfahlan R, Seidi K, Ebrahimi-Kalan A, Jaymand M, et al. Tumor microenvironment complexity and therapeutic implications at a glance. *Cell Commun Signal*. (2020) 18:59. doi: 10.1186/s12964-020-0530-4

2. Chen DS, Mellman I. Oncology meets immunology: the cancer-immunity cycle. *Immunity*. (2013) 39:1–10. doi: 10.1016/j.immuni.2013.07.012

3. Lindau D, Gielen P, Kroesen M, Wesseling P, Adema GJ. The immunosuppressive tumour network: myeloid-derived suppressor cells, regulatory T cells and natural killer T cells. *Immunology*. (2013) 138:105–15. doi: 10.1111/imm.2013.138.issue-2

4. Yang Q, Guo N, Zhou Y, Chen J, Wei Q, Han M. The role of tumor-associated macrophages (TAMs) in tumor progression and relevant advance in targeted therapy. *Acta Pharm Sin B*. (2020) 10:2156–70. doi: 10.1016/j.apsb.2020.04.004

5. Liu B, Zhou H, Tan L, Siu KTH, Guan XY. Exploring treatment options in cancer: Tumor treatment strategies. *Signal Transduct Target Ther*. (2024) 9:175. doi: 10.1038/s41392-024-01856-7

6. Shi R, Sun J, Zhou H, Hu T, Gao Z, Wang X, et al. Hypoxia within tumor microenvironment characterizes distinct genomic patterns and aids molecular subtyping for guiding individualized immunotherapy. *J Big Data*. (2024) 11:81. doi: 10.1186/s40537-024-00945-2

frontiers | Frontiers in Immunology

TYPE Original Research
PUBLISHED 28 July 2023
DOI 10.3389/fimmu.2023.1216585

OPEN ACCESS

EDITED BY
Xuanbin Wang,
Hubei University of Medicine, China

REVIEWED BY
Jiao Hu,
Central South University, China
Chen Yang,
German Cancer Research Center (DKFZ), Germany
Mario Perez-Medina,
National Polytechnic Institute (IPN), Mexico
Yi Liao,
Affiliated Hospital of Southwest Medical University, China

*CORRESPONDENCE
Fahui Liu
liufahui005@163.com
Yuhua Cao
caoyuhua78@163.com

†These authors have contributed equally to this work

‡These authors have contributed equally to this work

RECEIVED 04 May 2023
ACCEPTED 17 July 2023
PUBLISHED 28 July 2023

CITATION
Gong Q, Chen X, Liu F and Cao Y (2023) Machine learning-based integration develops a neutrophil-derived signature for improving outcomes in hepatocellular carcinoma.
Front. Immunol. 14:1216585.
doi: 10.3389/fimmu.2023.1216585

Machine learning-based integration develops a neutrophil-derived signature for improving outcomes in hepatocellular carcinoma

Qiming Gong[1,2†], Xiaodan Chen[3†], Fahui Liu[4*‡] and Yuhua Cao[1*‡]

[1]Department of Medical Oncology 2, The People's Hospital of Guangxi Zhuang Autonomous & Institute of Oncology, Guangxi Academy of Medical Sciences, Nanning, China, [2]Department of Nephrology, Affiliated Hospital of Youjiang Medical University for Nationalities, Baise, China, [3]Department of Medical Oncology 1, The People's Hospital of Guangxi Zhuang Autonomous & Institute of Oncology, Guangxi Academy of Medical Sciences, Nanning, China, [4]Xiamen Cell Therapy Research Center, The First Affiliated Hospital of Xiamen University, School of Medicine, Xiamen University, Xiamen, China

Introduction: The heterogeneity of tumor immune microenvironments is a major factor in poor prognosis among hepatocellular carcinoma (HCC) patients. Neutrophils have been identified as playing a critical role in the immune microenvironment of HCC based on recent single-cell studies. However, there is still a need to stratify HCC patients based on neutrophil heterogeneity. Therefore, developing an approach that efficiently describes "neutrophil characteristics" in HCC patients is crucial to guide clinical decision-making.

Methods: We stratified two cohorts of HCC patients into molecular subtypes associated with neutrophils using bulk-sequencing and single-cell sequencing data. Additionally, we constructed a new risk model by integrating machine learning analysis from 101 prediction models. We compared the biological and molecular features among patient subgroups to assess the model's effectiveness. Furthermore, an essential gene identified in this study was validated through molecular biology experiments.

Results: We stratified patients with HCC into subtypes that exhibited significant differences in prognosis, clinical pathological characteristics, inflammation-related pathways, levels of immune infiltration, and expression levels of immune genes. Furthermore, A risk model called the "neutrophil-derived signature" (NDS) was constructed using machine learning, consisting of 10 essential genes. The NDS's RiskScore demonstrated superior accuracy to clinical variables and correlated with higher malignancy degrees. RiskScore was an independent prognostic factor for overall survival and showed predictive value for HCC patient prognosis. Additionally, we observed associations between RiskScore and the efficacy of immune therapy and chemotherapy drugs.

Discussion: Our study highlights the critical role of neutrophils in the tumor microenvironment of HCC. The developed NDS is a powerful tool for assessing the risk and clinical treatment of HCC. Furthermore, we identified and analyzed the feasibility of the critical gene *RTN3* in NDS as a molecular marker for HCC.

KEYWORDS

neutrophils, HCC, *RTN3*, prognosis, machine learning

Background

Hepatocellular carcinoma (HCC), also known as liver cancer, is a common malignancy with a high incidence rate. Drugs such as sorafenib and lenvatinib (1), are widely used in the treatment of HCC, and new drugs like atezolizumab combined with bevacizumab and sintilimab combined with bevacizumab are being developed (2, 3). These drugs target specific populations, with some suitable for patients with unresectable HCC who have not undergone systemic treatment, like doxorubicin and lenvatinib (4, 5), while others are appropriate for patients with HCC who have received specific treatments, like regorafenib and cabozantinib (6). Despite promising results in clinical trials, these treatment methods only benefit a small proportion of patients, highlighting critical clinical challenges. Therefore, selecting the most appropriate treatment plan based on the specific conditions of the patients and the target population of the drug is crucial in the treatment of HCC. Advancements in biotechnology, particularly high-throughput sequencing technologies, have deepened our understanding of tumor molecular subtyping, enabling tumor treatment based on molecular subtypes. Gene-based molecular subtyping has emerged as a new approach to the treatment of tumors. Scientists have successfully developed personalized treatment plans based on molecular subtyping for various cancer types. For example, the *PAM50* gene subtyping technology has been successfully applied in chemotherapy decision-making for the treatment of breast cancer (7). *EGFR* gene mutation subtyping has also been widely adopted in the treatment of lung cancer for selecting targeted drugs against *EGFR (*8). Similarly, *BRAF* gene mutation subtyping has found extensive application in personalized treatment plans for colon cancer and melanoma (9, 10). These accomplishments indicate that gene-based molecular subtyping technologies will be crucial in future treatments of tumors, offering patients more accurate and effective treatment options.

The latest research has unveiled the immune microenvironment subtypes of HCC through large-scale single-cell sequencing and provided an in-depth analysis of the functional heterogeneity of tumor-associated neutrophils. This study demonstrates that targeting tumor-associated neutrophils may emerge as a new immunotherapy strategy for HCC (11). Neutrophils play a crucial role in the immune system by regulating immune responses, combating infections, and maintaining tissue homeostasis. Recent studies have indicated that neutrophil-mediated immune processes, known as neutrophil extracellular traps (NETs), have a significant impact on the development of tumors as they serve as a vital step in innate and adaptive immune responses triggered by infectious and sterile stimuli (12). Previous studies suggested that cancer-induced NETs primarily function in the circulation, promoting cancer-related thrombosis (13). Subsequent studies have revealed that NETs influence every stage of the metastatic cascade, including the progression, invasion, and migration of primary tumors, survival in circulation, chemoattraction to secondary sites, extravasation, colonization, and growth of metastatic tumor cells (14). These findings highlight the fact that the functional transformation of neutrophil subtypes in the tumor microenvironment is influenced by the specific characteristics of the tumor microenvironment, though the precise mechanisms remain unclear (15). In summary, neutrophils play pivotal roles in the development, metastasis, treatment, and immune evasion of HCC.

The advancement of single-cell research technology has brought about the ability to accurately analyze the heterogeneity of the tumor microenvironment in different clinical types of HCC and discern distinct subtypes of neutrophils with unique characteristics during the development of the tumor. These findings have been instrumental in uncovering the dynamic changes in levels of gene expression within these neutrophil subtypes, shedding light on the molecular mechanisms underlying the development of tumors, and identifying potential targets for diagnosis and treatment. However, it is important to note that neutrophils are fragile cell types that can easily be lost during tissue dissociation. Moreover, neutrophils have a limited number of expressed genes and tend to exhibit low expression levels of characteristic genes, further complicating the analysis of their cell subtypes and gene expression profiles. Additionally, the high cost associated with single-cell sequencing technology poses a significant barrier to its widespread clinical application for studying neutrophils. Nonetheless, it is feasible to differentiate patients with HCC based on neutrophils, thereby identifying subtypes and evaluating patient prognosis for clinical treatment and medication guidance. It is crucial to find a simple and effective method to describe the “neutrophil characteristics” of patients with HCC. With the advancements in bioinformatics technology, several prognostic gene characteristics have been developed (16, 17). In the case of HCC, numerous multi-gene signature characteristics, such as the well-known ferroptosis signature (18), m6A signature (19), and others (20), have been discovered to assess patient risk.

However, the efficacy of these multi-gene expression signatures can be challenging to validate and apply effectively due to single-machine learning and inappropriate statistical methods.

In this study, we used machine learning to develop and validate risk stratification characteristics for patients with HCC using neutrophil-related characteristic markers. We assessed the value of different risk stratifications in terms of biological and clinical pathological characteristics, prognosis, and their application in immunotherapy and targeted chemotherapy treatments across four independent public datasets. Furthermore, based on the analysis results, this study verified a new molecular marker for HCC. Overall, this study aims to optimize precision treatment and enhance the clinical outcomes of patients with HCC.

Materials and methods

Data resources

High-throughput sequencing data in TPM format for HCC were obtained from The Cancer Genome Atlas (TCGA) database, along with corresponding clinical phenotype data. We excluded samples that lacked survival time or status and retained only those with a survival time greater than 0 days. This resulted in 365 tumor samples. Similarly, we obtained another HCC high-throughput sequencing dataset, HCCDB18, from http://lifeome.net/database/hccdb/download.html. We removed normal samples to retain only tumor tissue and obtained survival data for all patients with a survival time greater than 0 days. This yielded a final set of 212 tumor tissues. For the datasets GSE14520 and GSE116174, we obtained expression profile data and survival times from the Gene Expression Omnibus (GEO) database of the National Center for Biotechnological Information (NCBI) database. We excluded samples lacking survival time or status and included all patients with a survival time greater than 0 days in the analysis. We downloaded platform files and converted probes to gene names. We removed data with one probe corresponding to multiple gene names and averaged data with multiple probes corresponding to a single gene. Ultimately, we identified 242 tumor tissues from the GSE14520 dataset and 64 tumor tissues from the GSE116174 dataset. Additionally, we obtained single-cell sequencing data for HCC (Accession number: GSE215428) from the GEO database.

Dimensionality reduction and cell annotation of single-cell clusters

First, we filtered the single-cell data that required each gene to be expressed in a minimum of three cells, while each cell had to express at least 250 genes. Additionally, we used the PercentageCharacteristicset function to calculate the proportions of mitochondrial and rRNA genes, ensuring that each cell expressed fewer than 2000 genes. Subsequently, we performed log-normalization on the data from six samples to standardize them. To identify highly variable genes, we utilized the FindVariableCharacteristics function, employing variance stabilization transformation ("vst"). All genes were then scaled using the ScaleData function, followed by dimensionality reduction using RunPCA to identify anchor points. The clustering of cells was achieved through the utilization of the FindNeighbors and FindClusters functions, and classical marker genes were used for cell annotation. The clusterProfiler package was used for the Kyoto Encyclopedia of Genes and Genomes (KEGG) pathway enrichment analysis of the marker genes across different subgroups.

Construction of molecular subtypes and risk model

Using single-cell analysis, 208 marker genes specific to neutrophils were identified. The ConsensusClusterPlus package in R was used to cluster patients based on the expression of these neutrophil marker genes in tumor tissues from the TCGA dataset. The partition around medoids (PAM) algorithm was used, with "pearson" serving as the distance metric. We performed 500 bootstraps, each including 80% of the patients from the training set. Clustering numbers ranging from 2 to 10 were set, and the optimal classification was determined by evaluating the consensus matrix and cumulative distribution function.

Based on the neutrophil marker genes, univariate Cox analysis was conducted to select prognostic-related genes with a P-value of <0.001. These genes were further integrated into a high-precision and stable model using our machine learning-based integration program. For the TCGA dataset, we fitted 101 prediction models using the LOOCV framework and calculated the concordance index (C-index) of each model on all validation datasets. The model with the highest average C-index was considered the best.

Analysis and comparison of biological features

We compared different cell scores among the three subtypes using the ESTIMATE algorithm, the MCPcounter package, and the CIBERSORT algorithm. To calculate the scores of 28 immune cells, we used single-sample gene set enrichment analysis (ssGSEA) with 28 characteristic genes of immune cells obtained from previous research (21). Additionally, the tumor immune dysfunction and exclusion (TIDE) software was used to evaluate the potential clinical effects of immunotherapy and risk models. To assess the scores of relevant pathways, we obtained the inflammatory pathway gene set from the KEGG website and calculated pathway scores using the ssGSEA method. Furthermore, the patient scores for KEGG database-related pathways were determined using the gene set variation analysis (GSVA) package in R, with gene sets downloaded from the GSEA website. The maftools package showed the top 20 mutated genes and generated a waterfall chart. The copy number variation (CNV) dataset was also obtained and analyzed to determine the proportion of deleted or amplified genes. To explore potential therapeutic targets for high- and low-risk groups, we used the Cancer Cell Line Encyclopedia (CCLE) database of drug-sensitive cell lines as the training set. Using the

Cancer Therapeutics Response Portal (CTRP) and Profiling Relative Inhibition Simultaneously in Mixture (PRISM) methods, we predicted the drug sensitivity of each patient in the TCGA dataset. Potential regulatory drugs were screened based on |log2 (Fold Change [FC])| >0.2.

Cell culture and transfection

The human HCC cell line HepG2 (KCB200507YJ) was obtained from the Chinese Academy of Sciences. The cells were cultured in Dulbecco's Modified Eagle's Medium (Gibco, Carlsbad, CA, USA) supplemented with 8.0% fetal bovine serum. To silence the expression of *RTN3*, HepG2 cells were transfected with small interfering RNA (siRNA) using hU6-MCS-CBh-gcGFP-IRES-puromycin (Shanghai Gene Chem Co., Ltd.). The HepG2 cells were divided into two groups: the control group and the si-RTN3 group.

Western blot assay

To obtain total cellular proteins from HepG2 cells, radioimmunoprecipitation assay buffer (RIPA) lysate (Beyotime, Shanghai, China) was used, and protein quantification was performed using the bicinchoninic acid (BCA) assay kit (Servicebio, Wuhan, China). Cell samples containing 30 μg of total protein were loaded onto sodium dodecyl sulfate-polyacrylamide gel electrophoresis (SDS-PAGE) and subsequently transferred to polyvinylidene fluoride (PVDF) membranes. The membranes were then incubated overnight at 4°C with anti-RTN3 (Abcam, Cat# Ab68328) and anti-β-tubulin (Affinity Biosciences, Cat# T0023). Subsequently, the membranes were incubated with goat anti-rabbit immunoglobulin G (IgG; S0001, 1:5000, Affinity Biosciences) and goat anti-mouse IgG (S0002, 1:5000, Affinity Biosciences) for 50 minutes and visualized using Tanon-5200 (Tanon, Shanghai, China). Further details regarding these experimental procedures have been described previously (22).

Colony formation and Transwell assay

For colony formation, cells were directly seeded into 6-well plates at a density of 3×10^2 cells per well. After 14 days, the wells were rinsed three times with phosphate-buffered saline (PBS) at room temperature. Subsequently, cells were stained with paraformaldehyde (1 ml/well) and incubated with crystal violet solution (1 ml/well) for 30 minutes. In the Transwell assay, 8-μm Transwell chambers (Corning, USA) were used. The upper chamber, pre-coated with Matrigel (Corning, USA), was used for cell plating, while the lower chamber was filled with a complete medium. After fixing the cells with paraformaldehyde, they were stained with a 0.1% crystal violet solution for five minutes and left to dry overnight. The specific steps of the Transwell assay were conducted as described previously (23).

Statistical analysis

Statistical analysis was conducted using R software (version 4.0.5). Spearman's correlation coefficient was used to evaluate the correlation between two continuous variables. The chi-square test was used to compare categorical variables, while the Wilcoxon rank sum test, or t-test, was used for comparing continuous variables. A significance level of $P < 0.05$ was used to determine statistical significance for all tests.

Results

Dimensionality reduction and clustering of single cells

After applying quality control measures and filtering, a total of 17,277 cells were obtained. The statistical analysis of cell numbers before and after filtering is shown in Figure S1A. To reduce dimensionality and identify anchor points, we performed Principal Component Analysis (PCA) using the RunPCA method (Figure S1B). Additionally, t-distributed Stochastic Neighbor Embedding (t-SNE) analysis was conducted on the 17,277 cells using the Runt-SNE function, and Figure S1C shows the t-SNE cell distribution maps for the six samples. For clustering analysis, we used the FindNeighbors and FindClusters functions with a resolution set at 0.2 and a dimensionality of 20. As a result, we identified 10 distinct subpopulations. Cell annotation was carried out using established marker genes, wherein subpopulations 0, 1, 2, and 4 exhibited expression of T-cell markers CD2, CD3D, CD3E, and CD3G, respectively. Subpopulation 6 showed expression of the B-cell markers CD19, CD79A, and MS4A1. The dendritic cell marker CLEC4C was expressed in subpopulation 9, while neutrophil markers CSF3R, S100A8, and S100A9 were found in subpopulations 3, 7, and 8, respectively (Figure S1D).

Figure 1A shows a t-SNE distribution map depicting different sample populations. Figure 1B shows a t-SNE distribution map specifically focusing on the 10 subpopulations. Furthermore, Figure 1C shows an annotated t-SNE distribution map highlighting the subpopulations. To identify marker genes within these subpopulations, the FindAllMarkers function was employed with specific parameters, including a logFC of 0.5 and a minimum percentage of differentially expressed genes (Minpct) of 0.35. This analysis yielded four subpopulations with a corrected P-value of <0.05. Figure 1D shows the expression of the top five significant marker genes in each of these subpopulations. Detailed information about the marker genes is provided in scRNA_marker_gene.txt (Table). Furthermore, KEGG annotation was conducted on the

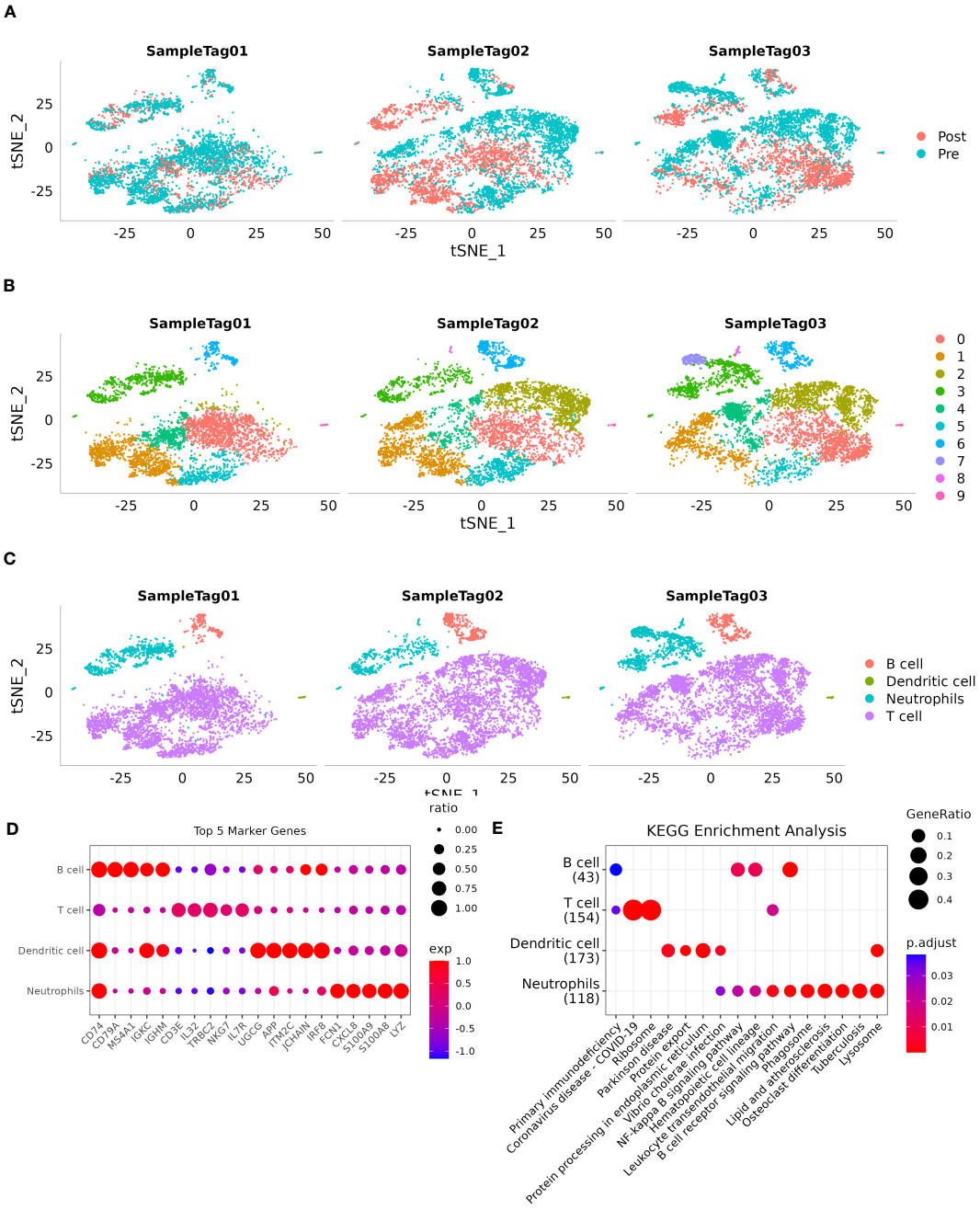

FIGURE 1
Single-cell landscape of patients with HCC. **(A)**: Distribution of each sample shown on a t-SNE plot; **(B)**: Distribution of 10 subtypes shown on a t-SNE plot; **(C)**: Subtypes after cell annotation shown on a t-SNE plot; **(D)**: Expression of the top five marker genes of annotated subtypes illustrated on a dot plot; **(E)**: KEGG enrichment analysis of annotated subtypes visualized on a dot plot.

marker genes from the four subpopulations. The results revealed their involvement in various functions and disease pathologies, highlighting the vital role of immune cells in maintaining overall health (Figure 1E).

Construction of molecular subtypes

Following the utilization of 208 markers specific to neutrophils, we proceeded to construct molecular subtypes. To determine the optimal number of clusters, we used cumulative distribution function (CDF) analysis. The CDF Delta area curve indicated that a cluster selection of 3 yielded relatively stable clustering results (Figures 2A, B). Consequently, we chose a "k" value of 3 to define three distinct molecular subtypes (Figure 2C). Notably, these three subtypes showed significant differences in prognosis (Figure 2D, P = 0.011), with patients in cluster 3 exhibiting the poorest prognosis. Similarly, when applying the same methodology to the HCCDB18 dataset, we obtained three subtypes with comparable prognostic implications (Figure 2E; P <0.0001). Detailed information about the

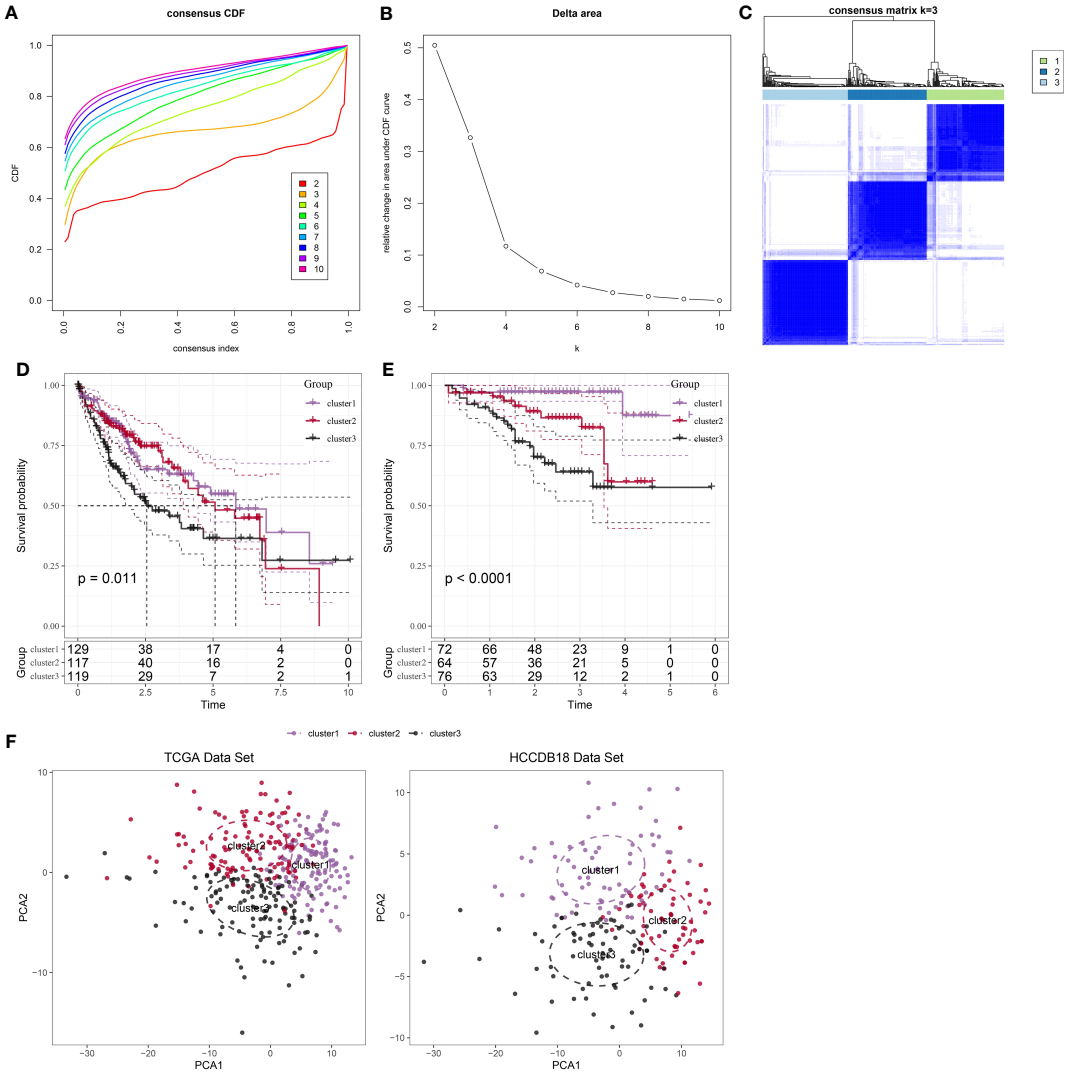

FIGURE 2
Identification and analysis of subtypes with neutrophil characteristics in patients with HCC. **(A)**: CDF curve of samples from the TCGA dataset. **(B)**: Delta area curve of consensus clustering for samples from the TCGA dataset, showing the relative change in the area under the CDF curve for each category number "k" compared to "k-1." The horizontal axis represents the category number "k," while the vertical axis represents the relative change in the area under the CDF curve. **(C)**: Heatmap showing the sample clustering at consensus "k = 3." **(D)**: KM curves demonstrating the prognosis of three subtypes in the TCGA dataset. **(E)**: KM curves demonstrating the prognosis of three subtypes in the HCCDB18 dataset. **(F)**: PCA showing the distribution of three subtypes in the TCGA and HCCDB18 datasets.

molecular subtypes for both datasets can be found in tables tcga.subtype.cli.txt and HCCDB18.subtype.cli.txt. Furthermore, we conducted PCA analysis based on the marker genes specific to neutrophils, generating a scatter plot that illustrates the distribution of the three subtypes as shown in Figure 2F. Our analysis suggests that the significant heterogeneity observed among patients with HCC may be attributed to distinct "neutrophil characteristics."

Clinical features of molecular subtypes

Furthermore, we conducted a comprehensive analysis of the clinical and pathological characteristics of different molecular subtypes in the TCGA dataset. Specifically, we compared the distribution of various clinical characteristics among the three molecular subtypes to identify potential differences. In our analysis, while applying a chi-square test, we found that cluster 3 samples exhibited a higher proportion of patients with G3 plus G4 stages compared to the other subtypes. This finding suggests a potential association between molecular subtypes and tumor grade (Figure 3).

Functional analysis of immune-related pathways among molecular subtypes

First, we used the ESTIMATE algorithm to calculate the immune scores of patients. The comparison showed that clusters 2 and 3, which were associated with a poor prognosis, exhibited higher

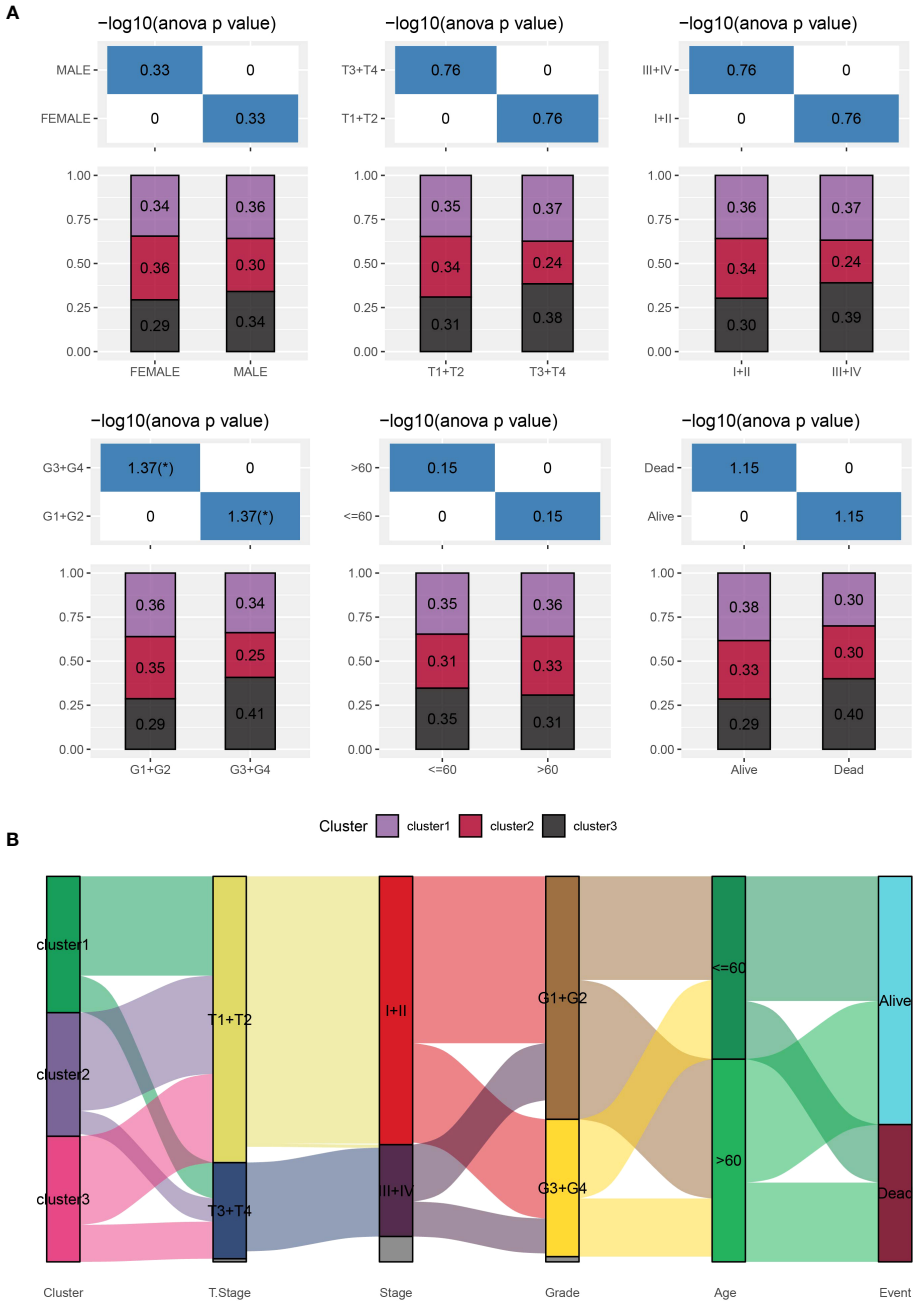

FIGURE 3
Distribution of clinical characteristics across different subtypes. **(A)**: Sample distribution of clinical characteristics across different subtypes in the TCGA-LIHC cohort. The horizontal axis represents the different sample groups, while the vertical axis represents the percentage of clinical information within the corresponding group samples. Different colors represent different molecular subtypes. **(B)**: Sankey Diagram showing the association between different subtypes and clinicopathological characteristics in patients with HCC.

immune cell scores (Figure 4A). Subsequently, we used the MCPcounter package to calculate scores for 10 different types of immune cells. These results also indicated that clusters 2 and 3 showed higher immune cell scores (Figure 4B). Furthermore, we used the Cell-type Identification by Estimating Relative Subsets of RNA Transcripts (CIBERSORT) method to calculate scores for 22 different types of immune cells. This analysis demonstrated significant differences in the majority of immune cell types among the three subtypes (Figure 4C). Moreover, we conducted a comparison of the expression levels of immune checkpoint genes. With the exception of *TNFSF4* and *ICOSLG*, the majority of the immune checkpoint genes showed varying expression levels among the three subtypes. Notably, clusters 2 and 3 showed higher levels of immune checkpoint gene expression (Figure 4D). In summary, our comprehensive analyses indicated that clusters 2 and 3, which were associated with a poor prognosis, showed higher levels of immune infiltration.

10.3389/fimmu.2023.1216585

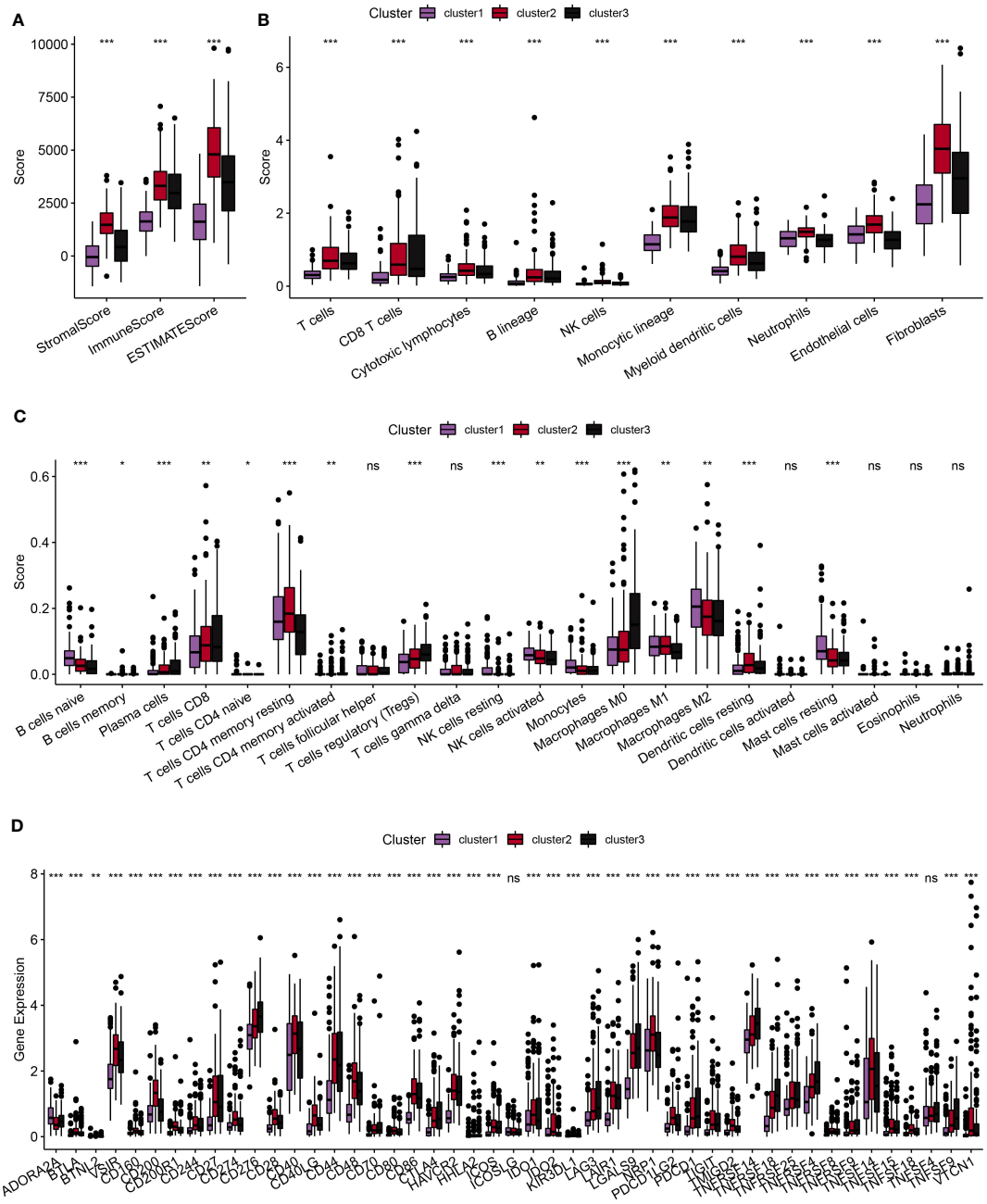

FIGURE 4
Comparative analysis of immune characteristics among different subtypes. **(A)**: Comparative analysis of immune characteristics among different subtypes in the TCGA dataset, focusing on the predicted immune scores by ESTIMATE. **(B)**: Comparative analysis among different subtypes in the TCGA dataset, examining the scores of 10 predicted immune cell types using the MCPcounter method. **(C)**: Comparative analysis of immune characteristics among different subtypes in the TCGA dataset of scores of 22 predicted immune cell types using the CIBERSORT algorithm. **(D)**: Comparative analysis of immune characteristics among different subtypes in the TCGA dataset, highlighting the expression of immune checkpoints across the three subtypes. ns, $p \geq 0.05$; *, $p < 0.05$; **, $p < 0.01$; ***, $p < 0.001$; ****, $p < 0.0001$.

Analysis of inflammatory pathways among molecular subtypes

We employed the TIDE online tool to predict the likelihood of immune evasion in patients, where a higher TIDE score indicates a more significant potential for immune evasion. As shown in Figure 5A, clusters 2 and 3, which were associated with poor prognoses, showed higher TIDE scores compared to cluster 1, suggesting a greater tendency for immune evasion. Since the molecular subtypes constructed were closely associated with the immune system, we acquired inflammation-related pathway gene sets from the KEGG website and calculated the pathway scores using the ssGSEA method.

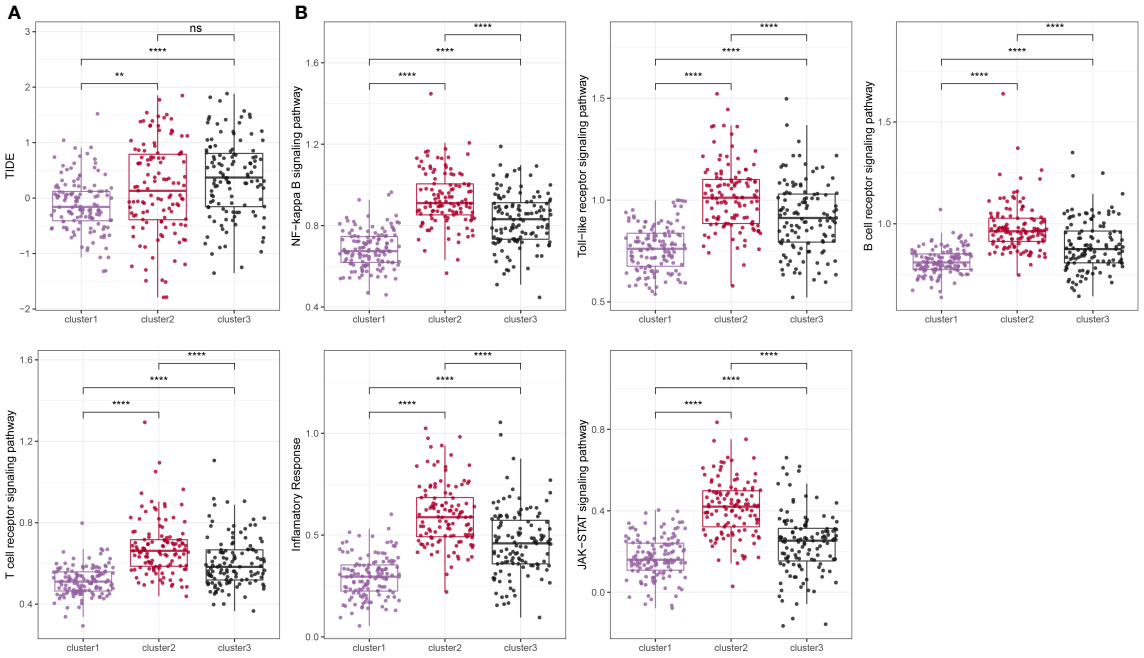

FIGURE 5
Comparison of TIDE score and inflammation-related pathway score among different subtypes. ns, $p \geq 0.05$; **, $p < 0.01$; ****, $p < 0.0001$.

As shown in Figure 5B, we observed that cluster 1 had significantly lower inflammatory pathway scores compared to the other subtypes.

KEGG pathway analysis of molecular subtypes

To explore the heterogeneity of patients with HCC, we obtained KEGG pathway-related gene sets from the GSEA website and calculated pathway scores for each patient using the R package GSVA. By analyzing these scores, we identified multiple pathways that showed significant differences among the three subtypes of HCC, as shown in Figure 6A. Further details and the results of our analysis are summarized in pathwy_p_fit.txt. Additionally, we conducted a comparison of differential gene expression among the different subtypes and performed GSEA analysis using the R package clusterProfiler. Figures 6B–D show the patterns of pathway activation and suppression observed across the distinct subtypes of HCC. In summary, our findings demonstrated that marker genes associated with neutrophils effectively distinguished the heterogeneity of patients with HCC. Intriguingly, these marker genes suggested the presence of "neutrophil characteristics" among patients with different subtypes of HCC.

Construction of a neutrophil-derived signature and investigation of the role of *RTN3* in HCC

Based on the identified "neutrophil characteristics" among patients with HCC, we conducted an analysis to identify prognosis-related genes. Using univariate Cox regression analysis with a significance level of P <0.001, we identified 20 genes, as shown in Figure 7A. These genes were derived from marker genes based on neutrophils and obtained from the TCGA database. To develop a consistent prognostic model, we used a machine learning-based integration program, using the 20 identified genes as input characteristics. Specifically, we fitted 101 prediction models using the Leave One Out Cross-Validation (LOOCV) framework. We calculated the C-index of each model across all validation datasets, as shown in Figure 7B. The optimal model, which combined CoxBoost and RSF, yielded the highest average C-index of 0.671.

Further analysis focused on 10 critical genes, such as *ANXA5, ATP6V0B, GAPDH, GRB2, PRKCD, RAC1, RTN3, S100A9, TALDO1*, and *TKT*. We examined the expression levels of these genes in both the TCGA dataset and other validation sets. By employing the rfsrc function, we predicted the risk score for each patient based on the expression levels of these 10 genes. Subsequently, we standardized the risk scores into z-scores. Using a cutoff of 0, we divided patients into high- and low-risk groups within different datasets, including GSE14520, GSE116174, HCCDB18, and TCGA-LIHC, as shown in Figure 7C. In summary, our findings suggest that this 10-gene signature could serve as a robust prognostic tool for patients with HCC.

The significant expression differences of *RTN3* in multiple HCC cohorts indicate an association between its expression level and HCC patient prognosis(Figure S2). We conducted an experiment using siRNA to manipulate the levels of *RTN3* in HepG2 cells. In comparison to the control group, the si-RTN3 group showed a significant decrease in the expression of the *RNT3* protein, as shown in Figure 7D. The colony formation assay showed that the proliferation ability of HepG2 cells was significantly inhibited in the

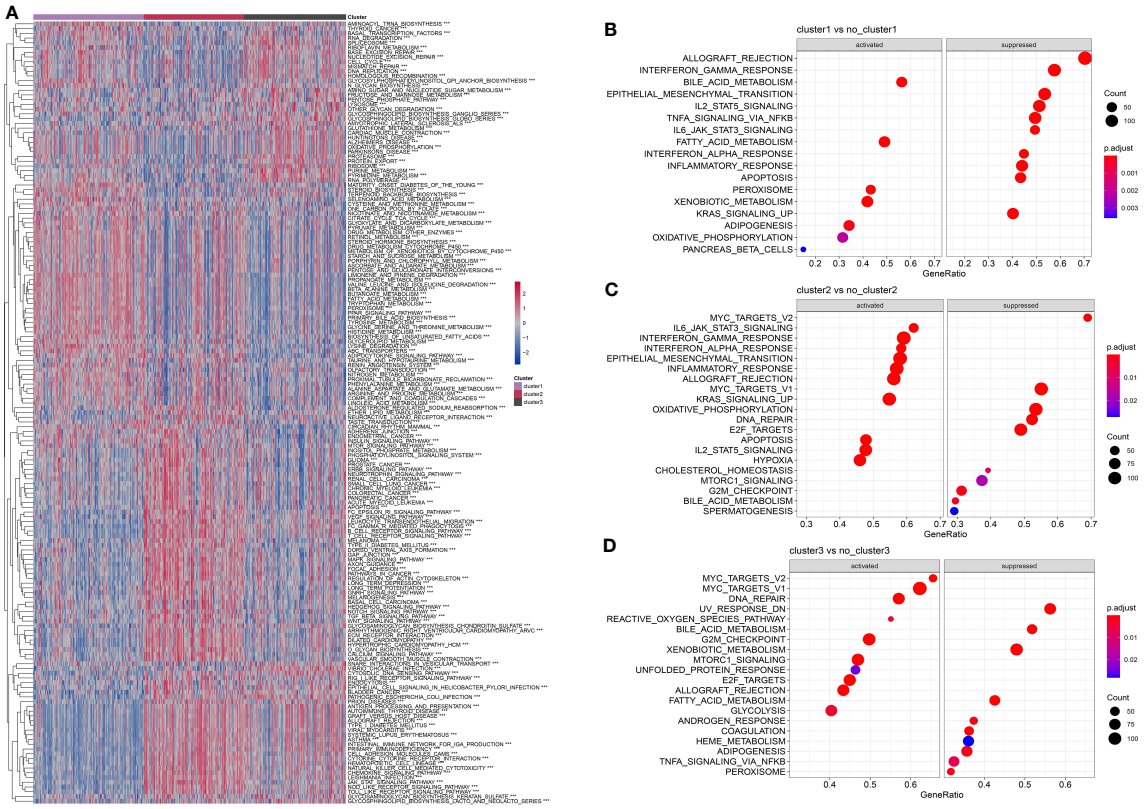

FIGURE 6
Comparison of pathway characteristics among different subtypes in the TCGA dataset. **(A)**: A heatmap showing the enrichment scores for enriched pathways in three subtypes of the TCGA dataset. **(B)**: A bubble plot showing the enriched pathways in cluster 1 of the TCGA dataset. **(C)**: A bubble plot showing the enriched pathways in cluster 2 of the TCGA dataset. **(D)**: A bubble plot showing the enriched pathways in cluster 3 of the TCGA dataset. ***, $p < 0.001$.

si-RTN3 group compared with the control group (Figure 7E). Additionally, the Transwell assay demonstrated that there was a decrease in the number of migrated and invaded cells in the si-RTN3 group compared to the control group (Figures 7F, G). Overall, our findings indicate that the knockdown of *RTN3* suppressed the proliferation, migration, and invasion of HepG2 cells.

Comparison of RiskScore based on different clinical characteristics

To examine the association between RiskScore and the clinical characteristics of tumors, we conducted an analysis using the TCGA dataset. Our findings revealed a positive correlation between clinical grade and risk score (Figures 8A, B). Additionally, we compared the high and low-risk scores across different clinical grades and observed that patients with higher clinical grades showed higher risk scores (Figure 8C). Subsequently, we performed both univariate and multivariate Cox regression analyses to investigate the prognostic significance of these clinical characteristics, as shown in Figures 8D, E. The results indicated that T-stage (P <0.001), Stage (P <0.001), and RiskScore (P <0.001) were all associated with prognosis and served as independent risk factors. However, the multivariable Cox regression analysis revealed that only RiskScore (P <0.001) remained significantly associated with prognosis. Additionally, we constructed a nomogram incorporating RiskScore, T-stage, and Stage. We assessed its performance by calculating the area under the curve (AUC) value and found that its predictive accuracy was similar to that of RiskScore alone (Figure 8F). These findings indicate that our RiskScore-based model holds significant prognostic value for patients.

Mutation features of the prognostic model

Using the R language maftools package, we generated a waterfall plot showing the top 20 genes with mutations. The data showed higher mutation frequencies in the high-risk group compared to the low-risk group (Figure 9A). Furthermore, we conducted a comparison between the high-risk and low-risk groups, examining the distribution of homologous recombination defects (P <0.001), fraction altered (P <0.001), number of segments (P <0.001), and tumor mutation burden (P <0.001). As shown in Figure 9B, there were significant differences in fraction altered, number of segments, and tumor mutation burden between the high- and low-risk groups. We also obtained CNV data and showed the proportions of deletions and amplifications for the 10 genes used in constructing the risk model (Figure 9C).

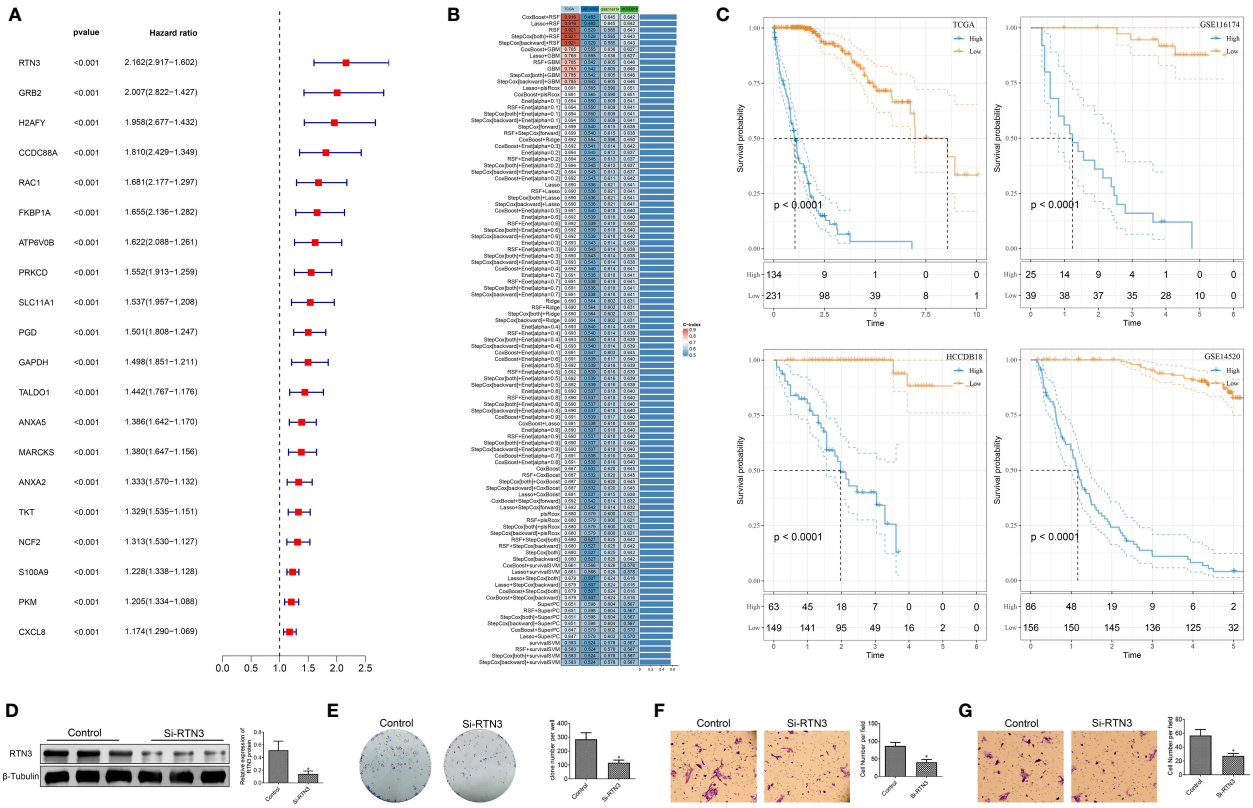

FIGURE 7
Construction of the prognostic model based on machine learning and biological functional analysis of RTN3. **(A)**: A forest plot showing prognostic-related genes identified in the analysis. **(B)**: Optimal combination of machine learning-based feature selection for constructing the risk model. **(C)**: Kaplan-Meier curves demonstrating the high- and low-risk groups in the training and validation sets. **(D)**: Western blot analysis showing the expression of RTN3 protein in HepG2 cells after transfection of si-DUSP1. **(E)**: Assessment of the proliferation activity of HepG2 cells using a colony formation assay. **(F, G)**: Evaluation of migration and invasion abilities of HepG2 cells using a Transwell assay. *, p < 0.05.

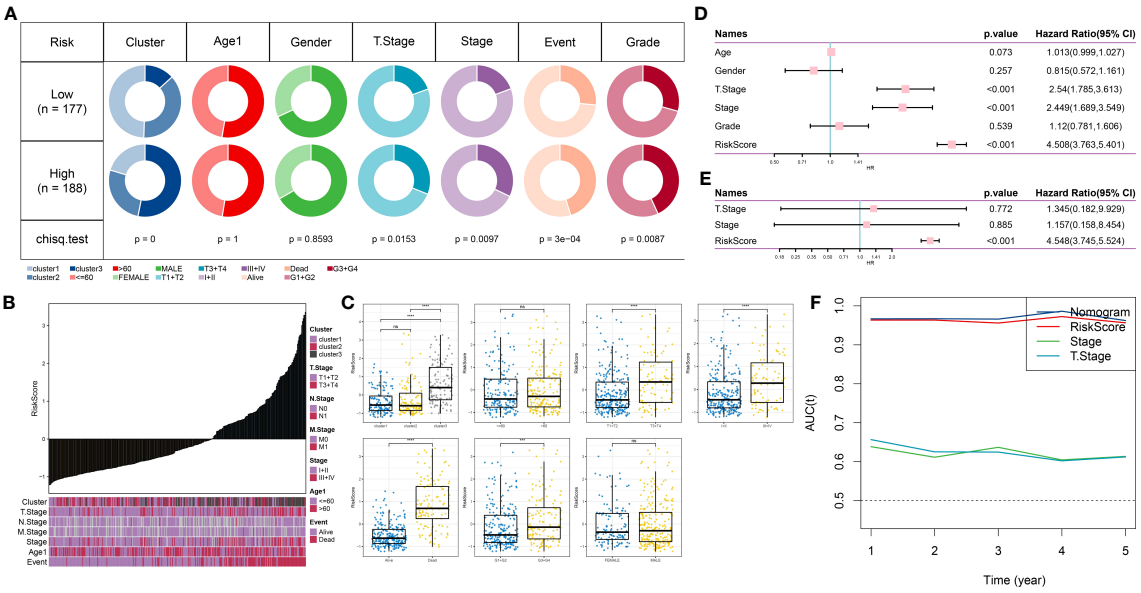

FIGURE 8
Clinical applications of the prognostic model. **(A)**: Comparison of different clinical characteristics between high-risk and low-risk groups. **(B)**: Distribution of different clinical characteristics with increasing risk scores. **(C)**: Comparison of risk scores among different clinical characteristics. **(D)**: Forest plot of univariate Cox analysis for clinical characteristics. **(E)**: Forest plot of multivariate Cox analysis for clinical characteristics. **(F)**: Trend of changes in AUC for T-stage, Stage, and Risk Score for one to five years. ns, p≥ 0.05; ***, p < 0.001; ****, p < 0.0001.

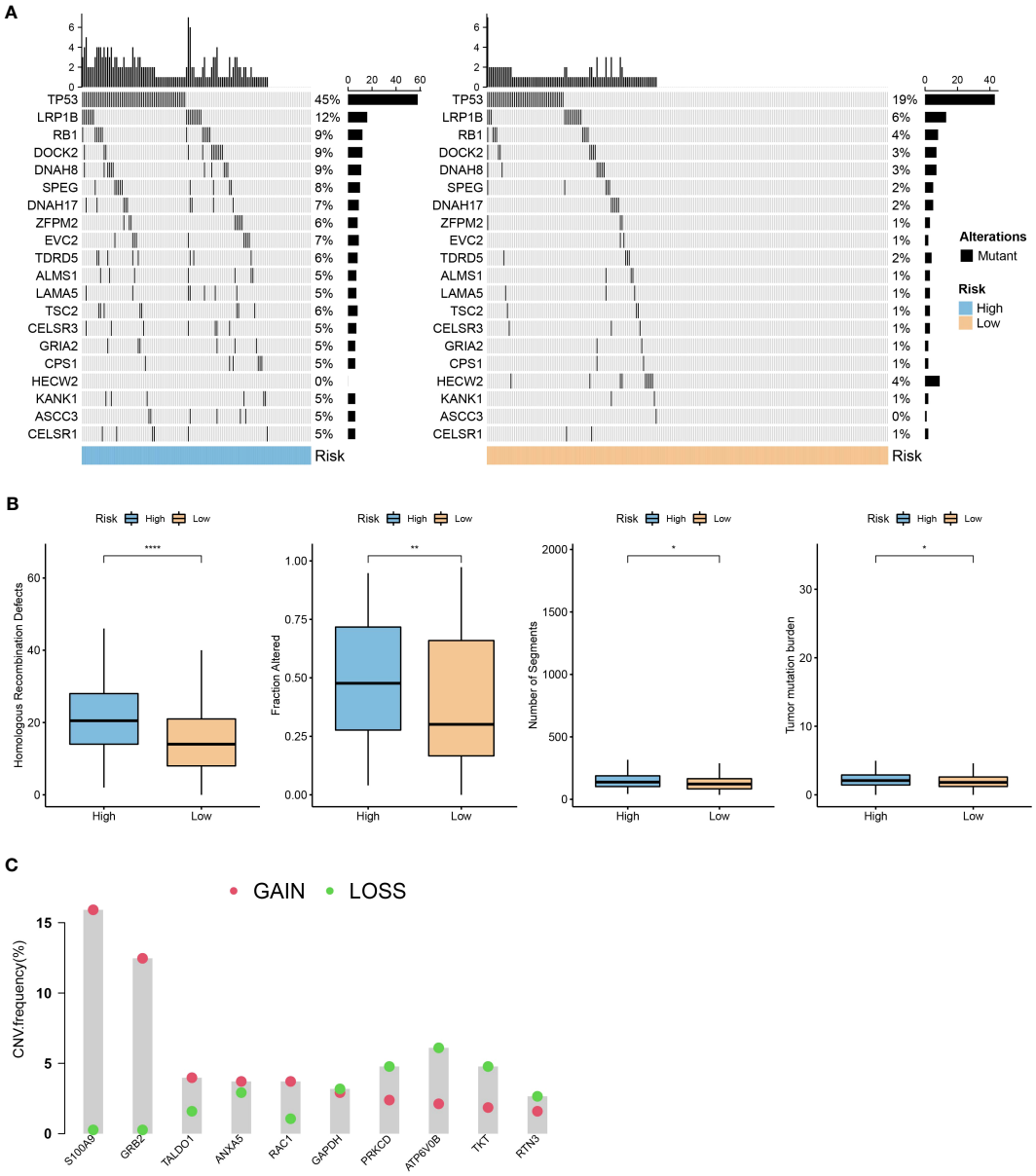

FIGURE 9
Mutation characteristics of the prognostic model. **(A)**: A waterfall plot of the top 20 gene mutations in high-risk and low-risk groups. **(B)**: Comparison of differences in homologous recombination defects, fraction altered, number of segments, and tumor mutation burden between high- and low-risk groups in the TCGA dataset. **(C)**: Distribution of the proportion of patients with gene CNV mutations in the TCGA dataset module. *, $p < 0.05$; **, $p < 0.01$; ****, $p < 0.0001$.

Immune features of the prognostic model

We conducted an analysis to examine the correlation between RiskScore and 28 immune cells using the ssGSEA method (Figure 10A). Notably, several immune cells showed a significant correlation with the RiskScore. To provide a visual representation of these correlations, scatter plots were generated to depict the correlation between 12 immune cells and RiskScore (Figure 10B). Furthermore, we used the TIDE software (available at http://tide.dfci.harvard.edu/) to assess the potential clinical effects of immune therapy in conjunction with our risk model. Higher TIDE prediction scores indicate a greater likelihood of immune evasion and a reduced possibility of benefiting from immune therapy. As shown in Figure 10C, patients with a high RiskScore tended to have higher TIDE prediction scores, suggesting a diminished likelihood of benefiting from immune therapy. Furthermore, our analysis revealed a higher proportion of high-risk patients in the non-responsive group compared to the responsive group (Figure 10D). Notably, the non-responsive group exhibited higher TIDE prediction scores (Figure 10E). These findings collectively indicate that our RiskScore-based model has the ability to predict the response to immune therapy and identify patients who may not derive substantial benefits from it.

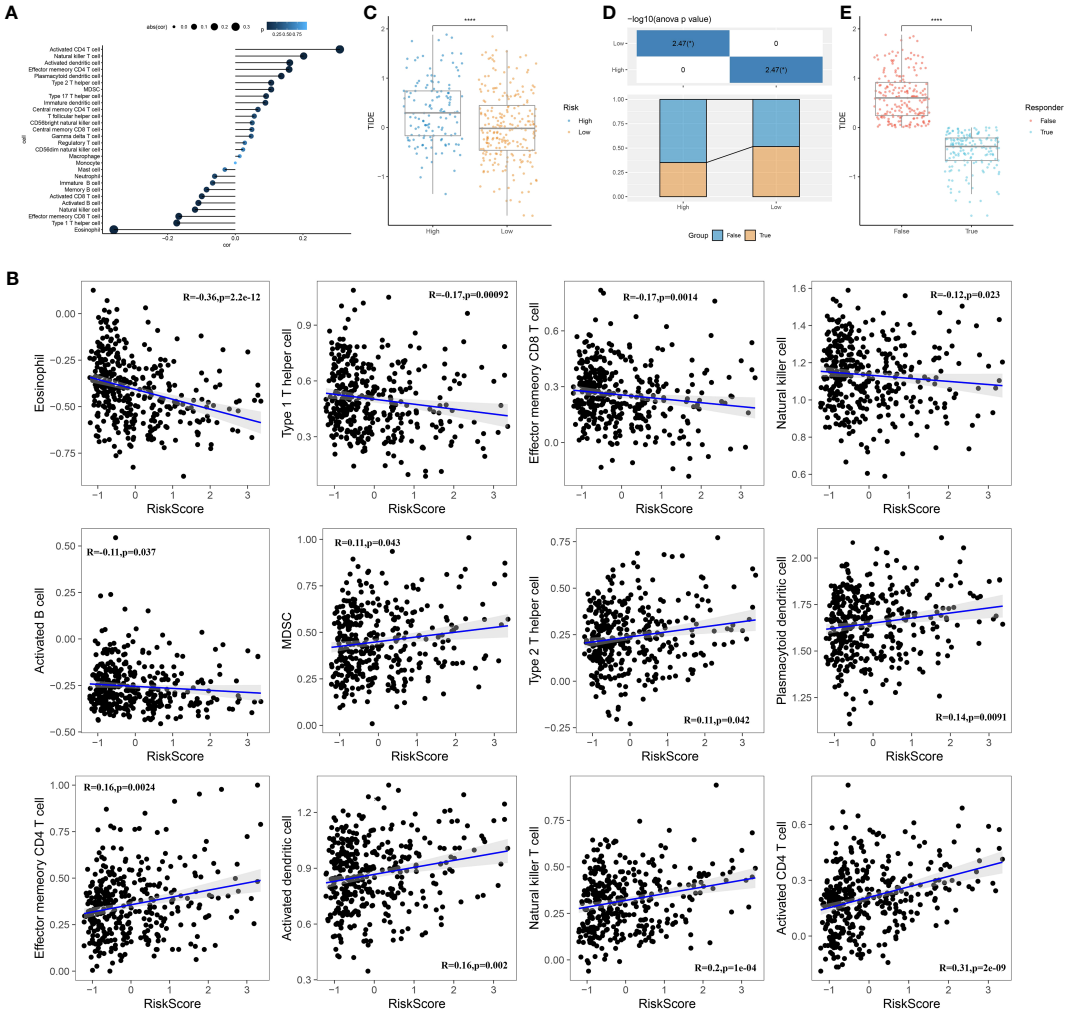

FIGURE 10
Immune characteristics of the prognostic model. **(A)**: Correlation analysis between the scores of 28 immune cells and risk scores. **(B)**: A scatter plot analysis of the correlation between risk scores and immune cells. **(C)**: Comparison of risk scores with TIDE scores. **(D)**: Comparison of the distribution of immune therapy response, non-response, and high- or low-risk groups. **(E)**: Comparison of TIDE scores between the immune therapy response and non-response groups. ****, $p < 0.0001$.

Identification of potential therapeutic drugs for HCC

To identify candidate drugs with higher drug sensitivity, we employed two distinct approaches using drug response data from the Cancer Therapeutics Response Portal (CTRP) and Profiling Relative Inhibition Simultaneously in Mixture (PRISM) datasets. First, we conducted a differential drug response analysis by comparing the top 10% and bottom 10% groups based on the pharmacological profiling score (PPS). This analysis allowed us to identify compounds with log2FC >0.10 that exhibited lower AUC estimates in the high RiskScore group. Second, we conducted a Spearman correlation analysis between the AUC values and the RiskScore. We selected compounds that showed negative correlation coefficients (Spearman's r for CTRP and PRISM, <-0.10 and <-0.1, respectively). The results from both approaches consistently demonstrated that all identified compounds had lower AUC estimates in the high RiskScore group and were negatively correlated with RiskScore (Figures 11A, B).

Discussion

Over the past few decades, the tumor, node, and metastasis (TNM) staging system has played a critical role in the clinical evaluation and treatment of cancer. It provides a framework for describing the clinical course of cancer and categorizing patients into different stages based on factors such as tumor size, lymph node involvement, and distant metastases. Recently, new staging systems have emerged, such as the eighth edition staging system by the American Joint Committee on Cancer. The choice of a staging system is important as it guides treatment selection and prognostic evaluation based on the individual circumstances of the patients. With advancements in molecular biology and immunology, the

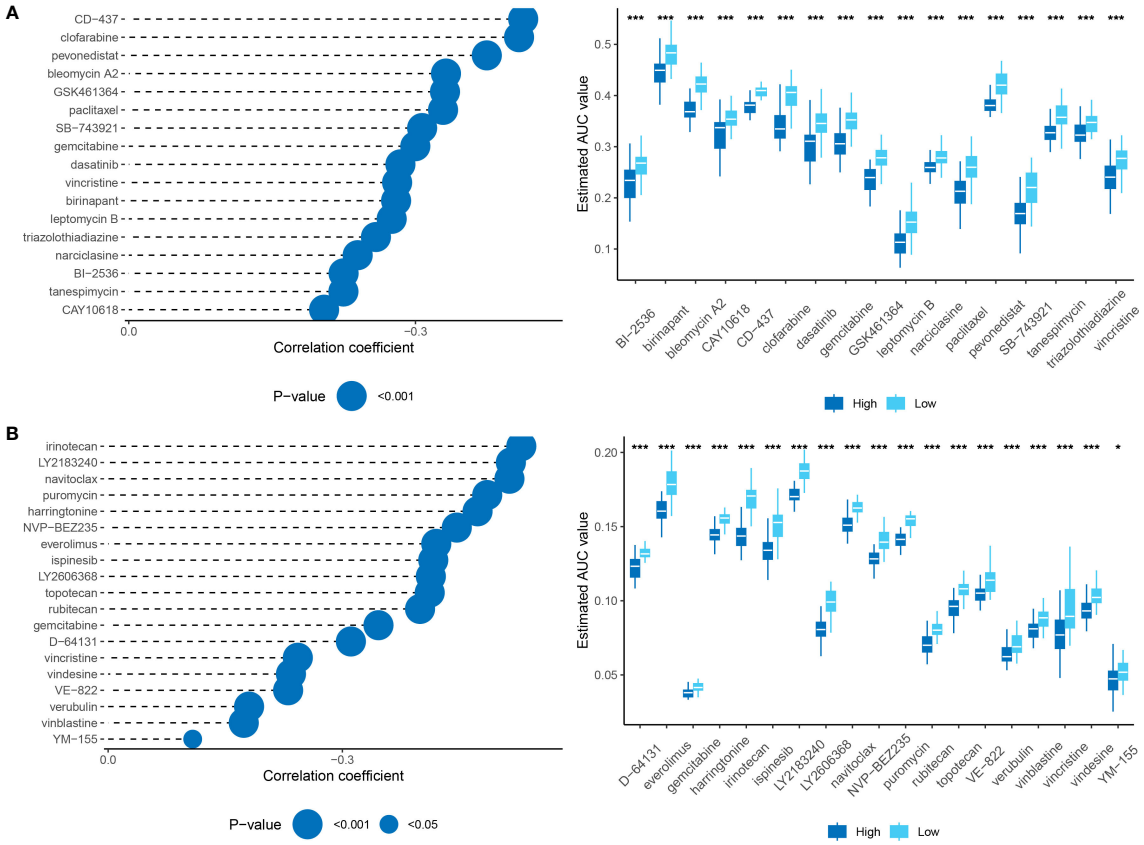

FIGURE 11
(A): Results of Spearman's correlation analysis and differential drug response analysis of CTRP-derived compounds. **(B)**: Results of Spearman's correlation analysis and differential drug response analysis of PRISM-derived compounds. Note that lower values on the y-axis of boxplots indicate greater drug sensitivity. *, $p < 0.05$; ***, $p < 0.001$.

treatment for HCC has become more diverse, including the use of anti-angiogenic drugs like sorafenib and combination targeted therapy with immune checkpoint inhibitors (24). This diversity highlights the need for better-personalized assessment methods to guide clinical decisions for patients. However, the identification of reliable biomarkers that can accurately identify "personalized" patients with HCC still requires further exploration. We deem it unfeasible to extrapolate this genetic feature to other tumor types due to the variability of biomarkers in different types and subtypes of tumors. Unique biological and genetic features in each tumor type may affect the expression of tumor biomarkers. Consequently, a more comprehensive analysis and assessment are necessary before exploring the suitability of biomarkers in specific tumors. Future research aims to identify more generalized and broadly applicable neutrophil characteristics, which will offer precise and convenient guidance for studying tumor subtypes.

Currently, gene signature models have gained widespread utilization in predicting and diagnosing various diseases, including cancer, cardiovascular disease, and diabetes. These models offer the advantage of simultaneously assessing the expression levels of multiple genes using high-throughput technology, allowing for comprehensive information gathering and a deeper understanding of the underlying biological mechanisms of diseases. By considering multiple genes, gene signature models can mitigate the impact of changes in the expression level of a single gene on the prediction outcomes, thereby improving the accuracy and reliability of the predictions. Recent studies have emphasized the significance of neutrophils as both a prognostic indicator and a target for immune therapy in HCC. However, there is a paucity of studies that accurately predict patient prognosis and determine the efficacy of drug treatment using large-scale machine-learning models specific to HCC. To address this gap, our study aimed to investigate the association between the expression characteristics of neutrophil markers and their potential for benefiting from specific drug therapies in HCC.

Recent advancements in high-dimensional single-cell analyses have provided insights into the heterogeneity of neutrophils present in both the circulation and tumor microenvironments. These studies have revealed variations in transcriptomics and surface protein expression among neutrophils, which can impact the efficacy of immune therapies in patients with cancer (11). The pivotal role of neutrophils in unraveling the heterogeneity of tumors through the identification of molecular markers on their surface has been elucidated. Based on these findings and the potential of neutrophils as effective biomarkers for distinguishing the heterogeneity of tumors, our study aimed to classify patients with HCC based on the expression of neutrophil marker genes at the transcriptome level. The results of the analysis showed significant

differences among patients belonging to different subtypes after stratification. Notably, these subtype differences correlated with variations in patient survival, which were further validated across multiple datasets. These findings highlight the feasibility of subtype differentiation based on neutrophil characteristics.

Furthermore, this study further explored the biological differences among the different subtypes of HCC and identified significant differences in signaling pathways by comparing the activity levels of key signal pathways. These findings imply that neutrophils may have a crucial role in the dysregulation of signaling pathways within tumors. However, intriguingly, when examining clinical pathological characteristics, we observed significant differences only in tissue grade among patients classified into different subtypes. On one hand, this observation suggests a potential correlation between subtype classification and the grading of tumors, indicating that neutrophils may serve as a key factor influencing the grading of patients with HCC—a relationship that has not been previously reported. It is important to note that these results may also be influenced by sample size or other factors, warranting further investigation to elucidate the specific underlying mechanisms. Nonetheless, the analysis outcomes of this study vividly demonstrate the presence of distinct "neutrophil characteristics" among patients with different subtypes of HCC.

Based on the feasibility of using "neutrophil characteristics" for the classification of HCC, this study employed univariate Cox regression analysis and a machine learning-based integration program to screen 20 prognosis-related genes derived from characteristic neutrophil genes. Subsequently, a prognostic model was constructed using 10 essential genes. By predicting the expression values of these 10 genes in the TCGA dataset and validation gene set, patients from different datasets were successfully classified into high-risk and low-risk groups. The validation across multiple datasets consistently demonstrated that the high-risk group exhibited a poorer prognosis, while the low-risk group showed a better prognosis.

Furthermore, significant variations were observed in immune cell infiltration levels and immune therapy responses among different cells. Similar research methodologies have been adopted in previous studies to investigate the long noncoding RNA (lncRNA) characteristics of patients with colorectal cancer (CRC), enabling effective evaluation of recurrence, prognosis, chemotherapy response, and immune therapy. These findings are consistent with the results obtained in our study (20). However, lncRNA has inherent challenges such as a low expression level, long and highly variable sequences, and complex detection and measurement processes. In contrast, mRNA-based gene models offer greater clinical translatability and the potential for in-depth research in the future. Additionally, while this study employed multiple datasets for verification, it primarily focused on liver cancer research. In future studies, it is important to validate the generalizability of the model across a broader range of cancer types using additional datasets. Moreover, it is worth noting that this study solely relied on RNA expression data and did not consider other genetic and environmental factors that contribute to the development of liver cancer. Therefore, further refinement of the model is necessary to improve its accuracy by incorporating additional relevant factors. Nevertheless, the existing research results presented in this study confirm and emphasize the feasibility and promising clinical application prospects of the methodology used.

In addition to identifying the "neutrophil characteristics" of HCC, this study also conducted a comprehensive investigation of the gene *RTN3*, which has a significant impact on prognosis. RTN3 is a membrane protein that plays a crucial role in the formation of the endoplasmic reticulum and the regulation of membrane protein acyltransferase activity in normal cells. Extensive research has focused on the role of RTN3 in Alzheimer's disease, where transgenic mice overexpressing RTN3 show neuroinflammatory abnormalities. Additionally, studies have highlighted the interaction between RTN3 and the oncogene *Ras* within the endoplasmic reticulum. Despite some studies reporting on RTN3 in research on HCC, there remain controversies surrounding its role. For example, certain studies have reported significant upregulation of the levels of RTN3 mRNA and proteins in tumor tissues as a risk factor in risk models (25). Conversely, another study showed that low expression of RTN3 in patients with HCC was significantly associated with poor prognosis, suggesting a potential tumor suppressor role for RTN3 (26). Based on previous studies, it is hypothesized that the role of *RTN3* in HCC is likely influenced by the viral infection status of patients with HCC. On the one hand, studies have reported that the hepatitis B virus (HBV) can induce non-mutational inactivation of the *p53* signaling pathway by interacting with RTN3, which is a crucial mechanism promoting the occurrence and development of HCC. Additionally, a study has demonstrated that RTN3 can directly interact with the non-structural protein of the hepatitis C virus (HCV), leading to the limitation of HCV replication. Therefore, viral infection status may serve as a key determinant of the role of *RTN3* in HCC, although the exact underlying mechanisms still require further investigation. In summary, the research on the role of *RTN3* in tumors remains relatively limited, and the associated mechanisms and biological significance necessitate further investigation. The results of this study indicate that the knockdown of *RTN3* effectively inhibits the proliferation, invasion, and metastasis of tumor cells, thereby confirming the importance of the genes identified in the risk model and providing initial insights into the role of *RTN3* in HCC.

The primary objective of this study is to demonstrate the effective stratification of patients with HCC using neutrophil characteristics of the genes. The application of NDS is theoretically more efficient in clinical decision-making as it primarily involves commonly expressed transcriptome genes. This approach offers cost-effective and personalized molecular feature descriptions to aid in formulating effective treatment strategies and assessing disease progression. However, the study has certain limitations that need to be considered. Firstly, differences in sample sources, data preprocessing, and analysis methods may lead to variations in gene signatures, affecting the stability and reproducibility of predictions. Secondly, gene signature models rely on differences in gene expression levels and may overlook other types of genetic variation, post-transcriptional modifications, and other factors that can influence predictions. Therefore, when applying gene signature models, it is important to acknowledge

their limitations and complement them with other biological knowledge and experimental results for a comprehensive analysis. Thirdly, although HepG2 cells have been widely used in the research of HCC, it is essential to recognize that this model may not fully replicate all aspects of human conditions. Future studies will explore the pathogenesis and progression of HCC by using an *RTN3* knockout mouse model. Nonetheless, based on extensive bioinformatics analysis and machine learning algorithms, a stable and powerful feature has been developed to effectively describe the "neutrophil characteristics" of patients with HCC. The NDS model shows promise as a tool for optimizing decision-making and monitoring plans for individual patients with HCC. This study provides a new perspective on understanding the role of neutrophils in HCC and establishes a prognostic model based on NDS, which can serve as a valuable tool for evaluating treatment efficacy and prognosis, offering new ideas and strategies for the treatment and prognosis assessment of patients with HCC.

Data availability statement

The original contributions presented in the study are included in the article/Supplementary Material. Further inquiries can be directed to the corresponding authors.

Author contributions

QG and XC designed the research. QG and XC performed the research and analyzed the data. FL drafted the paper. QG and YC revised the paper. All authors contributed to the article and approved the submitted version.

Conflict of interest

The authors declare that the research was conducted in the absence of any commercial or financial relationships that could be construed as a potential conflict of interest.

Publisher's note

Supplementary material

The Supplementary Material for this article can be found online at: https://www.frontiersin.org/articles/10.3389/fimmu.2023.1216585/full#supplementary-material

References

1. Kudo M, Finn RS, Qin S, Han K-H, Ikeda K, Piscaglia F, et al. Lenvatinib versus sorafenib in first-line treatment of patients with unresectable hepatocellular carcinoma: A randomised phase 3 non-inferiority trial. *Lancet* (2018) 391(10126):1163–73. doi: 10.1016/S0140-6736(18)30207-1

2. Finn RS, Qin S, Ikeda M, Galle PR, Ducreux M, Kim T-Y, et al. Atezolizumab plus bevacizumab in unresectable hepatocellular carcinoma. *New Engl J Med* (2020) 382 (20):1894–905. doi: 10.1056/NEJMoa1915745

3. Ren Z, Xu J, Bai Y, Xu A, Cang S, Du C, et al. Sintilimab plus a bevacizumab biosimilar (Ibi305) versus sorafenib in unresectable hepatocellular carcinoma (Orient-32): A randomised, open-label, phase 2-3 study. *Lancet Oncol* (2021) 22(7):977–90. doi: 10.1016/S1470-2045(21)00252-7

4. Hatanaka T, Naganuma A, Kakizaki S. Lenvatinib for hepatocellular carcinoma: A literature review. *Pharmaceuticals* (2021) 14(1):36. doi: 10.3390/ph14010036

5. Abou-Alfa GK, Shi Q, Knox JJ, Kaubisch A, Niedzwiecki D, Posey J, et al. Assessment of treatment with sorafenib plus doxorubicin vs sorafenib alone in patients with advanced hepatocellular carcinoma: phase 3 calgb 80802 randomized clinical trial. *JAMA Oncol* (2019) 5(11):1582–8. doi: 10.1001/jamaoncol.2019.2792

6. Merle P, Kudo M, Krotneva S, Ozgurdal K, Su Y, Proskorovsky I. Regorafenib versus cabozantinib as a second-line treatment for advanced hepatocellular carcinoma: an anchored matching-adjusted indirect comparison of efficacy and safety. *Liver Cancer* (2022) 12(2):145–155. doi: 10.1159/000527403

7. Ellis MJ, Suman VJ, Hoog J, Lin L, Snider J, Prat A, et al. Randomized phase ii neoadjuvant comparison between letrozole, anastrozole, and exemestane for postmenopausal women with estrogen receptor–rich stage 2 to 3 breast cancer: clinical and biomarker outcomes and predictive value of the baseline pam50-based intrinsic subtype—Acosog Z1031. *J Clin Oncol* (2011) 29(17):2342–9. doi: 10.1200/jco.2010.31.6950

8. Bivona TG, Hieronymus H, Parker J, Chang K, Taron M, Rosell R, et al. Fas and nf-Kb signalling modulate dependence of lung cancers on mutant egfr. *Nature* (2011) 471(7339):523–6. doi: 10.1038/nature09870

9. Chapman PB, Hauschild A, Robert C, Haanen JB, Ascierto P, Larkin J, et al. Improved survival with vemurafenib in melanoma with braf V600e mutation. *New Engl J Med* (2011) 364(26):2507–16. doi: 10.1056/NEJMoa1103782

10. Modest DP, Ricard I, Heinemann V, Hegewisch-Becker S, Schmiegel W, Porschen R, et al. Outcome according to kras-, nras- and braf-mutation as well as kras mutation variants: pooled analysis of five randomized trials in metastatic colorectal cancer by the aio colorectal cancer study group. *Ann Oncol* (2016) 27(9):1746–53. doi: 10.1093/annonc/mdw261

11. Xue R, Zhang Q, Cao Q, Kong R, Xiang X, Liu H, et al. Liver tumour immune microenvironment subtypes and neutrophil heterogeneity. *Nature* (2022) 612 (7938):141–7. doi: 10.1038/s41586-022-05400-x

12. Papayannopoulos V. Neutrophil extracellular traps in immunity and disease. *Nat Rev Immunol* (2018) 18(2):134–47. doi: 10.1038/nri.2017.105

13. Jung HS, Gu J, Kim J-E, Nam Y, Song JW, Kim HK. Cancer cell–induced neutrophil extracellular traps promote both hypercoagulability and cancer progression. *PloS One* (2019) 14(4):e0216055. doi: 10.1371/journal.pone.0216055

14. Chen Q, Zhang L, Li X, Zhuo W. Neutrophil extracellular traps in tumor metastasis: pathological functions and clinical applications. *Cancers* (2021) 13 (11):2832. doi: 10.3390/cancers13112832

15. Giese MA, Hind LE, Huttenlocher A. Neutrophil plasticity in the tumor microenvironment. *Blood* (2019) 133(20):2159–67. doi: 10.1182/blood-2018-11-844548

16. Hu J, Othmane B, Yu A, Li H, Cai Z, Chen X, et al. 5mc regulator-mediated molecular subtypes depict the hallmarks of the tumor microenvironment and guide precision medicine in bladder cancer. *BMC Med* (2021) 19(1):289. doi: 10.1186/s12916-021-02163-6

17. Hu J, Yu A, Othmane B, Qiu D, Li H, Li C, et al. Siglec15 shapes a non-inflamed tumor microenvironment and predicts the molecular subtype in bladder cancer. *Theranostics* (2021) 11(7):3089–108. doi: 10.7150/thno.53649

18. Dong L, Zhou S, Bai X, He X. Construction of a prognostic model for hcc based on ferroptosis-related lncrnas expression and its potential to predict the response and iraes of immunotherapy. *Front Pharmacol* (2023) 14:1090895. doi: 10.3389/fphar.2023.1090895

19. Yin L, Zhou L, Gao S, Feng Y, Zhu H, Xiang J, et al. Classification of hepatocellular carcinoma based on N6-methylandenosine–related lncrnas profiling. *Front Mol Biosci* (2022) 9:807418. doi: 10.3389/fmolb.2022.807418

20. Liu Z, Liu L, Weng S, Guo C, Dang Q, Xu H, et al. Machine learning-based integration develops an immune-derived lncrna signature for improving outcomes in colorectal cancer. *Nat Commun* (2022) 13(1):816. doi: 10.1038/s41467-022-28421-6

21. Charoentong P, Finotello F, Angelova M, Mayer C, Efremova M, Rieder D, et al. Pan-cancer immunogenomic analyses reveal genotype-immunophenotype relationships and predictors of response to checkpoint blockade. *Cell Rep* (2017) 18 (1):248–62. doi: 10.1016/j.celrep.2016.12.019

22. Liu F, Wang P, Sun W, Jiang Y, Gong Q. Identification of ligand-receptor pairs associated with tumour characteristics in clear cell renal cell carcinoma. *Front Immunol* (2022) 13:874056. doi: 10.3389/fimmu.2022.874056

23. Gong Q, Guo Z, Sun W, Du X, Jiang Y, Liu F. Cx3cl1 promotes cell sensitivity to ferroptosis and is associated with the tumor microenvironment in clear cell renal cell carcinoma. *BMC Cancer* (2022) 22(1):1184. doi: 10.1186/s12885-022-10302-2

24. Yang C, Zhang H, Zhang L, Zhu AX, Bernards R, Qin W, et al. Evolving therapeutic landscape of advanced hepatocellular carcinoma. *Nat Rev Gastroenterol Hepatol* (2023) 20(4):203–22. doi: 10.1038/s41575-022-00704-9

25. Li B, Feng W, Luo O, Xu T, Cao Y, Wu H, et al. Development and validation of a three-gene prognostic signature for patients with hepatocellular carcinoma. *Sci Rep* (2017) 7(1):5517. doi: 10.1038/s41598-017-04811-5

26. Song S, Shi Y, Wu W, Wu H, Chang L, Peng P, et al. Reticulon 3-mediated chk2/P53 activation suppresses hepatocellular carcinogenesis and is blocked by hepatitis B virus. *Gut* (2021) 70(11):2159–71. doi: 10.1136/gutjnl-2020-321386

frontiers | Frontiers in Immunology

TYPE Review
PUBLISHED 12 September 2023
DOI 10.3389/fimmu.2023.1258538

OPEN ACCESS

EDITED BY
Xuanbin Wang,
Hubei University of Medicine, China

REVIEWED BY
Hiroshi Yano,
Weill Cornell Medicine, Cornell University, United States
Eric Ubil,
University of Alabama at Birmingham, United States

*CORRESPONDENCE
Qi Gao
gaoqi2019@jlu.edu.cn

†These authors have contributed equally to this work

RECEIVED 14 July 2023
ACCEPTED 29 August 2023
PUBLISHED 12 September 2023

CITATION
Guo J, Wang S and Gao Q (2023) An integrated overview of the immunosuppression features in the tumor microenvironment of pancreatic cancer. *Front. Immunol.* 14:1258538. doi: 10.3389/fimmu.2023.1258538

An integrated overview of the immunosuppression features in the tumor microenvironment of pancreatic cancer

Jinglong Guo[1†], Siyue Wang[2†] and Qi Gao[1*]

[1]Department of Cardiovascular Disease, the First Hospital of Jilin University, Changchun, China, [2]Baylor College of Medicine, One Baylor Plaza, Houston, TX, United States

Pancreatic ductal adenocarcinoma (PDAC) is one of the deadliest malignancies. It is characterized by a complex and immunosuppressive tumor microenvironment (TME), which is primarily composed of tumor cells, stromal cells, immune cells, and acellular components. The cross-interactions and -regulations among various cell types in the TME have been recognized to profoundly shape the immunosuppression features that meaningfully affect PDAC biology and treatment outcomes. In this review, we first summarize five cellular composition modules by integrating the cellular (sub)types, phenotypes, and functions in PDAC TME. Then we discuss an integrated overview of the cross-module regulations as a determinant of the immunosuppressive TME in PDAC. We also briefly highlight TME-targeted strategies that potentially improve PDAC therapy.

KEYWORDS

pancreatic cancer, complex tumor microenvironment, diverse cellular cross-regulations, immunosuppression features, targeting strategy

1 Introduction

Pancreatic cancer is the third leading cause of cancer-related death in Western countries (1). Concerningly, it has been estimated there would be 64,050 people diagnosed with pancreatic cancer and 50,550 people would die from it in 2023 in the United States (1). This disease is mostly diagnosed at advanced stages, making current therapeutic regimens rather ineffective (2, 3). Pancreatic cancer is rapidly lethal, with an overall 5-year survival rate of only 11% (2, 3). Surgical resection and adjuvant chemoradiotherapy are viable options for only 10-20% of newly diagnosed patients, resulting in a 5-year survival rate of 15-25% among this subgroup (2, 3). Currently, most patients with advanced pancreatic cancer are mainly treated with chemotherapy regimens such as FOLFIRINOX (i.e., combination of drugs leucovorin calcium (folinic acid), fluorouracil, irinotecan hydrochloride, and oxaliplatin) and gemcitabine/nab-paclitaxel, however, their overall efficacy remains significantly limited, with the median overall survival < 1 year (2, 3). The factors causing the lethality of pancreatic cancer are

multifaceted, including multiple germline mutations, poor diagnosis, resistance to conventional therapies, and highly immunosuppressive tumor microenvironment (TME) (2–5).

Pancreatic ductal adenocarcinoma (PDAC) is the most common type of pancreatic malignancy (greater than 90%) (2). It features a complex TME that is composed of diverse acellular and cellular components, mostly including dense extracellular matrix (ECM), tumor cells, stromal cells, and immune cells (4, 5). Interactions between these various cellular elements occur through direct cell-cell contact and indirect communication mediated by secreted molecules, culminating in the establishment of an immunosuppressive milieu (4, 5). The immunosuppression feature has been recognized as a general hallmark of PDAC TME, characterized by heightened infiltration of tumor-promoting myeloid cells including tumor-associated macrophages (TAMs), tumor-associated neutrophils (TANs), myeloid-derived suppressor cells (MDSCs), and mast cells, along with impaired number and function of anti-tumor immune cells such as CD8 T cells, Dendritic cells (DCs), and natural killer cells (NKs) (4, 5). Concomitantly, this immunosuppressive milieu substantially influences the development, prognosis, and treatment outcomes of PDAC (4, 5).

Immunotherapies, such as immune checkpoint inhibitors (ICI) that disrupt the inhibitory pathways of T cells and thereby unleash their power against cancer, have revolutionized treatment paradigms for a range of human cancers over the past decade (2, 3, 6). However, PDAC has been reported to extremely resist monotherapy with ICIs (2, 3, 6), which likely attributes to the highly immunosuppressive nature of the PDAC TME (4, 5, 7). In this regard, we argue that an integrated understanding of the immunosuppressive TME will open new targeted opportunities to improve PDAC therapy more effectively. In this review, we integrate cellular sub(types), phenotypes, and functions of the diverse cellular components in PDAC TME to summarize five cellular composition modules. Then we discuss a comprehensive overview of the cross-module interactions and regulations as a potent determinant of the immunosuppressive TME in PDAC. Lastly, we briefly highlight novel TME-targeted approaches that potentiate the improvement of PDAC therapy.

2 Overview of five cellular composition modules in PDAC TME

PDAC exhibits high genetic heterogeneity and is characterized by an overarching TME, where diverse cellular compositions and acellular mediators contribute to a remarkable desmoplastic reaction (4, 5). Recent evidence has established the notion that the TME of PDAC is dominated by immunosuppression features, which significantly influence PDAC phenotypes and treatment outcomes including both conventional chemotherapies and revolutionary immunotherapies (4, 5). A comprehensive understating of the diversity and interactions within PDAC TME that unravels the mechanistic determinant of its immunosuppression feature will shed light on the development of new therapeutic interventions (4, 5). To this end, we integrate the cellular (sub)types, phenotypes, and functions of the diverse cellular components within PDAC TME and summarize five cellular composition modules (Figure 1). First, PDAC-intrinsic aspects are concluded as (I) the Tumor cell module since PDAC genetic mutations and related signal pathways have been recognized as a critical factor driving the formation of the immunosuppressive TME (8–11). (II) The Immunosuppression module is mostly composed of TAMs, TANs, MDSCs, Treg cells, and mast cells, given that they constitute an abundant component in PDAC TME and play notorious immunoregulatory and immunosuppressive roles (12–14). Particularly, its immunosuppressive capacity is significantly overwhelming compared with the anti-tumor immunity including CD8 T cells, DCs, and NKs, which are impaired in number and function in PDAC TME and therefore drive us to define (III) the Anti-tumor immunity impaired module (15–18). Besides, immune cells including CD4 helper T cell subsets (Th1, Th2, and Th17) and B cells have been shown to display features of a double-edged sword in PDAC TME and play either tumor-suppressing or tumor-supporting roles in context-dependent manners. Thus, emerging roles for them in PDAC TME and cancer immunity are discussed accordingly in the IV Module (19–23). Lastly, we describe the heterogeneity and functions of cancer-associated fibroblasts (CAFs) in the context of immunosuppressive TME of PDAC in (V) the Stromal module (24). By the summary and explicit discussion (in the following paragraphs) of above five cellular composition modules in PDAC TME, we argue that there are cross-interactions and -regulations among cellular modules that represent a resultant force essentially dictating the immunosuppression features, PDAC oncological hallmarks, and treatment efficacy. It is worth noting that each cell population in PDAC TME may exhibit a high degree of plasticity, and their behavior may not strictly align with the originally defined modules, particularly in the context of therapeutic interventions. Therefore, understanding and accounting for this plasticity is vital for developing effective PDAC treatment strategies.

3 PDAC-intrinsic aspects: the primary driver of immunosuppressive TME formation

An expanding body of evidence from preclinical mouse model studies and clinical observations underscores the crucial role of genetic mutations in oncogenes and/or tumor-suppressor genes in shaping important PDAC features, including tumor cell differentiation and heterogeneity, histopathological subtypes, and clinical outcomes (8–11, 25, 26). Besides, defined oncogenic mutations are also associated with changes in the composition of immune cells and immunotherapy efficacy in PDAC (8–11, 25, 26). A comprehensive understanding of how genetic oncogenes and related signaling pathways affect PDAC phenotypes and immune cell composition and function will provide valuable insights for the development of precise targeted therapies and immunotherapies aimed at combating this aggressive malignancy.

10.3389/fimmu.2023.1258538

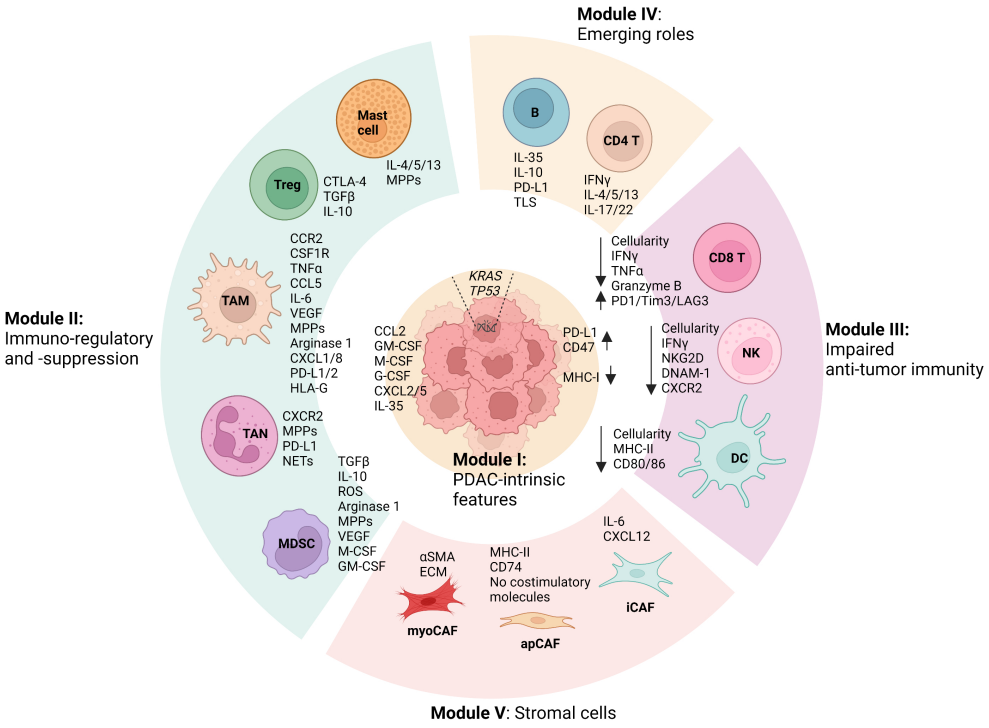

FIGURE 1
Summary of modular cell compositions and molecule mediators in PDAC TME. Pancreatic ductal adenocarcinoma (PDAC)-intrinsic features such as genetic mutations and related signal pathways are concluded as Cellular Module I, as they have been reported to profoundly shape the formation of the immunosuppressive tumor microenvironment (TME). Immunoregulatory and immunosuppressive Module II is primarily composed of tumor-associated macrophages (TAMs), tumor-associated neutrophils (TANs), myeloid-derived suppressor cells (MDSCs), mast cells, and regulatory T cells (Tregs), which play significant roles in fostering PDAC progression and in suppressing anti-tumor immunity. In PDAC TME, anti-tumor immune cells including CD8 T cells, Dendritic cells (DCs), and natural killer cells (NKs) are profoundly impaired in terms of both number and function, which can be dramatically regulated by the cells from other cellular modules, especially Module II. Besides, CD4 helper T cell subsets (Th1, Th2, and Th17) and B cells in PDAC TME have been shown to play either tumor-suppressing or tumor-supporting roles in context-dependent manners, of which emerging roles are discussed in Module IV. Lastly, the heterogeneity and functions of cancer-associated fibroblasts (CAFs) in the context of immunosuppressive TME of PDAC is summarized as Stromal module V, which includes myofibroblast-like CAFs (myoCAFs), inflammatory CAFs (iCAFs), and antigen-presenting CAFs (apCAFs). In addition, the primary molecular mediators used by the cells in terms of their functions discussed in the review are shown accordingly. Remarkable cross-interactions and -regulations among cellular modules occur through the molecular mediators, culminating in the formation of an immunosuppressive TME that essentially influences PDAC oncological hallmarks and treatment efficacy. (The figure was created in Biorender with the publication license).

3.1 Genetic mutations drive PDAC initiation and progression

PDAC progresses from noninvasive precursor lesions, including pancreatic intraepithelial neoplasia (PanIN), intraductal papillary mucinous neoplasm (IPMN), intraductal tubulopapillary neoplasm (ITPN), and mucinous cystic neoplasm (MCN) (26). Among them, PanINs are the most well-characterized preneoplasia lesions so far (26). PanINs originate within intralobular ducts and can be further classified into four grades, PanIN 1A, PanIN 1B, PanIN 2, and PanIN 3 (26). Of note, all preneoplastic lesions are likely to reflect the PDAC progression. Genetic mutations are the primary driver of PDAC initiation and progression (11, 25). It has been reported that a PDAC patient usually harbors 32 genetic mutations on average (11, 25). Among the mutations, activating mutations in KRAS are present in over 90% of tumors (11, 25). The mutations of cell cycle checkpoint genes, like CDKN2A, TP53, and SMAD4 account for 50-80% of cases (11, 25). In addition to these common mutations, there are less frequent mutated genes (~10% of tumors), including ARID1A, MLL3, and TGFBR2, which can contribute to a more aggressive phenotype of PDAC (11, 25). Despite enduring research endeavors, targeted therapies have not yet demonstrated significant benefits for PDAC patients (27).

3.2 Genetic mutations in PDAC cells shape immunosuppressive TME formation

Emerging evidence has shown that oncogenic mutations in cancer cells primarily dictate the immune contexture in the TME (9). Deciphering the underlying relationship between cancer cell-intrinsic genetic events and the immune cell contexture in the TME may enable the improvement of both chemotherapies and immunotherapies for cancer patients. We highlight a few examples of the studies to discuss how indicated oncogenic mutations in cancer cells modulate the immune cell composition and function in the TME of PDAC.

Oncogenic K-RAS represents one of the most abundant and common mutations during PDAC initiation and progression (11, 25). K-RAS mutations are involved in several signaling pathways such as RAF/MEK/ERK and PI3K/AKT/mTOR (28, 29). They not only determine PDAC phenotypes but also significantly regulate the immunosuppressive TME (28, 29). For example, studies from Pylayeva-Gupta et al. and Bayne et al. independently reported that oncogenic K-RASG12D in mouse pancreatic ductal epithelial cells drove elevated GM-CSF secretion, thereby recruiting Gr1+CD11b+ MDSCs into PDAC TME (30, 31). Further studies showed that neutralizing GM-CSF genetically or pharmacologically in mice was sufficient to reduce these cells, along with elevated tumoral infiltration of CD8 T cells and slowed PDAC growth (30, 31). It thus suggests GM-CSF and/or MDSCs to be potential targets for PDAC therapy. Additionally, K-RAS mutations are also involved in the suppression of innate and adaptive anti-tumor immunity through modulating PDAC expressions of immune checkpoints such as PD-L1 and CD47 (32, 33), as well as through autophagy-mediated MHC-I downregulation in PDAC (34, 35).

As one of the molecule events downstream of RAS signaling pathways, MYC activation and overexpression are commonly found in PDAC (36, 37). Beyond regulating PDAC phenotypes, MYC has also been linked to the immunosuppressive TME (38, 39). Using mouse models of PDAC that carry K-RASG12D and inducible MYC-ERT2, Sodir et al. showed that acute activation of MYC triggered rapid changes in stromal and immune cells (38). This included a marked influx of F4/80+CD206+ TAMs and Ly-6B.2+ neutrophils, significant loss of B220+ B lymphocytes and CD3+ T cells, and induction of α-SMA in proximal stellate and fibroblastic cells (38). As a result, it established a TME reminiscent of human PDAC (38). Interestingly, subsequent MYC deactivation or inhibition immediately reversed the advanced PDAC phenotypes back to PanIN, suggesting the requirement of sufficient levels of MYC for instructing the PDAC phenotypes and TME features (38). In this regard, elevated levels of MYC in tumor cells have been shown to promote PDAC metastasis through CXCL13- and macrophage migration inhibitory factor (MIF)-mediated recruitment of TAMs in a recent study (39). Additionally, concomitant MYC and K-RASG12D expression caused suppression of Type I IFNs, thereby resulting in decreased NK and B cell infiltration and advanced PDAC phenotypes (40). Together, these studies suggest an important role for MYC in dictating the immunosuppressive TME of PDAC and provide compelling insights for therapeutically targeting MYC.

The tumor suppressor TP53 mutations occur in 50-70% of human PDAC, which have been shown to affect immune cell composition in PDAC TME (8, 41). By analyzing human PDAC patient data from The Cancer Genome Atlas (TCGA), Maddalena et al. reported the significant association of TP53 missense mutations with reduced frequency of CD8 T cells in human PDAC (41). In addition, using mouse models of PDAC carrying p53R172H mutation, Siolas et al. reported an elevated secretion of CXCL2 and CXCL5, thereby leading to the accumulation of CD11b+Ly6G+ neutrophils in TME (42). On the other hand, p53 loss in mouse PDAC cells caused decrease of CD4 and CD8 T cells whereas increase in immunosuppressive CD11b+ myeloid cells and Treg cells in PDAC TME (42, 43). Thus, these data demonstrate a contribution of TP53 mutations to the immunosuppressive TME of PDAC.

4 Immunoregulatory and immunosuppressive cells: the main executor of immunosuppression in PDAC TME

4.1 Tumor-associated macrophages

Tumor-associated macrophages (TAMs) are abundant in the TME of PDAC. These cells appear to play important but potentially various roles in fostering tumorigenesis, shaping the TME, and suppressing anti-tumor immunity (44, 45). TAMs promote PDAC initiation and progression by secreting a variety of proinflammatory cytokines including TNFα, RANTES (CCL5), and IL-6 (46, 47). For instance, it has been reported that TAMs-secreted TNFα and RANTES activated NF-κB in acinar cells to drive their proliferation and survival. In turn, acinar cells expressed intercellular adhesion molecule-1 (ICAM-1) to mediate their cellular adhesion with TAMs. Thus, TAMs and acinar cells formed a paracrine loop, sustaining local inflammation and inducing acinar-to-ductal metaplasia (ADM) transformation in the early stage of carcinogenesis (46, 47). IL-6 can contribute to the development of the early premalignant pancreatic lesions ADM and PanIN through JAK-Stat3 or Stat3/Socs3 pathways (48, 49). Moreover, TAMs can regulate tumoral neoangiogenesis, epithelial-mesenchymal transition (EMT), and PDAC metastasis (44, 45). In response to TME hypoxia, TAMs upregulate the expression of HIF-1α, a master transcriptional factor that regulates cellular and tissue adaptive responses to hypoxia (44, 50). HIF-1α further regulates the expression of numerous angiogenesis-related genes such as VEGF, PDGF, βFGF, IL-1β, IL-8, TNF-α, thymidine phosphorylase, MMPs, CXCL1, and CXCL8 (44, 50). For example, by depleting TAMs pharmacologically or genetically in mouse models of PDAC, Griesmann H demonstrated a significant reduction in liver metastasis of tumor cells and impairment of neoangiogenesis. In addition, the study showed the presence of VEGF-expressing TAMs in pre-metastatic niches and their depletion caused the decrease in circulating VEGF levels. Based on these data, the authors claimed that VEGF-expressing TAMs promoted tumor cell extravasation and vascular permeability (51). Of note, the studies have not provided a clear answer regarding whether the observed effects were directly mediated by VEGF or influenced by other factors. Furthermore, functioning as immunosuppressive cells, TAMs produce a variety of immunoregulatory cytokines such as TGFβ, IL-10, and prostaglandin E2 (PGE2) and express inhibitory molecules PD-L1 and PD-L2, which promote Treg cell infiltration and inhibit anti-tumor CD8 T cell activity (44, 45). Besides, TAMs also suppress NK cell function by upregulating the expression of HLA-G, an inhibitory molecule for NK cells (44, 52). In summary, TAMs promote PDAC initiation and progression, regulate TME immunosuppression, and inhibit anti-tumor immunity.

Nonetheless, TAMs are heterogenous and high of plasticity, therefore possessing significant potential to mediate anti-tumor responses when purposely modulated.

Historically, TAMs have been recognized to exclusively originate from the differentiation of recruited monocytes (MoMΦ) (44, 45). However, recent studies demonstrated that they also derived from the expansion of pancreatic tissue-resident macrophages (TRM) in PDAC, which were phenotypically and functionally distinct from MoMΦ (53). In mouse models, CCR2 genetic knockout mediated-MoMΦ selective depletion didn't affect PDAC growth, indicating a dispensable role for them in tumor progression (53). Interestingly, PDAC growth was remarkably reduced in mouse models with specific depletion of pancreatic TRMs (53). These data suggested that TRM expansion-derived TAMs were more robust drivers of PDAC progression than MoMΦ (53). It is worth mentioning that macrophage heterogeneity has long been defined as M1 and M2 macrophages based on *in vitro* polarization studies (44, 45). Briefly, M1 macrophages are classically induced by bacterial products (lipopolysaccharide) and/or pro-inflammatory cytokines (IFNγ and TNFα), produce proinflammatory cytokines (such as IL-12, CXCL10), and mediate protective immune responses. By contrast, M2 macrophages are alternatively activated by immunoregulatory cytokines (such as IL-4, IL-10, or IL-13), producing factors (such as VEGF) associated with wound healing and tissue repair (44, 45). Of Note, more and more evidence has argued that TAMs rarely express bona-fide M1 or M2 phenotypes, implying that the diversity of these cells cannot simply be addressed with this binary categorization.

Recently, one of the striking research advancements in the field has been the characterization of the TAMs that are positive for triggering receptor expressed on myeloid cells 2 (TREM2) (54–56). TREM2 is overexpressed on TAMs in 75% of human tumors and its expression highly correlates with poor tumor prognosis in patients (54). Studies conducted on mice reveal that TREM2+ macrophages dampen the anti-tumor activities of CD8+ T cells and NK cells, signifying bona-fide immunosuppressive functions for these cells (54–56). Moreover, TREM2 modulation by genetic ablation or monoclonal antibodies can remodel the myeloid cell immunosuppression within the TME, restrict tumor growth, and further improve immunotherapies such as anti-PD-1 therapy and NK cell-based therapy in mouse models with different tumor types (54–56). Notably, fundamental questions regarding how TREM2 expression is induced in TAMs and how TREM2 regulates the immunosuppressive phenotypes of TAMs remain largely elusive (57). Potential explanations could involve in the TAM metabolism, given that TREM2 is a receptor for a wide array of ligands, including anionic molecules, DNA, lipoproteins, and phospholipids. These ligands are intimately associated with cellular metabolism and are abundantly present in the TME (57).

4.2 Tumor-associated neutrophils

Neutrophils represent one of the most abundant leukocytes in the blood of humans (up to 50-70%) in physiological settings, which have drawn a lot of attention to investigate their relationship with cancer (58). There were studies to report that PDAC cells, even tumor cells from the lesions of early stages such as PanIN, can significantly promote the expansion of neutrophil progenitors in bone marrow by secreting growth factors (GM-CSF, G-CSF, and M-CSF) (59, 60). Accordingly, the Neutrophils-Lymphocyte Ratio (NLR) of periphery blood has been identified as a faithful prognostic value of the outcomes of PDAC patients after treatment (61, 62). Specifically, a high NLR value (NLR>2.5) was remarkably associated with a decreased frequency of CD8 T cells within the tumor and predicted worse overall survival in PDAC patients after surgical resection and chemotherapy (57, 58). More recently, by analyzing PDAC mouse models and PDAC samples of patients, Jiang et al. found that neutrophil infiltration displayed a body-wide effect, including liver, lung, colon, stomach, kidney, heart, and brain (63). Thus, systemic neutrophil infiltration and associated inflammation can be a cautious marker of pancreatic cancer prognosis.

In addition to promoting neutrophil progenitor expansion in bone marrow, PDAC is involved in recruiting neutrophils to the TME and pre-metastatic niches through secretion of a variety of chemokines such as CXCL1, CXCL2, CXCL5, and CXCL8 (64–67). Using mouse models, Steele et al. reported the liver recruitment of CXCR2+ neutrophils contributing to PDAC metastasis (67). In the context of CXCR2+ neutrophil depletion genetically or pharmacologically, PDAC liver metastasis was remarkably reduced, along with significantly prolonged tumor-free survival of PDAC mouse models (67). Although not directly investigated in the study, it is reasonable to propose a link between the mechanistic action of CXCR2+ neutrophils in PDAC and CXCR2 ligands, given that CXCR2 is a receptor for a series of chemokines CXCL1, CXCL2, CXCL3, CXCL5, CXCL6, CXCL7, and CXCL8 (66, 67). Furthermore, CXCR2+ neutrophil depletion improved tumoral infiltration and function of CD8 T cells, which sensitized anti-PD1 therapy in mouse models of PDAC (67). Together with reports showing that TANs expressed PD-L1 to suppress anti-tumor T cell functions, TANs therefore have been considered as significant immunosuppressive cells in PDAC TME (66–68). Besides, like TAMs, TANs in PDAC TME are also a substantial source of ECM degradation mediators such as MMPs and Elastase, which can promote PanIN progression, PDAC invasiveness, and metastasis (58, 69). In recent years, the role of neutrophil extracellular traps (NETs) has gained attention in neutrophil biology and related diseases (70). NETs are network structures composed of DNA-histone complexes and proteins released by activated neutrophils (70). Studies showed that NETs activated IL-1β/EGFR/ERK pathway, and subsequently promoted PDAC EMT and metastasis (71, 72). Collectively, these studies support the notation that TANs represent one of the major immunosuppressive populations in the TME, inhibiting anti-tumor immunity and contributing to PDAC progression.

Like the definition of M1 and M2 for macrophages, TANs have been classified as N1 (anti-tumor) and N2 (pro-tumor) based on the activation and functional status in the TME (73). Fridlender et al. showed that TGFβ-induced differentiation of N2 TANs led to a pro-tumor phenotype in TME, whereas anti-tumor N1 TANs were

polarized when TGFβ was ablated. The study highlighted the phenotypic and functional heterogeneity of TANs in PDAC TME (73). Another important question is what are the functions of TANs in the context of cancer immunotherapy? Recent studies have shown that immunotherapy-activated T cells can recruit and induce the maturation of neutrophils, leading to an improved capacity of neutrophils to directly kill tumor cells (74, 75). This demonstrates an important role for neutrophils in the context of cancer immunotherapy.

4.3 Myeloid-derived suppressor cells

Myeloid-derived suppressor cells (MDSCs) are a heterogeneous population originating from myeloid progenitor cells of bone marrow. They are primarily classified into two populations, mononuclear (M-MDSC) and polymorphonuclear cells (PMN-MDSC), which accounts for 20-30% and 70-80% of the total MDSC population, respectively, in most tumors (76–78). Both M-MDSCs and PMN-MDSCs were reported to remarkably accumulate and expand in PDAC TME, and importantly, their frequency was negatively correlated with patient survival and response rates of immunotherapies (76, 77). M-MDSCs express higher levels of signal transducer and activator of transcription 1 (STAT1), inducible nitric oxide synthase (iNOS), and nitric oxide (NO, which is produced by iNOS-mediated L-arginine metabolism) (78). On the other hand, PMN-MDSCs have increased levels of STAT3, reactive oxygen species (ROS), but less NO (78). ROS is a detrimental agent for T cells, while simultaneously maintaining the survival of MDSCs themselves (78). These cellular events result in the suppression of anti-tumor T cell responses (78). Importantly, both M-MDSCs and PMN-MDSCs are an important source of arginase 1, which deprives L-arginine required for T cell metabolism, thus impairing their functions (76, 78). In PDAC TME, MDSCs (including both M-MDSCs and PMN-MDSCs) also directly maintain other immunosuppressive cells including TAMs and Tregs (76, 79). For example, by using light sheet fluorescent microscopy, Siret et al. observed the close associations of MDSCs and Tregs in tumor samples from PDAC mouse models and patients. Further studies demonstrated that MDSCs secreted TGFβ and IL-10, fostering Treg frequency and functions locally in PDAC TME (79). Besides, like TAMs and TANs, MDSCs can also promote neoangiogenesis, EMT, and metastasis of PDAC through secretion of a variety of mediators such as G-CSF, GM-CSF, stem cell factor (SCF), cyclooxygenase 2 (COX-2), PGE2, MPPs, VEGF, and HGF (78, 80). Lastly, it is especially worth mentioning that PMN-MDSCs are distinct from neutrophils, given that they have increased levels of arginase 1 and peroxynitrite, fewer granules, and reduced CD16 and CD62L expression (78, 80).

4.4 Regulatory T cells

Regulatory T cells (Tregs) are a subset of immunosuppressive cells, which have been largely reported to play tumor-promoting roles (81). Tregs are highly infiltrated into PDAC, and their abundance is often correlated with a poor prognosis and reduced survival in patients (82). Tregs exert their immunosuppressive effects through various mechanisms. One of the main mechanisms employed by Tregs is the expression of immune inhibitory molecules, such as CTLA-4, which can dampen the activation and function of CD8 T cells (81). Additionally, Tregs produce immune regulatory cytokines, including TGFβ and IL-10, which further contribute to the suppression of anti-tumor immune responses. Moreover, they also compete with other T cells for IL-2 via higher expression of the IL-2 receptor, and therefore suppressing T cell function (81). Interestingly, a recent study showed that depletion of Tregs accelerated PDAC growth due to compensatory infiltration of tumor-promoting myeloid cells, specifically, TAMs (83). The specific mechanisms underlying this phenomenon were not explored in the study, highlighting the need for further research. Nevertheless, these findings suggest that caution should be exercised when considering Treg depletion as a therapeutic strategy for PDAC.

4.5 Mast cells

Mast cells are also one of the immune cell subsets that have been shown increased infiltration in PDAC. There were studies to report the inverse correlations between the frequency of mast cells with pathological grades of tumors and the overall survival of patients with PDAC (84, 85). Chang et al. observed the increased infiltration of mast cells into the tumors in a mouse model of PDAC, compared to that in the pancreas of healthy mice (85). Furthermore, they orthotopically transplanted the PDAC cells, that were isolated from the mouse model, into mast cell-deficient mice ($Kit^{w\text{-}sh/w\text{-}sh}$) and found that the tumor growth was significantly slower than that in WT recipient mice. Reconstitution with mast cells in $Kit^{w\text{-}sh/w\text{-}sh}$ mice remarkably restored PDAC growth. These studies thus demonstrated a tumor-promoting role for mast cells in PDAC growth (85). In fact, mast cells have been shown to secrete a variety of tumor-supporting and/or immunoregulatory factors in PDAC TME, including IL-13, Tryptase, MMPs (84, 86). Despite the evidence pointing towards a tumor-promoting role for mast cells in PDAC, the specific targeting strategies for mast cells in PDAC therapies have received limited investigation so far.

5 Impaired anti-tumor immunity in PDAC TME: CD8 T cells, DCs, and NK cells

5.1 CD8 T cells

Cytotoxic CD8 T cells play a central role in anti-tumor immunity. Upon recognition of T cell receptor (TCR) of tumor cells, of which tumor-specific antigen is presented by major histocompatibility complex class I (MHC-I), CD8 T cells can kill tumor cells through producing cytotoxic molecules, such as granzymes and perforin (15). Generally, high tumoral infiltration

of CD8 T cells and/or their improved functional status are positively associated with responses to therapies and the outcomes in patients across many cancer indications (15, 87). In most patients with PDAC, however, CD8 T cells are either scarce or excluded from the tumor cores. Even though CD8 T cells are present intratumorally in some PDAC patients, they are usually dysfunctional or exhausted, evidenced by elevated expression of a set of checkpoint molecules including PD-1, Tim-3, and LAG-3, and reduced production of effector cytokines such as IFNγ, TNFα, and granzyme B. Many mechanisms that mediate PDAC immune escape have been reported (15, 87). For example, Yamamoto et al. showed that autophagy-mediated degradation in PDAC contributed to significantly downregulated MHC-I molecules, consequently preventing CD8 T cells from being fully activated (34). In general, it appears that nearly all cell types from the defined Immunosuppression module, including TAMs, TANs, MDSCs, and Treg cells, can suppress CD8 T cells (Figure 1) (13, 14). CAFs also contribute to CD8 T cell suppression through the secretion of immunoregulatory molecules such as TGFβ and CXCL12 (88, 89), as well as through forming a physical barrier to directly prevent their infiltration (90). In summary, CD8 T cells in the tumors of most PDAC patients are rare, dysfunctional, and excluded from the tumor cores.

5.2 Dendritic cells

Dendritic cells (DCs) are professional antigen-presenting cells and initiate immune responses when fully activated. Numerous studies have reported that DC numbers and functions are significantly low in PDAC samples of patients, compared with other tumor types (91, 92). Accordingly, most PDAC patients were found the remarkable lack of circulating DCs in peripheral blood, who were usually associated with worse survival outcomes. It suggested the significance of DCs in PDAC patients (91, 92). In this regard, immense efforts have been put into the development of DC-based therapies for PDAC (16, 93). For example, using tumor antigen-expressing mouse models of PDAC and lung cancer, Hegde et al. reported a remarked impairment of conventional DCs in numbers and functions in PDAC, but not in lung tumors, which resulted in different tumor controls (16). It was further demonstrated that treatment with Flt3L and CD40 agonism, a regimen to improve DCs, led to PDAC control. Importantly, this treatment rendered PDAC responses to radiotherapy and its control was further improved (16, 93). These studies suggest a significant potential of DC-based therapies for PDAC. However, the reasons causing the impairment of DCs in PDAC remain to be further characterized.

5.3 Natural killer cells

Natural killer cells (NK cells), a population of innate lymphoid cells, are important players in the immune surveillance of cancer. NK cell activation is controlled by integrating signals from activation and inhibitory receptors. Normal cells express MHC-I molecules, the ligands for the inhibitory receptors of NK cells, to keep them under check. On the other hand, tumor cells usually downregulate MHC-I to escape from CD8 T cell killing, making them susceptible to NK cell-mediated killing. Hence, NK cells and CD8 T cells coordinate to keep effective immune surveillance of tumor cells. However, both NK cells and CD8 T cells (abovementioned) are impaired in PDAC TME (18, 94). Lim et al. provided evidence showing a lower frequency of NK cells in tumor samples of PDAC patients, which was due to downregulated expression of CXCR2, a receptor of several chemokines important for NK cell recruiting (94). Furthermore, NK cell functional impairment was also evidenced, mechanistically attributed to decreased expression of NK cell activation receptors NKG2D and DNAM-1 (94). The molecular insights leading to the NK cell impairment in PDAC TME, such as what causes downregulated CXCR2, NKG2D, and DNAM-1 in NK cells, remain largely unknown. More recently, Muthalagu et al. provided a novel mechanistic study to explain the NK cell evasion in PDAC (40). Using mouse models of PDAC expressing oncogenes MYC and K-RAS, they showed that type I IFNs were suppressed due to the binding of repressive MYC-MIZ1 complexes directly to the gene promoters of type I IFN regulators IRF5, IRF7, STAT1, and STAT2. Consequently, it contributed to the ineffectiveness of NK cell infiltration and PDAC control. Further study showed that genetic or pharmacological removal of repressors of type I IFN regulator genes increased NK cell infiltration and mouse survival. This study not only shed light on the mechanisms underlying NK cell impairment but also highlighted the possibility of targeting IFN signaling to improve PDAC therapy (40). In addition, NK cell cytotoxicity and INFγ production can be impaired by TGFβ, an abundant cytokine of immunoregulatory in PDAC TME (18, 95). Therefore, strategies to restore NK cell infiltration and function in PDAC TME hold great value for improving therapeutic outcomes.

6 Emerging roles for CD4 T and B cells in PDAC TME

6.1 CD4 helper T cells: Th1, Th2, and Th17

CD4 T cells are major players and coordinators of innate and adaptive immune responses and have been increasingly implicated in cancer immunity. Upon functional polarization, they show a broad spectrum of differentiation into defined subsets, including T helper 1 (Th1), Th2, Th17, and Treg (discussed above), implying their functions in tumor immunity are multifaceted and highly dependent on contexts (19–22). Th1 cells have been well-recognized to mediate anti-tumor effects, as they produce effector cytokines IL-2 and IFNγ (19, 20). However, a lower abundance of Th1 cells in PDAC was also implicated in the prolonged survival of patients, although the underlying reasons remain undetermined (20). Th2 cells secrete type 2 cytokines IL-4, IL-5, and IL-13, which mediate macrophage immunosuppressive polarization, fibrotic responses, and angiogenesis in tumors (19, 21). In PDAC patients, Th2 cell frequency has been shown an inverse correlation with overall survival, highly suggesting a tumor-

supporting role for these cells (19, 21). Nonetheless, Jacenik et al. reported that Th2 cells suppressed colon and pancreatic tumor growth in mice. Mechanistically, it was associated with Th2 cell-secreted IL-5, which promoted anti-tumorigenic responses of macrophages and eosinophils (96). As the main producer of IL-17 family cytokines, Th17 cells have been shown divergent effects in tumor immunity. He et al. provided data showing that elevated Th17 cells and their cytokines IL-17 and IL-22 were associated with tumor invasiveness, metastasis, and poor survival of PDAC patients (97). In line with the study in humans, McAllister et al. reported a remarked reduction in tumor progression in a mouse model of PDAC, of which Th17 cells were depleted (98). In the study, overexpression of IL-17A cytokine in the pancreas significantly accelerated PanIN initiation and progression in mouse models, suggesting a tumor-promoting role for IL-17 signaling albeit the molecular mechanisms required further investigation (98). Interestingly, there were also studies to report the potential anti-tumor effects of Th17 cells, as increased Th17 cell infiltration was positively correlated with tumor control and survival of PDAC mouse models (22). Therefore, the paradoxical effects among Th1, Th2, and Th17 cells in tumor immunity may highly rely on contexts including PDAC TME status, which requires further characterization in order to use their anti-tumor immunity whereas reverse the tumor-promoting role for PDAC therapy.

6.2 B cells

B cells are highly infiltrated in PDAC, and their roles in cancer immunity have been the subject of increasing research (23, 99). By determining PanIN and PDAC lesions from both humans and mouse models, Pylayeva-Gupta et al. observed the prominent presence of B cells and that orthotopic PDAC growth was significantly slowed in B cell-deficient mice. Further analysis identified the contribution of IL-35-producing CD1dhiCD5+ B cells to PDAC progression in mice and that these cells were recruited through CXCL13 (100). A regulatory B cell population has been well-documented in PDAC, which, except for IL-35, was also characterized by the expression of IL-10 and PD-L1 (99). It thus explained the capabilities of the B cells to suppress anti-tumor immunity and promote PDAC. Besides, B cells have been implicated in other mechanisms contributing to PDAC progression. They have been found to play a role in programming tumor-supporting FCγR+ TAMs and to be functionally associated with hypoxia in PDAC (101, 102). Collectively, these studies highlighted a tumor-promoting role for B cells in PDAC albeit through various mechanisms. More recently, ectopic lymphoid aggregates, namely tertiary lymph structures (TLS), have been observed in many solid cancers including PDAC. Composed of organized B cells and T cells, TLS presence has been positively associated with immunotherapy efficacy and favorable survival of PDAC patients (103, 104). Underlying mechanisms most likely attributed to TLS functioning as tumor immunity hub readily available in TME (103, 104). In addition, it is postulated that the presence of sparse or organized B cells within tumors may play divergent roles in tumor immunity.

7 Cancer-associated fibroblasts in the immunosuppressive TME of PDAC

Cancer-associated fibroblasts (CAFs) represent the most abundant cell type in the TME of PDAC, in which they constitute up to 80% of all cells. CAFs behave with remarkable desmoplastic reaction, a typical feature of the PDAC TME that is largely involved in ECM deposition and vessel remodeling. CAFs are very heterogeneous populations in terms of cellular origin and function (24). Studies have shown that CAFs can derive from pancreatic stellate cells (PSCs), tissue-resident fibroblasts, adipocytes, pericytes, bone marrow-derived progenitors, and endothelial cells (24). PSCs have long been considered as the primary source of CAFs in PDAC, however, cell lineage tracing study targeting Fabp4+ PSCs showed them contributing to a numerically minor CAF subpopulation (24, 105). This suggests that multiple cellular origins contribute to the heterogeneity of CAFs in PDAC (24, 105). The extent to which each potential cellular origin contributes to the diverse population of CAFs in PDAC is still largely unknown. Additionally, the relationship between the different cellular origins and the phenotypic, spatial, and functional heterogeneity of CAFs in PDAC remains unclear.

In the context of PDAC, three subsets of CAFs have been widely appreciated from early efforts by scRNA sequencing analysis of tumors from mouse models and human patients. A myofibroblast-like subset of CAFs (myoCAF) was evidenced by upregulating expression of αSMA and ECM, meanwhile inflammatory CAFs (iCAF) expressed cytokines and chemokines such as IL-6 and CXCL12. Spatially, myoCAFs were located close to the neoplastic cells whereas iCAFs distributed distantly from the tumor cells, likely indicating the distinct modes of CAF-tumor interactions (106–108). In addition to myoCAFs and iCAFs, a distinct CAF population expressing high levels of antigen presentation molecules such as MHC-II molecule and CD74 has been characterized (termed antigen-presenting CAFs, or apCAF). Interestingly, these cells lacked costimulatory molecules, suggesting their inability of mounting a functional immune response (107, 109). Recently, a subset of CAFs expressing leucine-rich-repeat-containing protein 15 (LRRC15) was identified in PDAC, but not in the healthy pancreas, in both mice and humans. LRRC15 marked a myofibroblast population of CAFs that were dependent on TGFβ, although its function in CAFs were unknown. These cells were shown to promote tumor growth and limit anti-tumor immunity and responsiveness to immune checkpoint blockade (110, 111).

CAFs contribute to the immunosuppressive TME in PDAC in various manners. CAFs have been reported to promote the differentiation and/or recruitment of MDSCs in the TME by secreting IL-6, GM-CSF, and CCL2 (24, 106). A more recent study has shown that CAFs secreted CSF-1 to drive p21-mediated TAM proliferation and immunosuppressive phenotypes, which promoted PDAC progression (112). Moreover, CAFs impaired anti-tumor T cell immunity, through CXCL12-mediated T cell exclusion and/or TGFβ-mediated T cell functional suppression (24, 88, 89). Finally, costimulatory-deficient apCAFs presented antigens to T cells but were unable to activate them. ApCAFs

thus prevented T cells from being activated by professional antigen-presenting cells. More recently, apCAFs were shown to have an immunoregulatory function since they directly induced Treg differentiation from naïve CD4 T cells in an antigen-specific manner (107, 109). In summary, the fundamental investigation of CAF origin, phenotypic and functional heterogeneity, and how they contribute to the immunosuppressive TME in PDAC will generate instrumental knowledge for targeting them.

8 Targeting the immunosuppressive TME to improve PDAC therapy

Immunotherapies with immune checkpoint inhibitors (ICI) have revolutionized the treatment of several cancers. However, this new treatment, particularly monotherapy, seems not to be entirely effective for PDAC, except for the 1% of patients harboring high microsatellite instability in tumors. Reasons that contribute to the low efficacy of ICI therapy for PDAC are multiple, with the overarching TME representing the most notorious one (2–5). In this regard, TME-targeted strategies have long been investigated to improve PDAC therapy, among which novel examples will be highlighted in the section (Table 1).

8.1 Targeting the immunosuppression

CSF1/CSF1R pathway plays a crucial role in TAM recruitment, maintenance, and proliferation, which can be prevented either with monoclonal antibodies to block CSF1R dimerization or with small molecule inhibitors to impair CSF1R-mediated signal transduction (44, 45, 113, 114). CSF1R inhibition has been shown to reduce CD206hi TAMs in PDAC, thereby leading to M1-like macrophage polarization, increased T cell infiltration, and reduced tumor growth (113, 114). Importantly, CSF1R inhibition improved radiotherapy, anti-PD1 and anti-CTLA4 immunotherapies, and gemcitabine chemotherapy in preclinical mouse models of PDAC (113, 114). However, a cautious approach must be taken for future clinical applications due to the potential compensatory effect of TAM depletion, which may lead to the emergence of immunosuppressive G-MDSCs (66, 115).

CCL2/CCR2 axis is highly used for PDAC to mobilize and recruit inflammatory monocytes, which further differentiate into TAMs in TME (44, 45, 116, 117). In mice, pharmacologically blocking CCL2/CCR2 axis through an anti-CCL2 neutralizing antibody or CCR2 inhibitor resulted in reduced CCR2+ monocytes and TAMs in primary PDAC and pre-metastatic liver, which consequently contributed to improved anti-tumor immunity, reduced tumor growth, and decreased metastasis (116, 117). Notably, discrepancies have been observed in murine models when comparing the effects of pharmacological blockade of CCL2/CCR2 axis to those of germline genetic ablation of CCR2 in attenuating PDAC progression (53). Such findings underscore the necessity for more meticulous and comprehensive consideration when utilizing preclinical animal models in future research. In addition, CCL2-mediated recruitment of monocytes has been a critical mechanism for PDAC to resist radiotherapy, given that blocking CCL2/CCR2 axis improved ablative radiotherapy in mouse models of PDAC (116). Clinically, phase I trials NCT01413022 (CCR2 antagonist PF-04136309 + FOLFIRINOX) and NCT02345408 (CCR2 antagonist CCX872 + FOLFIRINOX) have seen objective responses for the PDAC patients treated with the combinations (118, 119).

Another strategy to target TAMs in PDAC involves the application of CD40 agonists to activate their anti-tumor responses (14, 87, 93, 120). CD40, a member of TNF superfamily, is broadly expressed by immune cells, including monocytes, macrophages, and DCs, and is crucial for their activation, antigen presentation, and other immune responses (93, 120). In mouse models of PDAC, treatment with agonistic CD40 antibodies reprogramed TAMs toward anti-tumor phenotypes. It was evidenced by the upregulation of MHC-II and CD86, and elevated production of pro-inflammatory cytokines IL-12, TNFα, and IFNγ (93, 120). Further, combined treatment with CD40 agonists and gemcitabine/nab-paclitaxel improved TAM responses and anti-tumor T-cell clonal expansion, consequently facilitating PDAC control in mouse models (87, 93, 120). Moreover, triple therapy with T-cell inducting vaccine, PD-1 blockade, and CD40 agonist significantly promoted anti-tumor T cell immunity, marked by elevated infiltration of IFNγ-, TNFα-, and granzyme B-secreting effector T cells (121). As a result, triple therapy further improved tumor control and prolonged mouse survival. Of note, macrophage depletion markedly compromised the anti-tumor effect of CD40 agonist, suggesting the significance of macrophages in the application of this therapy (121). In patients with PDAC, combined treatment with CD40 agonist (CP-870,893) and gemcitabine led to a reduction in tumor burden in phase I study (NCT00711191) (120). However, the phase II clinical trial (NCT03214250) for metastatic PDAC patients treated with the combination of CD40 agonist (Sotigalimab), gemcitabine/nab-paclitaxel, and PD-1 blockade (Nivolumab) did not show improvements in 1-year overall survival rates (122). Therefore, future studies to identify predictive biomarkers of response will be required to achieve higher efficiency.

TANs are abundant in PDAC and targeting them has been a subject of extensive research. TAN depletion with a small molecule inhibitor of CXCR2 led to a remarked reduction in PDAC progression and metastasis in mice, which was associated with improved T cell infiltration. In line with this, CXCR2 inhibition further synergized with anti-PD1 and/or FOLFIRINOX therapies (66, 67). However, PDAC patients treated with combined CXCR2 inhibitor (AZD5069) and anti-PD-L1 (Durvalumab) in a phase Ib/II clinical trial (NCT02583477) demonstrated limited efficacy, which warranted future studies. It has been shown that CXCR2 inhibition resulted in compensatory emergence of CCR2+ myeloid cells in mouse PDAC, which in turn remarkably compromised the effect of CXCR2 inhibition (66). Further, combined inhibition of CXCR2 and CCR2 successfully disrupted the recruitment of immunosuppressive myeloid cells in mouse PDAC and consequently improved chemotherapy responses (66). It suggests

TABLE 1 Selected clinical trials targeting TME for pancreatic cancer therapy.

Target	Class	Agent	Combination partners	Enrolled patients (n)	Response of combined treatment arm	Reported biological responses	Population	Phase	Trial status	Clinical trial
CSF1R	CSF1R inhibitor (mAb)	Cabiralizumab	FOLFIRINOX, Gemcitabine/Nab-Paclitaxel, anti-PD-1 (nivolumab)	206	NR	NR	Advanced PDAC	II	Complete: 06/01/2023	NCT03336216
CD40	CD40 agonist (mAb)	CP-870,893	Gemcitabine	21	ORR 40%; SDR 53%	Inflammation cytokines (up); B cells (down)	Advanced PDAC	I	Complete: 01/2011	NCT00711191
	CD40 agonist (mAb)	APX005M	Gemcitabine/Nab-Paclitaxel, anti-PD-1 (Nivolumab)	129	ORR 31%; SDR 69%	Intratumoral CD4T cells (up); circulating differentiated CD4T cells and antigen-presenting cells (up)	Metastatic PDAC	I/II	Complete: 02/25/2022	NCT03214250
CCR2	CCR2 antagonist (small molecule)	PF-04136309	FOLFIRINOX	44	ORR 49%; SDR 14%	Peripheral CCR2+ monocytes (down), TAMs (down); Tumoral Tregs (down), CD4T and CD8T cells (up); tumoral IL12a and TNFa mRNA (up); IL10, TGFβ, IL13 mRNA (down)	PDAC	Ib	Complete: 09/2016	NCT01413022
	CCR2 antagonist (small molecule)	PF-04136309	Gemcitabine/Nab-Paclitaxel	21	NR	Peripheral CD14+CCR2+ inflammatory monocytes (down)	Metastatic PDAC	Ib/II	Complete: 10/10/2017	NCT02732938
	CCR2 antagonist (small molecule)	CCX872-B	FOLFIRINOX	54	ORR 30-37%; DCR 78%	Peripheral CCR2+ monocytes (down); tumoral MDSC (down), TAMs (down), Tregs (down); CD4T and CD8T cells (up)	PDAC	Ib	Complete: 05/06/2020	NCT02345408
CCR2/5	Dual antagonist (small molecule)	BMS-813160	Gemcitabine/Nab-Paclitaxel, anti-PD-1 (Nivolumab)	40	NR	NR	Advanced PDAC	I/II	Estimated: 10/14/2024	NCT03496662
	Dual antagonist (small molecule)	BMS-813160	FOLFIRINOX, anti-PD-1 (Nivolumab)	332	NR	NR	including advanced PDAC	Ib/II	Complete: 06/14/2023	NCT03184870
CXCR2	CXCR2 antagonist (small molecule)	AZD5069	anti-PD-L1 (Durvalumab)	23	ORR 5.6%; SDR 11% at 6mos; 5.6% at 12mos	NR	Metastatic PDAC	Ib/II	Complete: 07/09/2018	NCT02583477
CXCR1/2	CXCR1/2 inhibitor	SX-682	anti-PD-1 (nivolumab)	20	NR	NR	PDAC	I	Estimated: 12/31/2024	NCT04477343

(Continued)

10.3389/fimmu.2023.1258538

TABLE 1 Continued

Target	Class	Agent	Combination partners	Enrolled patients (n)	Response of combined treatment arm	Reported biological responses	Population	Phase	Trial status	Clinical trial
	(small molecule)									
CXCR4	AMD3100 (small molecule)	Plerixafor	anti-PD-1 (Cemiplimab)	25	NR	Intratumor effector T cells (up); macrophages and neutrophils (up)	Metastatic pnacreatic cancer	II	Complete: 0519/2023	NCT04177810
	BL-8040 (small molecule)	Motixafortide	anti-PD-1 (Pembrolizumab), fluorouracil (5-FU) and leucovorin (LV)	80	ORR 32%; DCR 77%	Tumoral CD8+ effector T cells (up); MDSCs (down); circulating Tregs (down)	Metastatic pnacreatic cancer	II	Complete: 09/06/2022	NCT02826486
TGFβ	Anti-TGFβ (mAb)	NIS793	Gemcitabine/Nab-Paclitaxel, anti-PD-1 (Spartalizumab)	151	NR	NR	Metastatic PDAC	II	Estimated: 11/30/2023	NCT04390763
	TGFβRI inhibitor (small molecule)	Galunisertib	anti-PD-L1 (Durvalumab)	37	ORR 3.1%; DCR 25%	NR	Metastatic pnacreatic cancer	I	Complete: 04/17/2019	NCT02734160
IL-10	Pegylated IL-10	Pegilodecakin	Folinic acid, fluorouracil and oxaliplatin (FOLFOX)	567	ORR 4.6%	IL-18, IFN-γ, and granzyme B (up); TGFβ (down)	Pancreatic cancer	III	Complete: 03/05/2020	NCT02923921
Vaccine	Allogeneic GM-CSF-secreting cells	GVAX	CRS-207, Cy, anti-PD-1 (Nivolumab), anti-CTLA4 (Ipilimumab)	61	ORR 4%	CD8T cell (up); CD68+ myeloid cells (down)	PDAC	II	Estimated: 08/01/2023	NCT03190265

mAb, monoclonal antibody; CSF1R, colony-stimulating factor-1 receptor; FOLFIRINOX, leucovorin calcium (folinic acid), fluorouracil, irinotecan hydrochloride, and oxaliplatin; NR, not reported; PDAC, pancreatic ductal adenocarcinoma; ORR, objective response rate; SDR, stable disease rate; up, increase in analysis; down, decrease in analysis; TAM, tumor-associated macrophage; Treg, regulatory T cell; DCR, disease control rate; MDSC, myeloid-derived suppressor cell; PD1, programmed death protein 1; PD-L1, programmed cell death ligand 1; mos, months; Estimated, estimated complete date; TGFβRI, TGFβ type I receptor; GVAX, GM-CSF-secreting pancreatic cancer cell lines; CRS-207, live-attenuated listeria-encoding human mesothelin vaccine; Cy, cyclophosphamide; CTLA4, cytotoxic T-lymphocyte-associated protein 4.

10.3389/fimmu.2023.1258538

an important point to be considered in future clinical trials regarding therapies through myeloid cell depletion.

Different strategies to directly target Tregs have been investigated. One of the earliest studies was the incorporation of low-dose cyclophosphamide in different treatment regimens to target Tregs (123, 124). Studies showed that Tregs had higher susceptibility to the toxic effects of cyclophosphamide due to their low levels of intracellular ATP (Adenosine triphosphate) and glutathione, thus were selectively eliminated (123, 124). In combination with the allogeneic PDAC vaccine (GVAX, granulocyte macrophage colony-stimulating factor–secreting pancreatic cancer cell lines), cyclophosphamide has been shown to augment immune responses in PDAC patients (125, 126). Additionally, CTLA-4, neuropilin-1, and CCL5/CCR5 have been explored as targets for intratumoral Tregs (2, 4, 5). However, it is especially worth noting that a recent study has shown an acceleration of tumorigenesis in the context of Foxp3+ Treg cell-genetic depletion in a mouse model of PDAC, which mechanistically attributed to compensatory infiltration of myeloid cells, in particular TAMs (83). In this regard, chemotherapies that can delete Tregs, such as low-dose gemcitabine (127), could unintendedly contribute to pro-tumor consequences in PDAC patients. Thus, these studies imply that therapeutic strategies aimed at immunosuppressive cell modulation rather than depletion could hold more potential to benefit PDAC outcomes.

8.2 Targeting cancer-associated fibroblasts

Targeting cancer-associated fibroblasts (CAFs) to treat cancer was initially evaluated with inhibitors of fibroblast-activation protein (FAP), a type-II transmembrane serine protease highly expressed by fibroblasts. In mice with subcutaneous PDAC, FAP inhibitor (UAMC-1110) did not show any meaningful efficacy as a single agent (128). Similarly, in patients with metastatic PDAC, combined treatment with FAP inhibitor (Talabostat) and gemcitabine demonstrated very limited efficacy over historical gemcitabine monotherapy in a phase II clinical trial (129). Given the lack of success in targeting FAP, subsequent studies have been investigated to deplete active CAFs. Studies have shown that genetic depletion of aSMA-expressing CAFs (myoCAF) in mouse models of PDAC promoted tumor progression, suggesting a tumor-suppressing function of these cells (130). Interestingly, a recent study by Krishnamurty et al. reported that depletion of LRRC15+ myoCAFs slowed tumor growth in mouse models of subcutaneous PDAC (111). Moreover, LRRC15+ myoCAF depletion in combination with anti-PDL1 led to a significantly improved anti-tumor effect (111). According to these findings, the study instead noted a tumor-supporting role for LRRC15+ myoCAFs in PDAC (111). Notably, the paradoxical results of targeting myoCAFs from the abovementioned studies warranted a comprehensive understanding of CAF heterogeneity in PDAC therapy. In PDAC, ECM is primarily secreted by CAFs and highly deposited in the TME (24). Targeting ECM, such as modulating sonic hedgehog signaling, MMP activity, or hyaluronan deposition, has also been studied. Unfortunately, early clinical trials in PDAC patients did not yield satisfactory therapeutic efficacy with these strategies (24). Another strategy for targeting CAFs is to block CAF-mediated immunosuppression. For example, disrupting CXCL12-CXCR4 signaling by AMD3100, a small molecule inhibitor of CXCR4, demonstrated a synergistic anti-tumor activity in combination with anti-PD-1/PD-L1 therapy in mouse models of PDAC (84, 89). The combination therapy of CXCR4 inhibition (ADM3100) and anti-PD1 (Cemiplimab) is now being studied in a phase II clinical trial (NCT04177810) for patients with metastatic pancreatic cancer (131). CXCR4 inhibition has also been shown to result in the infiltration of additional myeloid cells into tumors, suggesting a potential mechanism of resistance against CXCR4-targeted therapies (131). Together, these findings generally raise a perspective that future strategies should aim at modulating the TME instead of targeted depletion.

9 Concluding remarks

Over the past years, increasing knowledge has been made in understanding the complex TME of PDAC and its significance on disease biology and treatment outcomes. Despite its heterogeneity and complex interplay among various cellular components, the PDAC TME consistently exhibits immunosuppressive characteristics, which strongly influence tumor progression, metastasis, as well as responses to therapies. Other research topics that were not covered due to the scope of this review, such as cancer metabolism, vessel remodeling, and cancer vaccines, can also be promisingly targeted for therapeutics. Overall, it can be expected that conceptual advances that understand the overarching TME of PDAC toward a comprehensive overview could help to develop new therapeutic strategies aimed at targeting multiple mechanisms with synergistic effects.

Author contributions

JG: Conceptualization, Writing – original draft, Writing – review & editing. SW: Conceptualization, Writing – review & editing. QG: Conceptualization, Writing – review & editing.

Conflict of interest

The authors declare that the research was conducted in the absence of any commercial or financial relationships that could be construed as a potential conflict of interest.

Publisher's note

References

1. Siegel RL, Miller KD, Wagle NS, Jemal A. Cancer statistics, 2023. *CA Cancer J Clin* (2023) 73:17–48. doi: 10.3322/caac.21763

2. Halbrook CJ, Lyssiotis CA, di Magliano MP, Maitra A. Pancreatic cancer: Advances and challenges. *Cell* (2023) 186:1729–54. doi: 10.1016/j.cell.2023.02.014

3. Springfeld C, Ferrone CR, Katz MH, Philip PA, Hong TS, Hackert T, et al. Neoadjuvant therapy for pancreatic cancer. *Nat Rev Clin Oncol* (2023) 20:318–37. doi: 10.1038/s41571-023-00746-1

4. Sherman MH, Beatty GL. Tumor microenvironment in pancreatic cancer pathogenesis and therapeutic resistance. *Annu Rev Pathol: Mech Dis* (2023) 18:123–48. doi: 10.1146/annurev-pathmechdis-031621-024600

5. Falcomatà C, Bärthel S, Schneider G, Rad R, Schmidt-Supprian M, Saur D. Context-specific determinants of the immunosuppressive tumor microenvironment in pancreatic cancer. *Cancer Discov* (2023) 13:278–97. doi: 10.1158/2159-8290.CD-22-0876

6. Bear AS, Vonderheide RH, O'Hara MH. Challenges and opportunities for pancreatic cancer immunotherapy. *Cancer Cell* (2020) 38:788–802. doi: 10.1016/j.ccell.2020.08.004

7. Li Y, Xiang S, Pan W, Wang J, Zhan H, Liu S. Targeting tumor immunosuppressive microenvironment for pancreatic cancer immunotherapy: Current research and future perspective. *Front Oncol* (2023) 13:1166860. doi: 10.3389/fonc.2023.1166860

8. Karamitopoulou E. Tumour microenvironment of pancreatic cancer: immune landscape is dictated by molecular and histopathological features. *Br J Cancer* (2019) 121:5–14. doi: 10.1038/s41416-019-0479-5

9. Wellenstein MD, de Visser KE. Cancer-cell-intrinsic mechanisms shaping the tumor immune landscape. *Immunity* (2018) 48:399–416. doi: 10.1016/j.immuni.2018.03.004

10. Xu L, Zhu S, Lan Y, Yan M, Jiang Z, Zhu J, et al. Revealing the contribution of somatic gene mutations to shaping tumor immune microenvironment. *Briefings Bioinf* (2023) 23:bbac064. doi: 10.1093/bib/bbac064

11. Waddell N, Pajic M, Patch AM, Chang DK, Kassahn KS, Bailey P, et al. Whole genomes redefine the mutational landscape of pancreatic cancer. *Nature* (2015) 518:495–501. doi: 10.1038/nature14169

12. Väyrynen SA, Zhang J, Yuan C, Väyrynen JP, Dias Costa A, Williams H, et al. Composition, spatial characteristics, and prognostic significance of myeloid cell infiltration in pancreatic cancer. *Clin Cancer Res* (2021) 27:1069–81. doi: 10.1158/1078-0432.CCR-20-3141

13. Tay C, Tanaka A, Sakaguchi S. Tumor-infiltrating regulatory T cells as targets of cancer immunotherapy. *Cancer Cell* (2023) 41:450–65. doi: 10.1016/j.ccell.2023.02.014

14. Barry ST, Gabrilovich DI, Sansom OJ, Campbell AD, Morton JP. Therapeutic targeting of tumour myeloid cells. *Nat Rev Cancer* (2023) 23:216–37. doi: 10.1038/s41568-022-00546-2

15. Tan Z, Lei Y, Zhang B, Shi S, Liu J, Yu X, et al. Mechanisms of T-cell exhaustion in pancreatic cancer. *Cancers* (2020) 12:2274. doi: 10.3390/cancers12082274

16. Hegde S, Krisnawan VE, Herzog BH, Zuo C, Breden MA, Knolhoff BL, et al. Dendritic cell paucity leads to dysfunctional immune surveillance in pancreatic cancer. *Cancer Cell* (2020) 37:289–307. doi: 10.1016/j.ccell.2020.02.008

17. Lin JH, Huffman AP, Wattenberg MM, Walter DM, Carpenter EL, Feldser DM, et al. Type 1 conventional dendritic cells are systemically dysregulated early in pancreatic carcinogenesis. *J Exp Med* (2020) 217:e20190673. doi: 10.1084/jem.20190673

18. Jun E, Song AY, Choi JW, Lee HH, Kim MY, Ko DH, et al. Progressive impairment of NK cell cytotoxic degranulation is associated with TGF-β1 deregulation and disease progression in pancreatic cancer. *Front Immunol* (2019) 10:1354. doi: 10.3389/fimmu.2019.01354

19. Tan Z, Lei Y, Zhang B, Shi S, Liu J, Yu X, et al. Analysis of immune-related signatures related to CD4+ T cell infiltration with gene co-expression network in pancreatic adenocarcinoma. *Front Oncol* (2021) 11:674897. doi: 10.3389/fonc.2021.674897

20. Wei R, Zhang H, Cao J, Qin D, Deng W, Li S. Type 1 T helper cell-based molecular subtypes and signature are associated with clinical outcome in pancreatic ductal adenocarcinoma. *Front Cell Dev Biol* (2022) 10:839893. doi: 10.3389/fcell.2022.839893

21. Piro G, Simionato F, Carbone C, Frizziero M, Malleo G, Zanini S, et al. A circulating TH2 cytokines profile predicts survival in patients with resectable pancreatic adenocarcinoma. *Oncoimmunology* (2017) 6:e1322242. doi: 10.1080/2162402X.2017.1322242

22. Gnerlich JL, Mitchem JB, Weir JS, Sankpal NV, Kashiwagi H, Belt BA, et al. Induction of Th17 cells in the tumor microenvironment improves survival in a murine model of pancreatic cancer. *J Immunol* (2021) 185:4063–71. doi: 10.4049/jimmunol.0902609

23. Delvecchio FR, Goulart MR, Fincham REA, Bombadieri M, Kocher HM. B cells in pancreatic cancer stroma. *World J Gastroenterol* (2022) 28:1088. doi: 10.3748/wjg.v28.i11.1088

24. Sherman MH, di Magliano MP. Cancer-associated fibroblasts: lessons from pancreatic cancer. *Annu Rev Cancer Biol* (2023) 7:43–55. doi: 10.1146/annurev-cancerbio-061421-035400

25. Bailey P, Chang DK, Nones K, Johns AL, Patch AM, Gingras MC, et al. Genomic analyses identify molecular subtypes of pancreatic cancer. *Nature* (2016) 531:47–52. doi: 10.1038/nature16965

26. Connor AA, Gallinger S. Pancreatic cancer evolution and heterogeneity: integrating omics and clinical data. *Nat Rev Cancer* (2022) 22:131–42. doi: 10.1038/s41568-021-00418-1

27. Fang YT, Yang WW, Niu YR, Sun YK. Recent advances in targeted therapy for pancreatic adenocarcinoma. *World J Gastrointest Oncol* (2023) 15:571. doi: 10.4251/wjgo.v15.i4.571

28. Dias Carvalho P, Guimaraes CF, Cardoso AP, Mendonca S, Costa AM, Oliveira MJ, et al. KRAS oncogenic signaling extends beyond cancer cells to orchestrate the microenvironment. *Cancer Res* (2018) 78:7–14. doi: 10.1158/0008-5472.CAN-17-2084

29. Ischenko I, D'Amico S, Rao M, Li J, Hayman MJ, Powers S, et al. KRAS drives immune evasion in a genetic model of pancreatic cancer. *Nat Commun* (2021) 12:1482. doi: 10.1038/s41467-021-21736-w

30. Pylayeva-Gupta Y, Lee KE, Hajdu CH, Miller G, Bar-Sagi D. Oncogenic Kras-induced GM-CSF production promotes the development of pancreatic neoplasia. *Cancer Cell* (2012) 21:836–47. doi: 10.1016/j.ccr.2012.04.024

31. Bayne LJ, Beatty GL, Jhala N, Clark CE, Rhim AD, Stanger BZ, et al. Tumor-derived granulocyte-macrophage colony-stimulating factor regulates myeloid inflammation and T cell immunity in pancreatic cancer. *Cancer Cell* (2012) 21:822–35. doi: 10.1016/j.ccr.2012.04.025

32. Hashimoto S, Furukawa S, Hashimoto A, Tsutaho A, Fukao A, Sakamura Y, et al. ARF6 and AMAP1 are major targets of KRAS and TP53 mutations to promote invasion, PD-L1 dynamics, and immune evasion of pancreatic cancer. *Proc Natl Acad Sci* (2019) 116:17450–9. doi: 10.1073/pnas.1901765116

33. Alausa A, Lawal KA, Babatunde OA, Obiwulu ENO, Oladokun OC, Fadahunsi OS, et al. Overcoming immunotherapeutic resistance in PDAC: SIRPα-CD47 blockade. *Pharmacol Res* (2022) 181:106264. doi: 10.1016/j.phrs.2022.106264

34. Yamamoto K, Venida A, Yano J, Biancur DE, Kakiuchi M, Gupta S, et al. Autophagy promotes immune evasion of pancreatic cancer by degrading MHC-I. *Nature* (2020) 581:100–5. doi: 10.1038/s41586-020-2229-5

35. Yamamoto K, Venida A, Perera RM, Kimmelman AC. Selective autophagy of MHC-I promotes immune evasion of pancreatic cancer. *Autophagy* (2020) 16:1524–5. doi: 10.1080/15548627.2020.1769973

36. Wirth M, Mahboobi S, Krämer OH, Schneider G. Concepts to target MYC in pancreatic cancer. *Mol Cancer Ther* (2016) 15:1792–8. doi: 10.1158/1535-7163.MCT-16-0050

37. Hessmann E, Schneider G, Ellenrieder V, Siveke JT. MYC in pancreatic cancer: novel mechanistic insights and their translation into therapeutic strategies. *Oncogene* (2016) 35:1609–18. doi: 10.1038/onc.2015.216

38. Sodir NM, Kortlever RM, Barthet VJ, Campos T, Pellegrinet L, Kupczak S, et al. MYC instructs and maintains pancreatic adenocarcinoma phenotype. *Cancer Discov* (2020) 10:588–607. doi: 10.1158/2159-8290.CD-19-0435

39. Maddipati R, Norgard RJ, Baslan T, Rathi KS, Zhang A, Saeid A, et al. MYC levels regulate metastatic heterogeneity in pancreatic adenocarcinoma. *Cancer Discov* (2022) 12:542–61. doi: 10.1158/2159-8290.CD-20-1826

40. Muthalagu N, Monteverde T, Raffo-Iraolagoitia X, Wiesheu R, Whyte D, Hedley A, et al. Repression of the type I interferon pathway underlies MYC-and KRAS-dependent evasion of NK and B cells in pancreatic ductal adenocarcinoma. *Cancer Discov* (2020) 10:872–87. doi: 10.1158/2159-8290.CD-19-0620

41. Maddalena M, Mallel G, Nataraj NB, Shreberk-Shaked M, Hassin O, Mukherjee S, et al. TP53 missense mutations in PDAC are associated with enhanced fibrosis and an immunosuppressive microenvironment. *Proc Natl Acad Sci* (2021) 118: e2025631118. doi: 10.1073/pnas.2025631118

42. Siolas D, Vucic E, Kurz E, Hajdu C, Bar-Sagi D. Gain-of-function p53R172H mutation drives accumulation of neutrophils in pancreatic tumors, promoting resistance to immunotherapy. *Cell Rep* (2021) 36:109578. doi: 10.1016/j.celrep.2021.109578

43. Blagih J, Zani F, Chakravarty P, Hennequart M, Pilley S, Hobor S, et al. Cancer-specific loss of p53 leads to a modulation of myeloid and T cell responses. *Cell Rep* (2020) 30:481–96. doi: 10.1016/j.celrep.2019.12.028

44. Yang S, Liu Q, Liao Q. Tumor-associated macrophages in pancreatic ductal adenocarcinoma: origin, polarization, function, and reprogramming. *Front Cell Dev Biol* (2021) 8:607209. doi: 10.3389/fcell.2020.607209

45. Pittet MJ, Michielin O, Migliorini D. Clinical relevance of tumour-associated macrophages. *Nat Rev Clin Oncol* (2022) 19:402–21. doi: 10.1038/s41571-022-00620-6

46. Liou GY, Döppler H, Necela B, Krishna M, Crawford HC, Raimondo M, et al. Macrophage-secreted cytokines drive pancreatic acinar-to-ductal metaplasia through NF-κB and MMPs. *J Cell Biol* (2013) 202:563–77. doi: 10.1083/jcb.201301001

47. Liou GY, Döppler H, Necela B, Edenfield B, Zhang L, Dawson DW, et al. Mutant KRAS–induced expression of ICAM-1 in pancreatic acinar cells causes attraction of macrophages to expedite the formation of precancerous lesions. *Cancer Discov* (2015) 5:52–63. doi: 10.1158/2159-8290.CD-14-0474

48. Lesina M, Kurkowski MU, Ludes K, Rose-John S, Treiber M, Klöppel G, et al. Stat3/Socs3 activation by IL-6 transsignaling promotes progression of pancreatic intraepithelial neoplasia and development of pancreatic cancer. *Cancer Cell* (2011) 19:456–69. doi: 10.1016/j.ccr.2011.03.009

49. Al-Ismaeel Q, Neal CP, Al-Mahmoodi H, Almutairi Z, Al-Shamarti I, Straatman K, et al. ZEB1 and IL-6/11-STAT3 signalling cooperate to define invasive potential of pancreatic cancer cells via differential regulation of the expression of S100 proteins. *Br J Cancer* (2019) 121:65–75. doi: 10.1038/s41416-019-0483-9

50. Zhang J, Song J, Tang S, Zhao Y, Wang L, Luo Y, et al. Multi-omics analysis reveals the chemoresistance mechanism of proliferating tissue-resident macrophages in PDAC via metabolic adaptation. *Cell Rep* (2023) 42:112620. doi: 10.1016/j.celrep.2023.112620

51. Griesmann H, Drexel C, Milosevic N, Sipos B, Rosendahl J, Gress TM, et al. Pharmacological macrophage inhibition decreases metastasis formation in a genetic model of pancreatic cancer. *Gut* (2017) 66:1278–85. doi: 10.1136/gutjnl-2015-310049

52. Gao Q, Mo S, Han C, Liao X, Yang C, Wang X, et al. Comprehensive analysis of LILR family genes expression and tumour-infiltrating immune cells in early-stage pancreatic ductal adenocarcinoma. *IET Syst Biol* (2023) 17:39–57. doi: 10.1049/syb2.12058

53. Zhu Y, Herndon JM, Sojka DK, Kim KW, Knolhoff BL, Zuo C, et al. Tissue-resident macrophages in pancreatic ductal adenocarcinoma originate from embryonic hematopoiesis and promote tumor progression. *Immunity* (2017) 47:323–38. doi: 10.1016/j.immuni.2017.07.014

54. Molgora M, Esaulova E, Vermi W, Hou J, Chen Y, Luo J, et al. TREM2 modulation remodels the tumor myeloid landscape enhancing anti-PD-1 immunotherapy. *Cell* (2020) 182:886–900. doi: 10.1016/j.cell.2020.07.013

55. Binnewies M, Pollack JL, Rudolph J, Dash S, Abushawish M, Lee T, et al. Targeting TREM2 on tumor-associated macrophages enhances immunotherapy. *Cell Rep* (2021) 37:109844. doi: 10.1016/j.celrep.2021.109844

56. Park MD, Reyes-Torres I, LeBerichel J, Hamon P, LaMarche NM, Hegde S, et al. TREM2 macrophages drive NK cell paucity and dysfunction in lung cancer. *Nat Immunol* (2023) 24:792–801. doi: 10.1038/s41590-023-01475-4

57. Colonna M. The biology of TREM receptors. *Nat Rev Immunol* (2023) 7:1–15. doi: 10.1038/s41577-023-00837-1

58. Hedrick CC, Malanchi I. Neutrophils in cancer: heterogeneous and multifaceted. *Nat Rev Immunol* (2022) 22:173–87. doi: 10.1038/s41577-021-00571-6

59. Jiang W, Li X, Xiang C, Zhou W. Neutrophils in pancreatic cancer: potential therapeutic targets. *Front Oncol* (2022) 12:1025805. doi: 10.3389/fonc.2022.1025805

60. Wang Y, Fang T, Huang L, Wang H, Zhang L, Wang Z, et al. Neutrophils infiltrating pancreatic ductal adenocarcinoma indicate higher Malignancy and worse prognosis. *Biochem Biophys Res Commun* (2018) 501:313–9. doi: 10.1016/j.bbrc.2018.05.024

61. Xiang ZJ, Hu T, Wang Y, Wang H, Xu L, Cui N. Neutrophil–lymphocyte ratio (NLR) was associated with prognosis and immunomodulatory in patients with pancreatic ductal adenocarcinoma (PDAC). *Biosci Rep* (2020) 40:BSR20201190. doi: 10.1042/BSR20201190

62. Yang JJ, Hu ZG, Shi WX, Deng T, He SQ, Yuan SG. Prognostic significance of neutrophil to lymphocyte ratio in pancreatic cancer: a meta-analysis. *World J gastroenterol: WJG* (2015) 21:2807. doi: 10.3748/wjg.v21.i9.2807

63. Jiang SH, Liu D, Hu LP, Zhang S, Yu Y, Sun YW, et al. Modeling of cancer-related body-wide effects identifies LTB4 as a diagnostic biomarker for pancreatic cancer. *EBioMedicine* (2022) 80:104050. doi: 10.1016/j.ebiom.2022.104050

64. Bianchi A, De Castro Silva I, Deshpande NU, Singh S, Mehra S, Garrido VT, et al. Cell-autonomous Cxcl1 sustains tolerogenic circuitries and stromal inflammation via neutrophil-derived TNF in pancreatic cancer. *Cancer Discov* (2023) 13:1428–53. doi: 10.1158/2159-8290.CD-22-1046

65. Nielsen SR, Strøbech JE, Horton ER, Jackstadt R, Laitala A, Bravo MC, et al. Suppression of tumor-associated neutrophils by lorlatinib attenuates pancreatic cancer growth and improves treatment with immune checkpoint blockade. *Nat Commun* (2021) 12:3414. doi: 10.1038/s41467-021-23731-7

66. Nywening TM, Belt BA, Cullinan DR, Panni RZ, Han BJ, Sanford DE, et al. Targeting both tumour-associated CXCR2+ neutrophils and CCR2+ macrophages disrupts myeloid recruitment and improves chemotherapeutic responses in pancreatic ductal adenocarcinoma. *Gut* (2018) 67:1112–23. doi: 10.1136/gutjnl-2017-313738

67. Steele CW, Karim SA, Leach JD, Bailey P, Upstill-Goddard R, Rishi L, et al. CXCR2 inhibition profoundly suppresses metastases and augments immunotherapy in pancreatic ductal adenocarcinoma. *Cancer Cell* (2016) 29:832–45. doi: 10.1016/j.ccell.2016.04.014

68. Wang X, Hu LP, Qin WT, Yang Q, Chen DY, Li Q, et al. Identification of a subset of immunosuppressive P2RX1-negative neutrophils in pancreatic cancer liver metastasis. *Nat Commun* (2021) 12:174. doi: 10.1038/s41467-020-20447-y

69. Gaida MM, Steffen TG, Günther F, Tschaharganeh DF, Felix K, Bergmann F, et al. Polymorphonuclear neutrophils promote dyshesion of tumor cells and elastase-mediated degradation of E-cadherin in pancreatic tumors. *Eur J Immunol* (2012) 42:3369–80. doi: 10.1002/eji.201242628

70. Canè S, Barouni RM, Fabbi M, Cuozzo J, Fracasso G, Adamo A, et al. Neutralization of NET-associated human ARG1 enhances cancer immunotherapy. *Sci Trans Med* (2023) 15:eabq6221. doi: 10.1126/scitranslmed.abq6221

71. Jin W, Yin H, Li H, Yu XJ, Xu HX, Liu L. Neutrophil extracellular DNA traps promote pancreatic cancer cells migration and invasion by activating EGFR/ERK pathway. *J Cell Mol Med* (2021) 25:5443–56. doi: 10.1111/jcmm.16555

72. Miller-Ocuin JL, Liang X, Boone BA, Doerfler WR, Singhi AD, Tang D, et al. DNA released from neutrophil extracellular traps (NETs) activates pancreatic stellate cells and enhances pancreatic tumor growth. *Oncoimmunology* (2019) 8:e1605822. doi: 10.1080/2162402X.2019.1605822

73. Fridlender ZG, Sun J, Kim S, Kapoor V, Cheng G, Ling L, et al. Polarization of tumor-associated neutrophil phenotype by TGF-β:"N1" versus "N2" TAN. *Cancer Cell* (2009) 16:183–94. doi: 10.1016/j.ccr.2009.06.017

74. Gungabeesoon J, Gort-Freitas NA, Kiss M, Bolli E, Messemaker M, Siwicki M, et al. A neutrophil response linked to tumor control in immunotherapy. *Cell* (2023) 186:1448–64. doi: 10.1016/j.cell.2023.02.032

75. Hirschhorn D, Budhu S, Kraehenbuehl L, Gigoux M, Schröder D, Chow A, et al. T cell immunotherapies engage neutrophils to eliminate tumor antigen escape variants. *Cell* (2023) 186:1432–47. doi: 10.1016/j.cell.2023.03.007

76. Karakhanova S, Link J, Heinrich M, Shevchenko I, Yang Y, Hassenpflug M, et al. Characterization of myeloid leukocytes and soluble mediators in pancreatic cancer: importance of myeloid-derived suppressor cells. *Oncoimmunology* (2015) 4:e998519. doi: 10.1080/2162402X.2014.998519

77. Diaz-Montero CM, Salem ML, Nishimura MI, Garrett-Mayer E, Cole DJ, Montero AJ. Increased circulating myeloid-derived suppressor cells correlate with clinical cancer stage, metastatic tumor burden, and doxorubicin–cyclophosphamide chemotherapy. *Cancer Immunol Immunother* (2009) 58:49–59. doi: 10.1007/s00262-008-0523-4

78. Veglia F, Sanseviero E, Gabrilovich DI. Myeloid-derived suppressor cells in the era of increasing myeloid cell diversity. *Nat Rev Immunol* (2021) 21:485–98. doi: 10.1038/s41577-020-00490-y

79. Siret C, Collignon A, Silvy F, Robert S, Cheyrol T, André P, et al. Deciphering the crosstalk between myeloid-derived suppressor cells and regulatory T cells in pancreatic ductal adenocarcinoma. *Front Immunol* (2020) 10:3070. doi: 10.3389/fimmu.2019.03070

80. Pergamo M, Miller G. Myeloid-derived suppressor cells and their role in pancreatic cancer. *Cancer Gene Ther* (2017) 24:100–5. doi: 10.1038/cgt.2016.65

81. Togashi Y, Shitara K, Nishikawa H. Regulatory T cells in cancer immunosuppression—implications for anticancer therapy. *Nat Rev Clin Oncol* (2019) 16:356–71. doi: 10.1038/s41571-019-0175-7

82. Liu L, Zhao G, Wu W, Rong Y, Jin D, Wang D, et al. Low intratumoral regulatory T cells and high peritumoral CD8+ T cells relate to long-term survival in patients with pancreatic ductal adenocarcinoma after pancreatectomy. *Cancer Immunol Immunother* (2016) 65:73–82. doi: 10.1007/s00262-015-1775-4

83. Zhang Y, Lazarus J, Steele NG, Yan W, Lee HJ, Nwosu ZC, et al. Regulatory T-cell depletion alters the tumor microenvironment and accelerates pancreatic carcinogenesis. *Cancer Discov* (2020) 10:422–39. doi: 10.1158/2159-8290.CD-19-0958

84. Ma Y, Hwang RF, Logsdon CD, Ullrich SE. Dynamic mast cell–stromal cell interactions promote growth of pancreatic cancer. *Cancer Res* (2013) 73:3927–37. doi: 10.1158/0008-5472.CAN-12-4479

85. Chang DZ, Ma Y, Ji B, Wang H, Deng D, Liu Y, et al. Mast cells in tumor microenvironment promotes the in *vivo* growth of pancreatic ductal adenocarcinoma. *Clin Cancer Res* (2011) 17:7015–23. doi: 10.1158/1078-0432.CCR-11-0607

86. Longo V, Tamma R, Brunetti O, Pisconti S, Argentiero A, Silvestris N, et al. Mast cells and angiogenesis in pancreatic ductal adenocarcinoma. *Clin Exp Med* (2018) 18:319–23. doi: 10.1007/s10238-018-0493-6

87. Beatty GL, Winograd R, Evans RA, Long KB, Luque SL, Lee JW, et al. Exclusion of T cells from pancreatic carcinomas in mice is regulated by Ly6Clow F4/80+ extratumoral macrophages. *Gastroenterology* (2015) 149:201–10. doi: 10.1053/j.gastro.2015.04.010

88. Principe DR, Park A, Dorman MJ, Kumar S, Viswakarma N, Rubin J, et al. TGFβ blockade augments PD-1 inhibition to promote T-cell–mediated regression of pancreatic cancer. *Mol Cancer Ther* (2019) 18:613–20. doi: 10.1158/1535-7163.MCT-18-0850

89. Feig C, Jones JO, Kraman M, Wells RJ, Deonarine A, Chan DS, et al. Targeting CXCL12 from FAP-expressing carcinoma-associated fibroblasts synergizes with anti–PD-L1 immunotherapy in pancreatic cancer. *Proc Natl Acad Sci* (2013) 110:20212–7. doi: 10.1073/pnas.1320318110

90. Ene–Obong A, Clear AJ, Watt J, Wang J, Fatah R, Riches JC, et al. Activated pancreatic stellate cells sequester CD8+ T cells to reduce their infiltration of the juxtatumoral compartment of pancreatic ductal adenocarcinoma. *Gastroenterology* (2013) 145:1121–32. doi: 10.1053/j.gastro.2013.07.025

91. Yamamoto T, Yanagimoto H, Satoi S, Toyokawa H, Yamao J, Kim S, et al. Circulating myeloid dendritic cells as prognostic factors in patients with pancreatic cancer who have undergone surgical resection. *J Surg Res* (2012) 173:299–308. doi: 10.1016/j.jss.2010.09.027

92. James CA, Baer JM, Zou C, Panni UY, Knolhoff BL, Hogg GD, et al. Systemic alterations in type-2 conventional dendritic cells lead to impaired tumor immunity in pancreatic cancer. *Cancer Immunol Res* (2023) 11:1055–67. doi: 10.1158/2326-6066.CIR-21-0946

93. Lau SP, van Montfoort N, Kinderman P, Lukkes M, Klaase L, van Nimwegen M, et al. Dendritic cell vaccination and CD40-agonist combination therapy licenses T cell-dependent antitumor immunity in a pancreatic carcinoma murine model. *J immunother Cancer* (2020) 8:e000772. doi: 10.1136/jitc-2020-000772

94. Lim SA, Kim J, Jeon S, Shin MH, Kwon J, Kim TJ, et al. Defective localization with impaired tumor cytotoxicity contributes to the immune escape of NK cells in pancreatic cancer patients. *Front Immunol* (2019) 10:496. doi: 10.3389/fimmu.2019.00496

95. Liu B, Zhu X, Kong L, Wang M, Spanoudis C, Chaturvedi P, et al. Bifunctional TGF-β trap/IL-15 protein complex elicits potent NK cell and CD8+ T cell immunity against solid tumors. *Mol Ther* (2021) 29:2949–62. doi: 10.1016/j.ymthe.2021.06.001

96. Jacenik D, Karagiannidis I, Beswick EJ. Th2 cells inhibit growth of colon and pancreas cancers by promoting anti-tumorigenic responses from macrophages and eosinophils. *Br J Cancer* (2023) 128:387–97. doi: 10.1038/s41416-022-02056-2

97. He S, Fei M, Wu Y, Zheng D, Wan D, Wang L, et al. Distribution and clinical significance of Th17 cells in the tumor microenvironment and peripheral blood of pancreatic cancer patients. *Int J Mol Sci* (2011) 12:7424–37. doi: 10.3390/ijms12117424

98. McAllister F, Bailey JM, Alsina J, Nirschl CJ, Sharma R, Fan H, et al. Oncogenic Kras activates a hematopoietic-to-epithelial IL-17 signaling axis in preinvasive pancreatic neoplasia. *Cancer Cell* (2014) 25:621–37. doi: 10.1016/j.ccr.2014.03.014

99. Senturk ZN, Akdag I, Deniz B, Sayi-Yazgan A. Pancreatic cancer: Emerging field of regulatory B-cell-targeted immunotherapies. *Front Immunol* (2023) 14:1152551. doi: 10.3389/fimmu.2023.1152551

100. Pylayeva-Gupta Y, Das S, Handler JS, Hajdu CH, Coffre M, Koralov SB, et al. IL35-producing B cells promote the development of pancreatic neoplasia. *Cancer Discovery* (2016) 6:247–55. doi: 10.1158/2159-8290.CD-15-0843

101. Gunderson AJ, Kaneda MM, Tsujikawa T, Nguyen AV, Affara NI, Ruffell B, et al. Bruton tyrosine kinase–dependent immune cell cross-talk drives pancreas cancer. *Cancer Discovery* (2016) 6:270–85. doi: 10.1158/2159-8290.CD-15-0827

102. Lee KE, Spata M, Bayne LJ, Buza EL, Durham AC, Allman D, et al. Hif1a deletion reveals pro-neoplastic function of B cells in pancreatic neoplasia. *Cancer Discovery* (2016) 6:256–69. doi: 10.1158/2159-8290.CD-15-0822

103. Castino GF, Cortese N, Capretti G, Serio S, Di Caro G, Mineri R, et al. Spatial distribution of B cells predicts prognosis in human pancreatic adenocarcinoma. *Oncoimmunology* (2016) 54:e1085147. doi: 10.1080/2162402X.2015.1085147

104. Kinker GS, Vitiello GAF, Diniz AB, Cabral-Piccin MP, Pereira PHB, Carvalho MLR, et al. Mature tertiary lymphoid structures are key niches of tumour-specific immune responses in pancreatic ductal adenocarcinomas. *Gut* (2023), gutjnl–2022-328697. doi: 10.1136/gutjnl-2022-328697

105. Helms EJ, Berry MW, Chaw RC, DuFort CC, Sun D, Onate MK, et al. Mesenchymal lineage heterogeneity underlies nonredundant functions of pancreatic cancer–associated fibroblasts. *Cancer Discovery* (2022) 12:484–501. doi: 10.1158/2159-8290.CD-21-0601

106. Öhlund D, Handly-Santana A, Biffi G, Elyada E, Almeida AS, Ponz-Sarvise M, et al. Distinct populations of inflammatory fibroblasts and myofibroblasts in pancreatic cancer. *J Exp Med* (2017) 214:579–96. doi: 10.1084/jem.20162024

107. Elyada E, Bolisetty M, Laise P, Flynn WF, Courtois ET, Burkhart RA, et al. Cross-species single-cell analysis of pancreatic ductal adenocarcinoma reveals antigen-presenting cancer-associated fibroblasts. *Cancer Discov* (2019) 9:1102–23. doi: 10.1158/2159-8290.CD-19-0094

108. Bernard V, Semaan A, Huang J, San Lucas FA, Mulu FC, Stephens BM, et al. Single-cell transcriptomics of pancreatic cancer precursors demonstrates epithelial and microenvironmental heterogeneity as an early event in neoplastic progression. *Clin Cancer Res* (2019) 25:2194–205. doi: 10.1158/1078-0432.CCR-18-1955

109. Huang H, Wang Z, Zhang Y, Pradhan RN, Ganguly D, Chandra R, et al. Mesothelial cell-derived antigen-presenting cancer-associated fibroblasts induce expansion of regulatory T cells in pancreatic cancer. *Cancer Cell* (2022) 40:656–73. doi: 10.1016/j.ccell.2022.04.011

110. Dominguez CX, Müller S, Keerthivasan S, Koeppen H, Hung J, Gierke S, et al. Single-cell RNA sequencing reveals stromal evolution into LRRC15+ myofibroblasts as a determinant of patient response to cancer immunotherapy. *Cancer Discov* (2020) 10:232–53. doi: 10.1158/2159-8290.CD-19-0644

111. Krishnamurty AT, Shyer JA, Thai M, Gandham V, Buechler MB, Yang YA, et al. LRRC15+ myofibroblasts dictate the stromal setpoint to suppress tumour immunity. *Nature* (2022) 611:148–54. doi: 10.1038/s41586-022-05272-1

112. Zuo C, Baer JM, Knolhoff BL, Belle JI, Liu X, Alarcon de la Lastra A, et al. Stromal and therapy-induced macrophage proliferation promotes PDAC progression and susceptibility to innate immunotherapy. *J Exp Med* (2023) 220:e20212062. doi: 10.1084/jem.20212062

113. Zhu Y, Knolhoff BL, Meyer MA, Nywening TM, West BL, Luo J, et al. CSF1/CSF1R blockade reprograms tumor-infiltrating macrophages and improves response to T-cell checkpoint immunotherapy in pancreatic cancer models. *Cancer Res* (2014) 74:5057–69. doi: 10.1158/0008-5472.CAN-13-3723

114. Ho WJ, Jaffee EM. Macrophage-targeting by CSF1/1R blockade in pancreatic cancers. *Cancer Res* (2021) 81:6071–3. doi: 10.1158/0008-5472.CAN-21-3603

115. Loeuillard E, Yang J, Buckarma E, Wang J, Liu Y, Conboy C, et al. Targeting tumor-associated macrophages and granulocytic myeloid-derived suppressor cells augments PD-1 blockade in cholangiocarcinoma. *J Clin Invest* (2020) 130:5380–96. doi: 10.1172/JCI137110

116. Kalbasi A, Komar C, Tooker GM, Liu M, Lee JW, Gladney WL, et al. Tumor-derived CCL2 mediates resistance to radiotherapy in pancreatic ductal adenocarcinoma. *Clin Cancer Res* (2017) 23:137–48. doi: 10.1158/1078-0432.CCR-16-0870

117. Wang J, Saung MT, Li K, Fu J, Fujiwara K, Niu N, et al. CCR2/CCR5 inhibitor permits the radiation-induced effector T cell infiltration in pancreatic adenocarcinoma. *J Exp Med* (2022) 219:e20211631. doi: 10.1084/jem.20211631

118. Nywening TM, Wang-Gillam A, Sanford DE, Belt BA, Panni RZ, Cusworth BM, et al. Targeting tumour-associated macrophages with CCR2 inhibition in combination with FOLFIRINOX in patients with borderline resectable and locally advanced pancreatic cancer: a single-centre, open-label, dose-finding, non-randomised, phase 1b trial. *Lancet Oncol* (2016) 17:651–62. doi: 10.1016/S1470-2045(16)00078-4

119. Linehan D, Noel MS, Hezel AF, Wang-Gillam A, Eskens F, Sleijfer S, et al. Overall survival in a trial of orally administered CCR2 inhibitor CCX872 in locally advanced/metastatic pancreatic cancer: Correlation with blood monocyte counts. *ASCO-SITC Clin Immuno-Oncol* (2018) 36:92. doi: 10.1200/JCO.2018.36.5_suppl.92

120. Beatty GL, Chiorean EG, Fishman MP, Saboury B, Teitelbaum UR, Sun W, et al. CD40 agonists alter tumor stroma and show efficacy against pancreatic carcinoma in mice and humans. *Science* (2011) 331:1612–6. doi: 10.1126/science.1198443

121. Winograd R, Byrne KT, Evans RA, Odorizzi PM, Meyer AR, Bajor DL, et al. Induction of T-cell immunity overcomes complete resistance to PD-1 and CTLA-4 blockade and improves survival in pancreatic carcinoma. *Cancer Immunol Res* (2015) 3:399–411. doi: 10.1158/2326-6066.CIR-14-0215

122. O'Hara MH, O'Reilly EM, Varadhachary G, Wolff RA, Wainberg ZA, Ko AH, et al. CD40 agonistic monoclonal antibody APX005M (sotigalimab) and chemotherapy, with or without nivolumab, for the treatment of metastatic pancreatic adenocarcinoma: an open-label, multicentre, phase 1b study. *Lancet Oncol* (2021) 22:118–31. doi: 10.1016/S1470-2045(20)30532-5

123. Le DT, Jaffee EM. Regulatory T-cell modulation using cyclophosphamide in vaccine approaches: a current perspective. *Cancer Res* (2012) 72:3439–44. doi: 10.1158/0008-5472.CAN-11-3912

124. Zhao J, Cao Y, Lei Z, Yang Z, Zhang B, Huang B. Selective depletion of CD4+ CD25+ Foxp3+ regulatory T cells by low-dose cyclophosphamide is explained by reduced intracellular ATP levels. *Cancer Res* (2010) 70:4850–8. doi: 10.1158/0008-5472.CAN-10-0283

125. Laheru D, Lutz E, Burke J, Biedrzycki B, Solt S, Onners B, et al. Allogeneic granulocyte macrophage colony-stimulating factor–secreting tumor immunotherapy alone or in sequence with cyclophosphamide for metastatic pancreatic cancer: a pilot study of safety, feasibility, and immune activation. *Clin Cancer Res* (2008) 14:1455–63. doi: 10.1158/1078-0432.CCR-07-0371

126. Lutz ER, Wu AA, Bigelow E, Sharma R, Mo G, Soares K, et al. Immunotherapy converts nonimmunogenic pancreatic tumors into immunogenic foci of immune regulation. *Cancer Immunol Res* (2014) 2:616–31. doi: 10.1158/2326-6066.CIR-14-0027

127. Shevchenko I, Karakhanova S, Soltek S, Link J, Bayry J, Werner J, et al. Low-dose gemcitabine depletes regulatory T cells and improves survival in the orthotopic Panc02 model of pancreatic cancer. *Int J Cancer* (2013) 133:98–107. doi: 10.1002/ijc.27990

128. Young KH, McCarty K, Friedman D, Cottam B, Newell P, Gough M, et al. Preclinical combination of radiation and fibroblast activation protein inhibition in pancreatic cancer. *ASCO Annu Meeting I* (2016) 34:e23117. doi: 10.1200/JCO.2016.34.15_suppl.e23117

129. Nugent FW, Cunningham C, Barve MA, Fisher W, Patel H, Meiri E, et al. Phase 2 study of talabostat/gemcitabine in Stage IV pancreatic cancer. *J Clin Oncol* (2007) 25:4616–6. doi: 10.1200/jco.2007.25.18_suppl.4616

130. Özdemir BC, Pentcheva-Hoang T, Carstens JL, Zheng X, Wu CC, Simpson TR, et al. Depletion of carcinoma-associated fibroblasts and fibrosis induces immunosuppression and accelerates pancreas cancer with reduced survival. *Cancer Cell* (2014) 25:719–34. doi: 10.1016/j.ccr.2014.04.005

131. Shin SM, Hernandez A, Coyne E, Zhang Z, Mitchell S, Durham J, et al. Combination of CXCR4 antagonist and anti-PD1 therapy results in significant mobilization and increased infiltration of myeloid cells into the metastatic liver microenvironment of PDAC. *Cancer Res* (2023) 83:2270–0. doi: 10.1158/1538-7445.AM2023-2270

frontiers | Frontiers in Immunology

TYPE Original Research
PUBLISHED 12 January 2024
DOI 10.3389/fimmu.2023.1297886

OPEN ACCESS

EDITED BY
Xuanbin Wang,
Hubei University of Medicine, China

REVIEWED BY
Zhenpeng Qiu,
Hubei University of Chinese Medicine, China
Ying Liu,
Hubei University of Medicine, China
Hai Zhang,
Chongqing Medical University, China

*CORRESPONDENCE
Jing Liu
lj8679@163.com
Xiaozhong Wang
wangxiaozhong@ncu.edu.cn

RECEIVED 20 September 2023
ACCEPTED 28 December 2023
PUBLISHED 12 January 2024

CITATION
Zhong F, Yao F, Xu S, Zhang J, Liu J and Wang X (2024) Identification and validation of hub genes and molecular classifications associated with chronic myeloid leukemia. *Front. Immunol.* 14:1297886. doi: 10.3389/fimmu.2023.1297886

Identification and validation of hub genes and molecular classifications associated with chronic myeloid leukemia

Fangmin Zhong, Fangyi Yao, Shuai Xu, Jing Zhang, Jing Liu* and Xiaozhong Wang*

Jiangxi Province Key Laboratory of Laboratory Medicine, Jiangxi Provincial Clinical Research Center for Laboratory Medicine, Department of Clinical Laboratory, The Second Affiliated Hospital, Jiangxi Medical College, Nanchang University, Nanchang, Jiangxi, China

Background: Chronic myeloid leukemia (CML) is a kind of malignant blood tumor, which is prone to drug resistance and relapse. This study aimed to identify novel diagnostic and therapeutic targets for CML.

Methods: Differentially expressed genes (DEGs) were obtained by differential analysis of the CML cohort in the GEO database. Weighted gene co-expression network analysis (WGCNA) was used to identify CML-related co-expressed genes. Least absolute shrinkage and selection operator (LASSO) regression analysis was used to screen hub genes and construct a risk score model based on hub genes. Consensus clustering algorithm was used for the identification of molecular subtypes. Clinical samples and *in vitro* experiments were used to verify the expression and biological function of hub genes.

Results: A total of 378 DEGs were identified by differential analysis. 369 CML-related genes were identified by WGCNA analysis, which were mainly enriched in metabolism-related signaling pathways. In addition, CML-related genes are mainly involved in immune regulation and anti-tumor immunity, suggesting that CML has some immunodeficiency. Immune infiltration analysis confirmed the reduced infiltration of immune killer cells such as CD8+ T cells in CML samples. 6 hub genes (LINC01268, NME8, DMXL2, CXXC5, SCD and FBN1) were identified by LASSO regression analysis. The receiver operating characteristic (ROC) curve confirmed the high diagnostic value of the hub genes in the analysis and validation cohorts, and the risk score model further improved the diagnostic accuracy. hub genes were also associated with cell proliferation, cycle, and metabolic pathway activity. Two molecular subtypes, Cluster A and Cluster B, were identified based on hub gene expression. Cluster B has a lower risk score, higher levels of CD8+ T cell and activated dendritic cell infiltration, and immune checkpoint expression, and is more sensitive to commonly used tyrosine kinase inhibitors. Finally, our clinical samples validated the expression and diagnostic efficacy of hub genes, and the knockdown of LINC01268 inhibited the proliferation of CML cells, and promoted apoptosis.

Conclusion: Through WGCNA analysis and LASSO regression analysis, our study provides a new target for CML diagnosis and treatment, and provides a basis for further CML research.

KEYWORDS

chronic myeloid leukemia, WGCNA, hub gene, diagnosis, biomarker

Introduction

Chronic myeloid leukemia is a malignant tumor that affects the blood and bone marrow (1). It is mainly induced by the BCR-ABL1 fusion gene, which encodes a protein with strong tyrosine kinase activity and activates various signaling pathways (2). At present, the main therapeutic drugs for CML are tyrosine kinase inhibitors (TKIs) targeting BCR-ABL1 (2). The development of the first-generation TKI imatinib (IM) has changed the treatment status of CML, and the prognosis of patients has been significantly improved (3). It is widely used and has a good therapeutic effect. However, due to the existence of escape mechanisms, tumor cells often develop resistance to kinase drugs, leading to the malignant progression of the disease, which seriously affects the health of patients (4). In addition, the long-term use of TKI will also produce many complications, affecting the quality of life of patients (5). Therefore, there is an urgent need to identify novel molecular targets for the diagnosis and treatment of CML.

With the progress and development of sequencing technology, bioinformatics has been widely used to explore the genetic changes of tumors, and to find new targets for early diagnosis and therapeutic intervention of tumors. The Gene Expression Omnibus (GEO) database contains gene expression profiles of various diseases and tumor samples and corresponding clinical information, which can be used for in-depth analysis (6). Weighted gene co-expression network analysis (WGCNA) is a bioinformatics tool to screen genes with similar expression patterns related to disease phenotypes by constructing free-scale gene co-expression networks (7). The reliability of this method has been widely verified (8–10), and to a large extent, it overcomes the limitations caused by only focusing on differentially expressed genes (DEGs). Therefore, hub genes that are highly correlated with clinical phenotypes can be defined as potential biomarkers and therapeutic targets.

In this study, we systematically analyzed the CML dataset GSE13159 in the GEO database, combined with differential expressed expression analysis and WGCNA analysis, identified a set of co-expressed genes significantly associated with CML, and determined the biological functions of these genes by enrichment analysis. Subsequently, the least absolute shrinkage and selection operator (LASSO) analysis was used to screen out signature genes that had high diagnostic value for CML and could predict treatment response in CML patients. We also identified two molecular subtypes with distinct immune landscapes based on hub gene expression. Finally, the diagnostic performance of the risk score model constructed by hub genes was further improved. These signatures were validated using an additional public cohort and our clinical real-world cohort. Therefore, these findings will help reveal more underlying mechanisms of CML, as well as the potential value of these targets in CML treatment.

Materials and methods

Data acquisition and processing

We downloaded the CML data sets (GSE13159, GSE144119) from the GEO database. GSE13159 contains 76 CML samples and 74 normal samples, and we normalized the original "cel" files. GSE144119 contained 48 newly diagnosed CML samples and 32 remission CML samples, as well as 17 normal samples, and the data were converted to transcripts per kilobase million (TPM) values for subsequent analyses. GSE13159 was used as the analysis cohort, and GSE144119 was used for subsequent validation. The normalized RNA-seq data (TPM values) of 173 TCGA-LAML (The Cancer Genome Atlas-Acute Myeloid Leukemia) samples containing clinical information were downloaded from the UCSC XENA database (https://xenabrowser.net/datapages/).

Pathway activity assessment and function enrichment analysis

The gene set variation analysis (GSVA) algorithm was used to calculate the enrichment score of the gene set to quantify the activity of the corresponding biological process or signaling pathway. The GSVA score was calculated based on the overall position of the gene set genes in the expression ranking of all genes, and the higher the overall expression level of these genes, the higher the GSVA score. KEGG enrichment analysis was used to analyze the function of phenotypic-related genes identified by WGCNA. We perform these analyses in the "clusterProfiler" package (11).

Analysis of immune cell infiltration

CIBERSORT algorithm based on support vector regression analysis was used to analyze the infiltration proportion of 22 kinds of immune cells in CML samples (12).

Weighted correlation network analysis

WGCNA is a tool for assessing gene expression correlations and visualizing co-expression networks. The "WGCNA" software package was used to identify CML-related genes in the GSE13159 cohort. Pearson correlation analysis was used to form an adjacency matrix for all matched genes, and the scale-free topology of the adjacency matrix was realized based on the optimal soft threshold power. Then, we further transform the adjacency matrix into a topological overlap matrix (TOM). Based on the TOM difference measure, the minimum module size was set to 30, the cutting height was set to 0.2, and the genes with similar expression patterns were divided into the same modules through average linkage hierarchical clustering. Then, the correlation between module characteristic genes (MEs) and CML was assessed, and the modules that met the purpose of the study were determined according to the degree of correlation.

Identification of DEGs between normal and CML samples

The empirical Bayesian approach via the "limma" package was used to determine DEGs between normal and CML samples (13). Genes with adjusted P-values < 0.05 and |logFC| > 1 were considered significantly different.

Construction of risk score model

Overlapping genes of CML-related genes and DEGs identified by WGCNA were used for the identification of CML hub genes. Then, the LASSO regression algorithm was used for dimensionality reduction analysis to screen out the most related genes with CML (14). In addition, based on the correlation of hub genes, LASSO regression analysis assigned a coefficient to each gene, and the expression of each gene was multiplied by its coefficient and added to obtain a risk score, which was used to analyze the diagnostic value of the combination of hub genes in CML. Risk score = NME8 × 1.160 + DMXL2 × 0.853 + CXXC5 × -0.126 + SCD × 0.610 + FBN1 × 0.405, where gene ID refers to the expression value of each gene.

Identification of molecular subtypes based on hub genes

Consensus cluster analysis was performed to identify CML molecular subtypes based on hub gene expression using the "consensusclusterplus" package. Clustering was performed for 1000 iterations to ensure reliable and stable results. t-distributedstochastic neighbor embedding (t-SNE) was used to validate the classification.

Construction of competing endogenous RNA network

Target miRNAs of hub genes were found in the miRTarBase, miRDB, and TargetScan databases. Perl programming language was used to perform the prediction analysis of the target lncRNAs of these miRNAs in the miRcode database.

Prediction of treatment response for different molecular subtypes

The half-maximal inhibitory concentrations (IC_{50}) of different CML samples to therapeutic drugs were predicted based on drug response data of blood cell lines from the Cancer Genome Project (CGP) database (https://cancer.sanger.ac.uk/cosmic) via the "pRRophetic" package. Tumor Immune Dysfunction and Exclusion (TIDE, http://tide.dfci.harvard.edu/) was considered a good predictor of immunotherapeutic response for molecular subtypes.

Clinical sample collection

CML samples and normal samples were collected for sequencing analysis in accordance with the Declaration of Helsinki and institutional guidelines, and informed consent was obtained from each patient and healthy volunteer who had undergone the appropriate workup. Our study was approved by the Ethics Committee of the Second Affiliated Hospital of Nanchang University, and sample processing was performed according to the norms. We collected samples from 5 untreated patients with newly diagnosed CML and 5 normal samples from healthy volunteers. The methods and details of sample collection, next-generation sequencing, and processing procedures were described in our previous report (15). Moreover, peripheral blood samples from 15 CML patients and 15 normal controls were collected for quantitative real-time polymerase chain reaction (RT-qPCR) assay to detect hub gene expression. RT-qPCR was performed using a Japanese TAKARA kit on an ABI7500 instrument. The primers are shown in Supplementary Table S1.

Cell culture and detection of cell proliferation and apoptosis

The CML cell line K562 was cultured in RPMI1640 medium supplemented with 10% fetal bovine serum and 1% penicillin-streptomycin in a humidified atmosphere incubator at 37°C with 5% CO_2. Two different siRNAs targeting LINC01268 (si-LINC01268) and control siRNA (si-NC) were procured from Ribobio (China) and transfected into K562 cells using Lipofectamine 3000 (Thermofisher Scientific) (Supplementary Table S1). RT-qPCR was employed to assess the transfection efficiency. Cell proliferation was evaluated using the Cell Counting Kit-8 (CCK-8). For the CCK8 assay, a total of 2×10^4 cells from various treatment groups were seeded in individual wells of a 96-well plate, with each group being repeated five times. Subsequently, at time points of 0, 24, 48, and 72 hours, respectively, 10 µl of CCK8 solution was added to each well. After incubation at 37°C for two hours, the optical density (OD) value at a wavelength of 450 nm was measured using a microplate reader. Apoptosis assays were performed by staining the cells with Annexin V-PE/7-AAD Apoptosis Assay Kit followed by analysis on a flow cytometer.

Statistical analysis

We performed the Wilcoxon rank sum test and the Kruskal-Wallis test to determine differences between two or more groups, respectively. The "survminer" package divides patients into high- and low-gene expression groups based on the cut-off point at the minimum p-value of the log-rank test, and the Kaplan-Meier survival curve analysis was used to analyze survival differences between the two groups. The receiver operating characteristic (ROC) curve was used to analyze the diagnostic efficacy of genes. A two-sided P value < 0.05 was considered statistically significant.

Results

CML-related genes were identified by WGCNA analysis

We first performed differential expression analysis between CML and normal samples and obtained a total of 378 DEGs. Heatmap analysis showed that more DEGs were down-regulated in CML (Figure 1A). We further performed WGCNA analysis to identify more CML-related genes. The cluster tree diagram showed the clustering characteristics of the samples, and the CML samples had a high degree of discrimination from the normal samples (Figure 1B). Figures 1C, D show the scale-free fit exponent and average connectivity analysis for various soft threshold powers. We set cut height = 0.25 to merge the blue and green module feature genes (Figure 1E). According to the optimal soft threshold power β = 12 (unscaled R2 = 0.9), the 5000 genes with the highest standard deviation were divided into eight independent co-expression modules (Figure 1F). The correlogram of module-trait relationships showed that the brown module, which contains 369 genes, had the highest correlation with CML (Figures 1G, H) (Supplementary Table S1). We also found that the blue, green, yellow, black, and pink modules were negatively correlated with CML, and these results were associated with the downregulated expression of most genes in CML.

Functional analysis of CML-related genes

The brown module genes were mainly related to metabolic-related signaling pathways such as Starch and sucrose metabolism, Pantothenate and CoA biosynthesis, Amino sugar and nucleotide sugar metabolism, Pentose phosphate pathway, and Galactose metabolism (Figure 2A). While yellow and turquoise module genes were negatively associated with CML, these genes were mainly enriched in immune-related signaling pathways such as Th17 cell differentiation, Th17 cell differentiation, Cytokine-cytokine receptor interaction, and Hematopoietic cell lineage, T cell receptor signaling pathway, NOD-like receptor signaling pathway, Natural killer cell mediated cytotoxicity (Figure 2B). These results indicate that CML has stronger metabolic activity and some immunodeficiency. Immune infiltration analysis showed that CML samples had fewer naive and memory B cells, plasma cells, CD8+ T cells, naive CD4+ T cells, activated memory CD4+ T cells, resting NK cells, and activated dendritic cells, and contained more regulatory T cells (Tregs) than normal samples (Figure 2C), which confirm the immunosuppressive features evident in CML samples.

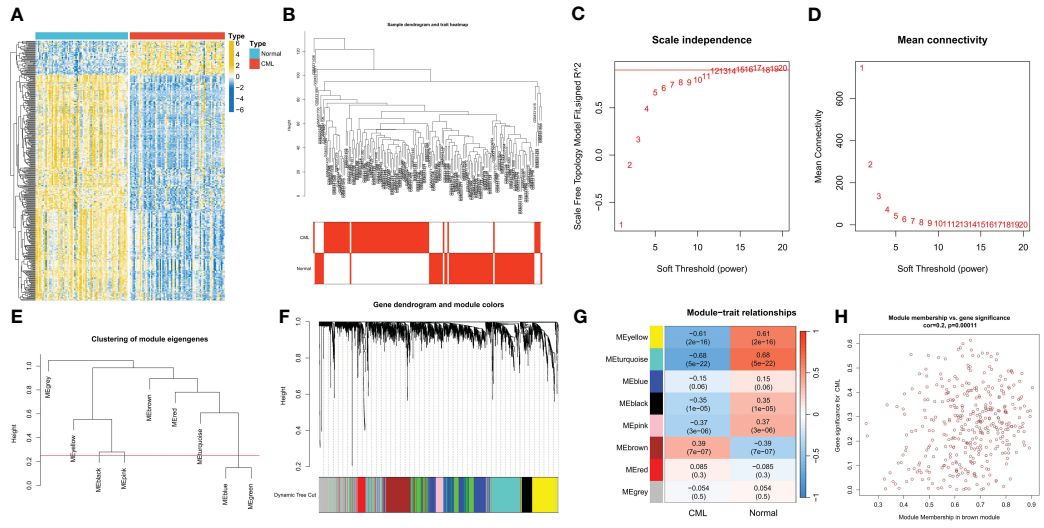

FIGURE 1
Identification of CML-related genes. **(A)** The heatmap shows differentially expressed genes (DEGs) between CML and normal samples. **(B)** Clustering dendrogram of CML and normal samples. **(C, D)** Scale-free fit index **(C)** and average connectivity **(D)** analysis of various soft threshold powers. **(E)** the cluster of module feature genes. The red line indicates the cutting height (0.25). **(F)** Dendrogram of clustering based on different measures (1-TOM). **(G)** Heatmap of correlation between module genes and phenotypes. Each cell contains a p-value and a correlation coefficient. **(H)** Scatter plot of module characteristic genes associated with CML samples in brown module.

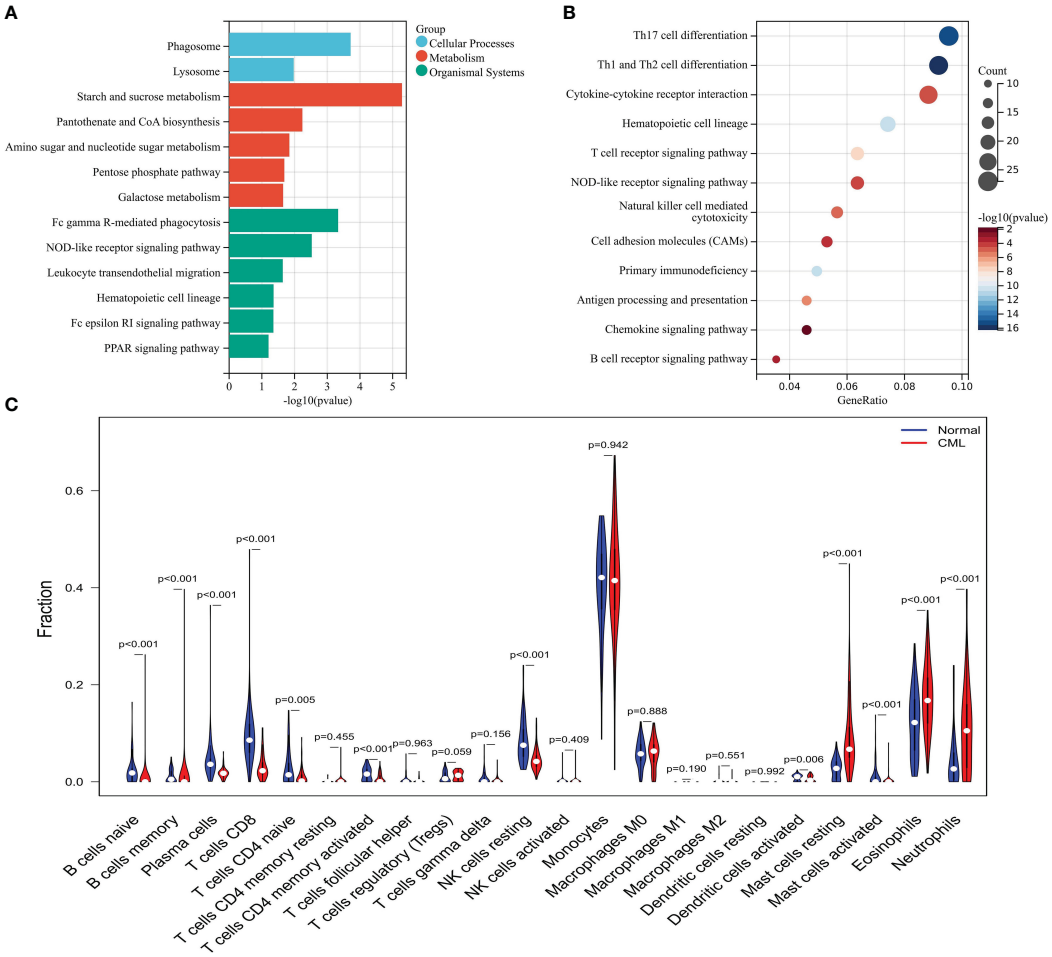

FIGURE 2
Functional analysis of CML-related genes and immune infiltration analysis. **(A)** KEGG enrichment analysis of brown module genes. **(B)** KEGG enrichment analysis of genes in yellow and turquoise modules. **(C)** Differences in infiltration of 22 immune cells between CML and normal samples.

Identification of CML hub genes

We intersected DEGs and WGCNA brown module genes and obtained 17 overlapping genes (Figure 3A), and the correlation coefficients of these genes with the brown module in WGCNA and with CML samples were greater than 0.4 (Supplementary Table S2), indicating that they were significantly positively correlated with both CML and brown module. LASSO regression analysis further reduced the dimension and screened out 6 hub genes most related to CML, which were LINC01268, NME8, DMXL2, CXXC5, SCD, and FBN1 (Figures 3B, C). Boxplots showed that LINC01268, NME8, DMXL2, SCD, and FBN1 were significantly up-regulated and CXXC5 was significantly down-regulated in CML samples compared with normal samples (Figure 3D).

Diagnostic value and prognostic correlation of CML hub genes

We further analyzed the predictive value of CML hub genes for CML. ROC curve analysis showed that all 6 hub gens had high AUC values for the diagnosis of CML, among which LINC01268 was 0.864 (95%CI: 0.796-0.924), NME8 was 0.869 (95%CI: 0.808-0.924), DMXL2 was 0.866 (95%CI: 0.805-0.91), CXXC5 was 0.831 (95%CI: 0.761-0.895), SCD was 0.856 (95%CI: 0.790-0.919), and FBN1 was 0.836 (95%CI: 0.767-0.900) (Figure 4A). In addition, considering that approximately 70% of CML cases in blast crisis progress to AML, we analyzed the prognostic predictive value of 6 hub genes in the TCGA-AML cohort. High expression groups of LINC01268, SCD, FBN1, and CXXC5 had significantly shorter overall survival than their low expression groups, respectively, while high expression groups of NME8 and DMXL2 showed better prognosis, but there was no statistical difference (Figure 4B).

Validation of the diagnostic value of CML hub genes

The GSE144119 cohort contains samples from newly diagnosed and treatment-remission CML. Encouragingly, the results of the differential analysis were consistent with the GSE13159 cohort, in which NME8, DMXL2, SCD, and FBN1 expression was

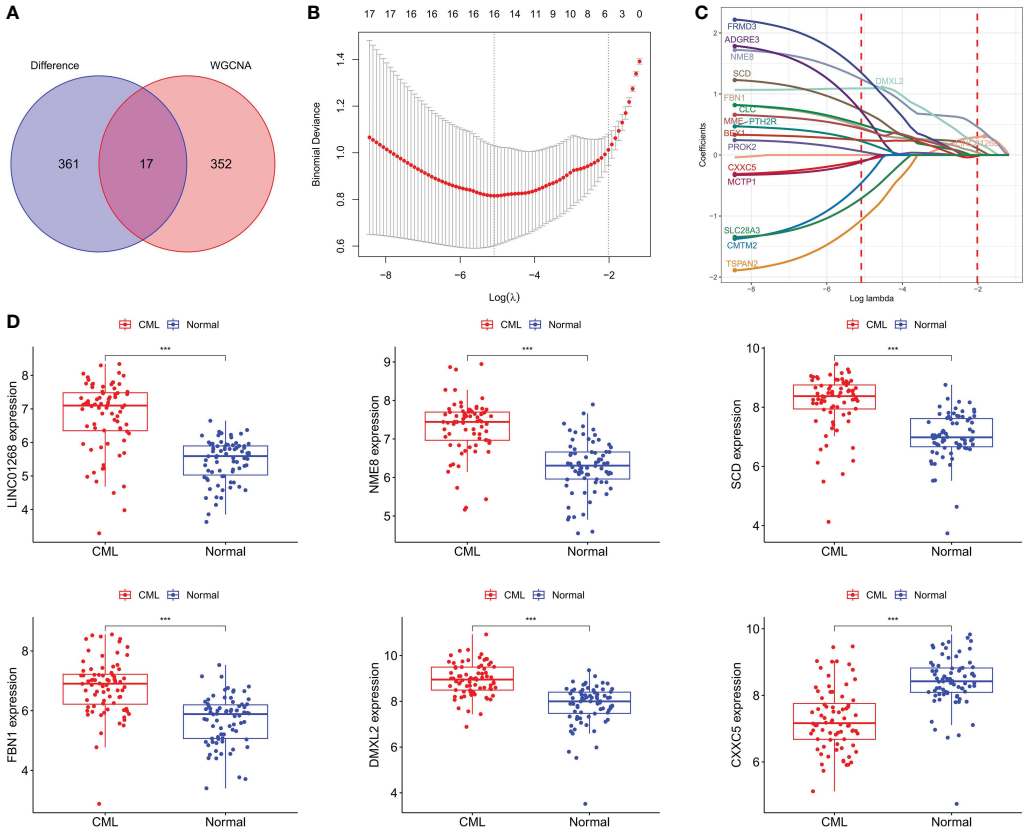

FIGURE 3
Identification of CML hub genes. **(A)** The intersection of DEGs and brown module genes in WGCNA. **(B)** The penalty coefficient of the minimum 10-fold cross-validation error point was calculated to determine the hub genes. **(C)** determination of hub gene coefficients. **(D)** Differences in the expression of hub genes between CML and normal samples. ***p < 0.001.

significantly increased and CXXC5 expression was significantly decreased in newly diagnosed (chronic phase) CML patients (The expression of LINC01268 was not detected). These hub genes also had predictive value for CML treatment remission. The expression levels of NME8, DMXL2, SCD, and FBN1 were significantly decreased in CML treatment-remission patients, while the CXXC5 expression level was significantly increased, and they all returned to normal control levels. ROC curve analysis confirmed the diagnostic value of these hub genes in CML (Figure 5A). The AUC values of NME8, SCD, FBN1, DMXL2, and CXXC5 were 0.906 (95% CI: 0.836-0.960), 0.958 (95% CI: 0.908-0.995), 0.933 (95% CI: 0.870-0.980), 0.795 (95% CI: 0.695-0.878), and 0.932 (95% CI: 0.868-0.982), respectively (Figure 5B). In our clinical cohort, we confirmed that SCD and FBN1 expression was significantly upregulated CXXC5 was significantly downregulated in CML, and NME8 and DMXL2 expression were not significantly different due to the small sample size (Figure 6A).

Potential biological mechanisms of CML hub genes

To better explore the biological functions of CML hub genes, we analyzed their correlation with tumor marker pathway activity and immune cell infiltration. CXXC5 expression was related to P53 PATHWAY, DNA REPAIR, MYC TARGETS, and APOPTOSIS, and may be involved in the regulation of CML cell proliferation. DMXL2 was positively correlated with cell cycle-related pathways such as MITOTIC SPINDLE, and G2M CHECKPOINT. FBN1, LINC01268, and SCD were related to the metabolic pathway activity of MTORC1 SIGNALING, GLYCOLYSIS, FATTY ACID METABOLISM, ADIPOGENESIS (Figure 6B). The expression of NME8 was negatively correlated with the activity of most tumor marker pathways. In addition, CXXC5 expression was positively correlated with infiltration of CD8+ T cells, resting memory CD4+ T cells, resting NK cells, activated dendritic cells, and memory B cells, suggesting that CXXC5 may be involved in CML anti-tumor immunity (Figure 6C). Figure 6D shows the location of five hub genes in chromosomes. In addition, we identified a group of transcription factors with potential regulatory effects on hub genes (Figure 6E). According to the construction of the CeRNA network (Figure 6F), lncRNA FAM13A-AS1 with upregulated expression may promote the expression of FBN1 by competitively binding hsa-miR-24-3p and hsa-miR-363-3p. lncRNA CRNDE may promote the expression of FBN1 by binding hsa-miR-363-3p, hsa-miR-508-3p and hsa-miR-140-5p. The downregulation of lncRNAs DLEU2 and HCP5 may reduce the binding of miR-363-3p, thereby inhibiting the expression of CXXC5.

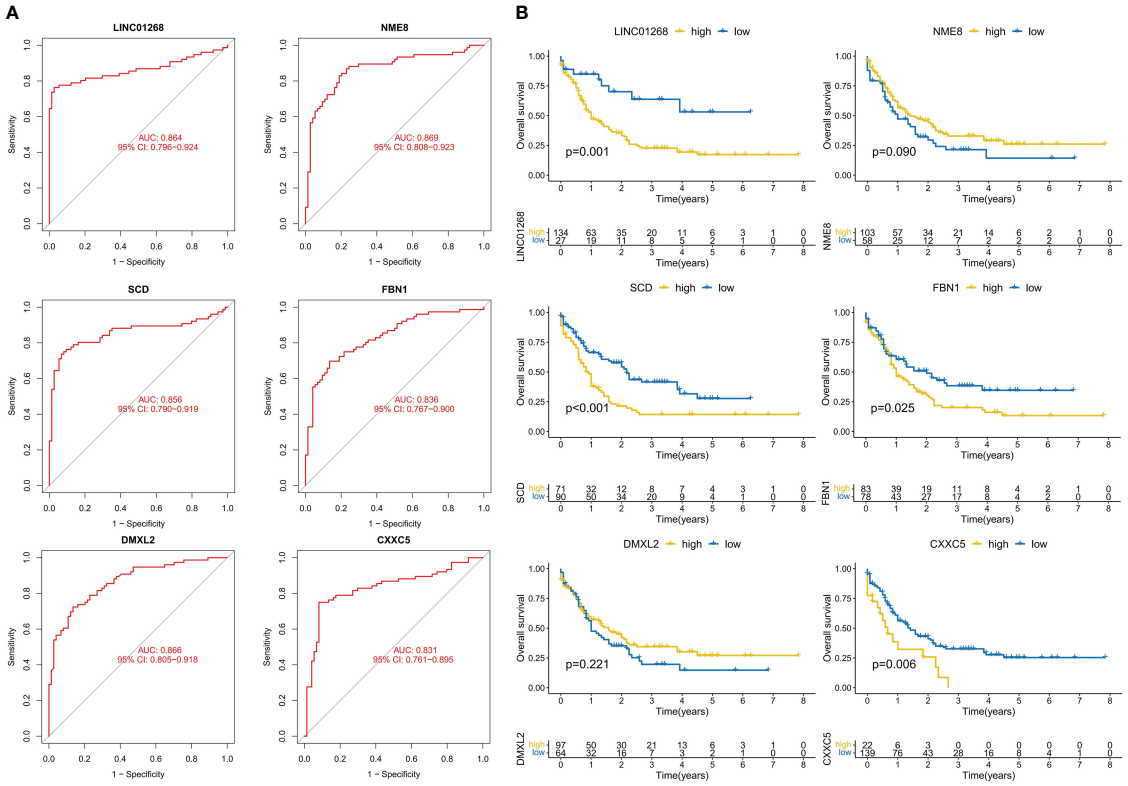

FIGURE 4
Analysis of the diagnostic and prognostic value of hub genes. **(A)** ROC curve analysis of hub genes. **(B)** K-M curve analysis of hub genes.

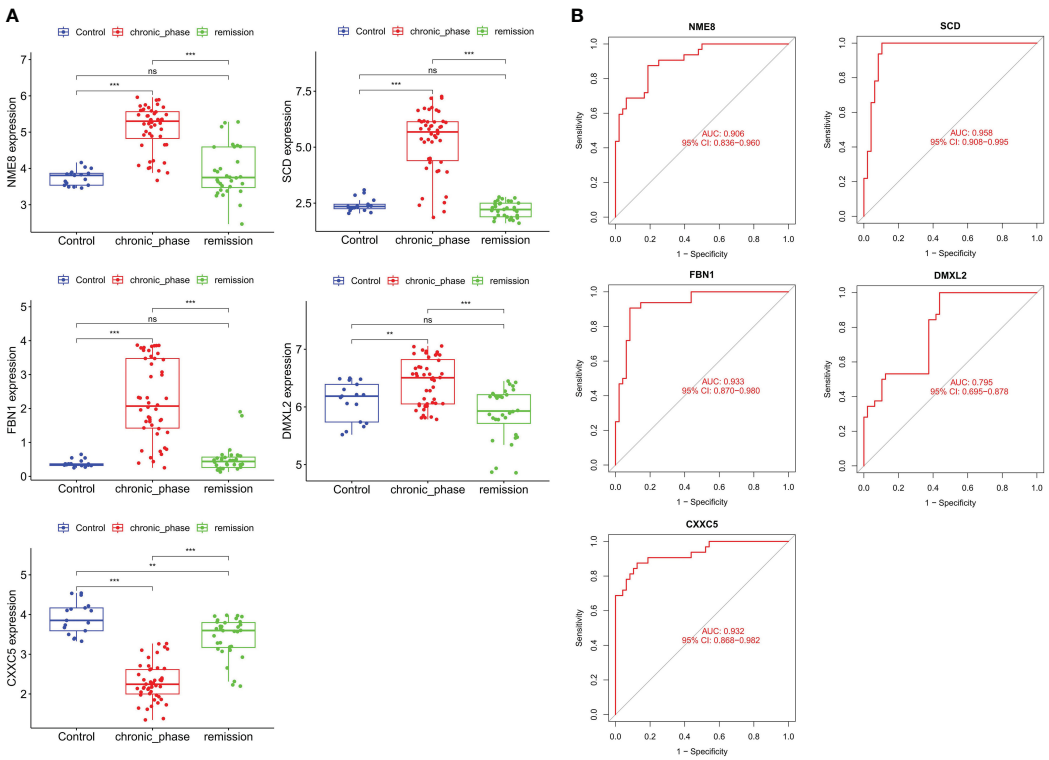

FIGURE 5
Validation of the expression and diagnostic value of hub genes in the validation cohort. **(A)** Differences in the expression of hub genes in normal samples, newly diagnosed CML samples, and treatment-remission samples. **(B)** ROC curve analysis of hub genes. **p < 0.01; ***p < 0.001; ns, no significance.

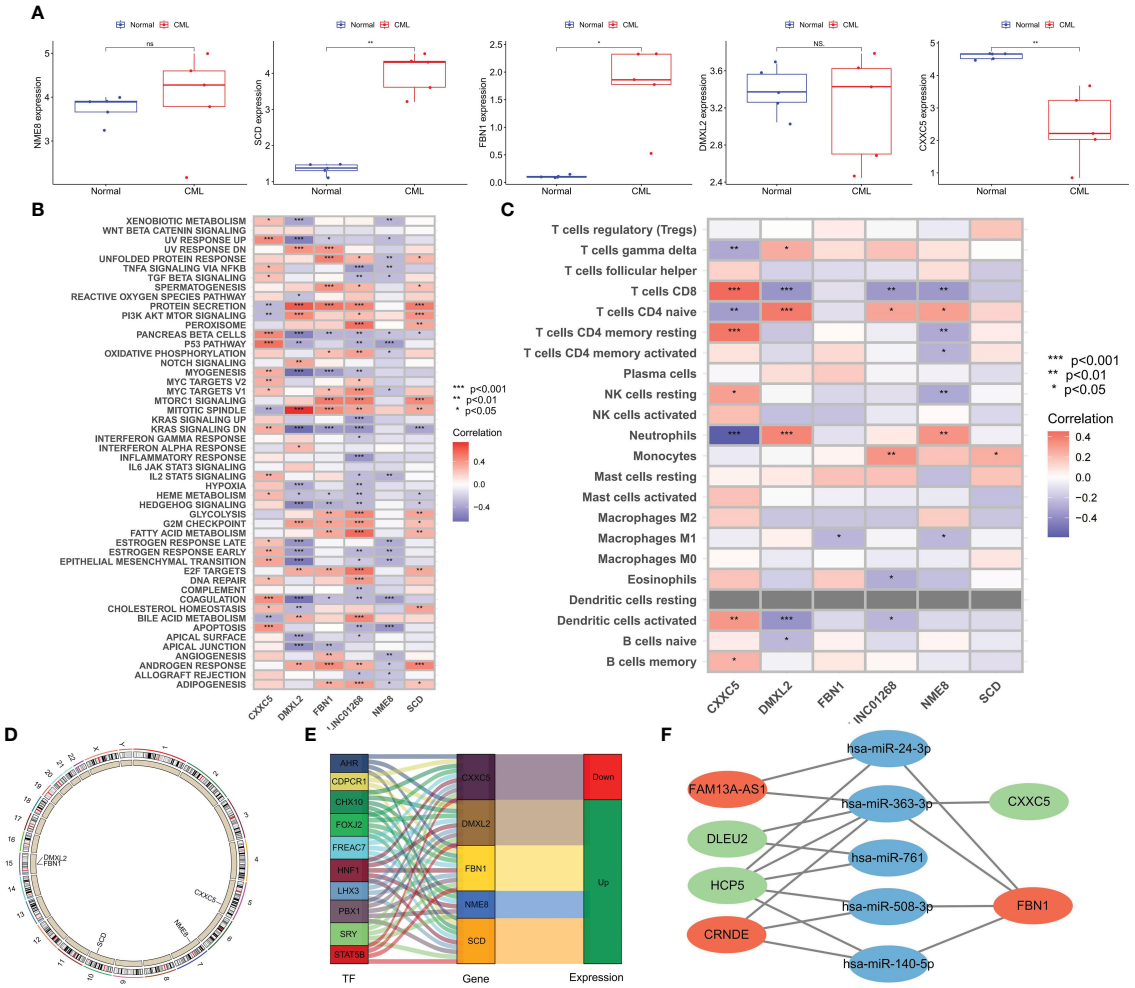

FIGURE 6
Expression Validation of hub genes in clinical cohort and biological function analysis. **(A)** Differences in the expression of hub genes between CML and normal samples in a clinical cohort. **(B)** Correlation analysis of hub genes and tumor marker pathway activity. **(C)** Correlation analysis of hub genes, and immune cell infiltration. **(D)** The location of hub genes on chromosomes. **(E)** Transcription factors with potential regulatory effects on hub genes expression. **(F)** CeRNA networks with potential regulatory effects on hub genes expression. *p < 0.05; **p < 0.01; ns, no significance.

The construction of a risk score model can further improve the diagnostic value of hub genes

To better improve the diagnostic value of hub genes, we used LASSO regression analysis to construct a risk score model for 5 genes shared by the three cohorts. All three cohorts observed significantly higher risk scores in CML samples than in normal samples, and risk scores in patients in remission tended to be normal (Figures 7A–C). ROC curve analysis showed that the diagnostic AUC values in the GSE13159 cohort, GSE144119 cohort, and clinical cohort were 0.925 (95% CI: 0.877-0.964), 1.000 (95% CI: 1.000-1.000) and 0.840 (95% CI: 0.520-1.000), respectively, confirming that the diagnostic value of risk score of hub genes combination was further improved.

Molecular subtypes identified based on hub genes and prediction of treatment response

We performed cluster analysis of CML samples based on hub gene expression and identified two distinct molecular subtypes (Cluster A and Cluster B) (Figure 8A). The t-SNE algorithm verified the reliability of the clustering (Figure 8B). Compared with Cluster B, LINC01268, DMXL2, SCD, and FBN1 were up-regulated and CXXC5 was down-regulated in Cluster A (Figure 8C). Cluster A also had a significantly higher risk score than Cluster B (Figure 8D). Immune infiltration analysis showed that the infiltration levels of CD8+ T cells and activated NK cells were significantly higher in Cluster B than in Cluster A (Figure 8E). The expression of immune checkpoints PD-L1, CTLA4, HAVCR2, and PD-1 was also

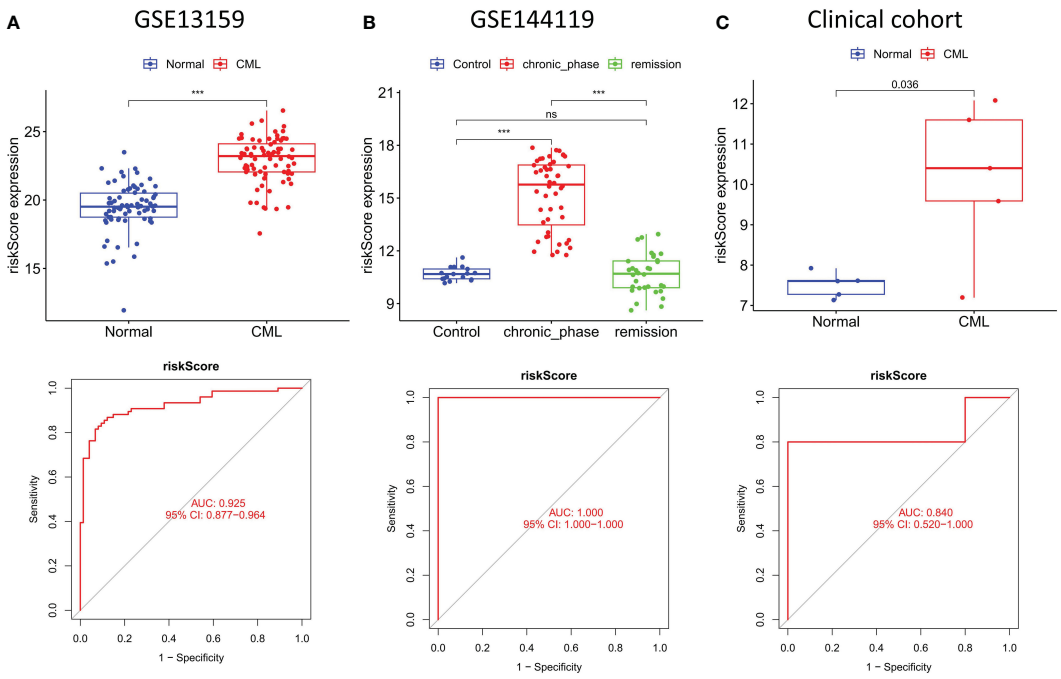

FIGURE 7
Construction and validation of risk score model. **(A–C)** Expression characteristics and diagnostic value of risk scores in the three cohorts. ***p < 0.001; ns, no significance.

significantly up-regulated in Cluster B (Figure 8F). In addition, the TIDE score of Cluster B was significantly higher than that of Cluster A (Figure 8G), indicating significant immunosuppression in Cluster B. We also compared the activity of tumor-marker gene sets in the two molecular subtypes (Figure 8E). We found metabolic and cell proliferation-related pathways such as MYC targets V1, oxidative phosphorylation, G2M checkpoint, E2F targets, mTORC1 signaling and fatty acid metabolism were more active. In Cluster B, the enrichment scores of cancer-promoting pathways such as hedgehog, epithelial-mesenchymal transition, and TNFA signaling via NFKB were higher (Figure 8H). We then predicted the response of different molecular subtypes to TKIs commonly used for CML treatment, and the results showed that Cluster B patients had higher therapeutic sensitivity to imatinib, nilotinib, bosutinib, and dasatinib. Moreover, there was a significant positive correlation between the risk score and the IC_{50} of the four drugs, that is, the higher the risk score, the less sensitive the treatment to the four drugs (Figure 8I).

Expand clinical sample size to validate the expression of hub genes and confirm the oncogenic role of LINC01268

The expression of hub genes was validated by RT-qPCR in expanded clinical samples. Encouragingly, the results also confirmed that LINC01268, NME8, DMXL2, SCD, and FBN1 were up-regulated while CXXC5 was down-regulated in CML samples (Figure 9A). Previous studies have shown that DMXL2, NME8, and FBN1 primarily exert oncogenic roles through mutations and splice variants (16–18); moreover, the role of SCD in CML has also been reported previously (19). Therefore, we chose to initially explore the biological function of LINC01268 in CML cells. The expression of LINC01268 was significantly inhibited by siRNA (Figure 9B). CCK8 assay showed that compared with the si-NC group, the proliferation ability of CML cells in the si-LINC01268 group was significantly reduced (Figure 9C). Moreover, the apoptosis rate of the si-LINC01268 group was higher than that of the si-NC group (Figures 9D–F). These results reveal the oncogenic role of LINC01268 and its potential as a therapeutic target for CML.

Discussion

The development and application of TKIs have significantly improved the prognosis of CML patients, but these drugs can only delay the progression of the disease, and cannot be used as a curative treatment (2). Due to the existence of resistance mechanisms, patients inevitably relapse (5). Therefore, it is particularly important to explore more potential therapeutic targets and markers for disease prediction and progression assessment in CML. In this study, we focused on the diagnostic markers of CML and their underlying biological mechanisms. Based on the DEGs between CML and normal samples and the CML-related genes identified by WGCNA analysis, we used LASSO regression analysis to screen out 6 hub genes (LINC01268, NME8, DMXL2, CXXC5, SCD, and FBN1).

We also focused on the co-expressed gene network identified by WGCNA analysis. The results showed that the brown module was significantly positively correlated with CML (Cor=0.39, P=7e-07). It

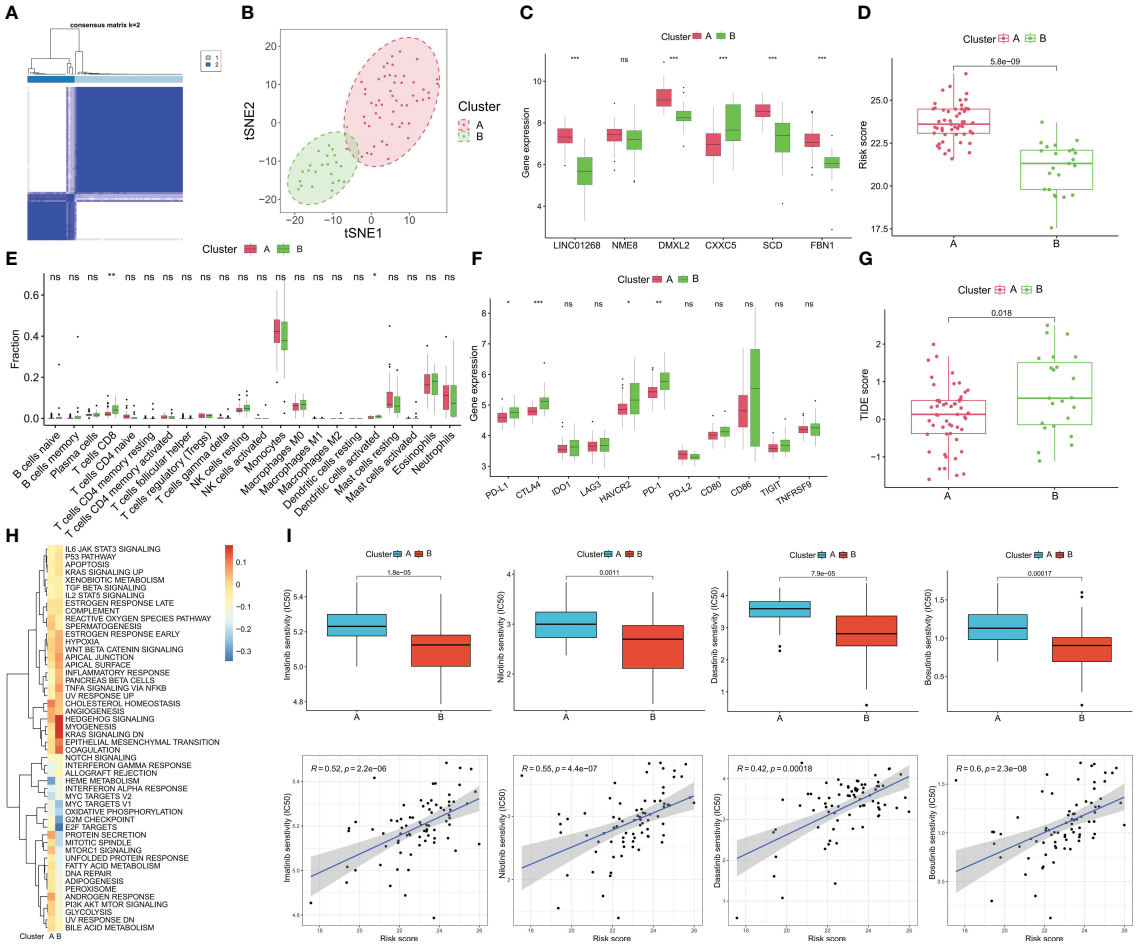

FIGURE 8
Identification of molecular subtypes of CML and prediction of drug response in different subtypes. **(A)** The consensus clustering algorithm divided CML patients into two different molecular subtypes based on the expression of hub genes. **(B)** t-SNE algorithm was used to verify the classification reliability of the two molecular subtypes. **(C–F)** Differences in expression of DEGs **(C)**, risk score **(D)**, infiltration of 22 immune cells **(E)**, expression of immune checkpoints **(F)**, TIDE scores **(G)**, and activity of tumor hallmark gene sets **(H)** between the two molecular subtypes. **(I)** Differences in therapeutic sensitivity of the two molecular subtypes to four TKIs. *p < 0.05; **p < 0.01; ***p < 0.001; ns, no significance.

reflects the correlation of the module as a whole with the CML phenotype. Although this correlation did not reach an exceptionally high level, a coefficient close to 0.4 suggests its reliability to some extent. Thus, it can be inferred that the brown module partially reflects gene co-expression patterns in CML transcriptome while uncovering underlying biological mechanisms. We found that the brown module genes positively correlated with CML were enriched in a variety of metabolic pathways, revealing the more active metabolic characteristics of CML cells. Several studies confirmed that targeting mitochondrial oxidative phosphorylation and glucose uptake is a potential therapeutic target for CML (20, 21). Most of the module genes negatively correlated with CML were involved in immune regulation and immune cell activation. Subsequent analysis showed that the infiltration of immune killer cells such as CD8+ T cells was significantly reduced in CML samples, confirming the immune deficiency characteristics. Cayssials et al. found that the sustained treat-free remission of CML was associated with an increased frequency of innate CD8+ T cells (22), and Harada et al. revealed that the inhibition of differentiation of dendritic cells in the hematopoietic microenvironment, as well as the up-regulation of immune checkpoint expression such as PD-L1, were responsible for the impairment of CML immune function (23). Based on this, we believe that targeted inhibition of metabolism and enhancement of immune response are important strategies for CML treatment.

It is worth noting that Figure 1G illustrates the association between module membership (MM) and gene significance (GS), it reflects the association of individual genes in the module with the module (x-axis, MM) and with the CML phenotype (y-axis, GS). If the correlation between MM and GS is high, the higher the correlation between the module gene and the module, the higher the correlation between the module gene and the CML phenotype, showing an overall distribution trend. We further calculated the correlation coefficient between these two types of coefficients; although Cor=0.2 with P=0.00011 indicates a weak positive relationship, it still signifies statistical significance. In this scatterplot analysis, we focused on points with strong correlations with both MM and GS. The correlation coefficients for both GS and

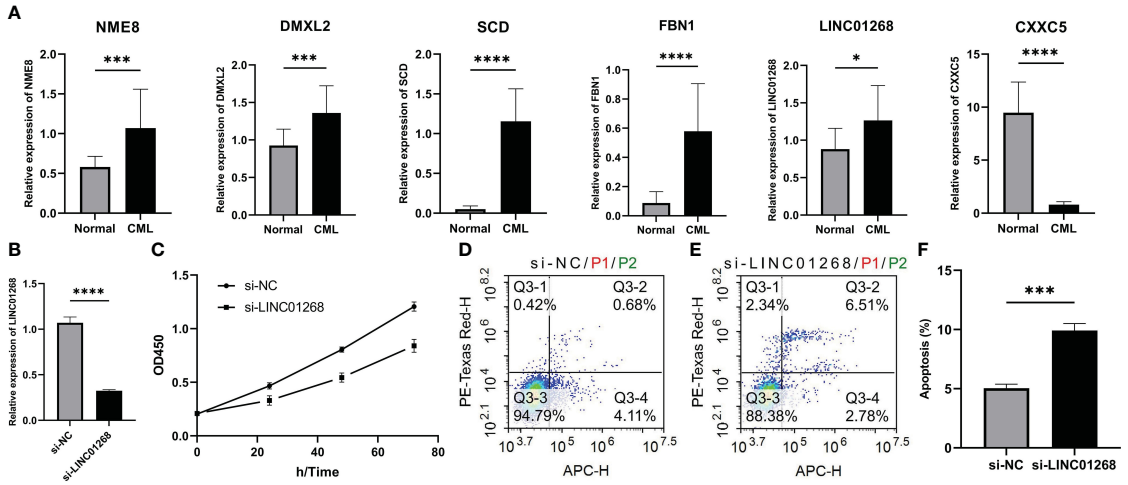

FIGURE 9
Expression characteristics of hub genes and its relationship with malignant phenotypes of CML cells. **(A)** Differences in mRNA expression of hub genes in peripheral blood samples from 15 CML patients and 15 normal controls. **(B)** mRNA expression level of LINC01268 in K562 cells in LINC01268 knockdown group (si- LINC01268) and control group (si-NC). **(C)** Absorbance at 450nm wavelength after CCK8 treatment in different LINC01268 treatment groups at different time nodes. **(D–F)** Apoptosis levels in different LINC01268 treatment groups. (*P < 0.05; *** P < 0.001; **** P < 0.0001).

MM of the 17 overlapping genes shared by differentially expressed genes and brown module genes were found to be greater than 0.4. Additionally, the correlation coefficients for both GS and MM of hub genes identified through LASSO regression analysis were greater than 0.5. This indicates that hub genes were significantly positively correlated with both the CML phenotype and the brown module. In this study, we utilized WGCNA analysis and LASSO regression analysis to identify hub genes of CML, and analyze their diagnostic value and potential biological functions. Therefore, WGCNA played a discriminating role to some extent. For the phenomenon that the correlation coefficients between module and phenotype and between MM and GS did not reach a high level, we believe that it may be due to the small size of CML samples included in the study. Since CML accounts for only about 15% of all leukemias, this disease is much less studied than other acute leukemias, and thus, the relevant sequencing data will be smaller. However, the two CML cohorts included in our study are currently the largest sample size cohorts with normal samples that can be found in public databases and are also representative.

The hub genes we identified are likely to be important molecules in CML metabolism and immune regulation. Stearoyl coenzyme A desaturase (SCD), a lipase that converts saturated fatty acids to monounsaturated fatty acids, is a key regulator of fatty acid metabolism pathways, its expression is also associated with poor prognosis in several cancer types (24), and elevated SCD levels also protect cancer cells from ferroptosis (25–27). Its upregulation in CML may also contribute to cancer cell growth and treatment resistance by affecting fatty acid metabolism. The high expression of LINC01268 promotes the progression of HCC by regulating MAP3K7 (28). Exosomal lncRNA LINC01268 is also a cancer-promoting factor for pancreatic cancer (29). NME/NM23 family member 8 (NME8) has been identified as a predisposition variant in breast cancer and a prognostic marker in diffuse large B-cell lymphoma (30, 31). DMXL2 has also been proposed as a potential therapeutic target for breast cancer and oral mucosal melanoma (32, 33). CXXC5 is a member of the CXXC-type zinc finger protein family. It can regulate various signal transduction processes, including TGF-β, Wnt, and ATM-p53 pathways, thereby regulating cell proliferation, differentiation, and apoptosis, and has been implicated in cancer occurrence and progression in many studies (34). Fibrillin-1 (FBN1) promotes gastric cancer progression by activating TGF-β1 and PI3K/Akt pathways, and is targeted by miR-486-5p to inhibit the growth of thyroid cancer cells (35, 36). These studies have all revealed the promoting role of hub genes in a variety of cancers, however, their relationship to CML has not been elucidated, and more in-depth mechanistic exploration is expected to reveal their role and potential value as therapeutic targets.

Moreover, we confirmed the diagnostic value of hub genes in both the analysis and validation cohorts. The risk score model constructed by LASSO regression analysis further improved the diagnostic accuracy. The discovery of these markers provides new targets for the diagnosis and treatment of CML. Finally, we identified two distinct molecular subtypes based on hub gene expression, with Cluster B having a lower risk score and infiltrating a higher proportion of CD8+ T cells and activated dendritic cells. However, the expression of immune checkpoints such as PD-L1, CTLA4, HAVCR2, and PD-1 was significantly up-regulated in Cluster B, as well as the higher TIDE score, indicating that this molecular subtype has a certain degree of immunosuppression, which inhibits the tumor-killing function of immune cells. Therefore, immunotherapy of patients in this subtype may have a higher response. In addition, drug prediction analysis showed that Cluster B was more sensitive to commonly used TKIs. The identification of molecular subtypes provides a new strategy for precise treatment of CML. Finally, we verified the expression of hub genes in larger clinical sample sizes, and confirmed that inhibition

of LINC01268 expression significantly reduced CML cell viability and promoted apoptosis *in vitro*. These results reveal the oncogenic role of LINC01268 and its potential as a therapeutic target for CML. Another study showed that LINC01268, a lncRNA involved in the epigenetic regulation of AML, exerts deacetylation by directly activating HDAC2 and generating positive feedback with HDAC2. In addition, HDAC2 stimulates the transcription of LINC01268, and the expression of LINC01268 is also associated with poor prognosis and cell proliferation in AML (37). Therefore, combined with our findings, LINC01268 is most likely a malignant regulator of myeloid leukemia. However, our study also has some limitations, such as the still small size of clinical samples for the validation of diagnostic signatures and the lack of a more in-depth experimental analysis of hub genes function in CML cells. In addition, the correlation and biological mechanisms of hub genes with CML progression and drug resistance deserve further exploration, thus providing new targets for CML drug resistance treatment, which we will further refine in future studies.

Conclusion

In summary, through WGCNA analysis and LASSO regression analysis, this study provides a better understanding of the role of biomarkers LINC01268, NME8, DMXL2, CXXC5, SCD, and FBN1, and provides a biological basis for further investigation of CML diagnosis and treatment.

Data availability statement

The datasets presented in this study can be found in online repositories. The names of the repository/repositories and accession number(s) can be found in the article/Supplementary Material.

Ethics statement

The studies involving humans were approved by ethics committee of The Second Hospital of Nanchang University. The studies were conducted in accordance with the local legislation and institutional requirements. The participants provided their written informed consent to participate in this study.

Author contributions

FZ: Data curation, Formal analysis, Funding acquisition, Methodology, Software, Validation, Visualization, Writing – original draft. FY: Validation, Visualization, Writing – original draft. SX: Validation, Visualization, Writing – original draft. JZ: Validation, Visualization, Writing – original draft. JL: Conceptualization, Funding acquisition, Project administration, Resources, Supervision, Writing – review & editing. XW: Conceptualization, Funding acquisition, Project administration, Resources, Supervision, Writing – review & editing.

Funding

The author(s) declare financial support was received for the research, authorship, and/or publication of this article. The study was funded by the National Natural Science Foundation of China (82260035, 82160405) and the Natural Science Foundation of Jiangxi Province (20202BAB216022, 20232BAB216037).

Conflict of interest

The authors declare that the research was conducted in the absence of any commercial or financial relationships that could be construed as a potential conflict of interest.

Publisher's note

Supplementary material

The Supplementary Material for this article can be found online at: https://www.frontiersin.org/articles/10.3389/fimmu.2023.1297886/full#supplementary-material

References

1. Jabbour E, Kantarjian H. Chronic myeloid leukemia: 2022 update on diagnosis, therapy, and monitoring. *Am J Hematol* (2022) 97:1236–56. doi: 10.1002/ajh.26642

2. Osman AEG, Deininger MW. Chronic Myeloid Leukemia: Modern therapies, current challenges and future directions. *Blood Rev* (2021) 49:100825. doi: 10.1016/j.blre.2021.100825

3. Rosti G, Castagnetti F, Gugliotta G, Baccarani M. Tyrosine kinase inhibitors in chronic myeloid leukaemia: which, when, for whom? *Nat Rev Clin Oncol* (2017) 14:141–54. doi: 10.1038/nrclinonc.2016.139

4. Poudel G, Tolland MG, Hughes TP, Pagani IS. Mechanisms of resistance and implications for treatment strategies in chronic myeloid leukaemia. *Cancers (Basel)* (2022) 14(14). doi: 10.3390/cancers14143300

5. Alves R, Gonçalves AC, Rutella S, Almeida AM, De Las Rivas J, Trougakos IP, et al. Resistance to tyrosine kinase inhibitors in chronic myeloid leukemia-from molecular mechanisms to clinical relevance. *Cancers (Basel)* (2021) 13(19). doi: 10.3390/cancers13194820

6. Clough E, Barrett T. The gene expression omnibus database. *Methods Mol Biol (Clifton N.J.)* (2016) 1418:93–110. doi: 10.1007/978-1-4939-3578-9_5

7. Langfelder P, Horvath S. WGCNA: an R package for weighted correlation network analysis. *BMC Bioinf* (2008) 9:559. doi: 10.1186/1471-2105-9-559

8. Li W, Gao Y, Jin X, Wang H, Lan T, Wei M, et al. Comprehensive analysis of N6-methylandenosine regulators and m6A-related RNAs as prognosis factors in colorectal cancer. *Mol Ther Nucleic Acids* (2022) 27:598–610. doi: 10.1016/j.omtn.2021.12.007

9. Liu K, Chen S, Lu R. Identification of important genes related to ferroptosis and hypoxia in acute myocardial infarction based on WGCNA. *Bioengineered* (2021) 12:7950–63. doi: 10.1080/21655979.2021.1984004

10. Yu H, Du X, Zhao Q, Yin C, Song W. Weighted gene Co-expression network analysis (WGCNA) reveals a set of hub genes related to chlorophyll metabolism process in chlorella (Chlorella vulgaris) response androstenedione. *Environ pollut (Barking Essex 1987)* (2022) 306:119360. doi: 10.1016/j.envpol.2022.119360

11. Yu G, Wang LG, Han Y, He QY. clusterProfiler: an R package for comparing biological themes among gene clusters. *Omics J Integr Biol* (2012) 16:284–7. doi: 10.1089/omi.2011.0118

12. Newman A, Liu C, Green M, Gentles A, Feng W, Xu Y, et al. Robust enumeration of cell subsets from tissue expression profiles. *Nat Methods* (2015) 12:453–7. doi: 10.1038/nmeth.3337

13. Ritchie M, Phipson B, Wu D, Hu Y, Law C, Shi W, et al. limma powers differential expression analyses for RNA-sequencing and microarray studies. *Nucleic Acids Res* (2015) 43:e47. doi: 10.1093/nar/gkv007

14. Tibshirani R. The lasso method for variable selection in the Cox model. *Stat Med* (1997) 16:385–95. doi: 10.1002/(sici)1097-0258(19970228)16:4<385::aid-sim380>3.0.co;2-3

15. Li SQ, Liu J, Zhang J, Wang XL, Chen D, Wang Y, et al. Transcriptome profiling reveals the high incidence of hnRNPA1 exon 8 inclusion in chronic myeloid leukemia. *J Adv Res* (2020) 24:301–10. doi: 10.1016/j.jare.2020.04.016

16. Esposito A, Falace A, Wagner M, Gal M, Mei D, Conti V, et al. Biallelic DMXL2 mutations impair autophagy and cause Ohtahara syndrome with progressive course. *Brain J Neurol* (2019) 142:3876–91. doi: 10.1093/brain/awz326

17. Liu Y, Yu JT, Wang HF, Hao XK, Yang YF, Jiang T, et al. Association between NME8 locus polymorphism and cognitive decline, cerebrospinal fluid and neuroimaging biomarkers in Alzheimer's disease. *PloS One* (2014) 9:e114777. doi: 10.1371/journal.pone.0114777

18. Milleron O, Arnoult F, Delorme G, Detaint D, Pellenc Q, Raffoul R, et al. Pathogenic FBN1 genetic variation and aortic dissection in patients with marfan syndrome. *J Am Coll Cardiol* (2020) 75:843–53. doi: 10.1016/j.jacc.2019.12.043

19. Zhang H, Li H, Ho N, Li D, Li S. Scd1 plays a tumor-suppressive role in survival of leukemia stem cells and the development of chronic myeloid leukemia. *Mol Cell Biol* (2012) 32:1776–87. doi: 10.1128/mcb.05672-11

20. Kominsky DJ, Klawitter J, Brown JL, Boros LG, Melo JV, Eckhardt SG, et al. Abnormalities in glucose uptake and metabolism in imatinib-resistant human BCR-ABL-positive cells. *Clin Cancer Res* (2009) 15:3442–50. doi: 10.1158/1078-0432.Ccr-08-3291

21. de Beauchamp L, Himonas E, Helgason GV. Mitochondrial metabolism as a potential therapeutic target in myeloid leukaemia. *Leukemia* (2022) 36:1–12. doi: 10.1038/s41375-021-01416-w

22. Cayssials E, Jacomet F, Piccirilli N, Lefèvre L, Roy L, Guilhot F, et al. Sustained treatment-free remission in chronic myeloid leukaemia is associated with an increased frequency of innate CD8(+) T-cells. *Br J Haematol* (2019) 186:54–9. doi: 10.1111/bjh.15858

23. Harada I, Sasaki H, Murakami K, Nishiyama A, Nakabayashi J, Ichino M, et al. Compromised anti-tumor-immune features of myeloid cell components in chronic myeloid leukemia patients. *Sci Rep* (2021) 11:18046. doi: 10.1038/s41598-021-97371-8

24. Tracz-Gaszewska Z, Dobrzyn P. Stearoyl-coA desaturase 1 as a therapeutic target for the treatment of cancer. *Cancers (Basel)* (2019) 11(7). doi: 10.3390/cancers11070948

25. Sen U, Coleman C, Sen T. Stearoyl coenzyme A desaturase-1: multitasker in cancer, metabolism, and ferroptosis. *Trends Cancer* (2023) 9:480–9. doi: 10.1016/j.trecan.2023.03.003

26. Zhao Y, Li M, Yao X, Fei Y, Lin Z, Li Z, et al. HCAR1/MCT1 regulates tumor ferroptosis through the lactate-mediated AMPK-SCD1 activity and its therapeutic implications. *Cell Rep* (2020) 33:108487. doi: 10.1016/j.celrep.2020.108487

27. Chen H, Qi Q, Wu N, Wang Y, Feng Q, Jin R, et al. Aspirin promotes RSL3-induced ferroptosis by suppressing mTOR/SREBP-1/SCD1-mediated lipogenesis in PIK3CA-mutatnt colorectal cancer. *Redox Biol* (2022) 55:102426. doi: 10.1016/j.redox.2022.102426

28. Jin X, Fu W, Li D, Wang N, Chen J, Zeng Z, et al. High expression of LINC01268 is positively associated with hepatocellular carcinoma progression via regulating MAP3K7. *Onco Targets Ther* (2021) 14:1753–69. doi: 10.2147/ott.S295814

29. Liu S, Di Y, Li Q, Chen L, Ma Y, He X, et al. Exosomal lncRNA LINC01268 promotes pancreatic cancer progression via the miR-217-KIF2A-PI3K/AKT axis. *Genes Dis* (2023) 10:1799–801. doi: 10.1016/j.gendis.2022.12.018

30. Shahi RB, De Brakeleer S, Caljon B, Pauwels I, Bonduelle M, Joris S, et al. Identification of candidate cancer predisposing variants by performing whole-exome sequencing on index patients from BRCA1 and BRCA2-negative breast cancer families. *BMC Cancer* (2019) 19:313. doi: 10.1186/s12885-019-5494-7

31. Wu W, Liu S, Tian L, Li C, Jiang Y, Wang J, et al. Identification of microtubule-associated biomarkers in diffuse large B-cell lymphoma and prognosis prediction. *Front Genet* (2022) 13:1092678. doi: 10.3389/fgene.2022.1092678

32. Menon R, Panwar B, Eksi R, Kleer C, Guan Y, Omenn GS. Computational inferences of the functions of alternative/noncanonical splice isoforms specific to HER2+/ER-/PR- breast cancers, a chromosome 17 C-HPP study. *J Proteome Res* (2015) 14:3519–29. doi: 10.1021/acs.jproteome.5b00498

33. Lyu J, Song Z, Chen J, Shepard MJ, Song H, Ren G, et al. Whole-exome sequencing of oral mucosal melanoma reveals mutational profile and therapeutic targets. *J Pathol* (2018) 244:358–66. doi: 10.1002/path.5017

34. Xiong X, Tu S, Wang J, Luo S, Yan X. CXXC5: A novel regulator and coordinator of TGF-β, BMP and Wnt signaling. *J Cell Mol Med* (2019) 23:740–9. doi: 10.1111/jcmm.14046

35. Wang X, Shi X, Lu H, Zhang C, Li X, Zhang T, et al. Succinylation inhibits the enzymatic hydrolysis of the extracellular matrix protein fibrillin 1 and promotes gastric cancer progression. *Adv Sci (Weinheim Baden-Wurttemberg Germany)* (2022) 9:e2200546. doi: 10.1002/advs.202200546

36. Ma X, Wei J, Zhang L, Deng D, Liu L, Mei X, et al. miR-486-5p inhibits cell growth of papillary thyroid carcinoma by targeting fibrillin-1. *Biomedicine pharmacotherapy = Biomedecine pharmacotherapie* (2016) 80:220–6. doi: 10.1016/j.biopha.2016.03.020

37. Lei L, Xia S, Liu D, Li X, Feng J, Zhu Y, et al. Genome-wide characterization of lncRNAs in acute myeloid leukemia. *Brief Bioinform* (2018) 19:627–35. doi: 10.1093/bib/bbx007

frontiers | Frontiers in Immunology

TYPE Review
PUBLISHED 13 February 2024
DOI 10.3389/fimmu.2024.1354604

OPEN ACCESS

EDITED BY
Xuanbin Wang,
Hubei University of Medicine, China

REVIEWED BY
Walter Hanel,
The Ohio State University, United States
Ou Bai,
First Affiliated Hospital of Jilin University, China

*CORRESPONDENCE
Jing-Jing Wang
wangjingjing78@csu.edu.cn
Xiao-Yan Zhou
Xyzhou100@163.com
Hong-Ling Peng
penghongling@csu.edu.cn

RECEIVED 12 December 2023
ACCEPTED 19 January 2024
PUBLISHED 13 February 2024

CITATION
Li J-W, Peng H-L, Zhou X-Y and Wang J-J (2024) Plasmablastic lymphoma: current knowledge and future directions. *Front. Immunol.* 15:1354604. doi: 10.3389/fimmu.2024.1354604

Plasmablastic lymphoma: current knowledge and future directions

Ji-Wei Li[1], Hong-Ling Peng[2]*, Xiao-Yan Zhou[3,4,5]* and Jing-Jing Wang[1]*

[1]Department of Oncology, The Second Xiangya Hospital, Central South University, Changsha, China, [2]Department of Hematology, The Second Xiangya Hospital, Central South University, Changsha, China, [3]Department of Pathology, Fudan University Shanghai Cancer Center, Shanghai, China, [4]Department of Oncology, Shanghai Medical College, Fudan University, Shanghai, China, [5]Institute of Pathology, Fudan University, Shanghai, China

Plasmablastic lymphoma (PBL) is an aggressive non-Hodgkin lymphoma associated with HIV infection and immunodeficiency. However, PBL can also be seen immunocompetent individuals in recent studies. PBL was characterized by distinct clinical and pathological features, such as plasmablastic morphology and universal expression of plasma cell markers. The clinicopathologic features were different between HIV-negative and HIV-positive patients. Gene expression analysis identified the unique molecular feature in PBL, including frequent c-*MYC* rearrangement and downregulation of BCR signaling pathway. Despite the recent advances in the treatment of PBL, the prognosis of PBL patients remains dismal. The objectives of this review are to summarize the current knowledge on the epidemiology, molecular profiles, clinical and pathological features, differential diagnosis, treatment strategies, prognostic factors, and potential novel therapeutic approaches in PBL patients.

KEYWORDS

plasmablastic lymphoma, HIV, molecular profiles, treatment, immunotherapy

1 Introduction

Plasmablastic lymphoma (PBL) is a rare subtype of diffuse large B-cell lymphoma (DLBCL), with high invasiveness and poor prognosis (1). Pathologically, the tumor cells showed large cell similar to immunoblastic B cells but expressed plasma cell associated antigens (1). In 1997, Delecluse et al. described 16 cases of primary oral DLBCL with special immunophenotype, of which 15 cases were positive for human immunodeficiency virus (HIV), and proposed the diagnosis of PBL for the first time (2). In 2001, PBL was classified as HIV infection associated lymphoma in the classification of lymphoid and hematopoietic system tumors by World Health Organization (WHO) (3). In 2008, the WHO classification of lymphoid and hematopoietic system tumors separated PBL from DLBCL and classified it as acquired immunodeficiency syndrome associated lymphoma (ARL) (4). In 2016, PBL was classified by WHO as an independent subtype of large B-cell lymphoma (5), which was associated with HIV and EB virus infections, or other immunodeficiency states, such as

long-term use of immunosuppressants, solid organ transplantation, or age-related immune decline.

The prognosis of PBL was significantly worse than DLBCL, with a median OS of around 12 months (6–8). although multiple new treatment regimens were developed and tried in PBL, the survival outcome remain poor (9–12). In the past 10 years, due to the rarity of this disease, most of the knowledge about it comes from clinical case reports and the etiology, molecular features and prognostic factors of this entity remain largely unknown (6). In this paper, the etiology, pathological features, treatment and prognostic factors of PBL are reviewed.

2 Epidemiology and clinical features

DLBCL and Burkitt's lymphoma (BL) are the most common subtypes of the AIDS-related lymphomas (ARLs), and PBL represents around 11% of ARLs (13, 14). ARLs account for approximately 3% of non-Hodgkin's lymphoma (15, 16), however, the exact incidence of HIV-positive PBL is still unknown. In the recent years, an increasing number of PBL cases with normal immune function have been reported (6, 17–19). The clinicopathologic features of PBL were significantly different between HIV positive and HIV negative individuals (18, 20). PBL occurred more commonly in adult men, especially in HIV positive patients (13, 21, 22), with a median age of 46 years old in HIV-positive patients (male/female:8/1) and 57 years old in HIV-negative patients (male/female: 1.7-1.9/1) (6, 20). Of the 135 cases of PBL from the LYSA group (20), HIV positive and negative patients accounted for 42% and 58%, respectively. Around one-third of HIV-negative PBL are associated with immunodeficiency such as solid organ transplantation and steroid hormone use (6, 20). A meta-analysis summarized the reported cases of PBL between 1997 and 2015 in China and the results demonstrated that all the patients were HIV negative (23). Recently, our group reported 56 cases of PBL from China and found that most patients were immunocompetent, and HIV infection was not observed (17). The above results showed that the immune status of PBL was significantly different between the eastern and western population. Similar to ARL such as Burkit lymphoma and primary exudative lymphoma (PEL), PBL is also associated with Epstein-Barr virus (EBV) infection, and Epstein-Barr virus-encoded RNA was positive in over half of the PBL patients (6, 20). The association between PBL and human herpes virus 8 (HHV-8) has yet to be elucidated, and HHV-8-related protein expression has been found in only a few cases (6, 19).

In HIV-negative PBL, the most common sites of extra-oral lesions were gastrointestinal tract, lymph nodes and skin, and extra-nodal lesions accounted for 82% (6, 17, 19). However, oral cavity is involved more frequently in HIV positive PBL than that in HIV negative PBL (6, 20). Only a few cases originate in the central nervous system (CNS), paranasal sinus, mediastinum, subcutaneous, lung and testis (6). The distribution of clinical stage is bimodal, with more than 80% of patients present at stage I and stage IV (6). Approximately 33% of HIV-positive PBL patients and 50% of HIV-negative PBL patients have B symptoms (6, 24). It has been reported that the average time from the diagnosis of AIDS to PBL was 5 years, while PBL was the first symptom in 5% of AIDS case (7). In addition, PBL could also be secondary to plasmacytoma, follicular lymphoma, and Richter's transformation of chronic lymphocytic leukemia (25–28).

3 Etiology and molecular features

The etiology and pathogenesis of PBL remain largely unclear. At present, it is believed that PBL originates from activated B cells in the terminal differentiation stage after the germinal center, and may be in the stage of development and transformation of immunoblastic cells into plasma cells (1). These cells have undergone high frequency of somatic mutations and immunoglobulin (lg) class switching. During this process, intracellular molecular signaling pathways and chromosomal abnormalities may lead to malignant transformation. *MYC* gene rearrangement (at 8q24) was the first cytogenetic abnormality identified in PBL patients [3]. *MYC* gene rearrangement was detected in over half of PBL patients (18, 29–32) and Ig gene was the main partner of *MYC* gene rearrangement (29). *MYC* gene rearrangement was more common in EBER positive patients (74%) than in EBER negative patients (43%) (29). In addition, the *MYC* rearrangement rate was significantly higher in EBV-positive PBL patients than that in EBV-negative patients (33). Targeted sequencing showed tha*t MYC* translocations was observed in as high as 87% PBL cases (34). The role of *MYC* gene rearrangement in the pathogenesis of PBL is not clear. It is believed that the plasmablastic morphology of tumor cells and the aggressiveness of PBL are related to MYC gene rearrangement.

Notch1 is an important regulatory signal for T - and B-lineage selection during lymphoid progenitor cell development, and it can inhibit the expression of some transcription factors in B-lineage lymphocytes. Notch l is also involved in signaling pathways associated with cell proliferation and survival, including mammalian target of rapamycin (mTOR) (35). Notch1 pathway was demonstrated to be activated in PBL by whole exome sequencing (WES) (36). Segmiller et al. found that Notch1 was detected by immunohistochemistry (IHC) in all 9 cases of PBL (37). The positive rates of mTOR substrate phosphorylated ribosomal protein S6 (mps6) and eukaryotic initiation factor 4E binding protein 1 (4EBP1) in PBL were 100% and 86%, respectively (37), which were similar to those in 5 PEL cases and 21 plasma cell myeloma cases. Notch protein may inhibit the normal phenotypic expression of B cells and activate mTOR signaling pathway.

Previous studies showed that the gene profiles and mutation spectrum were significantly different between PBL and DLBCL (17, 38). Gene expression analysis has identified the downregulation of B-cell receptor signaling genes in PBL compared to DLBCL (38). In contrast, mitochondrial genes such as ATP5G1, CYC1, NDUFAF1, NDUFB6, NDUFB7 and UQCRQ,

were higher in PBLs than DLBCL (38). Our previous study performed RNA-sequencing to identify the molecular features of PBL and the results showed that compared with DLBCL, some biological pathways were significantly downregulated in PBL, including BCR and TCR signaling pathways, whereas many pathways, such as cell adhesion molecules, calcium, and Wnt signaling pathways, were upregulated in PBL (17).

Matsuki et al. (39) first established PBL cell lines *in vitro* by incubating immunodeficient mice subcutaneously with lymph node biopsies from patients with PBL and culturing subcutaneous masses of mice. Comparison of this cell line with the cell lines from the patient's lymph node *in vitro* by genetic hybridization (CGH) and FISH revealed that t (9: The t (9:13) (p22; q22) and 1(4;7) (q35; q22) chromosomal translocations were observed in the former cell line could cause the loss of tumor suppressor gene p16 and thus upregulated the MDR-1 expression, which is related to the drug resistance.

4 Pathological features

Histologically, the tumor cells showed a morphologic spectrum ranging from immunoblastic to plasmacytoid (1). Monomorphic plasmablastic cell morphology was more common in HIV infected patients and was more likely to occur in the mouth, nose and paranasal region. PBL with plasmacytic differentiation was more likely to occur in the extraoral cavity. The "starry sky phenomenon" can be seen, including scattered mature small lymphocytes with frequent mitoses, occasional apoptosis cells and tingible body macrophages (1). However, PBL needs to be distinguished from other large B-cell lymphomas in morphology, Such as plasmablastic plasma cell lymphoma, Burkitt lymphoma, anaplastic lymphoma kinase (ALK) positive anaplastic DLBCL, primary exudative lymphoma (PEL), multicentric Castleman large B-cell lymphoma and HHV-8 positive DLBCL (1). It can be differentiated by clinical history, site of disease, immunophenotype of tumor cells, and EBER detection.

PBL had an immunophenotype of terminally differentiated B cells (6, 17, 20). The markers of mature B cells, such as CD19, CD20, PAX-5, and leukocyte common antigen CD45, and markers of mature T cells, such as CD2, CD3, CD5, and CD7, generally did not express or weakly expressed (6). However, the tumor cells universally expressed markers of plasma cells, such as CD38, Vs38c, CD138 and IRF4/MUM1 (6). Most of the HIV-negative patients had a Ki-67 index higher than 80% (6). Immunohistochemistry showed differences between HIV positive and negative patients, the former had significantly higher CD20 and CD56 expression than the latter (6, 7, 19, 20). The overall positive rate of CD56 was around 40% (6). Although EBER was positive in over half of the PBL cases, latent membrane protein 1 (LMP1) was rarely expressed (24). Positive regulatory proteins (PRDMI/BLIMPI) and activated transcription factor (XBPI) associated with the immunophenotypes of terminally differentiated B lymphocytes are shown in PBL (40).

5 Survival outcomes and prognostic factors

Previous case reports and literature review demonstrated that PBL is an aggressive lymphoma with poor prognosis, with a median OS of 14-15 months (5-year survival 31%) in HIV-positive patients and 9 months in HIV-negative patients (6, 7, 19, 24). However, some large multicenter studies in the recent years showed that the survival outcome of PBL seems to be better than previous literature reviews (17, 20, 41–43). In 2018, a French group reported 135 PBL patients from LYSA centers and found that the complete response (CR) rate of 55% and the median overall survival (OS) was 32 months (20), which was much better than previous reports (7, 19). Recently, our previous research retrospectively analyzed 56 cases of PBL from three cancer centers in China and found that the 2-year PFS and OS rates were 59.4% and 65.1%, respectively (17). A multi-institutional retrospective study from America demonstrated the outcomes of patients with limited-stage PBL, with a median follow up of 34 months (1–196), the 3-year PFS and OS of the whole cohort were 72% and 79%, respectively. The above results indicated that the prognosis of PBL was better than that reported in case series, especially in limited stage and HIV negative patients.

According to the previous studies, Age>60 years, Ann Arbor stage III or IV, Eastern Cooperative Oncology Group (ECOC) performance status >2, extraoral primary lesions, immunosuppression, bone marrow infiltration and EBER positive were adverse prognostic factors for HIV negative PBL (6, 20). A recent multi-institutional international retrospective study including 281 PBL patients showed that EBV-negative lymphoma, poor performance status, advanced tumor stage, and bone marrow involvement was associated with inferior OS, while immunosuppression and HIV infection did not influence OS (44).

6 Treatment

6.1 Chemotherapy

Chemotherapy is the first-line treatment for PBL. The median survival (OS) of patients without chemotherapy was around 3 months (7, 19). The NCCN recommends the use of more intensive chemotherapy regimens, such as CODOX-M/IVAC (cyclophosphamide, vincristine, doxorubicin, and high-dose methotrexate alternated with ifosfamide, etoposide, and high-dose cytarabine), dose-modified EPOCH (etoposide, prednisone, vincristine, cyclocarbonamide, and doxorubicin), or Hyper-CVAD (Cyclophosphamide, vincristine, doxorubicin, and dexamethasone alternated with high-dose methotrexate and cytarabine). However, several studies have demonstrated that no survival benefit was obtained in patients who received intensive chemotherapy (Table 1) (6, 8, 18, 20). In a group of 35 patients who received CHOP/CHOP-like chemotherapy and 16 patients who received more intensive chemotherapy, there was no statistically significant difference in survival between the two groups (8). Our

TABLE 1 The survival difference between CHOP and intensive chemotherapy.

	CHOP or CHOP-like chemotherapy	Intensive chemotherapy	Survival outcome	P value
Tchernonog et al. (20)	70	16	Data not shown	>0.05
Hess BT et al. (41)	11	14	3-year OS 84% vs. 73%	>0.05
Li YJ et al. (6)	124	44	mOS: Not reached vs. 23.0m	0.981
Loghavi et al. (14)	8	16	Data not shown	0.078
Castillo et al. (8)	35	16	Data not shown	>0.05

group summarized 394 reported HIV-negative PBL, including 124 patients treated with CHOP or CHOP-like chemotherapy and 44 treated with intensive chemotherapy, and no survival difference was found between these two groups (6). Since the tumor cells in PBL showed no expression or little expression of CD20, rituximab is only used in a few patients with CD20 expression (17, 20). Although intensive chemotherapy regimens were recommended by NCCN, most of the reported cases received CHOP/CHOP-like chemotherapy and the treatment efficacy remained controversial and need further investigation. For young patients with good performance status and high-risk factors, intensive chemotherapy might be a better choice.

6.2 Proteasome inhibitor-bortezomib

Bortezomib induces apoptosis by blocking the nuclear factor kB (NF-kB) signaling pathway, producing cytotoxic effects in activated B cell type (ABC) DLBCL (Figure 1) (45). Bortezomib alone or in combination with chemotherapy (dexamethasone, bortezomib, gemcitabine, Oxaliplatin, cytarabine) may be effective in the treatment of PBL, but the remission was temporary. Bortezomib combined with chemotherapy achieved well results and was tolerated in some PBL patients (Table 2). A retrospective study analyzed 8 cases of PBL (5 HIV-positive and 3 HIV-negative) treated with bortezomib combined with EPOCH, producing a CR rate of 100% and 2-year OS rate of 50%, indicating that this regimen was relatively safe and effective for PBL (46). Dittus et al. (47) reported that the CR rate and 2-year OS rate of PBL patients treated with the combination of bortezomib and EPOCH regimen were 100% and 50%, respectively. The 2-year OS rate also exceeded 50% and the ORR was as high as 90% in PBL patients who received bortezomib as a second-line therapy (48). Our previous study reported that the overall response rate of HIV negative patients treated with bortezomib-containing regimens was 71.4%, and the mOS time was only 11 months (17). In summary, bortezomib

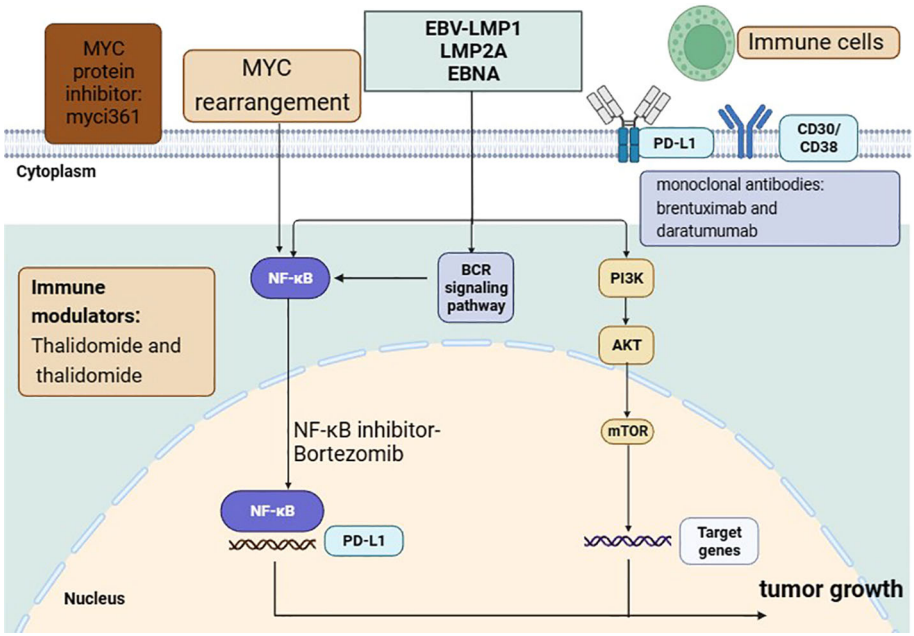

FIGURE 1
The molecular features and main treatment targets in PBL.

TABLE 2 Summary of the efficacy of Bortezomib-based treatment in PBL.

	Number	Treatment response	Survival outcome
Castillo JJ et al. (46)	11	ORR: 100%	Median OS: 11 months
Li YJ et al. (6)	14	ORR: 71.4%	Median OS: 11 months
Dittus C et al. (47)	8	CR:100%	2-year OS: 50% 2-year PFS: 50%

combined with or without chemotherapy may improve responses and outcomes in PBL, although all studies to date are retrospective and randomized study are still lacking.

6.3 Immune modulators

Thalidomide binds to CRBN targets on tumor cells, promotes ubiquitination and degradation of the transcription factors Ikaros and Aiolos, and activates an interferon-like response, thereby inducing tumor cell apoptosis (49). A newly diagnosed PBL patient achieved CR after fist-line treatment of thalidomide combined with dexamethasone, followed by autologous stem cell transplantation and the patients still maintained CR after 10 years of follow up (50). Lenalidomide is a thalidomide analogue with similar anti-tumor mechanisms. It has been reported that a patient with PBL who progressed after multiple lines of treatment was treated with lenalidomide orally due to severe peripheral neurotoxicity caused by bortezomib, and maintained PR status after 2 years of follow-up (51). Marrero et al. reported that a patient with PBL who relapsed after CHOP regimen was treated with lenalidomide combined with bortezomib as a second-line treatment and still maintained CR status after 12 months of follow-up (11). Although a large number of clinical studies are lacking, lenalidomide alone or in combination with other treatment regimens can help patients maintain long-term CR status for newly diagnosed or relapsed/refractory PBL patients.

6.4 Immune checkpoint inhibitors

Programmed death receptor 1(PD-1) expressed by T cells binds to programmed death receptor ligand 1(PD-L1) on the surface of tumor cells, which can inhibit the activation of T cells and induce their apoptosis, leading to the immune escape and tumor progression (52). In PBL, high expression of PD-1 and PD-L1 was detected and the PD-1/PD-L1 pathway was abnormally activated (33, 53–55). Only few reports have demonstrated the efficacy of immune checkpoint inhibitors in PBL patients (10, 56). This patient achieved PR with PD-1 inhibitor monoclonal antibody nivolumab and underwent allogeneic hematopoietic stem cell transplantation without signs of tumor progression as of the time of this article (56). Given the potential activity of PD-1 pathway blockade in PBL, further study of PD-1 blockade is warranted.

6.5 CAR-T therapy

Chimeric antigen receptor T cell (CAR-T cell) therapy is a newly developed immunotherapy where T lymphocytes are engineered with synthetic receptors known as chimeric antigen receptors (CAR) (57). The CAR-T cell could produce long-term specific antitumor effects by recognizing and eliminating specific cancer cells. CAR-T cell therapy was an effective anti-tumor for relapsed/Refractory DLBCL (9, 57). Raghunandan et al. reported a case of multiple refractory PBL emerging from B-cell acute lymphoblastic leukemia and failed to allogeneic hematopoietic cell transplant and sustained CR for one year after CAR-T cell therapy (12). Raychaudhuri et al. reported that a patient with PBL who was resistant to traditional chemotherapy, lenalidomide and bortezomib achieved CR after 4 months of CAR-T therapy (Yescarta treatment) (58). As the plasmablastic cells were frequently negative for B cell markers (19, 20), the use of CAR-19 therapies in PBL patients was limited. CAR-T provides a treatment option for patients with relapsed and refractory PBL, but the efficacy needs to be confirmed in the future.

6.6 Highly active antiretroviral therapy

HIV patients are often accompanied by CD4+Cell count reduction and immunosuppression (7, 59). The impact of highly active antiretroviral therapy (HAART)on survival outcome in patients with HIV-related PBL remains controversial as the condition is rare and the reported case series is small (7, 19, 60). A retrospective study in the United States explored the effect of HIV on lymphoma and found that HIV was associated with increased risk of death among lymphoma patients in the HAART era (61). Case report showed that a HIV-positive PBL patient achieved sustained remission after HAART alone (60). For HIV-positive patients with PBL, meta-analysis has shown that the combination of highly active antiretroviral therapy (HAART) and chemotherapy and/or radiotherapy can improve the prognosis (7). The possible explanation is that HAART can restore the immune surveillance function of patients so as to play a more effective role in tumor control. However, the prognosis of PBL in HIV-infected individuals remains dismal in the highly active antiretroviral therapy era and intensive chemotherapy regimens did not increase the survival outcome (62).

6.7 Hematopoietic stem cell transplantation

Some recent reports have demonstrated the application of autologous hematopoietic stem cell transplantation (ASCT) in PBL patients (Table 3) (20, 63, 64). Cattaneo et al. reported 24 PBL patients who received autologous hematopoietic stem cell transplantation and the 2-year OS was 58% (63). A retrospective study of 9 HIV-negative PBL patients from Moffitt Cancer Center showed that four patients received ASCT as consolidation therapy after first complete remission and the survival time was 36.5 months (65). LYSA group retrospectively analyzed 135 cases of PBL,

TABLE 3 A brief summary of autologous hematopoietic stem cell transplantation (ASCT) in PBL.

	n	Survival outcome
Hess BT. et al. (41)	8	3-year PFS: 63%, 3-year OS: 63%
Tchernonog et al. (20)	6	PFS: 8, 13, 17,26, 29, 78
Cattaneo et al. (63)	24	2-year OS: 58%
Hubel K, et al. (64)	24	2-year PFS: 52%, 2-year OS: 70%

including 6 patients who received autologous HSCT after the first CR, and the result showed that 3 patients remained remission at the last follow-up (13, 17 and 29 months after HSCT), 2 patients relapsed at 8 and 26 months, and 1 died after 78 months of remission (20). Recently, a multi-institutional retrospective study reported 8 cases who underwent Auto-SCT consolidation after chemotherapy and the 3-year PFS and 3-year OS were both 63.0% (41). As the above results were achieved based on the small case series, the clinical efficacy of ASCT in PBL need further investigation.

6.8 Other

Some PBL cells express CD30 on their surface. So far, three patients with relapsed/refractory PBL have been reported to have been treated with CD30 monoclonal antibody brentuximab (66–68). Two patients had significant tumor shrinkage after a few days of treatment with brentuximab, but one of these patients developed multiple mediastinal fistulas due to rapid tumor regression. As PBL showed a plasma cell immunophenotype, CD38 is commonly expressed in PBL (6, 20), and daratumumab can induce NK cells to produce antigen-dependent cell-mediated cytotoxicity (69, 70), suggesting that CD38 monoclonal antibody can be used for the treatment of PBL. Fedele et al. (71) revealed that immunomodulators can lead to Ikaros deletion and then upregulated CD38 expression on the surface of tumor cells, providing a theoretical basis for the combination of anti-CD38 monoclonal antibody and immunomodulators in PBL. Shi et al. (72) found that SLAMF7 (CD319/CS1) was detected in PBL, suggesting that it may serve as a potential diagnostic marker and therapeutic target for PBL. MYC rearrangement was observed in around half of the patients and this abnormality could inhibit transcription factor BLIMP-1 and thus promote tumor cell proliferation (73). Han et al. developed a new MYC protein inhibitor (myci361), which could inhibit tumor proliferation and increased the infiltration of the lymphocytes (74), but this drug was in the preclinical stage.

6.9 Radiation therapy in limited stage PBL

An increasing number of evidences have suggested that the prognosis of limited-stage PBL was much better than advanced stage patients (20, 41). However, the treatment recommendation of limited-stage was similar to advanced stage patients and many patients with limited-stage disease are treated with aggressive chemotherapy or auto-SCT (6, 7, 19). Previous studies have shown that patients treated with aggressive chemotherapy or consolidation with Auto-SCT had a trend toward better outcomes (63, 75). A recent study demonstrated that limited-stage PBL did not benefit from aggressive frontline treatment, including Hyper-CVAD or auto-SCT consolidation (41). However, improved PFS was observed in patients receiving EPOCH based frontline therapy versus CHOP (HR: 0.23; $p<0.05$). Patients receiving frontline chemotherapy followed by radiation consolidation had better OS than chemotherapy alone (41).

7 Conclusion

PBL is a special type of DLBCL, which often occurs in HIV positive patients, shows immunoblastic morphology but expresses plasma cell markers. Compared with DLBCL, NOS, some important biological pathways were abnormally activated or inactivated in PBL, such as BCR signaling and CAM signaling. As we have mentioned above, the prognosis of PBL was still dismal with current treatment strategies. Although intensive chemotherapy strategy was recommended by NCCN guideline, CHOP or CHOP-like chemotherapy achieved similar efficacy. Chemotherapy followed by radiation consolidation improved the survival outcome of limited-stage PBL and may be potential standard treatment for this group of patients in the future. Bortezomib combined with or without chemotherapy may improve the survival outcomes in PBL, but all studies to date are retrospective and large randomized study are sparse. PD-1/PD-L1 pathway was abnormally activated in PBL, although the efficacy of PD-1 inhibitor was only reported in case report, it may be a promising treatment and need further investigation. Other potential therapeutic approaches for patients include EBV-targeted therapies, including antiviral agents or EBV-targeted cellular immunotherapy, but the efficacy and tolerance of these approaches have not yet been evaluated in PBL patients. New treatment strategies such as thalidomide and anti-CD30 antibodies were explored in case reports, but the exact efficacy of these treatment remain to be validated in the future. It is urgent to further investigate the biological characteristics and develop more effective targeted therapeutic agents for PBL patients.

Author contributions

J-WL: Investigation, Writing – original draft. H-LP: Supervision, Writing – review & editing. X-YZ: Supervision, Validation, Funding acquisition, Writing – review & editing. J-JW: Supervision, Visualization, Writing – review & editing.

Funding

The author(s) declare financial support was received for the research, authorship, and/or publication of this article. This study

was supported by the Scientific Research Launch Project for new employees of the Second Xiangya Hospital of Central South University, Beijing Xisike Clinical Oncology Research Foundation (Grant No. Y-Young2023-0175), the Natural Science Foundation of Hunan Province (Grant No. 2023JJ60429), the National Natural Science Foundation of China (Grant No. 81470353, 81870155, 81700195), Innovation Group Project of Shanghai Municipal Health Commission (Grant No. 2019CXJQ03), Shanghai Science and Technology Development Fund (Grant No. 19MC1911000), Shanghai Municipal Key Clinical Specialty (Grant No. shslczdzk01301), Innovation Program of Shanghai Science and Technology Committee (Grant No. 20Z11900300) and Clinical Research Plan of Shanghai Hospital Development Center (Grant No. SHDC2020CR3046B).

Conflict of interest

The authors declare that the research was conducted in the absence of any commercial or financial relationships that could be construed as a potential conflict of interest.

Publisher's note

References

1. Castillo JJ, Bibas M, Miranda RN. The biology and treatment of plasmablastic lymphoma. *Blood* (2015) 125(15):2323–30. doi: 10.1182/blood-2014-10-567479

2. Delecluse HJ, Anagnostopoulos I, Dallenbach F, Hummel M, Marafioti T, Schneider U, et al. Plasmablastic lymphomas of the oral cavity: a new entity associated with the human immunodeficiency virus infection. *Blood* (1997) 89 (4):1413–20. doi: 10.1182/blood.V89.4.1413

3. Jafie ES HN, Stein H, Wardiman JW. *Tumors of haematopoietic and lymphoid tissues*. Lyon: IARCPress (2001).

4. Swerdlow SH, Campo E, Harris NL, Jaffe ES, Pileri SA, Stein H, et al. WHO classification of tumours of haematopoietic and lymphoid tissues. In: Bosman FT, Jaffe ES, Lakhani SR, Ohgaki H, editors. *World Health Organization Classification of Tumours*. Lyon, France: IARC (2008).

5. Swerdlow SH, Campo E, Pileri SA, Harris NL, Stein H, Siebert R, et al. The 2016 revision of the World Health Organization classification of lymphoid neoplasms. *Blood* (2016) 127(20):2375–90. doi: 10.1182/blood-2016-01-643569

6. Li YJ, Li JW, Chen KL, Li J, Zhong MZ, Liu XL, et al. HIV-negative plasmablastic lymphoma: report of 8 cases and a comprehensive review of 394 published cases. *Blood Res* (2020) 55(1):49–56. doi: 10.5045/br.2020.55.1.49

7. Castillo J, Pantanowitz L, Dezube BJ. HIV-associated plasmablastic lymphoma: lessons learned from 112 published cases. *Am J Hematol* (2008) 83(10):804–9. doi: 10.1002/ajh.21250

8. Castillo JJ, Winer ES, Stachurski D, Perez K, Jabbour M, Milani C, et al. Prognostic factors in chemotherapy-treated patients with HIV-associated Plasmablastic lymphoma. *Oncologist* (2010) 15(3):293–9. doi: 10.1634/theoncologist.2009-0304

9. Locke FL, Go WY, Neelapu SS. Development and use of the anti-CD19 chimeric antigen receptor T-cell therapy axicabtagene ciloleucel in large B-cell lymphoma: A review. *JAMA Oncol* (2020) 6(2):281–90. doi: 10.1001/jamaoncol.2019.3869

10. Lurain K, Ramaswami R, Mangusan R, Widell A, Ekwede I, George J, et al. Use of pembrolizumab with or without pomalidomide in HIV-associated non-Hodgkin's lymphoma. *J Immunother Cancer* (2021) 9(2):e002097. doi: 10.1136/jitc-2020-002097

11. Marrero WD, Cruz-Chacon A, Castillo C, Cabanillas F. Successful use of bortezomib-lenalidomide combination as treatment for a patient with plasmablastic lymphoma. *Clin Lymphoma Myeloma Leuk* (2018) 18(7):e275–7. doi: 10.1016/j.clml.2018.04.011

12. Raghunandan S, Pauly M, Blum WG, Qayed M, Dhodapkar MV, Elkhalifa M, et al. BCMA CAR-T induces complete and durable remission in refractory plasmablastic lymphoma. *J Immunother Cancer* (2023) 11(5):e006684. doi: 10.1136/jitc-2023-006684

13. Wang C, Liu J, Liu Y. Progress in the treatment of HIV-associated lymphoma when combined with the antiretroviral therapies. *Front Oncol* (2021) 11:798008. doi: 10.3389/fonc.2021.798008

14. Schommers P, Gillor D, Hentrich M, Wyen C, Wolf T, Oette M, et al. Incidence and risk factors for relapses in HIV-associated non-Hodgkin lymphoma as observed in the German HIV-related lymphoma cohort study. *Haematologica* (2018) 103(5):857–64. doi: 10.3324/haematol.2017.180893

15. Silverberg MJ, Leyden W, Hernandez-Ramirez RU, Qin L, Lin H, Justice AC, et al. Timing of antiretroviral therapy initiation and risk of cancer among persons living with human immunodeficiency virus. *Clin Infect Dis* (2021) 72(11):1900–9. doi: 10.1093/cid/ciaa1046

16. Ruffieux Y, Dhokotera T, Muchengeti M, Bartels L, Olago V, Bohlius J, et al. Cancer risk in adolescents and young adults living with HIV in South Africa: a nationwide cohort study. *Lancet HIV* (2021) 8(10):e614–22. doi: 10.1016/S2352-3018(21)00158-2

17. Shi D, Gao L, Wan XC, Li J, Tian T, Hu J, et al. Clinicopathologic features and abnormal signaling pathways in plasmablastic lymphoma: a multicenter study in China. *BMC Med* (2022) 20(1):483. doi: 10.1186/s12916-022-02683-9

18. Loghavi S, Alayed K, Aladily TN, Zuo Z, Ng SB, Tang G, et al. Stage, age, and EBV status impact outcomes of plasmablastic lymphoma patients: a clinicopathologic analysis of 61 patients. *J Hematol Oncol* (2015) 8:65. doi: 10.1186/s13045-015-0163-z

19. Liu M, Liu B, Liu B, Wang Q, Ding L, Xia C, et al. Human immunodeficiency virus-negative plasmablastic lymphoma: a comprehensive analysis of 114 cases. *Oncol Rep* (2015) 33(4):1615–20. doi: 10.3892/or.2015.3808

20. Tchernonog E, Faurie P, Coppo P, Bonnet A, Algarte Genin M, et al. Clinical characteristics and prognostic factors of plasmablastic lymphoma patients: analysis of 135 patients from the LYSA group. *Ann Oncol* (2017) 28(4):843–8. doi: 10.1093/annonc/mdw684

21. Sengayi-Muchengeti M, Singh E, Chen WC, Bradshaw D, de Villiers CB, Newton R, et al. Thirteen cancers associated with HIV infection in a Black South African cancer patient population (1995-2016). *Int J Cancer* (2023) 152(2):183–94. doi: 10.1002/ijc.34236

22. Zucman D, Mellot F, Couderc L. HIV-associated cancers and related diseases. *N Engl J Med* (2018) 378(22):2144–5. doi: 10.1056/NEJMc1804812

23. Han X, Duan M, Hu L, Zhou D, Zhang W. Plasmablastic lymphoma: Review of 60 Chinese cases and prognosis analysis. *Med (Baltimore)* (2017) 96(9):e5981. doi: 10.1097/MD.0000000000005981

24. Morscio J, Dierickx D, Nijs J, Verhoef G, Bittoun E, Vanoeteren X, et al. Clinicopathologic comparison of plasmablastic lymphoma in HIV-positive, immunocompetent, and posttransplant patients: single-center series of 25 cases and meta-analysis of 277 reported cases. *Am J Surg Pathol* (2014) 38(7):875–86. doi: 10.1097/PAS.0000000000000234

25. Yamada T, Hara T, Goto N, Iwata H, Tsurumi H. Follicular lymphoma suggested to transform into EBV-negative plasmablastic lymphoma. *Int J Hematol* (2019) 109 (6):723–30. doi: 10.1007/s12185-019-02591-4

26. Ise M, Kageyama H, Ikebe D, Araki A, Kumagai K, Itami M. Transformation of double-hit follicular lymphoma to plasmablastic lymphoma: a partial role of MYC gene rearrangement. *J Clin Exp Hematop* (2018) 58(3):128–35. doi: 10.3960/jslrt.18003

27. Hatzimichael E, Papathanasiou K, Zerdes I, Flindris S, Papoudou-Bai A, Kapsali E. Plasmablastic lymphoma with coexistence of chronic lymphocytic leukemia in an immunocompetent patient: a case report and mini-review. *Case Rep Hematol* (2017) 2017:2861596. doi: 10.1155/2017/2861596

28. Qing X, Sun N, Chang E, French S, Ji P, Yue C. Plasmablastic lymphoma may occur as a high-grade transformation from plasmacytoma. *Exp Mol Pathol* (2011) 90 (1):85–90. doi: 10.1016/j.yexmp.2010.10.007

29. Valera A, Balague O, Colomo L, Martinez A, Delabie J, Taddesse-Heath L, et al. IG/MYC rearrangements are the main cytogenetic alteration in plasmablastic lymphomas. *Am J Surg Pathol* (2010) 34(11):1686–94. doi: 10.1097/PAS.0b013e3181f3e29f

30. Taddesse-Heath L, Meloni-Ehrig A, Scheerle J, Kelly JC, Jaffe ES. Plasmablastic lymphoma with MYC translocation: evidence for a common pathway in the generation of plasmablastic features. *Mod Pathol* (2010) 23(7):991–9. doi: 10.1038/modpathol.2010.72

31. Montes-Moreno S, Martinez-Magunacelaya N, Zecchini-Barrese T, Villambrosia SG, Linares E, Ranchal T, et al. Plasmablastic lymphoma phenotype is determined by

genetic alterations in MYC and PRDM1. *Mod Pathol* (2017) 30(1):85–94. doi: 10.1038/modpathol.2016.162

32. Miao L, Guo N, Feng Y, Rao H, Wang F, Huang Q, et al. High incidence of MYC rearrangement in human immunodeficiency virus-positive plasmablastic lymphoma. *Histopathology* (2020) 76(2):201–11. doi: 10.1111/his.13959

33. Laurent C, Fabiani B, Do C, Tchernonog E, Cartron G, Gravelle P, et al. Immune-checkpoint expression in Epstein-Barr virus positive and negative plasmablastic lymphoma: a clinical and pathological study in 82 patients. *Haematologica* (2016) 101(8):976–84. doi: 10.3324/haematol.2016.141978

34. Ramis-Zaldivar JE, Gonzalez-Farre B, Nicolae A, Pack S, Clot G, Nadeu F, et al. MAPK and JAK-STAT pathways dysregulation in plasmablastic lymphoma. *Haematologica* (2021) 106(10):2682–93. doi: 10.3324/haematol.2020.271957

35. Sambandam V, Frederick MJ, Shen L, Tong P, Rao X, Peng S, et al. PDK1 mediates NOTCH1-mutated head and neck squamous carcinoma vulnerability to therapeutic PI3K/mTOR inhibition. *Clin Cancer Res* (2019) 25(11):3329–40. doi: 10.1158/1078-0432.CCR-18-3276

36. Frontzek F, Staiger AM, Zapukhlyak M, Xu W, Bonzheim I, Borgmann V, et al. Molecular and functional profiling identifies therapeutically targetable vulnerabilities in plasmablastic lymphoma. *Nat Commun* (2021) 12(1):5183. doi: 10.1038/s41467-021-25405-w

37. Seegmiller AC, Wang HY, Hladik C, Chen W. Uniform expression of Notch1, suppressor of B-cell-specific gene expression, in plasmablastic lymphoma. *Arch Pathol Lab Med* (2011) 135(6):770–5. doi: 10.5858/2009-0691-OA.1

38. Chapman J, Gentles AJ, Sujoy V, Vega F, Dumur CI, Blevins TL, et al. Gene expression analysis of plasmablastic lymphoma identifies downregulation of B-cell receptor signaling and additional unique transcriptional programs. *Leukemia* (2015) 29 (11):2270–3. doi: 10.1038/leu.2015.109

39. Matsuki E, Miyakawa Y, Asakawa S, Tsukada Y, Yamada T, Yokoyama K, et al. Identification of loss of p16 expression and upregulation of MDR-1 as genetic events resulting from two novel chromosomal translocations found in a plasmablastic lymphoma of the uterus. *Clin Cancer Res* (2011) 17(8):2101–9. doi: 10.1158/1078-0432.CCR-10-2945

40. Montes-Moreno S, Gonzalez-Medina AR, Rodriguez-Pinilla SM, Maestre L, Sanchez-Verde 499 L , Roncador G, et al. Aggressive large B-cell lymphoma with plasma cell differentiation: immunohistochemical characterization of plasmablastic lymphoma and diffuse large B-cell lymphoma with partial plasmablastic phenotype. *Haematologica* (2010) 95(8):1342–9. doi: 10.3324/haematol.2009.016113

41. Hess BT, Giri A, Park Y, Patel KK, Link BK, Nowakowski GS, et al. Outcomes of patients with limited-stage plasmablastic lymphoma: A multi-institutional retrospective study. *Am J Hematol* (2023) 98(2):300–8. doi: 10.1002/ajh.26784

42. Jessa R, Chien N, Villa D, Freeman CL, Slack GW, Savage KJ, et al. Clinicopathological characteristics and long-term outcomes of plasmablastic lymphoma in British Columbia. *Br J Haematol* (2022) 199(2):230–8. doi: 10.1111/bjh.18399

43. Florindez JA, Alderuccio JP, Reis IM, Lossos IS. Survival analysis in treated plasmablastic lymphoma patients: a population-based study. *Am J Hematol* (2020) 95 (11):1344–51. doi: 10.1002/ajh.25955

44. Di Ciaccio PR, Polizzotto MN, Cwynarski K, Gerrie AS, Burton C, Bower M, et al. The influence of immunodeficiency, disease features and patient characteristics on survival in plasmablastic lymphoma. *Blood* (2024) 143(2):152–65. doi: 10.1182/blood.2023021348

45. Davies AJ, Barrans S, Stanton L, Caddy J, Wilding S, Saunders G, et al. Differential efficacy from the addition of bortezomib to R-CHOP in diffuse large B-cell lymphoma according to the molecular subgroup in the REMoDL-B study with a 5-year follow-up. *J Clin Oncol* (2023) 41(15):2718–23. doi: 10.1200/JCO.23.00033

46. Castillo JJ, Guerrero-Garcia T, Baldini F, Tchernonog E, Cartron G, Ninkovic S, et al. Bortezomib plus EPOCH is effective as frontline treatment in patients with plasmablastic lymphoma. *Br J Haematol* (2019) 184(4):679–82. doi: 10.1111/bjh.15156

47. Dittus C, Grover N, Ellsworth S, Tan X, Park SI. Bortezomib in combination with dose-adjusted EPOCH (etoposide, prednisone, vincristine, cyclophosphamide, and doxorubicin) induces long-term survival in patients with plasmablastic lymphoma: a retrospective analysis. *Leuk Lymphoma* (2018) 59(9):2121–7. doi: 10.1080/10428194.2017.1416365

48. Guerrero-Garcia TA, Mogollon RJ, Castillo JJ. Bortezomib in plasmablastic lymphoma: A glimpse of hope for a hard-to-treat disease. *Leuk Res* (2017) 62:12–6. doi: 10.1016/j.leukres.2017.09.020

49. Jan M, Sperling AS, Ebert BL. Cancer therapies based on targeted protein degradation - lessons learned with lenalidomide. *Nat Rev Clin Oncol* (2021) 18(7):401–17. doi: 10.1038/s41571-021-00479-z

50. Broccoli A, Nanni L, Stefoni V, Agostinelli C, Argnani L, Cavo M, et al. A patient with plasmablastic lymphoma achieving long-term complete remission after thalidomide-dexamethasone induction and double autologous stem cell transplantation: a case report. *BMC Cancer* (2018) 18(1):645. doi: 10.1186/s12885-018-4561-9

51. Ando K, Imaizumi Y, Kobayashi Y, Niino D, Hourai M, Sato S, et al. Bortezomib- and lenalidomide-based treatment of refractory plasmablastic lymphoma. *Oncol Res Treat* (2020) 43(3):112–6. doi: 10.1159/000504608

52. Yamaguchi H, Hsu JM, Yang WH, Hung MC. Mechanisms regulating PD-L1 expression in cancers and associated opportunities for novel small-molecule therapeutics. *Nat Rev Clin Oncol* (2022) 19(5):287–305. doi: 10.1038/s41571-022-00601-9

53. Ahn JS, Al-Habib A, Vos JA, Sohani AR, Barboza-Quintana O, Flores JP, et al. Plasmablastic lymphomas: characterization of tumor microenvironment using CD163 and PD-1 immunohistochemistry. *Ann Clin Lab Sci* (2020) 50(2):213–8.

54. Liang Y, Wang H, Luo B. Exploration and analysis of differentially expressed genes in Epstein-Barr virus negative and positive plasmablastic lymphoma. *Clin Transl Oncol* (2023) 25(10):2884–91. doi: 10.1007/s12094-023-03150-4

55. Chen BJ, Chapuy B, Ouyang J, Sun HH, Roemer MG, Xu ML, et al. PD-L1 expression is characteristic of a subset of aggressive B-cell lymphomas and virus-associated Malignancies. *Clin Cancer Res* (2013) 19(13):3462–73. doi: 10.1158/1078-0432.CCR-13-0855

56. Damlaj M, Alzayed M, Alahmari B, Alhejazi A, Alaskar A, Alzahrani M. Therapeutic potential of checkpoint inhibitors in refractory plasmablastic lymphoma. *Clin Lymphoma Myeloma Leuk* (2019) 19(10):e559–63. doi: 10.1016/j.clml.2019.06.008

57. Vijenthira A, Kuruvilla J, Crump M, Jain M, Prica A. Cost-effectiveness analysis of frontline polatuzumab-rituximab, cyclophosphamide, doxorubicin, and prednisone and/or second-line chimeric antigen receptor T-cell therapy versus standard of care for treatment of patients with intermediate- to high-risk diffuse large B-cell lymphoma. *J Clin Oncol* (2023) 41(8):1577–89. doi: 10.1200/JCO.22.00478

58. Raychaudhuri R, Qualtieri J, Garfall AL. Axicabtagene ciloleucel for CD19+ plasmablastic lymphoma. *Am J Hematol* (2020) 95(1):E28–30. doi: 10.1002/ajh.25682

59. Chaudhary O, Trotta D, Wang K, Wang X, Chu X, Bradley C, et al. Patients with HIV-associated cancers have evidence of increased T cell dysfunction and exhaustion prior to cancer diagnosis. *J Immunother Cancer* (2022) 10(4):e004564. doi: 10.1136/jitc-2022-004564

60. Atallah-Yunes SA, Murphy D, Abdelmalak R, Mantle L, Ali SS. Plasmablastic lymphoma achieving sustained remission with antiretroviral therapy alone. *Eur J Haematol* (2019) 103(6):620–2. doi: 10.1111/ejh.13326

61. Han X, Jemal A, Hulland E, Simard EP, Nastoupil L, Ward E, et al. HIV infection and survival of lymphoma patients in the era of highly active antiretroviral therapy. *Cancer Epidemiol Biomarkers Prev* (2017) 26(3):303–11. doi: 10.1158/1055-9965.EPI-16-0595

62. Castillo JJ, Furman M, Beltran BE, Bibas M, Bower M, Chen W, et al. Human immunodeficiency virus-associated plasmablastic lymphoma: poor prognosis in the era of highly active antiretroviral therapy. *Cancer* (2012) 118(21):5270–7. doi: 10.1002/cncr.27551

63. Cattaneo C, Finel H, McQuaker G, Vandenberghe E, Rossi G, Dreger P. Autologous hematopoietic stem cell transplantation for plasmablastic lymphoma: the European Society for Blood and Marrow Transplantation experience. *Biol Blood Marrow Transplant* (2015) 21(6):1146–7. doi: 10.1016/j.bbmt.2015.03.008

64. Hubel K, Re A, Boumendil A, Finel H, Hentrich M, Robinson S, et al. Autologous stem cell transplantation for HIV-associated lymphoma in the antiretroviral and rituximab era: a retrospective study by the EBMT Lymphoma Working Party. *Bone Marrow Transplant* (2019) 54(10):1625–31. doi: 10.1038/s41409-019-0480-x

65. Liu JJ, Zhang L, Ayala E, Field T, Ochoa-Bayona JL, Perez L, et al. Human immunodeficiency virus (HIV)-negative plasmablastic lymphoma: a single institutional experience and literature review. *Leuk Res* (2011) 35(12):1571–7. doi: 10.1016/j.leukres.2011.06.023

66. Lai C, Kandahari AM, Ujjani C. The evolving role of brentuximab vedotin in classical hodgkin lymphoma. *Blood Lymphat Cancer* (2019) 9:63–71. doi: 10.2147/BLCTT.S231821

67. Holderness BM, Malhotra S, Levy NB, Danilov AV. Brentuximab vedotin demonstrates activity in a patient with plasmablastic lymphoma arising from a background of chronic lymphocytic leukemia. *J Clin Oncol* (2013) 31(12):e197–199. doi: 10.1200/JCO.2012.46.9593

68. Pretscher D, Kalisch A, Wilhelm M, Birkmann J. Refractory plasmablastic lymphoma-a review of treatment options beyond standard therapy. *Ann Hematol* (2017) 96(6):967–70. doi: 10.1007/s00277-016-2904-7

69. Hiemstra IH, Santegoets KCM, Janmaat ML, Goeij B, Ten Hagen W, van Dooremalen S, et al. Preclinical anti-tumour activity of HexaBody-CD38, a next-generation CD38 antibody with superior complement-dependent cytotoxic activity. *EBioMedicine* (2023) 93:104663. doi: 10.1016/j.ebiom.2023.104663

70. Kang L, Li C, Rosenkrans ZT, Huo N, Chen Z, Ehlerding EB, et al. CD38-targeted theranostics of lymphoma with (89)Zr/(177)Lu-labeled daratumumab. *Adv Sci (Weinh)* (2021) 8(10):2001879. doi: 10.1002/advs.202001879

71. Fedele PL, Willis SN, Liao Y, Low MS, Rautela J, Segal DH, et al. IMiDs prime myeloma cells for daratumumab-mediated cytotoxicity through loss of Ikaros and Aiolos. *Blood* (2018) 132(20):2166–78. doi: 10.1182/blood-2018-05-850727

72. Shi J, Bodo J, Zhao X, Durkin L, Goyal T, Meyerson H, et al. SLAMF7 (CD319/CS1) is expressed in plasmablastic lymphoma and is a potential diagnostic marker and therapeutic target. *Br J Haematol* (2019) 185(1):145–7. doi: 10.1111/bjh.15393

73. Linke-Serinsoz E, Fend F, Quintanilla-Martinez L. Human immunodeficiency virus (HIV) and Epstein-Barr virus (EBV) related lymphomas, pathology view point. *Semin Diagn Pathol* (2017) 34(4):352–63. doi: 10.1053/j.semdp.2017.04.003

74. Han H, Jain AD, Truica MI, Izquierdo-Ferrer J, Anker JF, Lysy B, et al. Small-molecule MYC inhibitors suppress tumor growth and enhance immunotherapy. *Cancer Cell* (2019) 36(5):483–97.e415. doi: 10.1016/j.ccell.2019.10.001

75. Al-Malki MM, Castillo JJ, Sloan JM, Re A. Hematopoietic cell transplantation for plasmablastic lymphoma: a review. *Biol Blood Marrow Transplant* (2014) 20(12):1877–84. doi: 10.1016/j.bbmt.2014.06.009

frontiers | Frontiers in Immunology

TYPE Review
PUBLISHED 27 February 2024
DOI 10.3389/fimmu.2024.1297473

OPEN ACCESS

EDITED BY
Xuanbin Wang,
Hubei University of Medicine, China

REVIEWED BY
Guillaume Darrasse-Jeze,
Universitéde Paris,
France
Pooya Farhangnia,
Iran University of Medical Sciences, Iran
Ali-Akbar Delbandi,
Iran University of Medical Sciences, Iran

*CORRESPONDENCE
E. Gulsen Gunes
eggunes@coh.org

†These authors have contributed equally to this work

RECEIVED 20 September 2023
ACCEPTED 05 February 2024
PUBLISHED 27 February 2024

CITATION
Gunes M, Rosen ST, Shachar I and Gunes EG (2024) Signaling lymphocytic activation molecule family receptors as potential immune therapeutic targets in solid tumors. *Front. Immunol.* 15:1297473. doi: 10.3389/fimmu.2024.1297473

Signaling lymphocytic activation molecule family receptors as potential immune therapeutic targets in solid tumors

Metin Gunes[1†], Steven T. Rosen[1,2], Idit Shachar[3] and E. Gulsen Gunes[1,2,4*†]

[1]Department of Hematology and Hematopoietic Cell Transplantation, Beckman Research Institute, City of Hope, Los Angeles, CA, United States, [2]Judy and Bernard Briskin Center for Multiple Myeloma Research, City of Hope, Los Angeles, CA, United States, [3]Department of System Immunology, Weizmann Institute of Science, Rehovot, Israel, [4]Toni Stephenson Lymphoma Center, City of Hope, Los Angeles, CA, United States

Recently, cancer immunotherapy has revolutionized cancer treatment. Various forms of immunotherapy have a manageable safety profile and result in prolongation of overall survival in patients with solid tumors, but only in a proportion of patients. Various factors in the tumor microenvironment play critical roles and may be responsible for this lack of therapeutic response. Signaling lymphocytic activation molecule family (SLAMF) members are increasingly being studied as factors impacting the tumor immune microenvironment. SLAMF members consist of nine receptors mainly expressed in immune cells. However, SLAMF receptors have also been detected in cancer cells, and they may be involved in a spectrum of anti-tumor immune responses. Here, we review the current knowledge of the expression of SLAMF receptors in solid tumors and tumor-infiltrating immune cells and their association with patient outcomes. Furthermore, we discuss the therapeutic potential of targeting SLAMF receptors to improve outcomes of cancer therapy in solid tumors. We believe the research on SLAMF receptor-targeted strategies may enhance anti-cancer immunity in patients with solid tumors and improve clinical outcomes.

KEYWORDS

signaling lymphocytic activation molecule family, SLAMF, cancer immunology, immunotherapy, solid tumors, tumor microenvironment

1 Introduction

Cancer immunotherapy has revolutionized cancer treatment in the past decade, becoming the fourth pillar of treatment next to surgery, chemotherapy, and radiotherapy. Blocking immune checkpoints with monoclonal antibodies has improved outcomes in solid tumor patients (1). Furthermore, cellular therapies, particularly chimeric

antigen receptor (CAR)-T cell therapy, have shown high effectiveness for various cancers (2). However, many patients with solid tumors do not benefit from these strategies. This has warranted research into resistance mechanisms and other treatment options. Some factors in the tumor microenvironment (TME) of solid tumors may contribute to resistance to immunotherapy (3). First, infiltration of cytotoxic lymphocytes is limited in many tumors (i.e., 'cold' tumors), which may be due to a lack of antigen presentation and recognition as well as physical and chemical barriers to infiltration. Furthermore, immunosuppressive TMEs, with infiltrates of suppressive immune populations that inhibit the anti-cancer immune response, may also limit the efficacy of cancer immunotherapies.

Signaling lymphocytic activation molecule family (SLAMF) receptors are increasingly being studied as potential factors that affect the immune environment in cancers and as potential targets for therapy. Numerous studies have overwhelmingly examined the structure and function of SLAMF receptors, their role in regulating the immune system, and possible strategies for targeting this receptor family therapeutically. However, our comprehension of the potential of SLAMF receptors in solid tumors is still incomplete. Our review highlights the potential of SLAMF receptors as targets for solid tumors and outlines their current targeting strategies.

2 SLAMF receptors

SLAMF receptors are a group of cell surface glycoproteins belonging to the immunoglobulin (Ig) superfamily of proteins involved in various immune functions. SLAMF consists of nine family members mostly expressed in immune cells. Most of these receptors are homophilic, except for SLAMF2 and SLAMF4, which can bind to one another (4). Each SLAMF receptor consists of an extracellular segment comprising two or four Ig-like domains, a transmembrane region, and a cytoplasmic tail. The cytoplasmic tails contain one or more copies of a tyrosine motif called immunoreceptor tyrosine-based switch motif (ITSM). However, SLAMF2, SLAMF8, and SLAMF9 lack most of the cytoplasmic tails (4) (Figure 1). When the receptors are engaged with their ligands, ITSMs get phosphorylated, which initiates interaction with intracellular SLAM-associated proteins, including SLAM-associated protein (SAP) and Ewing`s sarcoma-associated transcript 2 (EAT-2). These proteins contain an SH2 domain and serve as adaptor proteins to link SLAMF receptors to intracellular signaling pathways. When the N-terminal Ig domains of SLAMF receptors engage with their cognate ligands, these molecules are recruited, resulting in signaling transduction events that ultimately modulate various types of immune responses.

There is mounting evidence that SLAMF receptors and SAP-related adaptor molecules play essential and intricate roles in regulating the immune system. For instance, SAP adaptor molecules recruit Fyn, a Src family tyrosine kinase, leading to downstream phosphorylation and stimulation of activating signals within immune cells. SAP molecules also prevent recruitment of the SLAMF receptor to the inhibitory pathway mediated by SH2 domain-containing protein tyrosine phosphatase (SHP)-1, SHP-2, and SH2 domain-containing inositol phosphatase (SHIP)-1. In the absence of SAP adaptors, SLAMF receptors function as inhibitory signals in cellular activation. Similarly, EAT-2 functions by recruiting phospholipase C and preventing SLAMF receptors

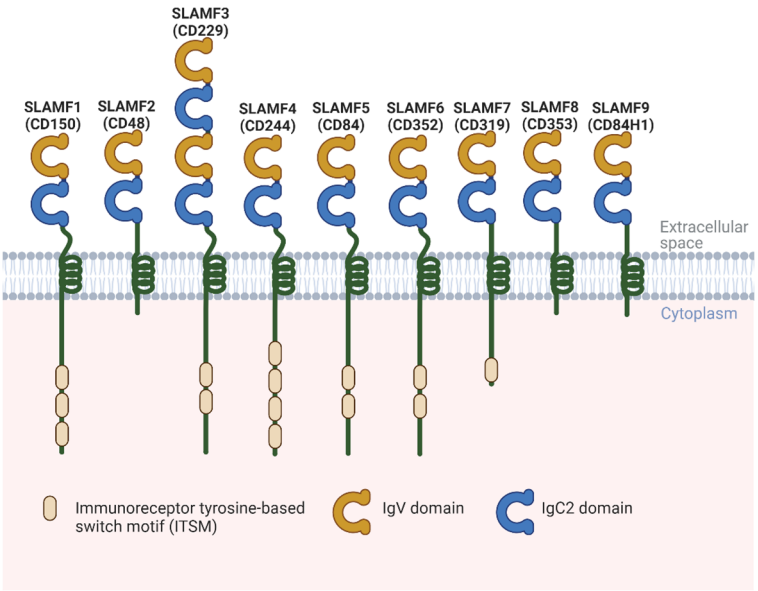

FIGURE 1
Structural representation of the human SLAMF receptors. SLAMF receptors are cell-surface receptors and are composed of nine members. They are type I glycoproteins that contain amino-terminal Ig-like variable domains (IgV) and membrane-proximal Ig-like constant two domains (IgC2) in their extracellular regions. The cytoplasmic region of every family member, except for SLAMF2, SLAMF8, and SLAMF9, contains ITSMs that mediate recruitment of SAP, as well as other SH2 domain-containing proteins such as EAT-2. Most of these receptors are homophilic, which can bind to one another, except for SLAMF2 and SLAMF4.

from coupling to inhibitory mediators. This enhances natural killer (NK) cell activity.

The importance of SLAMF receptors in the immune response became evident when the molecular defect responsible for X-Linked lymphoproliferative (XLP) syndrome was detected (5). The gene encodes SAP, and patients with this syndrome experience impaired immune responses. SLAMF receptors are known to be involved in NK- and T-cell development, expressed at various stages of B-cell development, and involved in B-cell regulation, antibody production, isotype switching, and NK-cell cytotoxicity. We have summarized the function of each SLAMF member and their expression on immune cells in Table 1 (6–10).

With recent research, the role of SLAMF receptors in solid tumors and the immune response against these tumors has become more evident. For instance, the upregulation of various dendritic cell (DCs) markers, including CD80, CD274, and SLAMF1, was associated with improved overall survival (OS) in a mixed cancer analysis (11). Here, we will describe the current data on SLAMF receptor expression in solid tumor types (Figure 2), potential associations with prognosis and therapy response, and potential targeted therapy strategies. Of note, the order of discussion will start with the solid tumor types that have more data available in the literature.

TABLE 1 SLAMF receptors and their function and location on immune cells (6–10).

SLAMF Receptor	Expression and Function
SLAMF1 (SLAM, CD150)	Expressed on thymocytes, T cells, natural killer cells (NK), B cells, dendritic cells (DCs), macrophages, and hematopoietic stem cells (HSCs) and is involved in lymphocyte activation. In Crohn's disease, an upregulation of SLAMF1 has been detected in monocytes and macrophages, and upregulation of SLAMF1 on T-cells was detected in rheumatoid arthritis. In contrast, in Chronic Lymphocytic Leukemia, it was found to be downregulated.
SLAMF2 (CD48, BLAST1, BCM1)	Expressed by NK cells, $CD8^+$ T cells, B cells, γδ T cells, DCs, basophils, eosinophils, mast cells, and multipotent progenitor cells. SLAMF2 can bind CD2 as well as SLAMF4 to initiate signaling.
SLAMF3 (CD229, LY9)	Expressed on thymocytes, T cells, follicular helper T cells, B cells, DCs, macrophages, and NK cells. During antigen presentation by B cells, it is involved in creating the immunological synapse at the contact site between the T- and B cells.
SLAMF4 (CD244, 2B4)	Expressed on $CD8^+$ T cells, γδ T cells, NK cells, DCs, macrophages, basophils, mast cells, and eosinophils. SLAMF4 binds SLAMF2, and this process is involved in NK-cell activation.
SLAMF5 (CD84, LY9B)	Expressed on thymocytes, T cells, follicular helper T cells, B cells, NK cells, macrophages, DCs, basophils, mast cells, eosinophils, and platelets. Its signaling can stimulate platelets and is involved in T-cell activation, resulting in IFNγ production.
SLAMF6 (CD352, NTBA, LY108)	Expression can be found on thymocytes, T cells, B cells, NK cells, DCs, neutrophils, and eosinophils. It has been found to be involved in NK-cell cytotoxicity and cytokine production, T-cell activation, and neutrophil functions.
SLAMF7 (CD319, CS1, CRACC)	Expressed by T cells, B cells, NK cells, NKT cells, DCs, and macrophages and has been shown to regulate NK-cell cytolysis and can partially rescue effector functions in NK- and $CD8^+$ T cells.
SLAMF8 (CD353, BLAME, SBBI42)	Expression detected on macrophages and faintly expressed on B-cell subsets.
SLAMF9 (CD2F10, CD84H1)	Expression was detected on T cells, B cells, NK cells, and DCs. It is the most recently described SLAMF member, and its ligand has not yet been discovered.

3 SLAMF receptors in solid tumors

3.1 Breast cancer

Several investigations have shown the variable expression of multiple SLAMF members in breast cancer. SLAMF1/CD150 was not found to be expressed on the cell surface of breast cancer cell lines. However, it was detected in the cytoplasm of 45% of cell lines. The highest expression levels were detected in cell lines representing a luminal subtype (T47D), while basal-type cell lines, such as MDA-MB-231, BCC/P, and BC/ML, expressed lower levels. Additionally, cell lines expressed variable levels of mRNA encoding the transmembrane mCD150 and the so-called novel CD150 (nCD150) isoforms. Assessment of public databases with patient DNA microarray data also showed that breast tumors express SLAMF1 (12). Furthermore, it was found that the SLAMF1 single nucleotide polymorphism (SNP) rs1061217 was associated with a decreased risk of breast cancer in overweight women, while it increased the risk of breast cancer in those with normal weight (13).

SLAMF2/CD48 has not been studied extensively in breast cancer. An analysis of the expression of NF-kappa B (NF-κB) related genes using RT-PCR in inflammatory breast cancer revealed that *CD48* was upregulated in these samples compared to invasive ductal carcinomas. When comparing biopsies of distant metastases of non-inflammatory breast cancer, *CD48* was one of six downregulated genes compared to the primary invasive ductal carcinomas (14).

In a large analysis of immune checkpoint genes in breast cancer, SLAMF4/CD244 expression in tumors was found to be lower than that in healthy breast tissue (15). In another study, a gene analysis in triple-negative breast cancer (TNBC) showed that overexpression of *Prune-1*, *IL-10*, *COL4A1*, *ILR1*, and *PDGFB*, as well as inactivating mutations of *PDE9A*, *CD244*, *Sirpb1b*, *SV140*, *Iqca1*, and *PIP5K1B* genes, are associated with metastasis to the lungs, suggesting low expression of CD244 may be associated with worse prognosis. This was confirmed in a The Cancer Genome Atlas (TCGA) analysis, which showed that low expression of the CD244 gene was associated with decreased survival (16). Additionally, in a BRCA2-deficient breast cancer mouse model, missense mutations in the *CD244* receptor domain were detected (17). These data suggest that a loss of CD244 signaling may contribute to a worse prognosis in breast cancer.

SLAMF5/CD84 was detected as an identifying marker for myeloid-derived suppressor cells (MDSCs) in breast cancer in a mouse model, and *in vitro* experiments showed that PBMC-

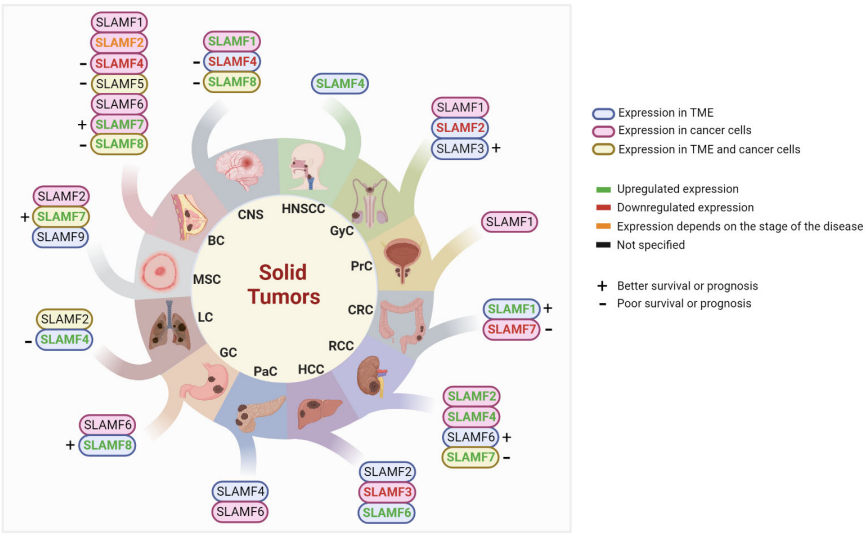

FIGURE 2
Studied SLAMF receptors in solid tumors. BC, breast cancer; CNS, central nervous system; CRC, colorectal cancer; GC, gastric cancer; GyC, gynecological cancer; HCC, hepatocellular carcinoma; HNSCC, head and neck squamous cell carcinoma; LC, lung cancer; MSC, melanoma skin cancer; PaC, pancreatic cancer; PrC, Prostate cancer; RCC, renal cell carcinoma; TME, tumor microenvironment.

derived human MDSCs upregulate SLAMF5. Co-culture experiments with such CD84^{hi} MDSC showed that they actively inhibit T-cell proliferation (18). In TCGA, *CD84* was found to be an independent negative prognostic factor for both disease-free survival (DFS) and OS. Furthermore, in circulating tumor cells, *CD84* expression was associated with a mesenchymal phenotype (19).

Another TCGA analysis that assessed core genes associated with breast cancer status revealed SLAMF6/CD352 as one of eight core genes. However, SLAMF6 had only a weak association with survival (P=0.042) and no significant association with tumor (T), node (N), and metastases (M) (TNM) status and was not further assessed (20).

SLAMF7/CD319 mRNA expression was found to be enriched in breast cancer TCGA analysis, as compared to healthy breast tissue (21, 22). A study in lymph node-positive breast cancer of various subtypes showed moderate or strong protein expression of SLAMF7 in the cytoplasm in approximately 20% of cases, while 80% had no or weak expression. In samples with high expression, up to 70% of tumor cells expressed high levels of SLAMF7. Higher levels were associated with younger age, less evasive tumors, and better prognosis. Patients with high expression had a lower relapse rate and longer disease-specific survival (DSS). However, multivariate analysis did not show SLAMF7 as an independent prognostic factor. The researchers also detected a weak association between highly vascular invasive cells and low expression levels (P=0.05) (21).

In addition, one study found a correlation between a high expression of SLAMF8/CD353, tumor necrosis factor (TNF), and lymphocyte infiltration with a poor response to therapy in postmenopausal estrogen receptor (ER)$^{+}$ breast cancer (23).

3.2 Central nervous system tumors

While SLAMF1 is not found in healthy brain tissue, 77.6% of the human central nervous system (CNS) tumors were found to express it. These tumors included glioblastoma, anaplastic astrocytoma, diffuse astrocytoma, and ependymoma. SLAMF1 was detected only in the cytoplasm of tumor cells. The novel CD150 (nCD150) transcript was also detected at high levels in these tumors, and this isoform was the predominant form in glioma cells (24).

In patients with glioblastoma, blood plasma was analyzed for the expression of various proteins that may be associated with prognosis. Low plasma levels of SLAMF4 were associated with short progression-free survival (PFS) (25).

In an assessment of TCGA glioma and the Chinese Glioma Genomic Atlas (CGGA) data, overexpression of SLAMF8 was associated with progression, higher grade glioma, and it was a biomarker for the mesenchymal subtype. The highest levels of SLAMF8 were found in glioblastoma, and in this cancer type, it was associated with reduced OS and chemoresistance. The overexpression of SLAMF8 was associated with higher infiltration of monocytes, myeloid DCs, and fibroblasts and with genes related to acute and chronic inflammation. Furthermore, it was strongly correlated with the expression of checkpoint molecules CTLA-4, PD-1, PD-L2, B7-H3, and TIM-3, but not PD-L1 (26). These data suggest SLAMF8 may be implicated in an immunosuppressive tumor microenvironment.

Besides CNS tumors, SLAMF proteins have also been implicated in stroke. Mice lacking SLAMF5 on platelets or T cells had reduced cerebral infiltration of CD4^{+} T-cells and reduced thrombolytic activity after experimental stroke, resulting in a

reduction of neurological damage. Furthermore, human arterial blood samples from the ischemic cerebral circulation showed local shedding of SLAMF5, and high expression of CD84 on platelets was associated with poor outcomes in patients with stroke (27).

3.3 Lung cancer

Non-small cell lung cancer (NSCLC) is relatively resistant to NK-cell-mediated cytotoxicity. Park et al. assessed various cell lines with variable sensitivity to NK-cell killing and found that SLAMF2 expression made the cells susceptible to killing. SLAMF2 increased the stability of the contact between the cancer cells and NK cells in live imaging experiments, which might explain this killing relationship (28).

In a lung cancer model with sepsis, PD-1 checkpoint inhibition has no effect on sepsis survival. SLAMF4 was found to be a checkpoint of interest in this condition, and the blockade of SLAMF4 improved sepsis survival. It was associated with T-cell costimulatory receptor expression and decreased coinhibitory receptor expression (29). In patients with stage I NSCLC, blood levels of SLAMF4 were found to be a prognostic factor, and those with high levels of SLAMF4 had worse PFS. This study suggested that the expression of SLAMF4 was mainly found on the immune infiltrate (30). This was confirmed in a mouse model with subcutaneous lung cancer. In these tumors, the frequencies of $PD1^+$, $BTLA^+$, and $SLAMF4^+$ $CD4^+$ and $CD8^+$ T-cells were increased, and CD8+ T-cells expressing SLAMF4 produced reduced levels of IL-2 and IFNγ (31). Therefore, the blockade of SLAMF4 might be of interest for the therapy of lung tumors.

SLAMF5 has been found to play a role in other lung diseases. In a mouse model for mycobacterium tuberculosis infection, levels of SLAMF5 increase on T- and B-cells in the lung tissue of infected mice, which is also seen in peripheral blood mononuclear cells (PBMCs) of patients with pulmonary tuberculosis. This expression resulted in immunosuppression, inhibiting T- and B-cell activation (32). SLAMF5 may, therefore, serve as a target for therapy in this disease, as well as in lung cancers, due to its potential on the immune cells of the lung tissue.

3.4 Pancreatic cancer

In a mouse model of pancreatic cancer infected with Listeria monocytogenes, bacteria antigen-specific $CD8^+$ and total T cells had increased expression of BTLA, PD-1, and SLAMF4. Expression of these markers reduced IFNγ and increased IL-2 production of $CD8^+$ T-cells. These data suggest that suppressive effects in the TME might also affect immune responses to bacterial infections (33).

In a screening of genes associated with OS and DFS in pancreatic ductal adenocarcinoma (PDAC), a 7-gene signature containing SLAMF6 was found to be associated with survival. This suggests SLAMF6 might play an interesting role in pancreatic cancer, but further research would be required to study the role it plays within this gene signature (34).

3.5 Prostate cancer

SLAMF1 cell surface and cytoplasmic expression have been detected in the prostate cancer cell lines LNCap, Du-145, and PC-3. The highest expression levels were found in the less aggressive androgen therapy-responsive non-metastatic LNCap cells. The cell lines also expressed novel nCD150 isoforms, and soluble CD150 was detected at low levels for the LNCap and PC-3 cell lines (12). Whether the expression of SLAMF1 is associated with clinical outcomes in prostate cancer remains to be determined.

3.6 Gastric cancer

SLAMF receptors have been implicated in some studies of gastric cancer. An analysis comparing cancerous with non-cancerous tissue found genes that could predict survival, and SLAM was one of the genes (35).

Circular RNA is a form of non-coding RNA, and circSLAMF6 can be generated from back splicing of the SLAMF6 first intron. In hypoxic conditions, circular RNA SLAMF6 (circSLAMF6) is increased in gastric cancer cells *in vitro*. This increase is associated with glycolysis, migration, and invasion of these tumor cells, and the knockdown of circSLAMF6 reverses these effects. In a mouse model for gastric cancer, circSLAMF6 deficiency inhibited tumor growth by regulating the miR-204-5p/MYH9 axis (36).

High levels of SLAMF8 have been detected in the serum of patients with gastric cancer (37). Furthermore, investigations in a gastric cancer model with Epstein-Barr virus (EBV) infection, which has been associated with improved responses to anti-PD-1 therapy, high SLAMF8 expression was found to be a factor that might be involved in these responses. High expression of SLAMF8 was associated with T-cell activation gene enrichment, CD8 expression, and better response to anti-PD-1 checkpoint blockade therapy. SLAMF8 in this setting was mostly expressed by macrophages, and overexpression of SLAMF8 in macrophages resulted in gene enrichment of multiple immune-related pathways. Therefore, SLAMF8 is correlated with immune 'hot' gastric cancers that respond better to immune checkpoint blockade (38).

3.7 Colorectal cancer

Research in CRC has suggested that SLAMF1 and SLAMF7 may be of interest. Transfection of CD3-activated T-cells with SLAMF1 increased their cytotoxic activity and IFNγ production *in vitro* against human colon cancer cells. In xenograft models, these T cells reduced tumor growth, suggesting increased SLAMF1 expression on T cells in colon cancer may be beneficial (39). In the human CRC TME, SLAMF1 was detected on tumor-specific innate lymphoid cells, and these cells were observed at higher levels in patient blood than in healthy controls. Patients with high levels of SLAMF1 expression had a better survival rate than those with low expression, suggesting SLAMF1 to be a marker for improved anti-tumor activity (40). Additionally, SLAMF1 was detected as one of

four core genes impacting prognosis in colon adenocarcinoma in an investigation into immune-related subtypes from TCGA (41).

SLAMF7 has been found to be downregulated in CRC tissue as compared to healthy tissue. In CRC cells overexpressing SLAMF7, CD68, and CD73 were downregulated after co-culture with a monocytic cell line, suggesting SLAMF7 might play a role in suppressing these markers (42). In another study, SLAMF7 expression did not differ between paracancer and tumor tissue or correlate with the TNM stage. In patients treated with chemoimmunotherapy and adjuvant immunotherapy based on cytokine-induced killer cells combined with chemotherapy, no correlation was found between SLAMF7 expression and $CD8^+$ T-cell or NK-cell infiltration. However, a higher expression of SLAMF7 was associated with better OS (43). Therefore, the role of SLAMF7 in CRC and its relationship to the immune response requires further investigation.

3.8 Hepatocellular carcinoma

In HCC, the number of activated, functional NK cells is associated with improved outcomes. In advanced HCC, fewer of these NK cells are detected, and the cells present have impaired TNFα and IFNγ production, suggesting limited functionality. This was shown to be associated with high infiltration of peritumoral stroma monocytes and macrophages. *In vitro*, NK cells exposed to these monocytes could undergo a rapid transient activation, resulting in exhaustion and, eventually, cell death, suggesting this might be the reason for limited NK-cell function in advanced HCC. The mechanisms behind this interaction might be associated with SLAMF signaling. Monocytes in HCC express high levels of SLAMF2, and *in vitro* experiments showed that the effects of monocytes on NK cells could be reduced by blocking SLAMF4 on the NK cells, suggesting a direct role of SLAMF2-4 signaling in these NK-cell exhaustion effects (44).

Healthy hepatocytes have been shown to express SLAMF3, but no other SLAMF members. In primary HCC samples, resected tumor samples, and HCC cell lines, the expression of SLAMF3 was significantly lower than in healthy cells, suggesting downregulation when hepatocytes undergo tumorigenesis. Restoration of high levels of SLAMF3 in cell lines was shown to inhibit cell proliferation and migration and enhance apoptosis. Additionally, these cells progressed less in nude mice than in their low SLAMF3 counterparts. Mechanistically, SLAMF3 may be associated with the signaling of various pathways, as expression resulted in decreased phosphorylation of MAPK, ERK 1/2, JNK, and mTOR (45). Follow-up studies showed that the inhibitory effect of SLAMF3 on HCC proliferation occurs through a retinoblastoma (RB) factor and PLK1-dependent pathway. Expression of SLAMF3 retained RB factor in its hypophosphorylated active form, which inactivates the transcription factor E2F, and represses the expression and activation of PLK1. PLK1 is a cell cycle protein that promotes cell cycle progression. In human samples, this was confirmed with an inverse correlation between SLAMF3 and PLK expression (46). Additionally, induction of SLAMF3 was associated with loss of MRP-1 expression, a drug resistance transporter. In patient samples, an inverse correlation between SLAMF3 and MRP-1 expression was also detected, suggesting that loss of SLAMF3 expression in tumor cells may be associated with drug resistance (47).

SLAMF6 levels were found to be increased on $CD14^+$ cells derived from blood from patients with HCC, which was associated with positive Hep B virus DNA status and high levels of α-fetoprotein. *In vitro* and *in vivo* experiments in mice showed that tumor-associated macrophages (TAMs) had higher levels of SLAMF6 (Ly108), and this was associated with the M2 phenotype. Small interfering RNA blocking Ly108 resulted in suppression of M2 macrophage polarization. Macrophages with suppressed SLAMF6 levels were able to reduce HCC cell migration and invasion and could prevent tumor growth. This latter effect was associated with the inhibition of the NF-κB pathway in macrophages, which plays a role in macrophage polarization (48).

3.9 Melanoma skin cancer

Several SLAMF members have been implicated in melanoma. In a murine model, inoculation with $SLAMF2^+$ and $SLAMF2^-$ metastatic B16 melanoma cells showed that WT mice had trouble rejecting the $SLAMF2^+$ tumors compared to $SLAMF2^-$ melanoma cells. In mice lacking SLAMF4, there was a difference between the rejection rates of these cells in male and female mice. Male mice lacking SLAMF4 rejected $SLAMF2^+$ melanoma cells, while female mice lacking SLAMF4 had trouble rejecting both $SLAMF2^+$ and $SLAMF2^-$ cells. These gender-specific differences might be related to differences in NK-cell function (49).

Eisenberg et al. created a 203-amino acid sequence of the human SLAMF6 (seSLAMF6) ectodomain. This molecule reduced activation-induced cell death in tumor-infiltrating lymphocytes (TIL). When $CD8^+$ T-cells were costimulated with seSLAMF6, the cells secreted more IFNγ and had improved cytolytic activity. When these cells were injected into the B16F10 melanoma mouse model, it delayed tumor growth, which could be further enhanced by treating the mice with seSLAMF6 (50). Another study showed that inhibition of SLAMF6 with an anti-SLAMF6 antibody affected tumor growth of the B16 melanoma model. Exhausted $CD8^+$ T-cells had increased degranulation when anti-SLAMF6 was added to the culture (51). Similar results were obtained when SLAMF6-negative Pmel-1 cells specific for gp100 were created. Upon activation, these cells acquired an effector memory phenotype and showed improved polyfunctionality and strong tumor cytolysis. Adoptive transfer of these cells into mice-bearing melanoma tumors resulted in lasting tumor regression. Given that the $CD8^+$ T-cells in this model expressed high levels of LAG3, adding anti-LAG3 checkpoint blockade could further improve anti-tumor responses (52).

TCGA analysis has revealed an enrichment of SLAMF7 in melanoma and a correlation between SLAMF7 and favorable prognosis. The expression of SLAMF7 was negatively correlated with NK-cell markers, suggesting that the expression of SLAMF7 in these tumors is unlikely NK-cell expression. *In vitro* studies showed that agonistic engagement of SLAMF7 on tumor-specific

$CD4^+$ T-cells enhanced their cytolytic activity, which, if expressed by $CD4^+$ T-cells in these tumors, may explain the relationship with favorable prognosis (22).

Finally, SLAMF9-expressing TAMs have been detected in 73.3% of human melanomas, 95.5% of naevi of melanoma patients, and 50% of naevi of healthy controls. SLAMF9 was also expressed in melanocytes in 20% of melanoma samples and 2.3% of naevi from melanoma patients but not in healthy controls. *In vitro* experiments showed that SLAMF9 gene expression was upregulated in murine bone marrow-derived macrophages stimulated with tumor-conditioned media of B16F10 melanoma cells. Furthermore, SLAMF9 expression enhanced TNFα secretion after LPS stimulation, and it delayed wound closure of RAW 264.7 cells in a scratch assay (53).

3.10 Renal cell carcinoma

A TCGA analysis into immune checkpoints in clear cell RCC (ccRCC) revealed that although these receptor/ligands were not found to be the most relevant in this study, genes encoding SLAMF2 and SLAMF4 were found to be more highly expressed in tumor tissue as compared to adjacent non-tumor tissue (54).

An analysis in ccRCC focused on regulatory T cells (Tregs) in tumor tissue and found that SLAMF6 is one of four hub genes related to prognosis and Tregs and associated with a better outcome (55).

Another TCGA analysis showed that SLAMF7 strongly correlated with various inhibitory receptors and that high expression was correlated with poor survival in ccRCC. CyTOF analysis of the TME of 73 ccRCC patients revealed that SLAMF7 was expressed by TAMs, with a unique subset of $SLAMF7^{hi}CD38^{hi}$ TAMs; these cells correlated with exhausted T-cells and were an independent prognostic factor. In co-culture experiments, it was shown that SLAMF7-SLAMF7 interactions between murine TAMs and $CD8^+$ T-cells induced the expression of inhibitory receptors. In mice lacking SLAMF7, B16F10 growth was restricted, and $CD8^+$ T-cells in these tumors expressed lower levels of PD-1 and TOX, suggesting a less exhausted phenotype (56).

3.11 Gynecological cancers

SLAMF1 was found to activate autophagy-related mechanisms that promoted resistance to methotrexate in choriocarcinoma cells. Depletion of SLAMF1 suppressed autophagy and induced apoptosis of MTX-resistant cell lines, which overexpressed SLAMF1 (57, 58).

Choriocarcinoma cells can be resistant to NK-cell lysis. This was associated with a lack of NK-cell activation, as choriocarcinoma cells lacked expression of SLAMF2, the ligand for SLAMF4 (59).

Limited research is available on SLAMF expression in ovarian cancer. Assessment of TCGA and University of California, Santa Cruz (UCSC) ovarian cancer datasets revealed that various SLAMF members were part of a hub gene profile in immune infiltrates. This hub gene profile included SLAMF1, SLAMF3, SLAMF6, and SLAMF7. Two of these, SLAMF1 and SLAMF3, were recognized as the real hub genes in immune infiltrates in ovarian cancer. These genes were associated with OS, which was related to their effect on the infiltration of activated B-cells (60). Therefore, these SLAMF members may be of interest for immunotherapy for ovarian cancer.

Attempting to construct a BRCAness signature for ovarian cancer, Chen et al. found that upregulation of CXCL1 with downregulation of SV2A and upregulation of SLAMF3 with downregulation of CHRNB3 can be constructed as a two-gene pair signature for BRCAness in ovarian cancer that predicts improved OS, PFS, and increased multi-omics alterations in homologous recombination genes. Furthermore, these could predict enhanced sensitivity to immune checkpoint blockade and poly ADP ribose polymerase (PARP) inhibitors, confirming SLAMF3 as an attractive immunotherapeutic target in ovarian cancer (61).

3.12 Head and neck squamous cell carcinoma

$CD8^+$ TIL in HNSCC tumors has been found to express increased levels of SLAMF4, and this expression was correlated with PD-1 expression. Furthermore, SLAMF4 was increased on intratumoral DC and MDSC, and high SLAMF4 correlated with PD-L1 expression and increased expression of immune-suppressive mediators. *In vitro* studies showed that activation of SLAMF4 inhibited the production of pro-inflammatory cytokines by human DCs. $CD244^{-/-}$ mice showed impaired tumor growth of HNSCC, and anti-SLAMF4 treatment also impaired the growth of established HNSCC tumors while it increased $CD8^+$ TIL infiltration, suggesting SLAMF4 plays an inhibitory role in the immune response to HNSCC (62).

We have summarized the described expression and roles of SLAMF members in the TME of solid tumors in Table 2.

4 Conclusion and future directions

Ample evidence suggests that SLAMF receptors are involved in in various solid tumor types is coming to light, suggesting that these receptors might be potential targets for therapy. SLAMF1 has been detected in various cancer types, but its role in prognosis remains to be established. However, the expression of SLAMF1 on immune cells in tumors might benefit the outcome. SLAMF2 and SLAMF4 have mainly been detected on T- and NK cells in tumors and may affect the ability of the immune system to control solid tumors. On the other hand, SLAM-family receptors, particularly SLAMF4, may be inhibitory or activatory in cells with SAP adaptor molecules, depending on the situation (63). Research on SLAMF3 remains limited. In a recent study, it has been reported that SLAMF3 stimulates the differentiation of Th17 cells from CD4+ T cells, leading to an increase in the secretion of IL-17A in a chronic (long-lasting) autoimmune disorder (64). However, in solid tumors, the expression loss on hepatic cancer cells is associated with poor outcomes, and expression on immune cells in ovarian cancer potentially results in better outcomes. SLAMF5 has also had

TABLE 2 Described expression and roles of SLAMF members in the TME of solid tumors.

SLAMF Receptor	Expression in Cancer	Role in Cancer	Tumor Microenvironment	References
SLAMF1 (CD150, SLAM)	• BC (incl. novel CD150) • CNS tumors (incl. novel CD150) • PrC • GyC • CRC	• Expressed in breast cancer cell lines, with high levels on those of the luminal type • Highest expression detected in aggressive prostate cancer cell lines • Drives autophagy and chemotherapy resistance in choriocarcinoma	• Expression on immune cells (T cells, B cells, and innate lymphoid cells) in CRC – associated with survival	(12, 24, 39–41, 56, 57, 59)
SLAMF2 (CD48, BLAST1, BCM1)	• BC • LC • MSC • ccRCC • HCC • GyC	• Upregulated in inflammatory breast cancer, downregulated in breast cancer metastases • Expression in lung cancer cell lines increases susceptibility to NK-cell killing • Expression in mouse melanoma tumors reduces tumor rejection • Upregulated in ccRCC	• Monocytes in HCC express high levels • SLAMF2 expression in NSCLC cells increases susceptibility to NK-cell killing • Lack of SLAMF2 associated with resistance to NK-cell lysis in choriocarcinoma cells	(14, 28, 44, 49, 53, 58)
SLAMF3 (CD229, LY9)	• GyC • HCC	• Loss of SLAMF3 in HCC might be associated with drug resistance	• Expressed on immune infiltrate (B cells) in ovarian cancer	(45, 47, 59, 60)
SLAMF4 (CD244, 2B4)	• HNSCC • NSCLC • ccRCC • PaC • BC • CNS	• Reduced expression in breast cancer associated with worse prognosis • Low levels in blood plasma in glioblastoma are associated with poor outcome • In NSCLC, high blood levels predict worse outcomes • Upregulated in ccRCC	• Expressed on immune cells in NSCLC • Expression on T cells in pancreatic cancer mouse model • Expressed on $CD8^+$ TIL, DCs, and MDSCs in HNSCC	(15, 16, 25, 30, 33, 61)
SLAMF5 (CD84, LY9B)	• BC	• Expression on circulating tumor cells of mesenchymal breast cancer	• Expressed by MDSC in breast cancer – correlated with worse outcomes	(18, 19)
SLAMF6 (CD352, NTBA, LY108)	• BC • PDAC • GC (circular SLAMF6) • RCC • HCC	• Weak association with survival in breast cancer • Potential role in PDAC outcomes • Gastric cancer mouse models: circular SLAMF6 in hypoxia associated with more aggressive subtypes	• Associated with Tregs in RCC – associated with improved outcomes • Increased on $CD14^+$ cells in HCC (M2 TAMs)	(20, 34, 36, 48, 54)
SLAMF7 (CD319, CS1, CRACC)	• BC CRC* • ccRCC • MSC	• Enriched in breast cancer – associated with better prognosis Downregulated in CRC* • Enriched in melanoma – associated with improved outcome • High expression in ccRCC is associated with worse outcome	• Expression in melanoma might be associated with $CD4^+$ T-cell expression • Expressed by TAMs in ccRCC	(21, 22, 42, 55)
SLAMF8 (CD353, BLAME, SBBI42)	• BC • CNS • GC (serum)	• High expression in breast cancer associated with poor therapy response • Overexpression in glioma associated with disease progression, poor survival, and chemoresistance	• Expression in breast cancer associated with TNF and lymphocyte infiltration • Associated with infiltration of myeloid cells, correlated with checkpoint expression in glioma.	(23, 26, 37, 38)

(Continued)

TABLE 2 Continued

SLAMF Receptor	Expression in Cancer	Role in Cancer	Tumor Microenvironment	References
		• Associated with better response to checkpoint inhibitors when expressed in serum gastric cancer	• Expressed by macrophages in gastric cancer	
SLAMF9 (CD2F10, CD84H1)	• MSC		• Expressed on TAMs in melanoma	(52)

BC, breast cancer; ccRCC, clear cell renal cell carcinoma; CNS, central nervous system; CRC, colorectal cancer; DC, dendritic cell; GC, gastric cancer; GyC, gynecological cancer; HCC, hepatocellular carcinoma; HNSCC, head and neck squamous cell carcinoma; LC, lung cancer; MSC, melanoma skin cancer; NK, natural killer; NSCLC, non-small cell lung cancer; MDSC, monocyte-derived suppressor cell; PaC, pancreatic cancer; PDAC, pancreatic ductal adenocarcinoma; PrC, Prostate cancer; RCC, renal cell carcinoma; SLAMF, signaling lymphocytic activation molecule family; TAM, tumor-associated macrophages; TIL, tumor-infiltrating lymphocyte; TNF, tumor necrosis factor.

limited investigation in solid tumors, but its detection on MDSC in breast cancer suggests it might be a therapeutic target of interest. SLAMF6 appears to be associated with outcomes in various cancer types and is expressed by various immune cells, with variable anti-tumor effects.

SLAMF7 has been found enriched in various solid tumor types, which may be associated with $CD4^+$ T-cells and TAMs expression. According to the researchers, the process of differentiation from monocytes to macrophages results in increased expression of SLAMF7. This up-regulation of SLAMF7 promotes the induction of cytokines by certain Toll-like receptor ligands, suggesting that the differentiation of macrophages in solid tumors might involve a pathway through SLAMF7 (65). SLAMF7 has also been shown to be effective in improving survival when combined with lenalidomide and dexamethasone with the monoclonal antibody elotuzumab in patients with multiple myeloma (66). The use of this antibody in the clinic paves the way for research into the effects of this treatment in tumor types overexpressing SLAMF7. However, given that current research shows potentially improved outcomes with high expression, the mechanism of action will be important to explore. SLAMF8 expression in tumors was associated with worse outcomes in breast cancer and glioma, while serum expression in gastric cancer was associated with a good response to immunotherapy. SLAMF9 has not been assessed in great detail in the solid cancer setting, but research showing expression on TAMs in melanoma suggests it might be a target for further research.

In this review, we have specifically discussed increasing evidence of the roles of SLAMF receptors in various solid tumors that may improve patient outcomes. We have also suggested several ways to target SLAMF receptors in solid tumors. Together, these data suggest that SLAMF members play variable roles in solid tumors. While research should be expanded to uncover their roles in prognosis and expression patterns on various cells in the TME, an argument can be made to investigate these molecules for therapeutic purposes. However, targeting SLAMF receptors could also impact the normal immune response and increase the risk of infections due to their complex regulatory functions within the immune system (67). Therefore, it is crucial to take into consideration the potential risks associated with targeting SLAMF receptors and to take appropriate safety measures to minimize the potential toxicities, such as neutropenia, thrombocytopenia, and hepatotoxicity (63).

Author contributions

MG: Data curation, Investigation, Writing – original draft, Writing – review & editing. SR: Supervision, Writing – review & editing. IS: Supervision, Writing – review & editing. EG: Conceptualization, Data curation, Investigation, Writing – original draft, Writing – review & editing, Supervision.

Funding

The author(s) declare financial support was received for the research, authorship, and/or publication of this article. This research was supported by the Judy and Bernard Briskin Family Foundation and the Margaret E. Early Medical Research Trust Grant (AWD-P065058).

Acknowledgments

MG, SR, IS, and EG would like to thank the Judy and Bernard Briskin Family Foundation for their generous support. Writing and editing support was provided by Maartje Wouters, PhD. All figures were created with BioRender.com.

Conflict of interest

The authors declare that the research was conducted in the absence of any commercial or financial relationships that could be construed as a potential conflict of interest.

Publisher's note

References

1. Ribas A, Wolchok JD. Cancer immunotherapy using checkpoint blockade. *Science* (2018) 359:1350–5. doi: 10.1126/science.aar4060

2. Sermer D, Brentjens R. CAR T-cell therapy: Full speed ahead. *Hematol Oncol* (2019) 37 Suppl 1:95–100. doi: 10.1002/hon.2591

3. Sharma P, Hu-Lieskovan S, Wargo JA, Ribas A. Primary, adaptive, and acquired resistance to cancer immunotherapy. *Cell* (2017) 168:707–23. doi: 10.1016/j.cell.2017.01.017

4. Ostrakhovitch EA, Li SS. The role of SLAM family receptors in immune cell signaling. *Biochem Cell Biol* (2006) 84:832–43. doi: 10.1139/o06-191

5. Morra M, Howie D, Grande MS, Sayos J, Wang N, Wu C, et al. Terhorst, C. X-linked lymphoproliferative disease: a progressive immunodeficiency. *Annu Rev Immunol* (2001) 19:657–82. doi: 10.1146/annurev.immunol.19.1.657

6. Dragovich MA, Mor A. The SLAM family receptors: Potential therapeutic targets for inflammatory and autoimmune diseases. *Autoimmun Rev* (2018) 17:674–82. doi: 10.1016/j.autrev.2018.01.018

7. Fouquet G, Marcq I, Debuysscher V, Bayry J, Rabbind Singh A, Bengrine A, et al. Signaling lymphocytic activation molecules Slam and cancers: friends or foes? *Oncotarget* (2018) 9:16248–62. doi: 10.18632/oncotarget.24575

8. Chen J, Zhong MC, Guo H, Davidson D, Mishel S, Lu YH, et al. SLAMF7 is critical for phagocytosis of haematopoietic tumour cells via Mac-1 integrin. *Nature* (2017) 544:493–7. doi: 10.1038/nature22076

9. Shachar I, Barak A, Lewinsky H, Sever L, Radomir L. SLAMF receptors on normal and Malignant B cells. *Clin Immunol* (2019) 204:23–30. doi: 10.1016/j.clim.2018.10.020

10. Llinàs L, Lázaro A, de Salort J, Matesanz-Isabel J, Sintes J, Engel P. Expression profiles of novel cell surface molecules on B-cell subsets and plasma cells as analyzed by flow cytometry. *Immunol Lett* (2011) 134:113–21. doi: 10.1016/j.imlet.2010.10.009

11. Kondou R, Akiyama Y, Iizuka A, Miyata H, Maeda C, Kanematsu A, et al. Identification of tumor microenvironment-associated immunological genes as potent prognostic markers in the cancer genome analysis project HOPE. *Mol Clin Oncol* (2021) 15:232. doi: 10.3892/mco.2021.2395

12. Gordiienko IM, Lykhova OO, Shcherbina VM, Shlapatska LM. SLAMF1/CD150 expression and topology in prostate and breast cancer cell lines. *Exp Oncol* (2021) 43:312–6. doi: 10.32471/exp-oncology.2312-8852.vol-43-no-4.17010

13. Lin W, Lin HD, Guo XY, Lin Y, Su FX, Jia WH, et al. Allelic expression imbalance polymorphisms in susceptibility chromosome regions and the risk and survival of breast cancer. *Mol Carcinog* (2017) 56:300–11. doi: 10.1002/mc.22493

14. Lerebours F, Vacher S, Andrieu C, Espie M, Marty M, Lidereau R, et al. NF-kappa B genes have a major role in inflammatory breast cancer. *BMC Cancer* (2008) 8:41. doi: 10.1186/1471-2407-8-41

15. Fang J, Chen F, Liu D, Gu F, Chen Z, Wang Y. Prognostic value of immune checkpoint molecules in breast cancer. *Biosci Rep* (2020) 40:BSR20201054. doi: 10.1042/BSR20201054

16. Ferrucci V, Asadzadeh F, Collina F, Siciliano R, Boccia A, Marrone L, et al. Prune-1 drives polarization of tumor-associated macrophages (TAMs) within the lung metastatic niche in triple-negative breast cancer. *iScience* (2021) 24:101938. doi: 10.1016/j.isci.2020.101938

17. Francis JC, Melchor L, Campbell J, Kendrick H, Wei W, Armisen-Garrido J, et al. Whole-exome DNA sequence analysis of Brca2- and Trp53-deficient mouse mammary gland tumours. *J Pathol* (2015) 236:186–200. doi: 10.1002/path.4517

18. Alshetaiwi H, Pervolarakis N, McIntyre LL, Ma D, Nguyen Q, Rath JA, et al. Defining the emergence of myeloid-derived suppressor cells in breast cancer using single-cell transcriptomics. *Sci Immunol* (2020) 5:eaay6017. doi: 10.1126/sciimmunol.aay6017

19. Popeda M, Stokowy T, Bednarz-Knoll N, Jurek A, Niemira M, Bielska A, et al. NF-kappa B signaling-related signatures are connected with the mesenchymal phenotype of circulating tumor cells in non-metastatic breast cancer. *Cancers (Basel)* (2019) 11:1961. doi: 10.3390/cancers11121961

20. Huang Y, Chen L, Tang Z, Min Y, Yu W, Yang G, et al. Novel immune and stroma related prognostic marker for invasive breast cancer in tumor microenvironment: A TCGA based study. *Front Endocrinol (Lausanne)* (2021) 12:774244. doi: 10.3389/fendo.2021.774244

21. Assidi M. Strong prognostic value of SLAMF7 protein expression in patients with lymph node-positive breast cancer. *Oncol Lett* (2022) 24:433. doi: 10.3892/ol.2022.13553

22. Cachot A, Bilous M, Liu YC, Li X, Saillard M, Cenerenti M, et al. Tumor-specific cytolytic CD4 T cells mediate immunity against human cancer. *Sci Adv* (2021) 7: eabe3348. doi: 10.1126/sciadv.abe3348

23. Dunbier AK, Ghazoui Z, Anderson H, Salter J, Nerurkar A, Osin P, et al. Molecular profiling of aromatase inhibitor-treated postmenopausal breast tumors identifies immune-related correlates of resistance. *Clin Cancer Res* (2013) 19:2775–86. doi: 10.1158/1078-0432.CCR-12-1000

24. Romanets-Korbut O, Najakshin AM, Yurchenko M, Malysheva TA, Kovalevska L, Shlapatska LM, et al. Expression of CD150 in tumors of the central nervous system: identification of a novel isoform. *PloS One* (2015) 10:e0118302. doi: 10.1371/journal.pone.0118302

25. Holst CB, Christensen IJ, Vitting-Seerup K, Skjoth-Rasmussen J, Hamerlik P, Poulsen HS, et al. Plasma IL-8 and ICOSLG as prognostic biomarkers in glioblastoma. *Neurooncol Adv* (2021) 3:vdab072. doi: 10.1093/noajnl/vdab072

26. Zou CY, Guan GF, Zhu C, Liu TQ, Guo Q, Cheng W, et al. Costimulatory checkpoint SLAMF8 is an independent prognosis factor in glioma. *CNS Neurosci Ther* (2019) 25:333–42. doi: 10.1111/cns.13041

27. Schuhmann MK, Stoll G, Bieber M, Vogtle T, Hofmann S, Klaus V, et al. CD84 links T cell and platelet activity in cerebral Thrombo-inflammation in acute stroke. *Circ Res* (2020) 127:1023–35. doi: 10.1161/CIRCRESAHA.120.316655

28. Park EJ, Jun HW, Na IH, Lee HK, Yun J, Kim HS, et al. CD48-expressing non-small-cell lung cancer cells are susceptible to natural killer cell-mediated cytotoxicity. *Arch Pharm Res* (2022) 45:1–10. doi: 10.1007/s12272-021-01365-z

29. Chen CW, Xue M, Zhang W, Xie J, Coopersmith CM, Ford ML. 2B4 but not PD-1 blockade improves mortality in septic animals with preexisting Malignancy. *JCI Insight* (2019) 4:e127867. doi: 10.1172/jci.insight.127867

30. Vaes RDW, Reynders K, Sprooten J, Nevola KT, Rouschop KMA, Vooijs M, et al. Identification of potential prognostic and predictive immunological biomarkers in patients with stage I and stage III non-small cell lung cancer (NSCLC): A prospective exploratory study. *Cancers (Basel)* (2021) 13:6259. doi: 10.3390/cancers13246259

31. Mittal R, Chen CW, Lyons JD, Margoles LM, Liang Z, Coopersmith CM, et al. Murine lung cancer induces generalized T-cell exhaustion. *J Surg Res* (2015) 195:541–9. doi: 10.1016/j.jss.2015.02.004

32. Zheng N, Fleming J, Hu P, Jiao J, Zhang G, Yang R, et al. CD84 is a Suppressor of T and B Cell Activation during Mycobacterium tuberculosis Pathogenesis. *Microbiol Spectr* (2022) 10:e0155721. doi: 10.1128/spectrum.01557-21

33. Mittal R, Wagener M, Breed ER, Liang Z, Yoseph BP, Burd EM, et al. 3rd; Coopersmith, C.M.; Ford, M.L. Phenotypic T cell exhaustion in a murine model of bacterial infection in the setting of pre-existing Malignancy. *PloS One* (2014) 9:e93523. doi: 10.1371/journal.pone.0093523

34. Feng Z, Qian H, Li K, Lou J, Wu Y, Peng C. Development and validation of a 7-gene prognostic signature to improve survival prediction in pancreatic ductal adenocarcinoma. *Front Mol Biosci* (2021) 8:676291. doi: 10.3389/fmolb.2021.676291

35. Chen CN, Lin JJ, Chen JJ, Lee PH, Yang CY, Kuo ML, et al. Gene expression profile predicts patient survival of gastric cancer after surgical resection. *J Clin Oncol* (2005) 23:7286–95. doi: 10.1200/JCO.2004.00.2253

36. Fang X, Bai Y, Zhang L, Ding S. Silencing circSLAMF6 represses cell glycolysis, migration, and invasion by regulating the miR-204-5p/MYH9 axis in gastric cancer under hypoxia. *Biosci Rep* (2020) 40:BSR20201275. doi: 10.1042/BSR20201275

37. Wu D, Zhang P, Ma J, Xu J, Yang L, Xu W, et al. Serum biomarker panels for the diagnosis of gastric cancer. *Cancer Med* (2019) 8:1576–83. doi: 10.1002/cam4.2055

38. Zhang Q, Cheng L, Qin Y, Kong L, Shi X, Hu J, et al. SLAMF8 expression predicts the efficacy of anti-PD1 immunotherapy in gastrointestinal cancers. *Clin Transl Immunol* (2021) 10:e1347. doi: 10.1002/cti2.1347

39. Mehrle S, Schmidt J, Buchler MW, Watzl C, Marten A. Enhancement of anti-tumor activity *in vitro* and *in vivo* by CD150 and SAP. *Mol Immunol* (2008) 45:796–804. doi: 10.1016/j.molimm.2007.06.361

40. Qi J, Crinier A, Escaliere B, Ye Y, Wang Z, Zhang T, et al. Single-cell transcriptomic landscape reveals tumor specific innate lymphoid cells associated with colorectal cancer progression. *Cell Rep Med* (2021) 2:100353. doi: 10.1016/j.xcrm.2021.100353

41. Qi W, Zhang Q. Identification and validation of immune molecular subtypes and immune landscape based on colon cancer cohort. *Front Med (Lausanne)* (2022) 9:827695. doi: 10.3389/fmed.2022.827695

42. Lee JL, Roh SA, Kim CW, Kwon YH, Ha YJ, Kim SK, et al. Clinical assessment and identification of immuno-oncology markers concerning the 19-gene based risk classifier in stage IV colorectal cancer. *World J Gastroenterol* (2019) 25:1341–54. doi: 10.3748/wjg.v25.i11.1341

43. Li X, Zhou H, Huang W, Wang X, Meng M, Hou Z, et al. Retrospective analysis of the efficacy of adjuvant cytokine-induced killer cell immunotherapy combined with chemotherapy in colorectal cancer patients after surgery. *Clin Transl Immunol* (2022) 11:e1368. doi: 10.1002/cti2.1368

44. Wu Y, Kuang DM, Pan WD, Wan YL, Lao XM, Wang D, et al. Monocyte/macrophage-elicited natural killer cell dysfunction in hepatocellular carcinoma is mediated by CD48/2B4 interactions. *Hepatology* (2013) 57:1107–16. doi: 10.1002/hep.26192

45. Marcq I, Nyga R, Cartier F, Amrathlal RS, Ossart C, Ouled-Haddou H, et al. Identification of SLAMF3 (CD229) as an inhibitor of hepatocellular carcinoma cell proliferation and tumour progression. *PLoS One* (2013) 8:e82918. doi: 10.1371/journal.pone.0082918

46. Bouhlal H, Ouled-Haddou H, Debuysscher V, Singh AR, Ossart C, Reignier A, et al. RB/PLK1-dependent induced pathway by SLAMF3 expression inhibits mitosis

and control hepatocarcinoma cell proliferation. *Oncotarget* (2016) 7:9832–43. doi: 10.18632/oncotarget.6954

47. Fouquet G, Debuysscher V, Ouled-Haddou H, Eugenio MS, Demey B, Singh AR, et al. Hepatocyte SLAMF3 reduced specifically the multidrugs resistance protein MRP-1 and increases HCC cells sensitization to anti-cancer drugs. *Oncotarget* (2016) 7:32493–503. doi: 10.18632/oncotarget.8679

48. Meng Q, Duan X, Yang Q, Xue D, Liu Z, Li Y, et al. SLAMF6/Ly108 promotes the development of hepatocellular carcinoma via facilitating macrophage M2 polarization. *Oncol Lett* (2022) 23:83. doi: 10.3892/ol.2022.13203

49. Vaidya SV, Stepp SE, McNerney ME, Lee JK, Bennett M, Lee KM, et al. Targeted disruption of the 2B4 gene in mice reveals an *in vivo* role of 2B4 (CD244) in the rejection of B16 melanoma cells. *J Immunol* (2005) 174:800–7. doi: 10.4049/jimmunol.174.2.800

50. Eisenberg G, Engelstein R, Geiger-Maor A, Hajaj E, Merims S, Frankenburg S, et al. Soluble SLAMF6 receptor induces strong CD8(+) T-cell effector function and improves anti-melanoma activity *in vivo*. *Cancer Immunol Res* (2018) 6:127–38. doi: 10.1158/2326-6066.CIR-17-0383

51. Yigit B, Wang N, Ten Hacken E, Chen SS, Bhan AK, Suarez-Fueyo A, et al. SLAMF6 as a regulator of exhausted CD8(+) T cells in cancer. *Cancer Immunol Res* (2019) 7:1485–96. doi: 10.1158/2326-6066.CIR-18-0664

52. Hajaj E, Eisenberg G, Klein S, Frankenburg S, Merims S, Ben David I, et al. SLAMF6 deficiency augments tumor killing and skews toward an effector phenotype revealing it as a novel T cell checkpoint. *Elife* (2020) 9:e52539. doi: 10.7554/eLife.52539

53. Dollt C, Michel J, Kloss L, Melchers S, Schledzewski K, Becker K, et al. The novel immunoglobulin super family receptor SLAMF9 identified in TAM of murine and human melanoma influences pro-inflammatory cytokine secretion and migration. *Cell Death Dis* (2018) 9:939. doi: 10.1038/s41419-018-1011-1

54. Tronik-Le Roux D, Sautreuil M, Bentriou M, Verine J, Palma MB, Daouya M, et al. Comprehensive landscape of immune-checkpoints uncovered in clear cell renal cell carcinoma reveals new and emerging therapeutic targets. *Cancer Immunol Immunother* (2020) 69:1237–52. doi: 10.1007/s00262-020-02530-x

55. Chen YH, Chen SH, Hou J, Ke ZB, Wu YP, Lin TT, et al. Identifying hub genes of clear cell renal cell carcinoma associated with the proportion of regulatory T cells by weighted gene co-expression network analysis. *Aging (Albany NY)* (2019) 11:9478–91. doi: 10.18632/aging.102397

56. O'Connell P, Hyslop S, Blake MK, Godbehere S, Amalfitano A, Aldhamen YA. SLAMF7 signaling reprograms T cells toward exhaustion in the tumor microenvironment. *J Immunol* (2021) 206:193–205. doi: 10.4049/jimmunol.2000300

57. Jun F, Peng Z, Zhang Y, Shi D. Quantitative proteomic analysis identifies novel regulators of methotrexate resistance in choriocarcinoma. *Gynecol Oncol* (2020) 157:268–79. doi: 10.1016/j.ygyno.2020.01.013

58. Shi D, Zhang Y, Tian Y. SLAMF1 promotes methotrexate resistance via activating autophagy in choriocarcinoma cells. *Cancer Manag Res* (2020) 12:13427–36. doi: 10.2147/CMAR.S278012

59. Avril T, Iochmann S, Brand D, Bardos P, Watier H, Thibault G. Human choriocarcinoma cell resistance to natural killer lysis due to defective triggering of natural killer cells. *Biol Reprod* (2003) 69:627–33. doi: 10.1095/biolreprod.102.009290

60. Su R, Jin C, Zhou L, Cao Y, Kuang M, Li L, et al. Construction of a ceRNA network of hub genes affecting immune infiltration in ovarian cancer identified by WGCNA. *BMC Cancer* (2021) 21:970. doi: 10.1186/s12885-021-08711-w

61. Chen T, Yu T, Zhuang S, Geng Y, Xue J, Wang J, et al. Upregulation of CXCL1 and LY9 contributes to BRCAness in ovarian cancer and mediates response to PARPi and immune checkpoint blockade. *Br J Cancer* (2022) 127:916–26. doi: 10.1038/s41416-022-01836-0

62. Agresta L, Lehn M, Lampe K, Cantrell R, Hennies C, Szabo S, et al. CD244 represents a new therapeutic target in head and neck squamous cell carcinoma. *J Immunother Cancer* (2020) 8:e000245. doi: 10.1136/jitc-2019-000245

63. Farhangnia P, Ghomi SM, Mollazadehghomi S, Nickho H, Akbarpour M, Delbandi AA. SLAM-family receptors come of age as a potential molecular target in cancer immunotherapy. *Front Immunol* (2023) 14:1174138. doi: 10.3389/fimmu.2023.1174138

64. Hu P, Cai J, Yang C, Xu L, Ma S, Song H, et al. SLAMF3 promotes Th17 differentiation and is reversed by iguratimod through JAK1/STAT3 pathway in primary Sjögren's syndrome. *Int Immunopharmacol* (2024) 126:111282. doi: 10.1016/j.intimp.2023.111282

65. Choe U, Pham Q, Kim YS, Yu L, Wang TTY. Identification and elucidation of cross talk between SLAM Family Member 7 (SLAMF7) and Toll-like receptor (TLR) pathways in monocytes and macrophages. *Sci Rep* (2023) 13:11007. doi: 10.1038/s41598-023-37040-0

66. Dimopoulos MA, Lonial S, White D, Moreau P, Weisel K, San-Miguel J, et al. Elotuzumab, lenalidomide, and dexamethasone in RRMM: final overall survival results from the phase 3 randomized ELOQUENT-2 study. *Blood Cancer J* (2020) 10:91. doi: 10.1038/s41408-020-00357-4

67. Sun L, Gang X, Li Z, Zhao X, Zhou T, Zhang S, et al. Advances in understanding the roles of CD244 (SLAMF4) in immune regulation and associated diseases. *Front Immunol* (2021) 12:648182. doi: 10.3389/fimmu.2021.648182

frontiers | Frontiers in Immunology

TYPE Original Research
PUBLISHED 18 March 2024
DOI 10.3389/fimmu.2024.1295011

OPEN ACCESS

EDITED BY
Xuanbin Wang,
Hubei University of Medicine, China

REVIEWED BY
Liang-min Fu,
The First Affiliated Hospital of Sun Yat-sen University, China
Wenjun Meng,
Sichuan University, China

*CORRESPONDENCE
Suna Zhou
annyzhou0913@163.com
Haihua Yang
yhh93181@163.com

†These authors have contributed equally to this work

RECEIVED 15 September 2023
ACCEPTED 05 March 2024
PUBLISHED 18 March 2024

CITATION
Bi Y, Liu J, Qin S, Ji F, Zhou C, Yang H and Zhou S (2024) CDKL3 shapes immunosuppressive tumor microenvironment and initiates autophagy in esophageal cancer. *Front. Immunol.* 15:1295011. doi: 10.3389/fimmu.2024.1295011

CDKL3 shapes immunosuppressive tumor microenvironment and initiates autophagy in esophageal cancer

Yanping Bi[1†], Jie Liu[2†], Songbing Qin[3], Fuqing Ji[4], Chao Zhou[5], Haihua Yang[5,6*] and Suna Zhou[5,6*]

[1]Department of Radiation Oncology, Xi'an No.3 Hospital, The Affiliated Hospital of Northwest University, Xi'an, Shaanxi, China, [2]Department of Medical Research Center, Xi'an No.3 Hospital, The Affiliated Hospital of Northwest University, Xi'an, Shaanxi, China, [3]Department of Radiation Oncology, The First Affiliated Hospital of Soochow University, Suzhou, Jiangsu, China, [4]Department of Thyroid Breast Surgery, Xi'an No.3 Hospital, The Affiliated Hospital of Northwest University, Xi'an, Shaanxi, China, [5]Department of Radiation Oncology, Taizhou Hospital Affiliated to Wenzhou Medical University, Taizhou, Zhejiang, China, [6]Key Laboratory of Minimally Invasive Techniques & Rapid Rehabilitation of Digestive System Tumor of Zhejiang Province, Taizhou, Zhejiang, China

Background: CDKL3 has been associated with the prognosis of several tumors. However, the potential role of CDKL3 in immunotherapy and the tumor microenvironment (TME) in esophageal carcinoma (ESCA) remains unclear.

Methods: In this study, Cox regression analysis was used to assess the predictive value of CDKL3 for ESCA outcomes. We systematically correlated CDKL3 with immunological features in the TME. The role of CDKL3 in predicting the efficacy of immunotherapy was also analyzed. Correlation analysis, Cox analysis and LASSO Cox regression were used to construct the CDKL3-related autophagy (CrA) risk score model. The relationship between CDKL3 expression and postoperative pathological complete response (pCR) rate in esophageal squamous cell carcinoma (ESCC) patients undergoing neoadjuvant chemoradiotherapy (nCRT) was evaluated using Immunohistochemical staining (IHC). The relationship between CDKL3 expression and autophagy induction was confirmed by immunofluorescence staining and western blot, and the effect of CDKL3 expression on macrophage polarization was verified by flow cytometry.

Results: High expression of CDKL3 was found in ESCA and was associated with poor prognosis in ESCA. Moreover, CDKL3 expression was negatively correlated with tumor-infiltrating immune cells (TIICs), the integrality of the cancer immunity cycles, and anti-tumor signatures, while CDKL3 expression was positively correlated with suppressive TME-related chemokines and receptors, immune hyperprogressive genes, and suppressive immune checkpoint, resulting in immunosuppressive TME formation in ESCA. An analysis of immunotherapy cohorts of the ESCA and pan-cancer showed a better response to immunotherapy in tumor patients with lower CDKL3 levels. The CrA risk score model was constructed and validated to accurately predict the prognosis of ESCA. Notably, the CrA risk score of ESCA patients was significantly positively

correlated with M2 macrophages. Furthermore, knockdown CDKL3 in KYSE150 cells could inhibit autophagy induction and M2 macrophage polarization. And, radiation could downregulate CDKL3 expression and autophagy induction, while ESCC patients with high CDKL3 expression had a significantly lower response rate after nCRT than those with low CDKL3 expression.

Conclusion: CDKL3 may play an important role in anti-tumor immunity by regulating autophagy to promote the formation of immunosuppressive TME, thus playing a critical role in the prognosis of ESCA.

KEYWORDS

esophageal carcinoma, prognosis, tumor microenvironment, autophagy, macrophage polarization

Introduction

Esophageal carcinoma (ESCA) is a common malignancy affecting the gastrointestinal tract, with high incidence and mortality worldwide, of which 85% is esophageal squamous cell carcinoma (ESCC) (1, 2). ESCA typically does not present with early symptoms, resulting in the majority of patients being diagnosed in locally advanced or advanced stages. The primary treatment options for these locally advanced ESCA patients are neoadjuvant or definitive chemoradiotherapy (CRT), chemoradiation, or the combination of CRT and immunotherapy (3). The therapeutic efficacy of immunotherapy has continued to make breakthroughs in recent years, bringing light to the treatment of ESCA patients (4–7). Unlike conventional chemotherapy, immunotherapy can lead to unprecedented and durable remissions in advanced cancer patients. Unfortunately, only a subset of patients respond to immunotherapy, and clinical outcomes in ESCA patients vary widely (8). Therefore, the search for predictive biomarkers of immunotherapy benefits could help to personalize the treatment regimen for each patient and improve their prognosis.

The anti-tumor effects of immunotherapy require not only a tumor microenvironment (TME) with rich infiltration of immune cells but also active T cells by immune checkpoint inhibitors (ICIs) blocking immunosuppression (9, 10). Chemoradiotherapy can not only kill the fast-growing cancer cells, but it can also remodel the TME (11, 12). Autophagy, a mechanism of cellular self-protection and maintenance of homeostasis, removes senescent, damaged, or abnormal proteins and organelles from the cell (13). Aberrant activation of autophagy leads to tumor growth, endurance, and resistance to chemoradiotherapy. Radiotherapy is accompanied by abnormal expression of autophagy related-genes. Resistance to chemotherapy drugs is at least partially mediated by increased autophagy in tumor cells (14, 15). There is emerging evidence that autophagy causes immune dysfunction by acting on the TME. For example, TRAF2 promotes the polarization of M2 macrophages by inhibiting autophagy (16). Hence, exploring the features of the TME, the molecular features of autophagy and the interaction with chemoradiotherapy will help to understand the genesis and development of ESCA and the potential mechanisms of action of immunotherapy.

Members of the cyclin-dependent kinase (CDK) family regulate cell cycle progression and are considered crucial targets for cancer therapy (17). Cyclin-dependent kinase-like (CDKL) proteins contain MAPK TXY phosphorylation motifs, and putative cell cycle protein-binding domains and are characterized by their high sequence similarity to CDK. Cyclin-dependent kinase-like 3 (CDKL3) is both a protein-coding gene and a member of the CDKL family (18). Existing research demonstrates that tumor patients with CDKL3 up-regulation are closely related to inferior survival status (19–22). Our previous study identified CDKL3 as an important oncogene in esophageal squamous cell carcinoma (ESCC) and autophagy-related gene ATG5 was a potential target of CDKL3 in KYSE-150 cell line (19, 22). However, the effect of CDKL3 on TME and its role in autophagy are still unknown. Accordingly, our study aimed to investigate the association of CDKL3 with the TME and autophagy genes in ESCA based on public databases and experimental validation.

Materials and methods

Study design

This study is performed according to the flow chart, which is shown in Figure 1. Firstly, data on ESCA patients were collected from public databases. Then, bioinformatics analysis was performed to explore the relationship between CDKL3 and immune status and the predictive role of CDKL3 in immunotherapy. Subsequently, the CDKL3-related autophagy (CrA) risk score model was developed and validated, and the correlation between the CrA risk score and

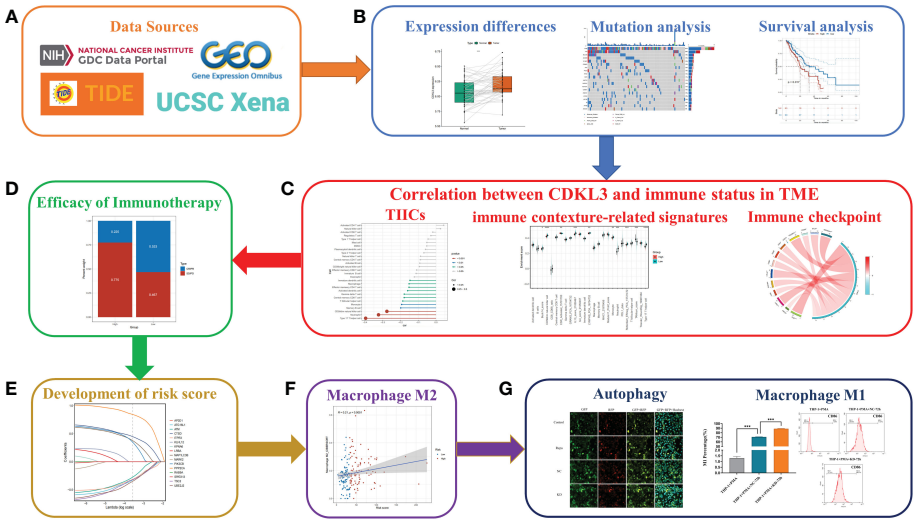

FIGURE 1
Flowchart of the study design. **(A)** Source of data used in this study. **(B)** Differential expression of CDKL3, mutation analysis, and survival analysis. **(C)** Correlation between CDKL3 and immune status in the TME. Immune status includes tumor-infiltrating immune cells (TIICs), immune-associated gene sets, and immune checkpoints. **(D)** The predicted role of CDKL3 in the efficacy of immunotherapy. **(E)** Establishing and validating CrA risk score model. **(F)** The association between the CrA risk score and M2 macrophages. **(G)** The correlation between CDKL3 expression and autophagy induction was verified by immunofluorescence staining, and the effect of CDKL3 expression on M1 macrophage polarization was verified by flow cytometry.

M2 macrophages was found. Finally, through *in vitro* experiments, we confirmed the correlation between CDKL3 expression and autophagy induction and investigated the effect of CDKL3 on macrophage polarization.

Data collection

We downloaded RNA sequencing (RNA-seq) data (transcripts per kilobase million, TPM values), mutation profiles, and clinical data of ESCA from TCGA-GDC interface (https://portal.gdc.cancer.gov/). Log2 was used to transform the RNA-seq data. 198 samples were included in the TCGA-ESCA sequencing data, of which 13 were normal tissues and 185 were tumor tissues. Somatic mutation information of ESCA patients from TCGA was plotted using the maftools R package. Copy number variation (CNV) data were accessed from the UCSC Xena data portal (http://xena.ucsc.edu/). Gene expression matrices for the GSE161533, GSE23400 (GPL97 platform), and GSE47404 cohorts were obtained from the Gene Expression Omnibus (GEO) database. Gene expression matrices and clinical data for cohorts GSE53624, GSE53625, and GSE19417 cohorts were downloaded. Autophagy genes (ATGs) were derived from the Autophagy Database (http://www.tanpaku.org/autophagy/) (Supplementary Table 1).

Download of immunotherapy cohorts

The data for the GSE165252, GSE91061, and GSE176307 cohorts were downloaded from GEO. Visit http://researchpub.gene.com/IMvigor210CoreBiologies/ for more information on the IMvigor210 cohort (23). In addition, the data from the Gide2019 and Nathanson2017 cohorts were obtained from the TIDE (http://tide.dfci.harvard.edu/) database (24). The Supplementary Table 2 presented these detailed data.

Survival analysis

Clinical information (age, gender, stage, pathology, etc.) was collected for ESCA patients in the TCGA cohort. 185 samples were considered eligible after screening for transcriptomic and clinicopathological information. After excluding one duplicate sample and one sample with 0 days of follow-up, Kaplan-Meier analysis was performed on these 183 samples using the survival and survminer R packages. Univariate Cox regression analysis was conducted to screen out risk variables, of which $p<0.2$ were further included in multivariate Cox regression analysis.

Construction of a nomogram

Variables with clinical significance and multivariate Cox regression $p<0.05$ were screened to establish a predictive nomogram. The regplot package was used to plot the nomogram. Calibration curves were calculated with the use of the rms package. Decision curve analysis (DCA) was conducted using the "stdca.R" function. Receiver operating characteristic (ROC) curve analysis was calculated using the timeROC R package (version 0.4) (25).

Immunological characterization of the TME

We have obtained gene set labels including 28 types of immune cells to accurately evaluate the atlas of immune cells infiltrating in the TME. We calculated the enrichment fraction within each immune cell subtype for each individual using the single sample gene set enrichment analysis (ssGSEA) algorithm of the GSVA package. The anticancer immune response also is recognized as a stepwise multiplicity of processes called the cancer immunity cycles. By analyzing the 23 gene sets associated with the seven-step cancer immunity cycles, the researchers were able to explore the tumor immune phenotype (26). We received a total of 92 immune-related signatures from previous work (Supplementary Table 3) (10). The ssGSEA algorithm of the GSVA package was used to calculate the enrichment score (ES) of these immune-related signatures. We collected 23 chemokines and receptors from previous literature associated with the recruitment of myeloid-derived suppressor cells (MDSCs), tumor-associated macrophages (TAMs), and Treg cells (27). Some patients treated with immune checkpoint inhibitors (ICIs) may experience the side effect of cancer hyper-progression. We summarize several predictive genes for hyper-progression (28, 29). In addition, we have identified 22 inhibitory immune checkpoints that have therapeutic potential (30). The researchers used CIBERSORT, TIMER, QUANTISEQ, MCPCOUNTER, XCELL, EPIC, and other algorithms to quantify immune cell infiltration (TIMER 2.0 database, http://timer.cistrome.org/) (31).

Predicting immunotherapy response

The TIDE algorithm, and the IPS score were used to investigate the value of CDKL3 in the prediction of response to immunotherapy. TIDE scores were calculated from the official TIDE website (http://tide.dfci.harvard.edu/). IPS scores were calculated using the IOBR package (version 0.99.9) (32).

Construction and validation of the CrA risk score model

Spearman correlation analysis was used to filter the CDKL3-related ATGs (p-value<0.1). Further, Univariate Cox regression (p-value<0.2) and LASSO Cox regression were used to construct the appropriate signature. Using 'lambda. min' from the R package 'glmnet' to obtain the optimal lambda value. Finally, the model-derived CrA risk score could be calculated the following equation.

$$\text{CrA risk score} = \sum_{i=1}^{9} \beta i * Ei$$

βi is the risk factor and Ei is the expression of each gene. Kaplan-Meier analysis was used to examine the correlation between the CrA risk score and overall survival (OS).

Tissue collection and Immunohistochemical staining (IHC)

Tissue samples were collected from 24 ESCC patients receiving neoadjuvant chemoradiotherapy (nCRT) plus surgery at Taizhou Hospital, Zhejiang Province, between November 2011 and December 2020. The samples from every patient included cancer tissues before neoadjuvant chemoradiotherapy and after surgery. Analysis of postoperative pathological tumors (pT) and postoperative pathological lymph nodes (pN) were based on pathological assessment after surgical treatment. The definition of postoperative pathological complete response (pCR) was negative postoperative pathological tumor and postoperative pathological lymph nodes (pT^-N^-), and postoperative pathological complete response (non-pCR) was defined as pT^+ and/or pN^+. The inclusion criteria were: (1) The pathologic diagnosis of the primary tumor was confirmed as ESCC; (2) Tissue samples were stored in the tissue bank of Taizhou Hospital; (3) Having a completed postoperative report of pathological assessment; (4) Having enough sample to perform immunohistochemical staining (IHC); (5) Patients who completed nCRT and surgery. The exclusion criteria were: (1) Non-ESCC patients; (2) Without a completed postoperative report of pathological assessment;(3) Without enough samples stored in the tissue bank of Taizhou Hospital. The flow of immunohistochemical staining (IHC) was carried out as we described in the previous study (22). Two observers blinded to the purpose of the study independently evaluated the stained sections. The score of CDKL3 expression was evaluated and calculated by independent blinded observers. The patients with scores > 8 were classified as a high CDKL3-expression group, otherwise as a low CDKL3-expression group.

Cell cultures, macrophage induction

The human ESCC cell line KYSE-150 were obtained from the Shanghai Institute of Cell Biology, Chinese Academy of Sciences (Shanghai, China). Cells were maintained in RPMI 1640 with 10% FBS (Sigma, St Louis, USA) 100μg mL-1 streptomycin and 100μg mL-1 penicillin, 37°C, 5% CO2.THP-1 cells (ATCC, Manassas, USA), as human peripheral blood monocytes, were incubated with serum-free RPMI 1640 containing 200 nM PMA (Sigma, St Louis, USA) for 48h to induce M0 macrophage.

Cells co-culture and macrophage polarization analysis

The supernatant harvested from 48h incubation of KD and NC groups of KYSE-150 was co-cultured with M0 macrophage in 24-well transwell plates (Millipore Co., Bedford, MA) for 72h. Macrophages without co-culture were set as the control. After polarization induction, macrophages were harvested and incubated with specific primary anti-bodies against relative surface markers (CD86 as an M1 marker, and CD206 as an M2

marker) on ice for 30 minutes. Then, these stained cells were resuspended in 400 μL of PBS after twice of cold PBS washing. Finally, flow cytometry (BD LSRII system, BD Biosciences, Franklin Lakes, USA) was applied to evaluate the specific surface markers. Simultaneously, macrophages were harvested to extract total RNA using Trizol reagent (Invitrogen, Carlsbad, CA) in accordance with instructions. qRT-PCR (Mx3000Ps, Biosystems Inc., Foster City, CA, USA) was performed after reverse transcription to cDNA (PrimeScript RT reagent Kit, Takara, Shiga, Japan). The PCR reaction condition was as follows: pre-denaturing at 95°C for 15s, then 45 cycles at 95°C for 5s, ended after 60°C for 30s. The internal reference used in this study was GAPDH. The primers of targeted genes were shown as follows: CDKL3: 5′- AAAGTGGGCAAT TTGTCACCT-3′(forward), 5′-TTGGGGTGTTGAACTTGAG GA-3′(reverse); GAPDH: 5′-AGAAGGCTGGGGCTCATTTG-3′ (forward), 5′-AGGGGCCATCCACAGTCTTC-3′ (reverse); IL-12: 5′-CCTTGCACTTCTGAAGA GATTGA-3′(forward), 5′-ACA GGGCCATCATAAAAGAGGT-3′(reverse); TNF-α: 5′-CCTCT CTC TAATCAGCCCTCTG-3′(forward), 5′-GAGGACCTGG GAGTAGATGAG-3′(reverse); IL-10: 5′-GACTTTAAGGGTTAC CTGGGTTG-3′(forward), 5′-TCACATGCGCCTTGATGTCTG-3′ (reverse); TGF-β: 5′-GGCCAGATCCTGTCCAAGC-3′(forward), 5′- GTGGGTTTCCACCATTAGCAC-3′(reverse). Relative gene expression was determined using the $2^{-\Delta\Delta CT}$ method. In other ways, co-culture supernatants were collected and tested for specific cytokines (TNF-α and IL-12 as M1 markers, TGF-β and IL-10 as M2 marker) using ELISA kits (eBioscience, San Diego, USA) according to the manufacturer's protocols.

Confocal imaging of autophagosomes and autolysosomes

Cells were plated in 6-well chambers at 10000 cells/well followed by transfection with tandem fluorescently tagged LC3B (pLVX-Puro-RFP-GFP-hLC3B) lasting 24h. Then, indicated drugs were added to co-incubate with the cells for another 24 h. Subsequently, DAPI or Hochest was used to stain the cell nuclei for 15 min after the fixation with 4% Paraformaldehyde (PFA). Finally, autophagic flux was monitored and scanned by Pannoramic Midi (3DHistech, Budapeste, Hungary).

Gene silencing

For transfection, cells were cultured in 6-well plates containing $5x10^5$ cells. Transient transfection of small interfering RNA (siRNA) was carried out using Lipofectamine 3000 Transfection Reagent (L3000015, Thermo Fisher Scientific, California, USA). siRNAs targeting human CDKL3 were obtained from GenePharma (Shanghai, China) and transfected into cells using Lipofectamine 3000 (Invitrogen, California, USA). The detailed sequences of siRNA were as follows: CDKL3 siRNA1 (KD), 5′-UCAGGAAAGAUGAAAGAAATT-3′, 5′-UUUCUUUCAUC UUUCCUGATT-3′; CDKL3 siRNA2 (KD), 5′-GCUGCAAAUC UCAGUUCAAAU-3′, 5′-UUGAACUGAGAUUUGCAGCCA-3′; CDKL3 siRNA3 (KD), 5′-AGUUCUUCCUCAAGUUCAACA-3′, 5′-UUGAACUUGAGGAAGAACUAC-3′; CDKL3 siRNA4 (KD), 5′-GACUAUCUUCACAGUAAUAAU-3′, 5′-UAUUACUG UGAAGAUAG UCAA-3′; NC siRNA (NC), 5′-UUCU CCGAACGUGUCACGUTT-3′, 5′-ACGUGACACGUUCGGA GAATT-3′.

Western blot assay

Briefly, total proteins were extracted from ESCC cells and protein quantification was performed using the BCA protein assay kit (Beyotime, Shanghai, China). 10% SDS-PAGE was used to separate protein samples, transferred to PVDF membranes, and then the PVDF membranes were blocked with 5% skim milk for 1 hour. The membranes were then incubated overnight with mouse anti-CDKL3 antibody (Sigma-Aldrich, St. Louis, MO, USA) or rabbit anti-LC3B antibody (Cell Signaling Technology, Danvers, MA, USA) at 1:1000 dilution. Mouse anti-GAPDH antibody (Santacruz, Santa Cruz, CA, United States) (1:2000) was incubated overnight at 4°C as a control for the top sample. Finally, an HRP-coupled IgG antibody (Santacruz, Santa Cruz, CA, United States) was used as a secondary antibody. Signal bands were also quantified using ImageJ software.

Ingenuity pathway analysis (IPA)

Our previous study analyzed the profile of differential expressed genes between KYSE-150-NC and KYSE-150-CDKL3-KD cells using GeneChip® PrimeViewTM human gene expression arrays (22). In this study, we used IPA to perform gene enrichment analysis based on the results of CDKL3 expression-related differential gene expression.

Statistical analysis

All statistical data analysis and graphs were performed using R software (version 4.2.1) and GraphPad Prism (version 8.0.2) for analysis. All experiments were replicated at least three times. Differences between the two groups were analyzed using a t-test or Wilcoxon test. Correlations between variables were examined using Spearman's coefficient. Survival curves were plotted using the Kaplan-Meier method, and the log-rank test was used to compare between groups. Two-tailed statistical tests were applied and $p < 0.05$ was used to define as statistically significant ("NS" indicates no significant difference, *p<0.05, **p<0.01, ***p<0.001, and ****p<0.0001).

Results

CDKL3 expression pattern and mutation analysis

Expression data from the TCGA and GEO databases were comprehensively analyzed. In the TCGA database, we found no

10.3389/fimmu.2024.1295011

differences in CDKL3 expression between tumor and normal tissue of ESCA. Compared to the paired normal tissue samples in GEO databases, CDKL3 was highly overexpressed in the tumor tissues of ESCA (GSE161533 and GSE23400, (Supplementary Figure 1A). We obtained ESCA mutation data and divided patients into two groups based on CDKL3 expression. Patients with higher CDKL3 expression typically had a higher TP53 mutation rate (87% vs. 82%) and lower TTN (38% vs. 42%) and MUC16 (18% vs. 26%) mutation rates (Supplementary Figures 1B, C) than that of patients with lower CDKL3 expression.

Elevated CDKL3 expression predicts poor clinical outcomes in ESCA patients

To further determine the clinical significance of CDKL3 in ESCA patients, our study of clinical data from the TCGA-ESCA dataset revealed a significant association between high CDKL3 expression and pathology (squamous cell carcinoma vs. adenocarcinoma), race (Asian vs. White), T (T3 vs. T1) and tumor stage (stage II&III vs. stage I) (Figure 2A). This suggests that CDKL3 expression levels increase with increasing ESCA malignancy. To further understand the significance of CDKL3 in ESCA, we investigated the relationship of its expression with prognosis in ESCA patients. According to the median value of CDKL3 expression, patients were grouped into high- and low-expression cohorts. Log-rank test analysis then indicated that those with high CDKL3 expression had a worse outcome than patients with low CDKL3 expression in the TCGA-ESCA (n=183), GSE53624 (n=119), and GSE53625 (n=179) cohorts, while a similar but non-significant trend was found in the GSE19417 cohort (n=70) (Figure 2B). Univariate analysis showed that patients with high CDKL3 expression (HR:1.695, 95% confidence interval (CI):1.010-2.844, p=0.046) had shorter overall survival (Figure 2C). After adjustment for other confounders (gender and stage), multivariate analysis indicated that CDKL3 remained an

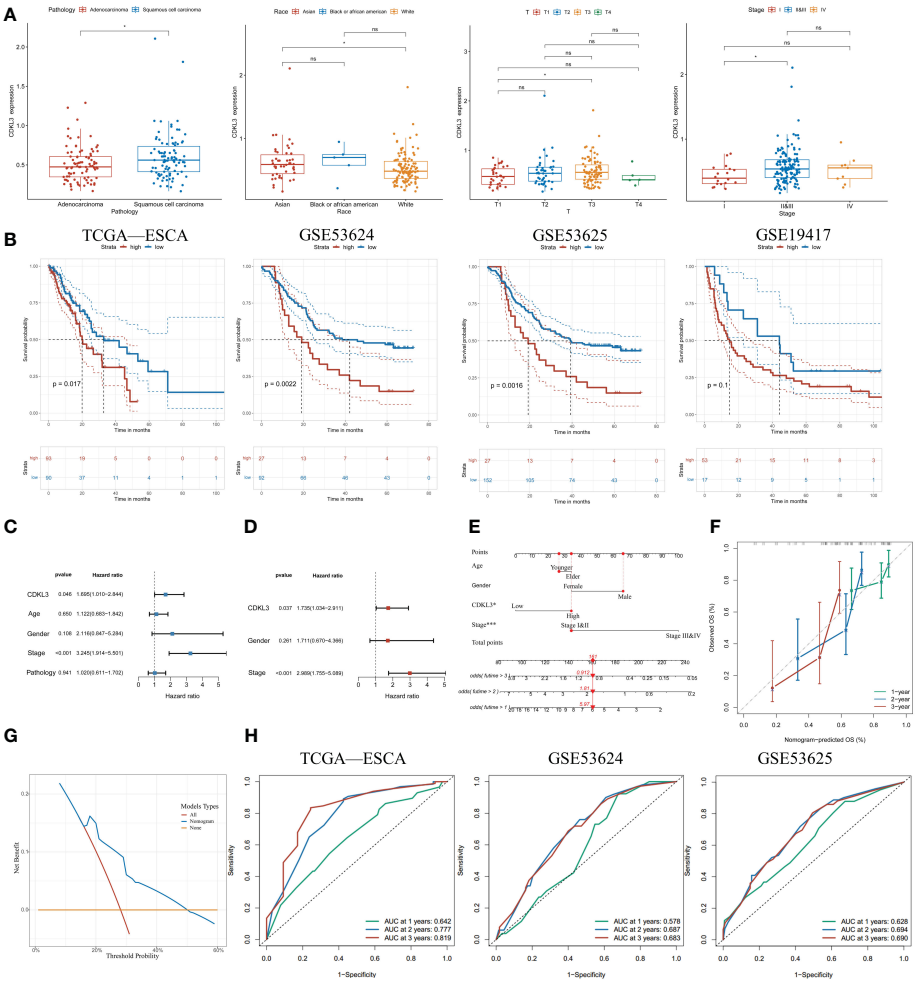

FIGURE 2
Increased expression of CDKL3 indicates poor prognosis. **(A)** The association between CDKL3 and pathology, race, T, and stage. **(B)** Prognosis of high and low CDKL3 expression groups in the TCGA, GSE53624, GSE53625, and GSE19417 cohorts. **(C)** Univariate analysis and **(D)** Multivariate analysis of CDKL3 expression and clinicopathological features in the TCGA cohort. **(E)** Nomogram for predicting the prognosis of ESCA patients. **(F)** Calibration plots indicate the predicted overall survival at 1, 2, and 3 years. **(G)** Decision curve analysis (DCA) of the nomogram. **(H)** Receiver operator characteristic (ROC) analysis of the nomogram in the TCGA, GSE53624, and GSE53625 cohorts. *p<0.05; ns, no significance.

independent prognostic risk factor in ESCA patients (HR:1.735, 95% CI:1.034-2.911, p=0.037) (Figure 2D). A nomogram was created to estimate the outcome of ESCA patients and the variables considered in the nomogram were age, gender, CDKL3, and stage (Figure 2E). The C-index value of the nomogram was 0.675 (95% CI: 0.635-0.715). The calibration curve showed the accuracy of the nomogram in the prediction of survival at 1, 2, and 3 years (Figure 2F). A decision curve analysis (DCA) was performed (Figure 2G), which suggested a good probability of diagnosis between a probability threshold of 20% and 50%. In conclusion, ROC analysis was performed to evaluate the sensitivity and specificity of this nomogram in the prediction of OS at 1, 2, and 3 years. The AUC for 1-, 2-, and 3-year OS were 0.642, 0.777, and 0.819 in the TCGA cohort, respectively. The AUC for 1-, 2-, and 3-year OS were 0.578, 0.687, and 0.683 in the GSE53624 cohort, respectively. The AUC for 1-, 2-, and 3-year OS were 0.628, 0.694, and 0.690 in the GSE53625 cohort, respectively (Figure 2H). These findings suggest that the expression level of CDKL3 can be considered a powerful prognostic predictor in ESCA patients.

Correlation between CDKL3 and immune phenotype

Spearman analysis indicated that CDKL3 expression was significantly and negatively related to the majority of tumor-infiltrating immune cells (TIICs) (Figure 3A). Patients were stratified into high and low CDKL3 expression groups according to median CDKL3 expression. The relative abundance of immunoreactive cells was markedly decreased lower in CDKL3 high-expressed group (Figure 3B). Using the GSE47404 cohort as a validation set, the results were highly consistent with the above findings (Figures 3C, D). In ESCA, CDKL3 expression was closely associated with the remodeling of the TME. In the TCGA cohort, CDKL3 expression was negatively correlated with the activity of step 4 of the cancer immunity cycles, i.e. immune cell trafficking to the tumor (Supplementary Figure 2A), which was further validated in the GSE47404 cohort (Supplementary Figure 2B). This explains why higher CDKL3 expression was associated with lower infiltration of immunoreactive cells.

ES heatmaps were presented for the correlation among CDKL3 and 92 immune-related signatures in the TCGA and GSE47404 cohorts (Supplementary Figures 2C, D). CDKL3 was strongly related to 25 immune-related signatures in the TCGA cohort, most of which were anti-tumor signatures that were negatively associated with CDKL3. Notably, CDKL3 had a significantly positive correlation with the ES of the TAM-related signature (TAMsurr_score). Furthermore, the ES for the anti-tumor signatures was considerably lower in the CDKL3 high expression group with a higher ES for the TAMsurr_score (Figures 3E, F). This finding was further validated in the GSE47404 cohort (Figures 3G, H). In summary, raised CDKL3 expression promoted the tumor immune phenotype to become a 'cold' type. Subsequently, the analysis about the relation between CDKL3 expression and suppressive TME-related chemokines and receptors (Supplementary Table 4) revealed that high CDKL3 expression positively correlated to the expression of chemokines (CXCL2, CXCL3, CCL8) and chemokine receptors (CXCR4, CCR5, CCR8) (Figure 3I).

CDKL3 expression levels predict response to immunotherapy

We explored the correlation of CDKL3 expression with that of 14 suppressive immune checkpoint inhibitors to determine the potential efficacy of CDKL3 in the prediction of response to ICIs in ESCA patients (Figure 3J). The results indicated that CDKL3 had a positive correlation with most of the inhibitory immune checkpoint inhibitors. Therefore, we suggest that CDKL3 may be a candidate biomarker for immunotherapy response prediction. It was discovered that the expression of CDKL3 exhibited a significant positive correlation to most of the hyper-progressive genes (Figure 3K), and CDKL3 may be associated with hyper-progression in immunotherapy. We also assessed the significance of CDKL3 as a predictor of immunotherapy response in ESCA patients using TIDE and IPS scores. Patients with low CDKL3 expression had significantly decreased TIDE scores and increased IPS scores, indicating that low CDKL3 patients have a reduced potentiality for immune escape and may have better efficacy with immune checkpoint inhibition therapy (Figures 4A–C). TIDE prediction showed that patients with lower CDKL3 expression group response to immunotherapy more significantly in the TCGA cohort (low group: 57.0%, 53/93 vs. high group: 42.4%, 39/92) (Figure 4D). Similarly, TIDE predicted that the low CDKL3 group in the GSE53625 cohort was more likely to respond to immunotherapy (low group: 53.3%, 48/90 vs. high group: 22.5%, 20/89) (Figure 4E). Based on GSE165252 (an immunotherapy cohort for ESCA), the group with CDKL3 low expression showed more superior response to the immunotherapy (low group: 40%, 6/15 vs. high group: 21.4%, 3/14) (Figure 4F). Thus, CDKL3 gene expression levels may help predict response to immunotherapy in ESCA patients. As there are fewer immunotherapy cohorts for ESCA, we investigated the role of CDKL3 in predicting the response to immunotherapy in other cancers. We discovered that the prognosis, including OS and progression-free survival (PFS), was worse for the high CDKL3 group in the metastatic urothelial cancer and melanoma cohorts ($p < 0.05$) (Figures 4G–I, M–O). Moreover, a trend toward a worse PFS was found in the high CDKL3 group of GSE176307 and Gide2019 PD-1 cohorts, while a trend toward a worse OS in the high CDKL3 group of Gide2019 PD-1+CTLA4 cohorts, yet the p-value was not statistically different (Supplementary Figures 3A–C). We also found that immunotherapy response rates were considerably lower among the high CDKL3 group than among the low CDKL3 group (Figures 4J–L, P–R). These results confirm that CDKL3 expression is a powerful indicator in pan-cancer immunotherapy cohorts.

Establishment and validation of CrA-risk score model

Utilizing 1183 ATGs downloaded from the autophagy database, we constructed and validated a CrA risk score model (Figure 5A). Correlation analysis and univariate COX regression analysis

10.3389/fimmu.2024.1295011

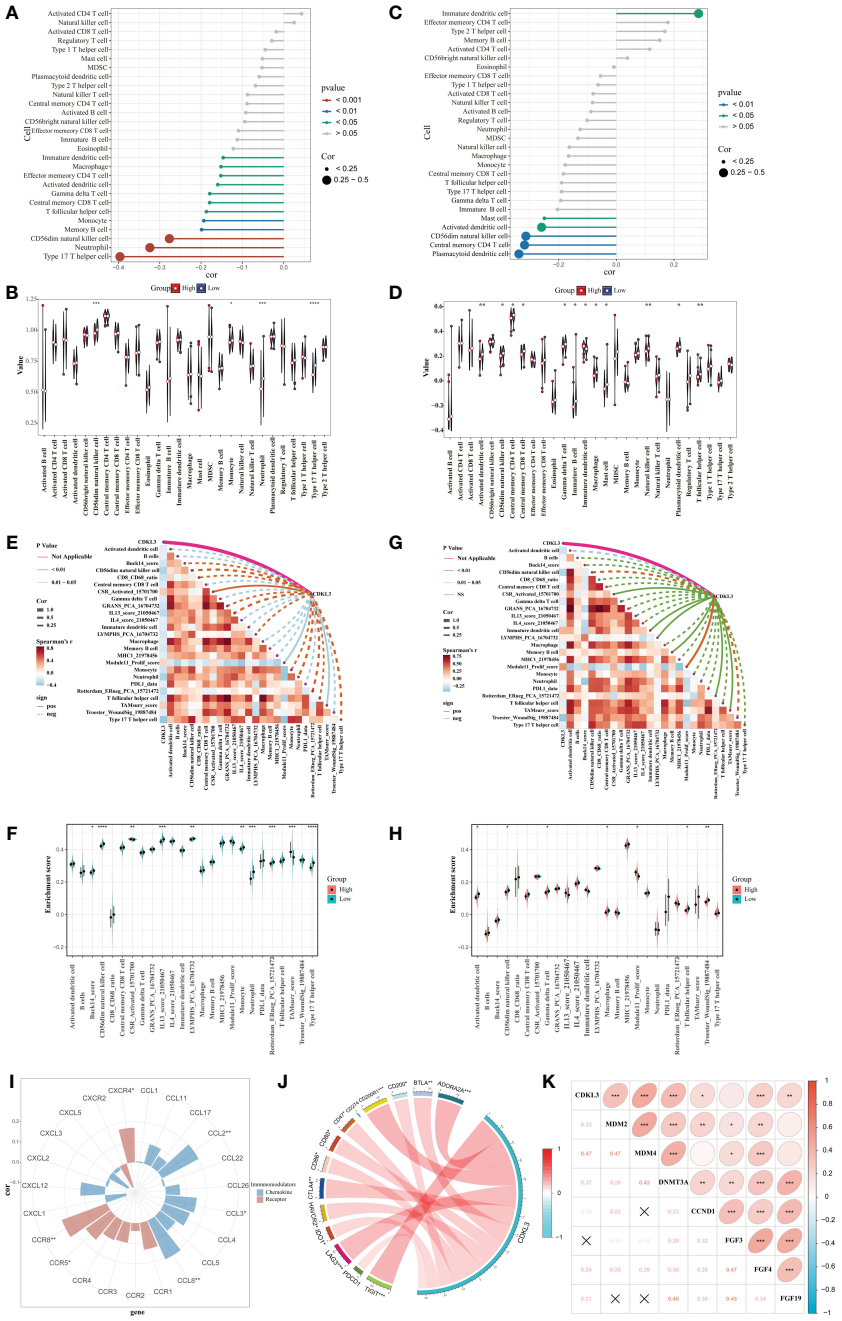

FIGURE 3
Correlation between CDKL3 and immunological characteristics in the TME. **(A)** Correlation of CDKL3 with infiltration levels of TIICs in the TCGA cohort. **(B)** Violin plots of infiltrating degrees of TIICs in the TCGA cohort. **(C)** Correlation of CDKL3 with infiltration levels of TIICs in the GSE47404 cohort. **(D)** Violin plots of infiltration levels of TIICs in the GSE47404 cohort. **(E)** Correlation of CDKL3 with 25 immune-related signatures in the TCGA cohort. **(F)** Violin plots of enrichment scores of immune-related signatures in the TCGA cohort. **(G)** Correlation of CDKL3 with 25 immune-related signatures in the GSE47404 cohort. **(H)** Violin plots of enrichment scores of immune-related signatures in the GSE47404 cohort. **(I)** Correlation of CDKL3 with chemokines and chemokine receptors. **(J)** Correlation of CDKL3 with inhibitory immune checkpoints. **(K)** Correlation of CDKL3 with hyperprogressive genes for immunotherapy. *p<0.05; **p<0.01; ***p<0.001; ****p<0.0001.

identified 16 genes at the output intersection of the TCGA and GSE19417 cohorts (MAP1LC3B, TSC2, PPP2CA, UBE2J2, ATM, PIK3CB, KPNA6, KLHL12, CTSD, SPATA13, RAB9A. MARK2, ITPR3, LRBA, AP3D1, ATG16L1). Univariate Cox regression revealed 16 predictive ATGs in the TCGA and GSE19417 cohorts (Figures 5B, C). The ESCA patients from the TCGA cohort were grouped into a training set (n = 129) and a validation set (n = 54) according to 7:3. Subsequently, a CrA risk score model for ESCA patients was developed via LASSO cox regression. Finally, 9 of the 16 ATGs were considered to be the best candidate genes (Figures 5D, E). The model of the CrA risk score was shown as the following.

CrA risk score = (0.380889116*MAP1LC3B exp) + (-0.32148 4102*TSC2 exp) + (0.846337455*PPP2CA exp) + (-0.3515841

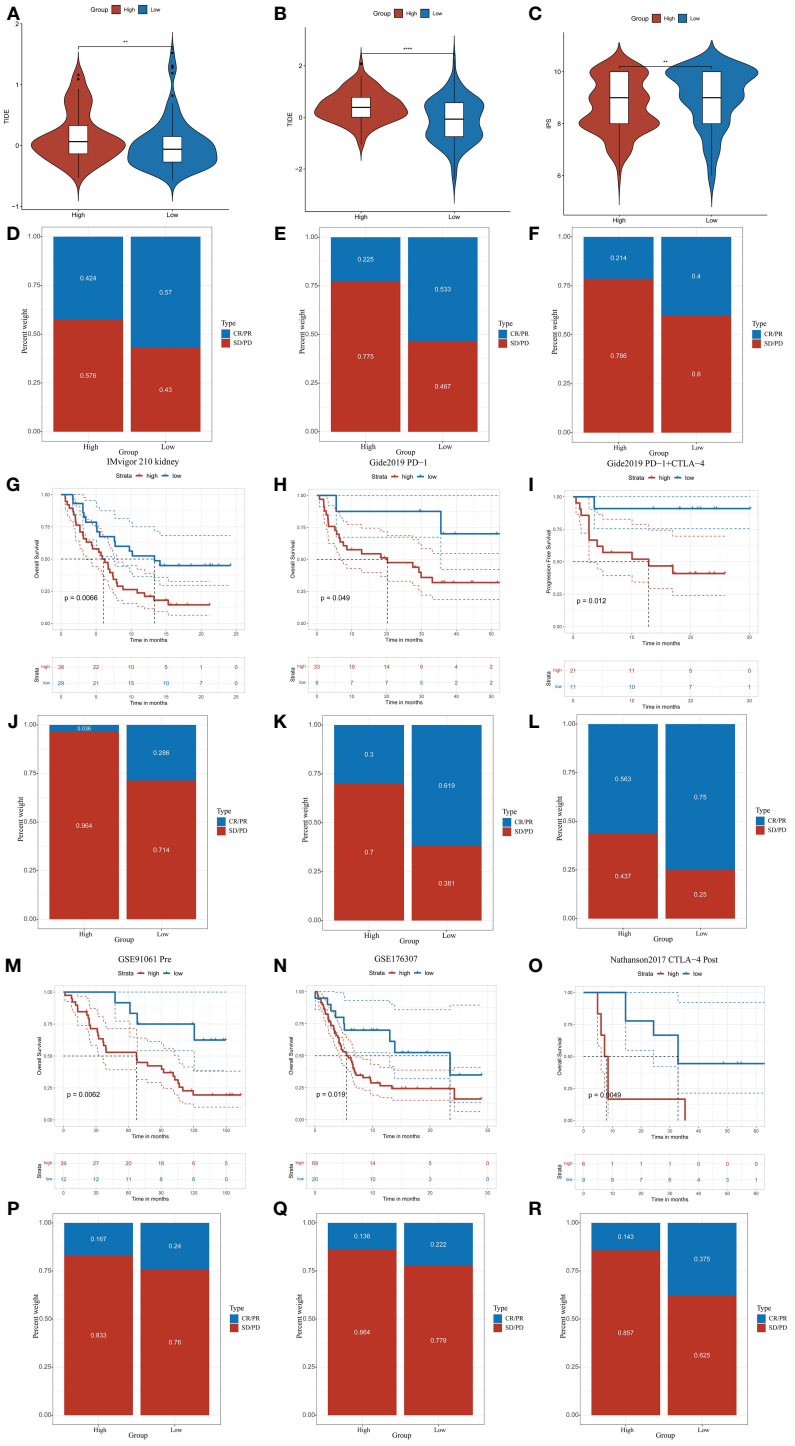

FIGURE 4
CDKL3 predicts response to immunotherapy. **(A, B)** TIDE scores in the TCGA and GSE53625 cohorts. **(C)** IPS scores in the TCGA cohort. **(D, E)** TIDE predicted immunotherapy response rates in the TCGA and GSE53625 cohorts. **(F)** Immunotherapy response rates based on GSE165252 (an immunotherapy cohort for ESCA). **(G–I, M–O)** Survival analysis of CDKL3 in the pan-cancer immunotherapy cohorts. **(J–L, P–R)** The proportion of pan-cancer immunotherapy responders in the high and low CDKL3 groups. **p<0.01; ****p<0.0001.

02*UBE2J2 exp) + (-0.277601266*ATM exp) + (0.354855247*PIK3CB exp) + (0.450974523*CTSD exp) + (-0.315185584*ITPR3 exp) + (-0.327763971*ATG16L1 exp).

Genes involved in the signature included MAP1LC3B, TSC2, PPP2CA, UBE2J2, ATM, PIK3CB, CTSD, ITPR3, ATG16L1. The distribution of the above genes and CDKL3 on their respective chromosomes in ESCA was depicted in Supplementary Figure 4A. CNV alterations were prevalent in these genes. ATG16L1 showed the highest loss frequency, whereas PIK3CB showed the highest gain frequency (Supplementary Figure 4B). The correlation and

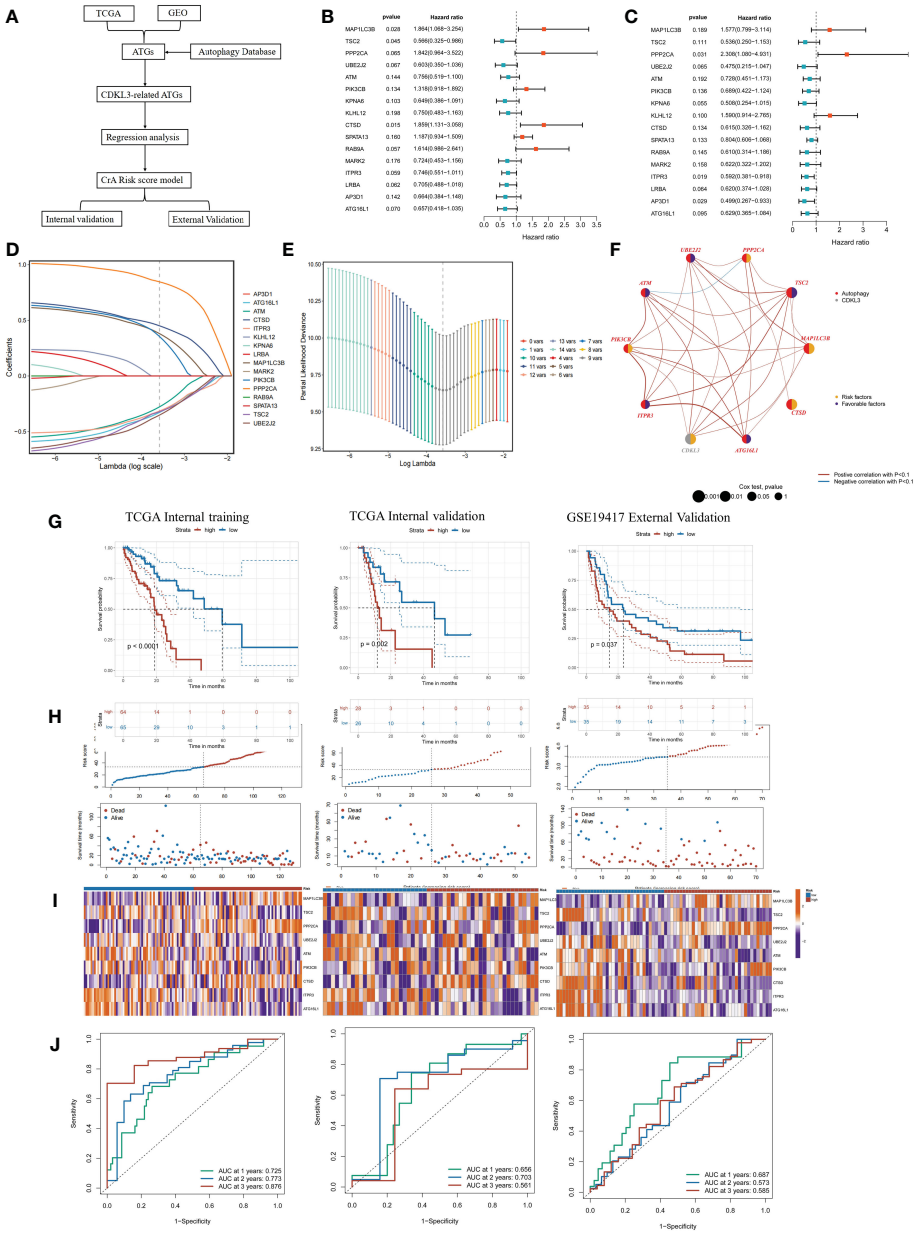

FIGURE 5
Construction and validation of the CrA risk score model. **(A)** Flowchart of the CrA risk score model. **(B)** Univariate analysis of 16 ATGs genes in the TCGA cohort. **(C)** Univariate analysis of 16 ATGs genes in the GSE19417 cohort. **(D)** Choosing the 9 model genes by LASSO Cox regression. **(E)** Cross-validation of the constructed signature. **(F)** Correlation and prognostic value of CDKL3 and model genes in TCGA. **(G)** Kaplan-Meier curves in TCGA internal training, TCGA internal validation and GSE19417 external validation cohorts. **(H)** Distribution of the CrA risk score adjusted for survival status and time in the TCGA internal training, TCGA internal validation and GSE19417 external validation cohorts. **(I)** Model gene expression heatmap from TCGA internal training, TCGA internal validation and GSE19417 external validation cohorts. **(J)** Receiver operator characteristic (ROC) analysis of the CrA risk score in the TCGA internal training, TCGA internal validation and GSE19417 external validation cohorts.

prognostic impact of these genes in TCGA-ESCA were investigated (Figure 5F). Patients in the TCGA-ESCA internal training set (n=129), the TCGA-ESCA internal validation set (n=54) and the GSE19417 external validation set (n=70) were separated into high- and low-risk groups according to the median value of CrA-risk score model. Those belonging to the high-risk group of both the training and validation cohorts experienced shorter OS than those in the low-risk group (Figures 5G–I). In the TCGA-ESCA internal training set, ROC curves indicated that AUC values for 1-year, 2-year, and 3-year time points were 0.725, 0.773, and 0.876, respectively. The TCGA-ESCA internal validation and the GSE19417 external validation set also confirmed that the CrA risk score was highly reliable in predicting ESCA patients (Figure 5J). According to the Sankey plots, patients belonging to the high CDKL3 group were associated with the high-risk group and showed a tendency to have a poorer prognosis (Supplementary Figure 4C).

Relationship between CrA risk score and immune infiltrating cells

The association between the CrA risk score and the level of TIICs was explored to further investigate the relevance of autophagy to the immune system in ESCA. Notably, the CrA risk score of ESCA patients had a positive correlation with M2 macrophage infiltration in three algorithms (Figures 6A–C). Moreover, there was a positive association between the CrA risk score and the level of multiple infiltrating immunosuppressive cells, which promote tumor progression, while negative with levels of anti-tumor immune cells (Figure 6D). The CIBERSORT algorithm showed that lower infiltration of immune-activating cells and higher infiltration of M2 macrophages were found in the high-risk group (Figure 6E). In other words, patients in the high-risk group had enhanced immunosuppression, which accounted for their worse prognosis.

The relationship among CDKL3 expression, radiotherapy, and autophagy predicts in ESCC patients

The results of the western blot demonstrated that radiotherapy caused a significant dose-dependent reduction in the expression levels of both CDKL3 and the autophagy marker LC3B (Figure 7E). To study the role of CDKL3 in autophagy and macrophage polarization, KYSE-150 cells were transfected with CDKL3-siRNAs. KYSE-150 transfected with CDKL3-siRNA1 showed distinctly reduced CDKL3 expression, and KYSE-150-CDKL3-siRNA1 (defined as KD group) was used for further study (Figure 7F). Analysis of 24 samples from ESCC patients receiving nCRT found that low pre-treatment CDKL3 expression was positively related to pCR (pT-N-) (Figure 7A), pT- (Figure 7B), and pN- (Figure 7C) ($p<0.01$). The typical staining of CDKL3 in ESCC patients with pCR or non-pCR was significantly different. That is, ESCC subjects with higher CDKL3 levels had a poorer response to nCRT than ESCC subjects with lower CDKL3 levels (Figure 7D).

CDKL3 expression affects autophagy induction in ESCC

The addition of the autophagy inducer Rapa significantly increased autophagosomes, autophagic flow toward autophagic lysosomes and relative dots count red/green compared to CON ($p<0.05$). Relative dots count red/green decreased in KD vs. NC group ($p<0.05$), but the difference in values was within 20%, suggesting that CDKL3 knockdown alone may not have a significant effect on the flow of autophagosomes to autophagic lysosomes in KYSE150 cells (Figure 8A). The red/green count per cell was increased by the addition of the autophagy inducer Rapa in comparison to the CON group ($p<0.05$), indicating autophagic flow to autophagosomes. Compared to the NC+Rapa group, the KD +Rapa group had less red/green ($p<0.05$), significantly more autophagosomes (yellow dots) and significantly fewer autophagolysosomes (free red dots), suggesting that CDKL3 knockdown can significantly inhibit the flow of autophagosomes to autophagolysosomes in the autophagy-induced activated state of KYSE150 cells, i.e. inhibit autophagy induction (Figure 8B). The addition of the autophagy inducer Rapa significantly increased the autophagy marker LC3B compared to CON ($p<0.05$). Compared to the NC group, LC3B tended to decrease in the KD group, but was not statistically different. This suggests that CDKL3 knockdown alone may not have a significant effect on autophagy induction in

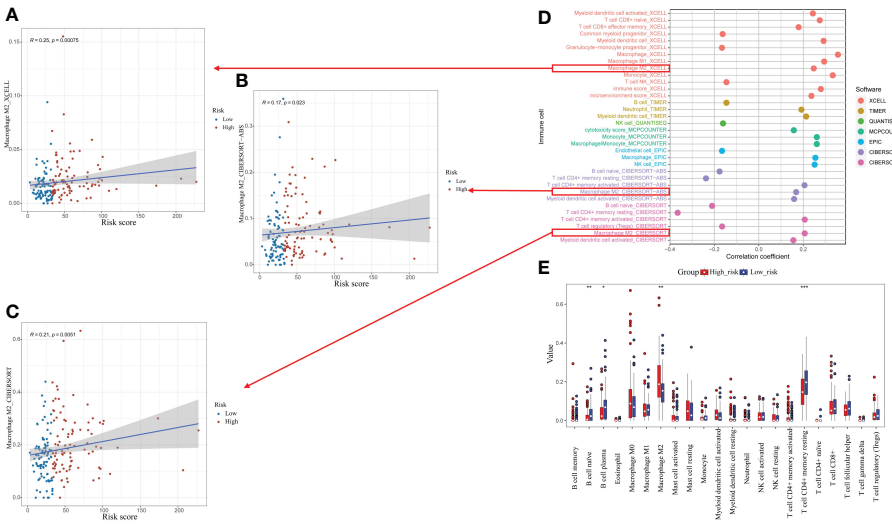

FIGURE 6
Relationship between the CrA risk score and tumor-infiltrating immune cells (TIICs). **(A–C)** Correlation between the CrA risk score and M2 macrophages based on XCELL, CIBERSORT-ABS and CIBERSORT algorithms. **(D)** Correlation between the CrA risk score and infiltrated TIICs. **(E)** The differences in TIICs levels between high- and low-risk groups. *p<0.05; **p<0.01; ***p<0.001.

10.3389/fimmu.2024.1295011

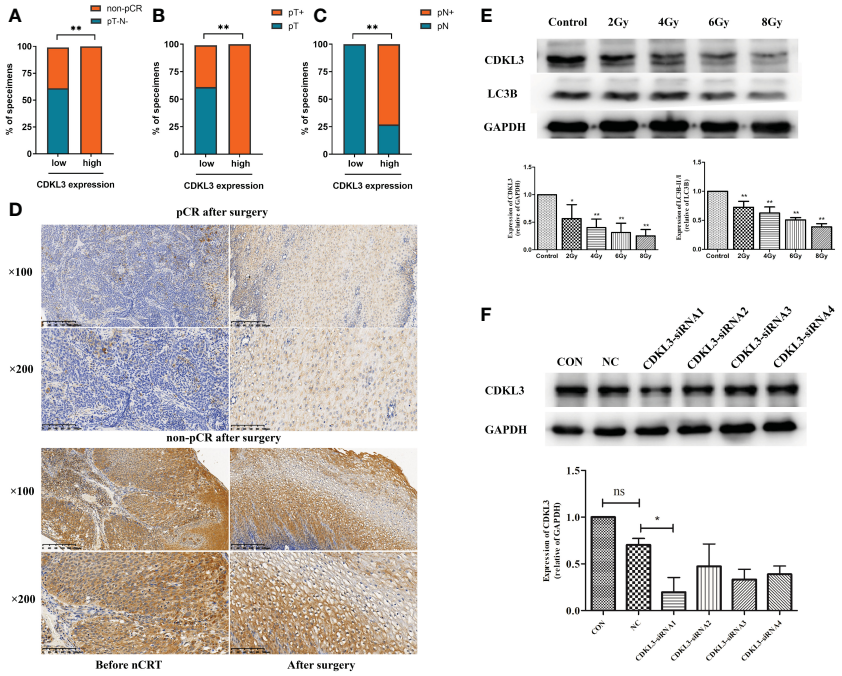

FIGURE 7
Relationship among CDKL3 expression, radiotherapy, and autophagy predicts in ESCC patients. **(A–C)** Correlation between high and low expression of CDKL3 and pathological complete response (pCR), pathological lymph node (pN), and pathological tumor (pT). **(D)** Representative immunohistochemical images of CDKL3 staining before and after nCRT in ESCC patients with pCR or non-pCR after surgery. The scale bars correspond to 200 μm (magnification ×100) and 100 μm (magnification ×200). **(E)** Expression levels of CDKL3 and LC3B in KYSE-150 cells after 0, 2, 4, 6, and 8 Gy radiotherapy were evaluated by western blot. **(F)** The expression of CDKL3 was detected in the CON group, NC group, CDKL3-siRNA1 group, CDKL3-siRNA2 group, CDKL3-siRNA3 group, and CDKL3-siRNA4 group by western blot. *p<0.05; **p<0.01; ns, no significance.

KYSE150 cells (Figure 8C). LC3B was significantly higher in the CON+Rapa group than in the CON group. LC3B levels were also significantly lower in the KD+Rapa group than in the NC+Rapa group. It is suggested that CDKL3 knockdown can significantly inhibit autophagy induction in KYSE150 cells in the activated state of autophagy induction (Figure 8D). The above results suggested that downregulation of CDKL3 could inhibit autophagy activation.

CDKL3 downregulation in ESCC promotes M1-type macrophage polarization

THP-1 cells were induced into macrophages by PMA and then co-cultured with cultures of harvested KYSE-150-siCDKL3 cells for 72 h. Macrophage polarization (M1: CD86; M2: CD206) was detected by flow cytometry (Figures 9A, B) as well as qRT-PCR (Figure 9C), ELISA assay (Figure 9D) for cytokine secretion (M1: IL-12, TNF-α; M2: IL-10, TGF-β). The findings clearly indicated downregulation of CDKL3 expression in ESCC greatly promoted M1-type polarization and cytokine secretion in macrophages.

Activation of autophagy in ESCC inhibits M1-type polarization of macrophage

KYSE-150 cells were induced with Rapa, an autophagy inducer, for 12 hours and then substituted with Rapa-free medium for another 12 hours. The cell supernatant was obtained and co-cultured with M0 macrophages for 72hours, and then RNA was extracted to detect macrophage polarization markers (M1: CD86) and cytokine secretion (M1 type: IL-12, TNF-α) by qRT-PCR. The results showed that ESCC cell supernatant after autophagy activation could inhibit macrophage M1-type polarization and cytokine secretion (Figure 9E).

Downregulation of CDKL3 expression in ESCC activates the Interferon (IFN) pathway

IPA bioinformatics pathway analysis of KYSE-150-NC versus KYSE-150-CDKL3-KD cells revealed that the Interferon (IFN) pathway was significantly activated (Figure 9F). Therefore, we hypothesized that the high expression of CDKL3 in ESCC may attenuate anti-tumor immunity by inhibiting the IFN pathway.

Discussion

We have previously published results showing that CDKL3 is highly overexpressed in ESCC and has a worse prognostic value (19, 22). Based on the public database of ESCA (mainly adenocarcinoma), the results of this study also showed that CDKL3 was highly expressed and associated with shorter survival.

10.3389/fimmu.2024.1295011

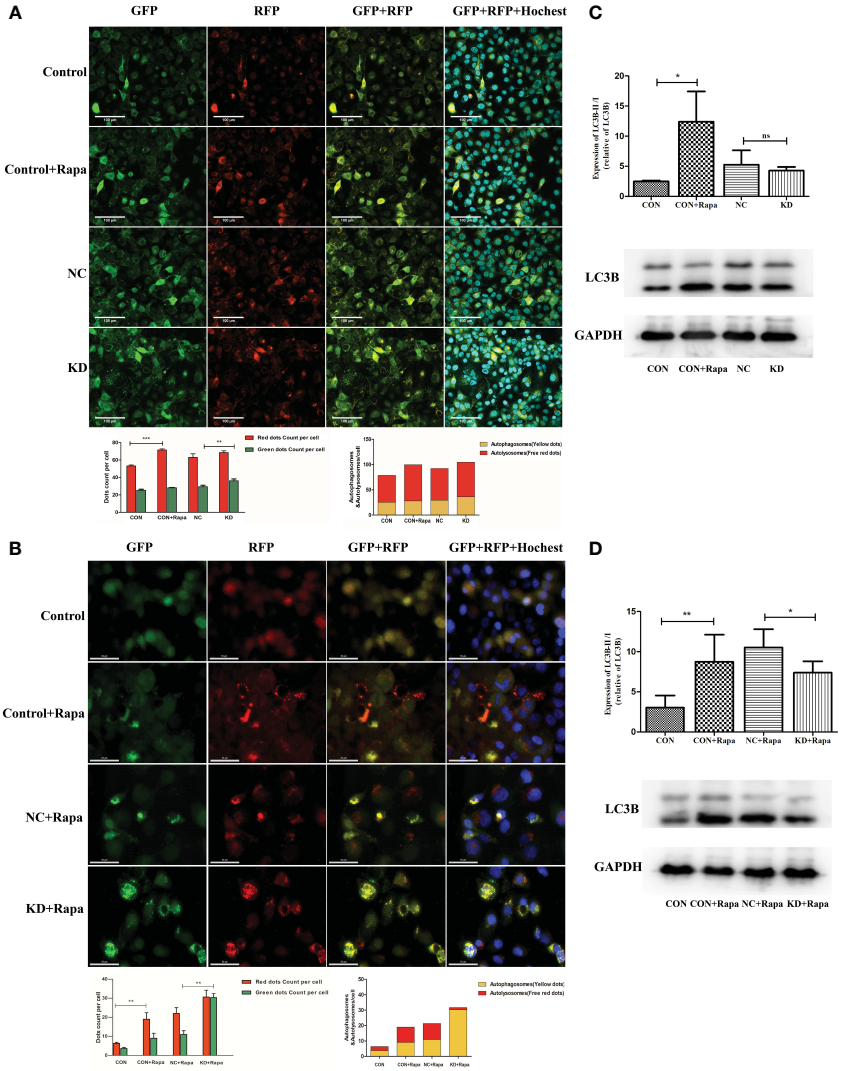

FIGURE 8
Effect of CDKL3 expression on autophagy in ESCC. **(A)** Expression of GFP, RFP, GFP+RFP, and GFP+RFP+Highest was detected by immunofluorescence. Representative co-staining images of the control group, Rapa group, NC group, and KD group. The scale bars correspond to 100 μm. **(B)** Expression of GFP, RFP, GFP+RFP, and GFP+RFP+DAPI was detected by immunofluorescence. Representative co-staining images of the control group, Rapa group, NC+Rapa group, and KD+Rapa group. The scale bars correspond to 50 μm. **(C)** The expression of LC3B in the CON group, CON+Rapa group, NC group, and KD group was assessed by western blot. **(D)** Expression of LC3B in the CON group, CON+Rapa group, NC +Rapa group, and KD+Rapa group was assessed by western blot. *p<0.05; **p<0.01; ***p<0.001; ns, no significance.

Recent studies suggested that upregulated CDKL3 expression is critical for promoting tumor development and poor prognosis in various solid tumors, including glioma and prostate cancer (20, 21). For example, Cui et al. found that overexpression of CDKL3 in glioma cells promotes cell proliferation and that RRM2 is a potential target of CDKL3. Upregulation of CDKL3 expression in glioma tissue independently predicts poor patient prognosis (20). Jiang et al. found that reducing CDKL3 levels substantially hindered cell proliferation and migration while promoting apoptosis and G2 cell cycle blockade in prostate cancer (21). Mutation analysis identified that those with high CDKL3 expression had more TP53 mutations and fewer TTN and MUC16 mutations. TP53 is linked to a poorer outcome in ESCA. Patients with TTN, MUC16 mutations have a higher tumor mutation load and may benefit from immunotherapy (33–35). As a result, patients with a high level of CDKL3 expression may benefit less from immunotherapy and result in a worse prognosis.

It is necessary to explore the reasons why CDKL3 represents a poor prognostic factor in ESCA. Building on previous research, our study provided the first look at the relationship between CDKL3 and the TME, autophagy, and response to immunotherapy in ESCA. We hypothesized that CDKL3 may alter tumor immunogenicity and immune infiltrating cells within the TME by influencing autophagy induction, thereby affecting immunotherapy patient response and prognosis in ESCA.

The TME comprises a multitude of distinct immune cell populations. TIICs may play a crucial effect on carcinogenesis and influenced tumor response to immunotherapy (36). The concept of the cancer immunity cycles was introduced by Chen and Mellman (37). The eventual killing of tumor cells by anti-tumor

10.3389/fimmu.2024.1295011

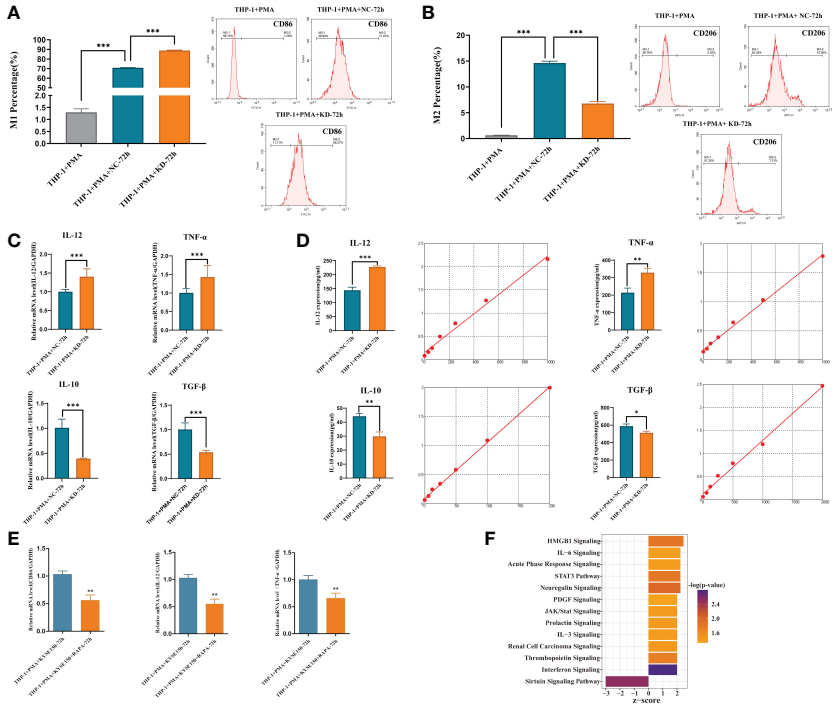

FIGURE 9
Effect of CDKL3 expression and autophagy activation on macrophage polarization. **(A)** The differences of M1 macrophages in the THP-1+PMA group, THP-1+PMA+NC-72h group, and THP-1+PMA+KD-72h group were evaluated by flow cytometry. **(B)** The differences of M2 macrophages in the THP-1+PMA group, THP-1+PMA+NC-72h group, and THP-1+PMA+KD-72h group were analyzed by flow cytometry. **(C, D)** Cytokine secretion (type M1: IL-12, TNF-α; type M2: IL-10, TGF-β) in THP-1+PMA+ NC-72h group and THP-1+PMA+KD-72h group were detected by qRT-PCR and ELISA, respectively. **(E)** Macrophage polarization markers (M1: CD86) and cytokine secretion (M1: IL-12, TNF-α) in THP-1+PMA+ KYSE150-72h group and THP-1+PMA+ KYSE150+RAPA-72h group were detected by qRT-PCR. **(F)** Downregulation of CDKL3 activates the Interferon (IFN) pathway, according to Ingenuity Pathway Analysis (IPA). The vertical coordinate is the pathway name and the horizontal coordinate is z-score (|z-score| ≥ 2 and -log(p-value) > 1.3). *p<0.05; **p<0.01; ***p<0.001.

immune cells is the result of a series of seven steps accompanied by positive and negative regulation. Step 4 is the phase that activating T cells transfers into the circulation and migrates to the tumor, which is related to the infiltration level of TIICs (37). In this study, we observed that higher CDKL3 expression was related to reduced infiltration of a variety of immunoreactive cells. In the cancer immunity cycles, CDKL3 expression showed a negative correlation with the activity of step 4, and we speculated that CDKL3 may reduce the infiltration level of TIICs by inhibiting step 4. TAMs primarily promote the malignant transformation of tumors through the release of various factors. Recent studies have shown that TAM-derived CCL22 can activate the FAK signaling axis in tumor cells, thereby promoting ESCC progression (38). In our study, CDKL3 was significantly and positively associated with the TAM related signature (TAMsurr_score). Recruitment of different types of immune cell subpopulations in the TME is associated with chemokines and chemokine receptors. We collected chemokines and receptors associated with suppressive TME from previous study (27). These chemokines and receptors were associated with the recruitment of MDSCs (CXCL2, CXCL3), TAMs (CXCR4), Treg cells (CCR5), Treg cells (CCL8, CCR8). This suggested that CDKL3 may reshape the TME by regulating these chemokines and chemokine receptors, leading to the infiltration of immunosuppressive cells, ultimately affecting the response to immunotherapy and the promotion of tumor progression.

Research in tumor immunotherapy has progressed significantly in the last few years, and the application of ICIs has become a unique therapeutic approach for a variety of malignancies, including ESCA (4–7). It is crucial to find predictive markers for immunotherapy in ESCA. A recent meta-analysis included 5,257 patients with advanced ESCA who were treated with ICIs. The benefit of ICIs in the reduction of the risk of death in patients with ESCA was dependent on the PD-L1 CPS status. Further studies of immunotherapy biomarkers in the CPS <10 subgroup are needed (8). Our study also investigated CDKL3 as a candidate biomarker to predict response to immunotherapy. The findings indicated that CDKL3 showed a positive correlation with most of the inhibitory ICIs. However, no statistically significant correlation was found between CDKL3 and CD274 (PD-L1). The up-regulated inhibitory immune checkpoint of TME is associated with decreased anti-tumor immunity (30). This explains the poorer prognosis of ICIs in those with higher CDKL3 expression. The TIDE and IPS scores were used to assess how ESCA patients responded to immunotherapy. Poor response to immunotherapy in patients with high CDKL3 expression was also demonstrated in pan-cancer immunotherapy cohorts.

Both radical chemoradiotherapy and neoadjuvant chemoradiotherapy are the main anti-tumor treatment modalities for patients with locally advanced ESCA (39–41). There is emerging evidence that chemoradiotherapy may remodel the TME and thus interfere with the efficacy of immunotherapy (11, 12). Patients with ESCA who have a high rate of pCR after surgery have a favorable prognosis (39, 40). Considering that neoadjuvant immunotherapy combined with chemotherapy (or chemoradiotherapy) has only been used in a small number of clinical trials (42, 43). Therefore, we collected tumor samples from ESCA patients undergoing nCRT. The findings indicated that those expressing high levels of CDKL3 had a poorer response to chemoradiotherapy.

We have previously reported that CDKL3 has a regulatory relationship with ATG5, a gene that regulates autophagy, in KYSE-150 cells (22). Autophagy is essential for tumor migration, invasion, and tumor immunity, and it is regulated by chemoradiotherapy (14, 15). Immune cell subpopulations whose survival, activation, differentiation, and function in the TME are linked to the autophagy pathway (44). Recent reports indicated that inhibition of autophagy restores cell surface MHC-I levels, increases antigen presentation, and enhances the anti-tumor response. The anti-tumor effect of autophagy inhibition was dependent on CD8+ T cells and cell surface MHC-I expression. ICIs combined with autophagy inhibitors enhanced anti-tumor immune responses (45). Autophagy activation has also been associated with chemoradiotherapy resistance in ESCC, leading to poor patient prognosis. Xia et al. found that Nrf2 enhances radiation resistance through the targeting of CaMKIIα and subsequent activation of autophagy in ESCC (46). Our further studies also confirmed that radiotherapy affects autophagy activation, and the expression of CDKL3 affects autophagy induction. We developed a CrA risk score based on public databases and validated it in internal and external cohorts.

Macrophages are diverse and plastic and can polarize into different phenotypes and thus perform different functions in response to different stimuli. M1 macrophages have pro-inflammatory and anti-tumor activity. M2 macrophages may be involved in the immune escape of tumor cells due to their inhibition of inflammation and concomitant promotion of tumor proliferation (47). The researchers found that USP19 promoted autophagy and thus downregulated NLRP3 inflammasome activation. And USP19 promoted M2 macrophage polarization (48). Tumor cells could also induce M2 polarization by transferring genetic information via exosomal non-coding RNAs (49). Our study found that patients with a high CrA risk score had higher infiltration levels of M2 macrophages based on the XCELL, CIBERSORT-ABS, and CIBERSORT algorithms. In another study, the Necroptosis-Pyroptosis Genes (NPG) scores established for prognostic prediction were found to be negatively correlated with infiltrating M2 Macrophage in patients with clear cell renal cell carcinoma (ccRCC) by the CIBERSOR algorithm (50). Moreover, this study showed that CDKL3 knockdown in KYSE150 cells could significantly inhibit autophagy induction in an autophagy-induced activated state. ESCC cells with downregulated CDKL3 could secrete some soluble factors or proteins to promote M1 macrophage polarization. Activation of autophagy in ESCC inhibited macrophage M1 polarization. This suggests that high CDKL3 expression in ESCC cells may be associated with the activation of autophagy, which promotes macrophage M2 polarization. Lin et al. also found that silencing IL4I1 in ccRCC cell lines (786-O, 769-P) could inhibit M2-like macrophage polarization by indirectly co-culturing with M0 macrophages (51). These results suggest that tumor cells with specific altered genes might influence immune cell infiltration and functional polarization.

IFN-γ exerts its biological effects mainly through the JAK/STAT pathway by activating intracellular signaling networks (52). Grasso et al. found that this conserved IFN-γ transcriptome response enhanced the anti-tumor immune response in melanoma (53). Our study found that downregulation of CDKL3 expression in ESCC activated the IFN pathway. This provided a different perspective on the mechanism by which high CDKL3 expression leads to attenuated anti-tumor immunity.

The ESCA samples in TCGA were from a Western population. However, there are differences in the pathology of ESCA between Eastern and Western populations, in particular, squamous cell carcinoma is the main pathological subtype in Eastern patients while the vast majority of Western patients are adenocarcinoma (54). There are still some limitations and deficiencies in this study. The sample size of patients with ESCA retrieved from the TCGA and GEO databases was limited, especially for ESCC. Although bioinformatics analysis was conducted in ESCA patients including ESCC and esophageal adenocarcinoma, the vitro study evidence only confirmed the role of CDKL3 in ESCC cell lines while lacking data in esophageal adenocarcinoma. It is necessary to further distinguish the role of CDKL3 in ESCC patients from esophageal adenocarcinoma patients. The potential function of CDKL3 in the modulation of tumor microenvironment and autophagy has been initially identified in this study, but a further prospective exploration needs to be designed to confirm. Moreover, it is significant to investigate and compare the differences in the atlas of immune infiltrating cells, such as specific T cells and macrophages, of the ESCA population with different CDKL3 expression in the clinic. In summary, our next step is to collect clinical samples from ESCA patients receiving immunotherapy and conduct further research in multicenter cohorts in China.

Conclusions

Overall, CDKL3 may play an important role in anti-tumor immunity by regulating autophagy to promote the formation of immunosuppressive TME, thus playing a critical role in the prognosis of ESCA.

Data availability statement

The datasets presented in this study can be found in online repositories. The names of the repository/repositories and accession number(s) can be found in the article/Supplementary Material.

Ethics statement

The studies involving humans were approved by the Institutional Review Board of Taizhou Hospital (K20230833). The studies were conducted in accordance with the local legislation and institutional requirements. The participants provided their written informed consent to participate in this study.

Author contributions

YB: Data curation, Formal analysis, Investigation, Methodology, Software, Validation, Visualization, Writing – original draft, Writing – review & editing. JL: Data curation, Formal analysis, Investigation, Validation, Visualization, Writing – review & editing. SQ: Data curation, Software, Writing – review & editing. FJ: Data curation, Software, Writing – review & editing. CZ: Data curation, Investigation, Software, Writing – review & editing. HY: Conceptualization, Supervision, Validation, Visualization, Writing – review & editing. SZ: Conceptualization, Formal analysis, Funding acquisition, Supervision, Validation, Visualization, Writing – original draft, Writing – review & editing.

Funding

The author(s) declare financial support was received for the research, authorship, and/or publication of this article. This study was supported by National Natural Science Foundation of China (NSFC 81872458), and Natural Science Foundation of Shaanxi Province (2023-JC-YB-645), and Xi'an Health Commission (2022ms11).

Acknowledgments

We thank the public databases for providing useful data.

Conflict of interest

The authors declare that the research was conducted in the absence of any commercial or financial relationships that could be construed as a potential conflict of interest.

Publisher's note

Supplementary material

The Supplementary Material for this article can be found online at: https://www.frontiersin.org/articles/10.3389/fimmu.2024.1295011/full#supplementary-material

SUPPLEMENTARY FIGURE 1
Differential expression and mutational analysis of CDKL3. **(A)** CDKL3 expression differences between normal and tumor tissues in TCGA, GSE161533, and GSE23400 datasets. **(B, C)** Oncoplot of the top 20 most mutated genes between high and low CDKL3 groups.

SUPPLEMENTARY FIGURE 2
Association of CDKL3 with cancer immunity cycles and immune-related signatures. **(A, B)** Correlation between CDKL3 and cancer immunity cycles in TCGA and GSE47404 cohorts. **(C, D)** Heat maps of CDKL3 and 92 immune-related signatures in TCGA and GSE47404 cohorts.

SUPPLEMENTARY FIGURE 3
Survival analysis of CDKL3 in the pan-cancer immunotherapy cohorts. **(A)** GSE176307 **(B)** Gide2019PD-1 **(C)** Gide2019PD-1+CTLA-4.

SUPPLEMENTARY FIGURE 4
The landscape in CDKL3 and the model genes in ESCA. **(A)** Circos plot of chromosomal distribution of CDKL3 and model genes. **(B)** CNV frequency of CDKL3 and model genes. The horizontal axis represents the change in frequency. **(C)** Sankey diagram of the relationship between CDKL3 group, risk group, and survival status.

References

1. Siegel RL, Miller KD, Wagle NS, Jemal A. Cancer statistics, 2023. *CA Cancer J Clin*. (2023) 73:17–48. doi: 10.3322/caac.21763

2. Morgan E, Soerjomataram I, Rumgay H, Coleman HG, Thrift AP, Vignat J, et al. The global landscape of esophageal squamous cell carcinoma and esophageal adenocarcinoma incidence and mortality in 2020 and projections to 2040: new estimates from GLOBOCAN 2020. *Gastroenterology*. (2022) 163:649–58.e2. doi: 10.1053/j.gastro.2022.05.054

3. Wang R, Liu S, Chen B, Xi M. Recent advances in combination of immunotherapy and chemoradiotherapy for locally advanced esophageal squamous cell carcinoma. *Cancers (Basel)*. (2022) 14:5168. doi: 10.3390/cancers14205168

4. Doki Y, Ajani JA, Kato K, Xu J, Wyrwicz L, Motoyama S, et al. Nivolumab combination therapy in advanced esophageal squamous-cell carcinoma. *N Engl J Med*. (2022) 386:449–62. doi: 10.1056/NEJMoa2111380

5. Kato K, Cho BC, Takahashi M, Okada M, Lin CY, Chin K, et al. Nivolumab versus chemotherapy in patients with advanced oesophageal squamous cell carcinoma refractory or intolerant to previous chemotherapy (ATTRACTION-3): a multicentre, randomised, open-label, phase 3 trial. *Lancet Oncol*. (2019) 20:1506–17. doi: 10.1016/S1470-2045(19)30626-6

6. Huang J, Xu J, Chen Y, Zhuang W, Zhang Y, Chen Z, et al. Camrelizumab versus investigator's choice of chemotherapy as second-line therapy for advanced or metastatic oesophageal squamous cell carcinoma (ESCORT): a multicentre, randomised, open-label, phase 3 study. *Lancet Oncol*. (2020) 21:832–42. doi: 10.1016/S1470-2045(20)30110-8

7. Kojima T, Shah MA, Muro K, Francois E, Adenis A, Hsu CH, et al. Randomized phase III KEYNOTE-181 study of pembrolizumab versus chemotherapy in advanced esophageal cancer. *J Clin Oncol*. (2020) 38:4138–48. doi: 10.1200/JCO.20.01888

8. Leone AG, Petrelli F, Ghidini A, Raimondi A, Smyth EC, Pietrantonio F. Efficacy and activity of PD-1 blockade in patients with advanced esophageal squamous cell carcinoma: a systematic review and meta-analysis with focus on the value of PD-L1 combined positive score. *ESMO Open*. (2022) 7:100380. doi: 10.1016/j.esmoop.2021.100380

9. Hanahan D, Weinberg RA. Hallmarks of cancer: the next generation. *Cell*. (2011) 144:646–74. doi: 10.1016/j.cell.2011.02.013

10. Thorsson V, Gibbs DL, Brown SD, Wolf D, Bortone DS, Ou Yang TH, et al. The immune landscape of cancer. *Immunity*. (2018) 48:812–30.e14. doi: 10.1016/j.immuni.2018.03.023

11. Charpentier M, Spada S, Van Nest SJ, Demaria S. Radiation therapy-induced remodeling of the tumor immune microenvironment. *Semin Cancer Biol*. (2022) 86:737–47. doi: 10.1016/j.semcancer.2022.04.003

12. Lv J, Wei Y, Yin JH, Chen YP, Zhou GQ, Wei C, et al. The tumor immune microenvironment of nasopharyngeal carcinoma after gemcitabine plus cisplatin treatment. *Nat Med*. (2023) 29:1424–36. doi: 10.1038/s41591-023-02369-6

13. Mizushima N, Komatsu M. Autophagy: renovation of cells and tissues. *Cell*. (2011) 147:728–41. doi: 10.1016/j.cell.2011.10.026

14. Li X, He S, Ma B. Autophagy and autophagy-related proteins in cancer. *Mol cancer*. (2020) 19:12. doi: 10.1186/s12943-020-1138-4

15. Onorati AV, Dyczynski M, Ojha R, Amaravadi RK. Targeting autophagy in cancer. *Cancer*. (2018) 124:3307–18. doi: 10.1002/cncr.31335

16. Xu Y, Li L, Yang W, Zhang K, Zhang Z, Yu C, et al. TRAF2 promotes M2-polarized tumor-associated macrophage infiltration, angiogenesis and cancer progression by inhibiting autophagy in clear cell renal cell carcinoma. *J Exp Clin Cancer Res CR*. (2023) 42:159. doi: 10.1186/s13046-023-02742-w

17. Asghar U, Witkiewicz AK, Turner NC, Knudsen ES. The history and future of targeting cyclin-dependent kinases in cancer therapy. *Nat Rev Drug Discov*. (2015) 14:130–46. doi: 10.1038/nrd4504

18. Canning P, Park K, Gonçalves J, Li C, Howard CJ, Sharpe TD, et al. CDKL family kinases have evolved distinct structural features and ciliary function. *Cell Rep*. (2018) 22:885–94. doi: 10.1016/j.celrep.2017.12.083

19. Ye W, Zhu J, He D, Yu D, Yang H, Wang W, et al. Increased CDKL3 expression predicts poor prognosis and enhances Malignant phenotypes in esophageal squamous cell carcinoma. *J Cell Biochem*. (2019) 120:7174–84. doi: 10.1002/jcb.27991

20. Cui Y, Yang Z, Wang H, Yan Y, Huang Q, Gong Z, et al. Identification of CDKL3 as a critical regulator in development of glioma through regulating RRM2 and the JNK signaling pathway. *Cancer Sci*. (2021) 112:3150–62. doi: 10.1111/cas.15010

21. Jiang Q, Li J, Wang J, Zhang W. Inhibition of CDKL3 downregulates STAT1 thus suppressing prostate cancer development. *Cell Death Dis*. (2023) 14:189. doi: 10.1038/s41419-023-05694-3

22. Zhou S, Zhang M, Zhou C, Wang W, Yang H, Ye W. CDKL3 targets ATG5 to promote carcinogenesis of esophageal squamous cell carcinoma. *Front Oncol*. (2020) 10:1602. doi: 10.3389/fonc.2020.01602

23. Mariathasan S, Turley SJ, Nickles D, Castiglioni A, Yuen K, Wang Y, et al. TGFβ attenuates tumour response to PD-L1 blockade by contributing to exclusion of T cells. *Nature*. (2018) 554:544–8. doi: 10.1038/nature25501

24. Fu J, Li K, Zhang W, Wan C, Zhang J, Jiang P, et al. Large-scale public data reuse to model immunotherapy response and resistance. *Genome Med*. (2020) 12:21. doi: 10.1186/s13073-020-0721-z

25. Blanche P, Dartigues JF, Jacqmin-Gadda H. Estimating and comparing time-dependent areas under receiver operating characteristic curves for censored event times with competing risks. *Stat Med*. (2013) 32:5381–97. doi: 10.1002/sim.5958

26. Xu L, Deng C, Pang B, Zhang X, Liu W, Liao G, et al. TIP: A web server for resolving tumor immunophenotype profiling. *Cancer Res*. (2018) 78:6575–80. doi: 10.1158/0008-5472.CAN-18-0689

27. Ozga AJ, Chow MT, Luster AD. Chemokines and the immune response to cancer. *Immunity*. (2021) 54:859–74. doi: 10.1016/j.immuni.2021.01.012

28. Singavi AK, Menon S, Kilari D, Alqwasmi A, Ritch PS, Thomas JP, et al. 1140PD - Predictive biomarkers for hyper-progression (HP) in response to immune checkpoint inhibitors (ICI) – analysis of somatic alterations (SAs). *Ann Oncol*. (2017) 28:v405. doi: 10.1093/annonc/mdx376.006

29. Kato S, Goodman A, Walavalkar V, Barkauskas DA, Sharabi A, Kurzrock R. Hyperprogressors after immunotherapy: analysis of genomic alterations associated with accelerated growth rate. *Clin Cancer Res*. (2017) 23:4242–50. doi: 10.1158/1078-0432.CCR-16-3133

30. Auslander N, Zhang G, Lee JS, Frederick DT, Miao B, Moll T, et al. Robust prediction of response to immune checkpoint blockade therapy in metastatic melanoma. *Nat Med*. (2018) 24:1545–9. doi: 10.1038/s41591-018-0157-9

31. Li T, Fu J, Zeng Z, Cohen D, Li J, Chen Q, et al. TIMER2.0 for analysis of tumor-infiltrating immune cells. *Nucleic Acids Res*. (2020) 48:W509–w14. doi: 10.1093/nar/gkaa407

32. Zeng D, Ye Z, Shen R, Yu G, Wu J, Xiong Y, et al. IOBR: multi-omics immuno-oncology biological research to decode tumor microenvironment and signatures. *Front Immunol*. (2021) 12:687975. doi: 10.3389/fimmu.2021.687975

33. Ma Y, Li W, Chen S, Lin S, Ding S, Zhou X, et al. Characteristics and response to next-generation sequencing-guided therapy in locally advanced or metastatic esophageal cancer. *Int J cancer*. (2023) 152:436–46. doi: 10.1002/ijc.34315

34. Su C, Wang X, Zhou J, Zhao J, Zhou F, Zhao G, et al. Titin mutation in circulatory tumor DNA is associated with efficacy to immune checkpoint blockade in advanced non-small cell lung cancer. *Trans Lung Cancer Res*. (2021) 10:1256–65. doi: 10.21037/tlcr

35. Li X, Pasche B, Zhang W, Chen K. Association of MUC16 mutation with tumor mutation load and outcomes in patients with gastric cancer. *JAMA Oncol*. (2018) 4:1691–8. doi: 10.1001/jamaoncol.2018.2805

36. de Visser KE, Joyce JA. The evolving tumor microenvironment: From cancer initiation to metastatic outgrowth. *Cancer Cell*. (2023) 41:374–403. doi: 10.1016/j.ccell.2023.02.016

37. Chen DS, Mellman I. Oncology meets immunology: the cancer-immunity cycle. *Immunity*. (2013) 39:1–10. doi: 10.1016/j.immuni.2013.07.012

38. Chen J, Zhao D, Zhang L, Zhang J, Xiao Y, Wu Q, et al. Tumor-associated macrophage (TAM)-derived CCL22 induces FAK addiction in esophageal squamous cell carcinoma (ESCC). *Cell Mol Immunol*. (2022) 19:1054–66. doi: 10.1038/s41423-022-00903-z

39. Eyck BM, van Lanschot JJB, Hulshof M, van der Wilk BJ, Shapiro J, van Hagen P, et al. Ten-year outcome of neoadjuvant chemoradiotherapy plus surgery for esophageal cancer: the randomized controlled CROSS trial. *J Clin Oncol*. (2021) 39:1995–2004. doi: 10.1200/JCO.20.03614

40. Yang H, Liu H, Chen Y, Zhu C, Fang W, Yu Z, et al. Long-term efficacy of neoadjuvant chemoradiotherapy plus surgery for the treatment of locally advanced esophageal squamous cell carcinoma: the NEOCRTEC5010 randomized clinical trial. *JAMA Surg*. (2021) 156:721–9. doi: 10.1001/jamasurg.2021.2373

41. Hulshof M, Geijsen ED, Rozema T, Oppedijk V, Buijsen J, Neelis KJ, et al. Randomized study on dose escalation in definitive chemoradiation for patients with locally advanced esophageal cancer (ARTDECO study). *J Clin Oncol*. (2021) 39:2816–24. doi: 10.1200/JCO.20.03697

42. Liu J, Yang Y, Liu Z, Fu X, Cai X, Li H, et al. Multicenter, single-arm, phase II trial of camrelizumab and chemotherapy as neoadjuvant treatment for locally advanced esophageal squamous cell carcinoma. *J Immunother Cancer*. (2022) 10(3):e004291. doi: 10.1136/jitc-2021-004291

43. Li C, Zhao S, Zheng Y, Han Y, Chen X, Cheng Z, et al. Preoperative pembrolizumab combined with chemoradiotherapy for oesophageal squamous cell carcinoma (PALACE-1). *Eur J Cancer (Oxford Engl 1990)*. (2021) 144:232–41. doi: 10.1016/j.ejca.2020.11.039

44. Xia H, Green DR, Zou W. Autophagy in tumour immunity and therapy. *Nat Rev Cancer*. (2021) 21:281–97. doi: 10.1038/s41568-021-00344-2

45. Yamamoto K, Venida A, Yano J, Biancur DE, Kakiuchi M, Gupta S, et al. Autophagy promotes immune evasion of pancreatic cancer by degrading MHC-I. *Nature*. (2020) 581:100–5. doi: 10.1038/s41586-020-2229-5

46. Xia D, Zhang XR, Ma YL, Zhao ZJ, Zhao R, Wang YY. Nrf2 promotes esophageal squamous cell carcinoma (ESCC) resistance to radiotherapy through the CaMKIIα-associated activation of autophagy. *Cell Biosci*. (2020) 10:90. doi: 10.1186/s13578-020-00456-6

47. Bosco MC. Macrophage polarization: Reaching across the aisle? *J Allergy Clin Immunol*. (2019) 143:1348–50. doi: 10.1016/j.jaci.2018.12.995

48. Liu T, Wang L, Liang P, Wang X, Liu Y, Cai J, et al. USP19 suppresses inflammation and promotes M2-like macrophage polarization by manipulating NLRP3 function via autophagy. *Cell Mol Immunol*. (2021) 18:2431–42. doi: 10.1038/s41423-020-00567-7

49. Xu Z, Chen Y, Ma L, Chen Y, Liu J, Guo Y, et al. Role of exosomal non-coding RNAs from tumor cells and tumor-associated macrophages in the tumor microenvironment. *Mol Ther*. (2022) 30:3133–54. doi: 10.1016/j.ymthe.2022.01.046

50. Fu L, Bao J, Li J, Li Q, Lin H, Zhou Y, et al. Crosstalk of necroptosis and pyroptosis defines tumor microenvironment characterization and predicts prognosis in clear cell renal carcinoma. *Front Immunol*. (2022) 13:1021935. doi: 10.3389/fimmu.2022.1021935

51. Lin H, Fu L, Li P, Zhu J, Xu Q, Wang Y, et al. Fatty acids metabolism affects the therapeutic effect of anti-PD-1/PD-L1 in tumor immune microenvironment in clear cell renal cell carcinoma. *J Transl Med*. (2023) 21:343. doi: 10.1186/s12967-023-04161-z

52. Majoros A, Platanitis E, Kernbauer-Hölzl E, Rosebrock F, Müller M, Decker T. Canonical and non-canonical aspects of JAK-STAT signaling: lessons from interferons for cytokine responses. *Front Immunol*. (2017) 8:29. doi: 10.3389/fimmu.2017.00029

53. Grasso CS, Tsoi J, Onyshchenko M, Abril-Rodriguez G, Ross-Macdonald P, Wind-Rotolo M, et al. Conserved interferon-γ Signaling drives clinical response to immune checkpoint blockade therapy in melanoma. *Cancer Cell*. (2020) 38:500–15.e3. doi: 10.1016/j.ccell.2020.08.005

54. He Y, Li D, Shan B, Liang D, Shi J, Chen W, et al. Incidence and mortality of esophagus cancer in China, 2008-2012. *Chin J Cancer Res*. (2019) 31:426–34. doi: 10.21147/j.issn.1000-9604.2019.03.04

frontiers | Frontiers in Immunology

TYPE Original Research
PUBLISHED 29 April 2024
DOI 10.3389/fimmu.2024.1323199

OPEN ACCESS

EDITED BY
Xuanbin Wang,
Hubei University of Medicine, China

REVIEWED BY
Shaohui Wang,
Chengdu University of Traditional Chinese Medicine, China
Esperanza Bas Infante,
University of Miami, United States
Zhi Dai,
Fudan University, China
Hai-long Piao,
Chinese Academy of Sciences (CAS), China

*CORRESPONDENCE
Guandong Pan
pgdhx@126.com
Jianqing Yang
yangjianqingxy@sina.com
Tao Gan
gantao11@sina.com

†These authors have contributed equally to this work

‡These authors have contributed equally to this work and share first authorship

RECEIVED 17 October 2023
ACCEPTED 15 April 2024
PUBLISHED 29 April 2024

CITATION
Ouyang G, Li Q, Wei Y, Dai W, Deng H, Liu Y, Li J, Li M, Luo S, Li S, Liang Y, Pan G, Yang J and Gan T (2024) Identification of PANoptosis-related subtypes, construction of a prognosis signature, and tumor microenvironment landscape of hepatocellular carcinoma using bioinformatic analysis and experimental verification. *Front. Immunol.* 15:1323199. doi: 10.3389/fimmu.2024.1323199

Identification of PANoptosis-related subtypes, construction of a prognosis signature, and tumor microenvironment landscape of hepatocellular carcinoma using bioinformatic analysis and experimental verification

Guoqing Ouyang[1,2,3,4‡], Qiuyun Li[1,4‡], Yangnian Wei[5‡], Wenbin Dai[6], Haojian Deng[7], Youli Liu[6], Jiaguang Li[6], Mingjuan Li[1], Shunwen Luo[1], Shuang Li[1], Yunying Liang[1], Guandong Pan[1,4*†], Jianqing Yang[1,4*†] and Tao Gan[1,7,8*†]

[1]Department of General Surgery, Liuzhou People's Hospital Affiliated to Guangxi Medical University, Liuzhou, Guangxi, China, [2]Guangxi Key Laboratory of Early Prevention and Treatment for Regional High Frequency Tumor, Guangxi Medical University, Nanning, Guangxi, China, [3]Key Laboratory of Early Prevention and Treatment for Regional High Frequency Tumor, Guangxi Medical University, Ministry of Education, Nanning, Guangxi, China, [4]Liuzhou Hepatobiliary and Pancreatic Diseases Precision Diagnosis Research Center of Engineering Technology, Liuzhou People's Hospital Affiliated to Guangxi Medical University, Liuzhou, Guangxi, China, [5]Department of Hepatobiliary Surgery, Ruikang Hospital, Guangxi University of Chinese Medicine, Nanning, Guangxi, China, [6]Department of Pathology, Liuzhou People's Hospital Affiliated to Guangxi Medical University, Liuzhou, Guangxi, China, [7]Department of Emergency Medical, Liuzhou People's Hospital Affiliated to Guangxi Medical University, Liuzhou, Guangxi, China, [8]Key Specialty Department of Emergency Medicine in Guangxi, Liuzhou People's Hospital Affiliated to Guangxi Medical University, Liuzhou, Guangxi, China

Background: Hepatocellular carcinoma (HCC) is one of the most lethal malignancies worldwide. PANoptosis is a recently unveiled programmed cell death pathway, Nonetheless, the precise implications of PANoptosis within the context of HCC remain incompletely elucidated.

Methods: We conducted a comprehensive bioinformatics analysis to evaluate both the expression and mutation patterns of PANoptosis-related genes (PRGs). We categorized HCC into two clusters and identified differentially expressed PANoptosis-related genes (DEPRGs). Next, a PANoptosis risk model was constructed using LASSO and multivariate Cox regression analyses. The relationship between PRGs, risk genes, the risk model, and the immune microenvironment was studies. In addition, drug sensitivity between high- and low-risk groups was examined. The expression profiles of these four risk genes were elucidate by qRT-PCR or immunohistochemical (IHC). Furthermore, the effect of CTSC knock down on HCC cell behavior was verified using *in vitro* experiments.

Results: We constructed a prognostic signature of four DEPRGs (CTSC, CDCA8, G6PD, and CXCL9). Receiver operating characteristic curve analyses underscored the superior prognostic capacity of this signature in assessing the

outcomes of HCC patients. Subsequently, patients were stratified based on their risk scores, which revealed that the low-risk group had better prognosis than those in the high-risk group. High-risk group displayed a lower Stromal Score, Immune Score, ESTIMATE score, and higher cancer stem cell content, tumor mutation burden (TMB) values. Furthermore, a correlation was noted between the risk model and the sensitivity to 56 chemotherapeutic agents, as well as immunotherapy efficacy, in patient with. These findings provide valuable guidance for personalized clinical treatment strategies. The qRT–PCR analysis revealed that upregulated expression of CTSC, CDCA8, and G6PD, whereas downregulated expression of CXCL9 in HCC compared with adjacent tumor tissue and normal liver cell lines. The knockdown of CTSC significantly reduced both HCC cell proliferation and migration.

Conclusion: Our study underscores the promise of PANoptosis-based molecular clustering and prognostic signatures in predicting patient survival and discerning the intricacies of the tumor microenvironment within the context of HCC. These insights hold the potential to advance our comprehension of the therapeutic contribution of PANoptosis plays in HCC and pave the way for generating more efficacious treatment strategies.

KEYWORDS

PANoptosis, hepatocellular carcinoma, tumor microenvironment, prognosis signature, drugs susceptibility

Introduction

Liver cancer ranking as the seventh most commonly diagnosed malignancy and the second leading cause of cancer-related mortality, is a significant global health concern. In 2020, 906,677 new cases and 830,180 deaths attributed to liver cancer were reported (1). The burden of liver cancer is steadily increasing, with the number of estimated incident projected to exceed one million by 2025 (2). The majority of liver cancer cases are hepatocellular carcinoma (HCC), accounting for 90% of live cancer (2). Current mainstay curative management options for HCC include surgical resection, radiofrequency ablation, and liver transplantation. However, a significant number of patients are diagnosed at an advanced stage, limiting the curative treatment options to transarterial chemoembolization (TACE), tyrosine kinase inhibitors (TKI), and immune checkpoint inhibitors (3). The prognosis for HCC remains poor, with an overall 5-year survival rate of only 18% (4). Therefore, it is essential to uncover the genomic characteristics of HCC and develop reliable and effective models for developing reliable and effective models to predict HCC prognosis and assess therapeutic responses, thereby enabling individualized and precise treatments.

Programmed cell death (PCD), including apoptosis, pyroptosis, and necroptosis has been implicated in the pathophysiology of HCC (5). Although these PCD pathways were traditionally considered independent, mounting evidence suggests intricate crosstalk among apoptosis, pyroptosis, and necroptosis (6). Thus an additional PCD pathway known as PANoptosis has recently emerged (7). It is a newly recognized form of inflammatory programmed cell death, which underscores the coordination and crosstalk between pyroptosis, apoptosis, and necroptosis (6, 7). During PANoptosis, these three pathways are collectively activated, forming the PANoptosome complex, which exhibits characteristics not explained by any individual death pathway (6, 8, 9). Although numerous studies have identified the roles of pyroptosis, apoptosis, and necroptosis in HCC (10–12), the relationship between HCC and PANoptosis, as well as its impact on anticancer immunity, remains unclear. Therefore, understanding the characteristics of PANoptosis may provide vital insight into the mechanisms underlying HCC tumorigenesis and facilitate the development of promising immunotherapy strategies for HCC.

In this study, we comprehensively integrated the expression profiles of 486 HCC patients to assess the PANoptosis-related

Abbreviations: OS, overall survival; HCC, hepatocellular carcinoma; TME, tumor microenvironment; KEGG, Kyoto Encyclopedia of Genes and Genomes; GO, Gene Ontology; MF, Molecular Function; BP, Biological process; CNV, copy number variation; TIME, tumor immune microenvironment; DEPRGs, differentially expressed PANoptosis-related genes; ssGSEA, single-sample gene set enrichment analysis; PRGs, PANoptosis-related genes; CSC, cancer stem cell; PCD, Programmed cell death; GSVA, gene set variation analysis.

molecular patterns into mechanisms contributing to HCC tumorigenesis and facilitate the development of promising immunotherapy strategies for HCC. A novel PANoptosis risk scoring system was developed to predict the prognosis of HCC patients and characterize the TME phenotype. Finally, we validated the expression levels of the four genes in our signature using quantitative polymerase chain reaction (qPCR) in both human samples and cells.

Materials and methods

HCC dataset and preprocessing

The RAN-sequencing and corresponding clinical data of 371 HCC cases and 50 healthy cases were download from the TCGA database (https://portal.gdc.cancer.gov/) (13). The HCC gene expression profiles and clinical characteristics of GSE76427 (n=115) were enrolled from the GEO database (https://www.ncbi.nlm.nih.gov/geo/) (14). Gene symbols were converted from probes based on the GPL10558 platform annotation file. The patients with HCC whose survival information was unavailable excluded from the analysis. The data of TCGA and GEO databases were merged using the "sva" R package (15) to remove the batch effects. A total of 29 PANoptosis-related genes (PRGs) were enrolled from previous studies (6, 8, 16). The data of copy number variation (CNV) was downloaded from UCSC Xena (https://xenabrowser.net). The flowchart of this study is shown in Figure 1.

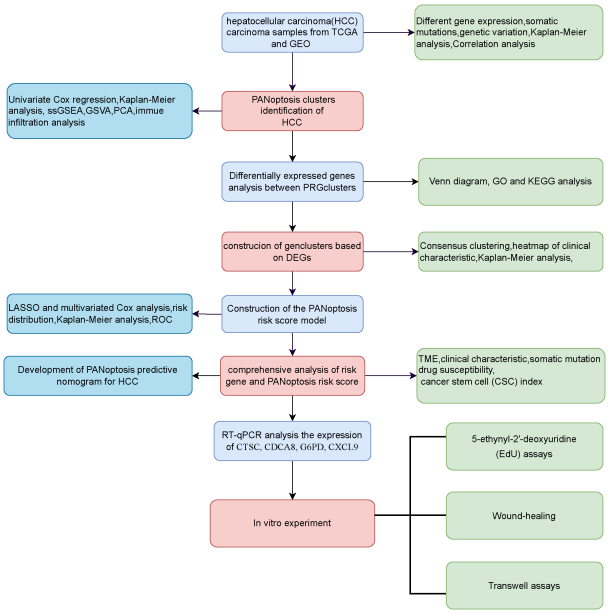

FIGURE 1
Flowchart of the present study.

Differential expression gene and consensus clustering analysis of CRGs

Wilcoxon rank-sum test was used to analysis the differential PRGs expression level between HCC patients and healthy samples using "limma" package (17). DEGs were selected with the threshold of p-value<0.05. We applied consensus clustering algorithms to categorize HCC patients into distinct molecular subtypes based on the expression of PRGs. This analysis was performed using the "ConsensusClusterPlus" (18) R package, and 1000 repetitions were conducted to ensure robustness. We next determined determine the optimal number of subtypes, we utilized a Cumulative Distribution Function (CDF) and evaluated the CDF Delta area. Additionally, Principal Component Analysis (PCA) was performed to confirm the differentiation of transcriptome profiles among the identified subgroups using the "ggplot2" R packages (19).

Gene set variation analysis and functional enrichment analysis

We used the "GSVA" (20) R package to perform the GSVA analysis to detect biological functions distinguishing different PANoptosis subtypes. The gene sets of KEGG gene set "c2.cp.kegg.symbols.gmt" download from the MSigDB database (https://www.gsea-msigdb.org/gsea/index.jsp), was employed to conducted the GSVA analysis (21). The "clusterProfiler" (22) R package was used to performed the Kyoto Encyclopedia of Genes and Genomes (KEGG) and gene ontology (GO) analysis. The pathways exhibiting a $p< 0.05$, logFC > 0.5 were deemed statistically significant.

Construction of PANoptosis risk model

A total of 485 HCC patients were randomly classified into testing and training group with a ratio of 1:1. Afterward, we identified 153 differentially expressed genes (DEGs) through performed three pairwise comparisons between the three PANoptosis subtypes, each time with a Log2 (fold change)> 0.585 and an adjusted P-value<0.05. The DEGs between three PANoptosis subtypes was intersected with each other to create PANoptosis gene signature.

Subsequently, we conducted univariate Cox regression analysis and identify 93 DEGs which significant associations with HCC prognosis to estimate significant genes. To mitigate overfitting, we employed LASSO Cox regression analysis (23). The best-performing gene was selected through multivariate Cox regression analysis, and a PANoptosis risk model was established using the formula: PANoptosis score = $\sum_{i=1}^{n} \exp(Xi) \times \text{coef}(Xi)$, where exp (Xi) represents the expression level and coef(Xi) represents the coefficient. Patients were stratified into high- and low-risk groups based on the median risk score. Time-dependent receiver operating characteristic (ROC) analysis was conducted to assess the sensitivity and specificity of the risk signature. A bootstrap method employing 1,000 resamplings was employed to generate the test set.

Assessment of tumor microenvironment

The CIBERSORT algorithm (24) was utilized to estimate the fractions of 22 immune cell phenotypes in each HCC patients, with the sum of the proportion of all calculated immune cell phenotypes in each sample being equal to 1. Samples with a p-value of< 0.05 were deemed statistically significant. Utilizing CIBERSORT results, correlation analysis was conducted between risk genes and 22 phenotypes of immune cells using the "limma" and "ggplot2" packages. The R "ESTIMATE" package (25) was used to calculated the immune scores, stromal scores, and ESTIMATE scores for each HCC sample (26). Subsequently, we conducted Wilcoxon tests to analyze the differences in these scores between the two risk groups. For a more detailed assessment of immune cell infiltration, we applied the single-sample gene set enrichment analysis (ssGSEA) based on "gsva" package (27).

Survival analysis of HCC

Afterward, we identified "survminer" and "survival" packages to generate Kaplan–Meier survival plots and assess the significance of differences using log-rank tests. The HCC patients were stratified into different subtypes, including PANoptosisCluster subtype, geneCluster subtype, PANoptosisScore subtype, and TMB subtype.

Development of nomograms

We developed nomograms to quantitatively predict of 1-, 3-, and 5-year overall survival (OS) by incorporating both clinical characteristics and risk score based on HCC patients' survival. Within the nomogram scoring system, individual variables such as gender, age, stage, and PRG Risk score were paired with corresponding scores. The cumulative score for each sample was derived by summing the assigned scores across all variables. The prognostic performance of the nomograms was assessed by calibration plots, which evaluated the concordance between predicted and actual values. The "rms" R package was used to construct the nomograms and conducting the calibration plot analysis.

Assessment of mutation, and cancer stem cell index

We next analyzed the mutations in HCC patients from both high- and low-risk groups, using the R package "maftools" (28) to generate mutation annotations. Initially, the total count of nonsynonymous mutations in each sample was computed. Subsequently, genes with high mutation frequencies were discerned utilizing a threshold of mutation frequency>5. The discrepancies in mutation frequency between different groups were then evaluated. Additionally, we examined the correlation between the cancer stem cell index and risk scores using the Spearman method (29).

Drug sensitivity analysis

We next assessed the drug sensitivity of every patient utilizing 198 drugs obtained from the genomics of drug sensitivity in the cancer v2 (GDSC) database (https://www.cancerrxgene.org/) and calculated their sensitivity by the "oncoPredict" R package (30). Statistical significance was determined at p< 0.05.

Cell culture and siRNA transfection

The HCCLM3, huh7, sun449, HepG2, HCCLM3, MHCC97-H of HCC cell lines and THLE-3 of normal liver cells, were cultured in Dulbecco's Modified Eagle Medium (DMEM) supplemented with penicillin G (100 mg/mL), streptomycin (100 mg/mL), and 10% fetal bovine serum (FBS; Gibco; USA). These cultures were incubated at 37°C in a 5% CO_2 atmosphere. Logarithmically growing cells were selected to conduct experiments. SUN449 was employed for siRNA transfection. For transfection, we employed Lipofectamine 3000 Transfection Reagent (Invitrogen, Waltham, Massachusetts, USA) in conjunction with 5 nmol of the specified siRNA fragments and a negative control si-NC (GenePharma, Shanghai, China) into approximately 4×105 SUN449 cells following the manufacturer's instructions. Si-NC (GenePharma) was used as a negative control. To assess transfection efficiency, quantitative reverse transcription-polymerase chain reaction (qRT-PCR) were employed. The sequences listed in Supplementary Table 1.

RNA extraction and quantitative real-time PCR

Total RNA was isolated from human samples of adjacent tumor tissues, HCC, normal liver cells (THLE-3), and HCC cells (huh7, sun449, HepG2, HCCLM3, MHCC97-H) using the Trizol reagent (Thermo Fisher Scientific, United States) following the manufacturer's instructions. Reverse transcription was carried out using the PrimeScriptTM RT reagent Kit (Takara, Japan). Next, qRT-PCR was performed on an FX Connect system (Bio-Rad, United States) using the SYBR ® Green Supermix (Bio-Rad, United States) to measure the expression levels of hub genes. β-actin was used as an internal control for normalization. RT-qPCR was measured 3 times, with 3 biological replicates each time. The relative expression levels of the target genes were calculated using the $2^{-\Delta\Delta CT}$ method. 15 patient's HCC tissue and adjacent tissue were used for qRT-PCR and a Student's t-test used to analyzed. Primer sequences used in the qRT-PCR assays are provided in Supplementary Table 1.

Human specimens and immunohistochemical staining

Human specimens were collected from 15 patients diagnosed with HCC at LiuZhou People's Hospital affiliated to Guangxi medical university. The study protocol was reviewed and

approved by the Medical Ethics Committee of LiuZhou People's Hhospital affiliated to Guangxi medical university. All patients provided written informed consent in accordance with the Declaration of Helsinki. Human tissue specimens were fixed with 4% paraformaldehyde, embedded in paraffin, and sectioned into 5 mm slices by a slicer. The specimens were dewaxed with xylene, following which the tissue sections were rehydrated using a graded series of ethanol solutions for antigen retrieval. The tissue sections were repaired with a sodium citrate repair solution (from Fuzhou Maixin Biotechnology Development Co., Ltd.), followed by allowing the sections to cool. Subsequently, an adequate amount of endogenous peroxidase blocker (supplied by Beijing Zhongshan Jinqiao Biotechnology Co., Ltd.) was added, and the sections were incubated at room temperature for 10 minutes. Afterward, the sections were washed three times with PBS, with each wash lasting 3 minutes. The sections were then blocked with 10% goat serum and incubated overnight at 4°C with anti-CTSC antibody (1:100) (Santa Cruze, U.S.A, cat#:sc-74590). Following three washes with PBS, the sections were incubated with a secondary antibody for 30 mins at 25°C, followed by development and then developed with DAB for 10 mins. Next, the sections were counterstained with hematoxylin for 2 mins to visualize nuclei. 15 patient's tumor and adjacent tumor tissue were used to qRT-PCR and immunohistochemical staining. Student's t-test or Wilcoxon test was used to compared the two group and $p< 0.05$ was regarded as significance.

Wound-healing and Transwell assays

We next studied the invasion capability and cell migration capacity by conducting Transwell assays and wound healing assays, respectively. For the Transwell assays, Prior to the experiment, the experimental cells underwent a period of serum starvation and were cultured in serum-free medium for 24 hours. Following this, the cells were digested, the digestion process was halted, and then centrifuged at 1500 rpm for 3 minutes. After aspirating the supernatant, the cells were washed with PBS and counted. Subsequently, the cells were resuspended in serum-free medium. The cell density was adjusted to 1 × 10^4 cells/mL, and 500 µL of culture medium containing 15% FBS was added to each well of a 24-well plate. Next, 200 µL of cell suspension was added to the chamber, which was carefully placed into the well of a 24-well plate containing complete culture medium to prevent the formation of air bubbles. The cells were then incubated in a cell culture incubator for 48 hours. Following incubation, the cells on the chamber were aspirated, and any remaining cells were gently wiped off using a PBS-dried cotton swab. The cells were fixed with a 10% methanol solution for 30 seconds, stained with 0.1% crystal violet for 20 minutes, and washed with tap water until the background was clear. Finally, 3-5 fields of view were randomly selected under an upright microscope, and the number of cells passing through the membrane was counted. Photomicrographs were captured and counted using Image J software. For the wound-healing assay, transfected SUN449 cells were seeded in a 6-well plate. When the cells reached 90% confluence, a 200 µL pipette tip was used to create a vertical scratch in the cell monolayer. Washed 3 times with PBS, removed the scratched cells, and added serum-free medium. The cells were then cultured for an additional 24 hours in a 37°C 5% CO2 incubator. Images were acquired and documented initially at the 0-hour time point, with additional imaging performed at 24 hours. Kruskal-Wallis test was used to analysis the Wound-healing and transwell assays results.

5-ethynyl-2′-deoxyuridine assays

SUN449 cells were seeded into a 12-well plate. After overnight incubation and return to a normal state, the cells were transfected with siRNA. Subsequently, an equal volume of 2X EdU working solution (20 µM) (Beyotime, China), preheated to 37°C, was added to the 12 wells plate, and the cells were incubated for 2 hours. Once EdU labeling was completed, the culture medium was removed, and the cells were fixed with 500 µl of fixative solution for 15 minutes. Following fixation, the cells were washed three times with 500 µl washing solution per well, with each wash lasting 3-5 minutes. After washing, permeabilization solution (500 µl per well) was added and incubated for 15 minutes, followed by 2 additional washes with 1 ml washing solution per well. Subsequently, 200 µl of Click reaction solution (Beyotime, China) was added, and the cells were incubated in the dark for 30 minutes. After removing the Click reaction solution, the cells were washed three times with washing solution for 3-5 minutes each. Nuclear staining was performed using Hoechst 33342, with protection from light, for 10 minutes. Following staining, the cells were washed three times with washing solution for 3-5 minutes each. Finally, fluorescence detection could be carried out.

Immunohistochemistry

Paraffin sections of HCC tissue from 15 patients and adjacent tumor tissue from the same group were subjected to immunostaining using antibodies against CTSC. Prior to staining, a dual endogenous enzyme blocker (MXB Biotechnologies, China) was applied for 30 minutes. The primary antibodies were left to incubate overnight at 4°C. Following thorough washing, the tissues were treated with the appropriate secondary antibodies and incubated at 37°C for 30 minutes. Next, an appropriate amount of DAB solution was applied for staining, followed by counterstaining with hematoxylin. To complete the process, a layer of neutral gum was used to cover the slides and the slides were sealed. The staining results was observed using an inverted microscope.

Statistical analysis

All statistical analyses were performed using the R software version 4.2.2 and GraphPad Prism 9. Continuous data are presented as means ± standard deviations. Student's t-test was used for normally distributed data in two-group comparisons, whereas the Wilcoxon test was used for non-normally distributed data. For

comparisons involving more than two groups, the Kruskal-Wallis test was used. Statistical significance was defined as $p < 0.05$. ALL experiment was repeated three times independently.

Results

Differential expression and genetic variation of PRGs in HCC

We first collected a set of 29 PRGs from previously published studies (6, 8, 16). As shown in Figure 2A, 33 (8.89%) of 371 samples had somatic mutations. Among the 29 PRGs, NLRP3 and MEFV exhibited the highest mutation frequency. Copy number variation (CNV) analysis showed that AIM2, GSDMD, RIPK1, NLRP3, RIPK3, PARP1, FADD, ZBP1, NLRC4, CASP8, IRF1, PYCARD, and MEFV had the increased CNV, whereas, CASP6, TAB2, TRADD, CASP7, CASP1, TNFAIP3, MLKL, TAB3, and PSTPIP2 displayed decreased an CNV decrease (Figure 2B). The locations of the CNV alterations of PRGs on the chromosomes were shown in Figure 2C. Furthermore, we conducted mRNA differential expression analysis of these 29 PRGs between 374 HCC samples and 50 healthy samples from TCGA. The result showed that gene, including CASP8, FADD, CASP6, TAB3, PSTPIP2, TNFAIP3, PARP1, GSDMD, MKLK, IRF1, RIPK1, TRADD, PYCARD, was upregulated in HCC, whereas only NLRP3, AIM2, and MEFV were significantly downregulated in HCC samples (Figure 2D).

Identification of PRGs clusters in HCC

To explore the overall landscape of PRGs interaction, relationships, and prognostic significances, a network map was constructed (Figure 3A). The network map showed 14 of 29 genes showed significant correlation in interaction, relationship and prognostic. The relationship between the prognosis of HCC patients and 14 PRGs were assessed using the Kaplan-Meier curves and shown in Supplementary Figure 1. The expression of 20 PRGs in HCC were used to conduct an unsupervised clustering algorithm and group the 486 HCC patients into three distinct patterns. The most effective clustering result was achieved at K=3 among K = 2 to K = 9 (Figures 3B, C). Thus, we categorized 128 HCC patients into PRGcluster A, 226 into PRGcluster B, and the remaining 132 into PRGcluster C. The principal component analysis (PCA) indicated a satisfactory separation between the three clusters (Figure 3D). PRGcluster C exhibited higher expression levels for most PRGs, whereas PRGcluster A displayed lower expression levels for most PRGs (Figure 3E). Next, we investigated the relationship between these three PRGcluster and clinical characteristics. Kaplan-Meier curves demonstrated significant differences in OS among the three

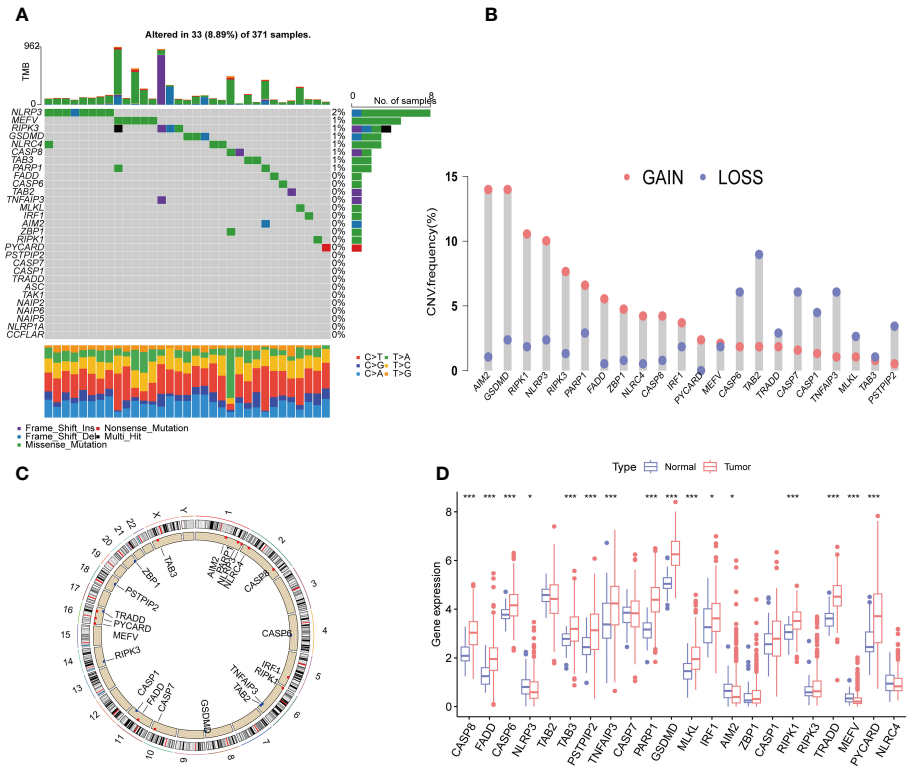

FIGURE 2
Expression and genetic alteration of PRG in HCC. **(A)** The maftool exhibited incidence of somatic mutations of PRG in 371 HCC patients from TCGA database; **(B)** The CNV frequency of PRG in TCGA cohort. The height of the column showed the proportions of gain or loss variations; **(C)** The location of CNV alteration of 22 PRG on 23 chromosomes. **(D)** The expression of 22 PRG in HCC and normal tissues;. PRGs, PANoptosis-related genes; HCC, hepatocellular carcinoma; CNV, Copy number variation. The p-values were showed as: *p < 0.05; ***p < 0.001.

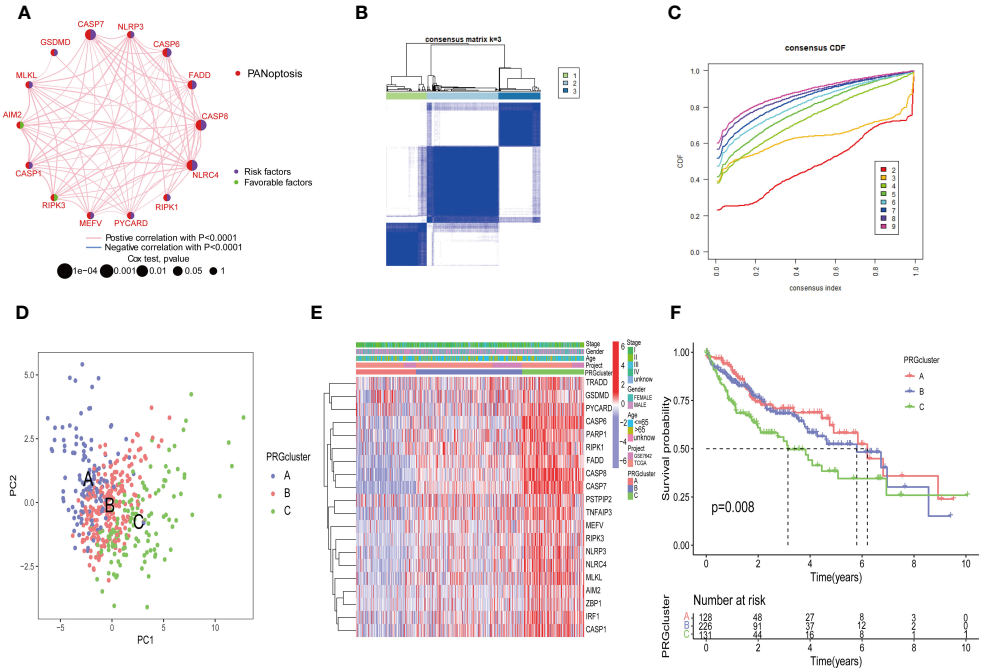

FIGURE 3
Identification of molecular subtypes of PRGs for HCC. **(A)** A network between PRGs in HCC; **(B, C)** Consensus matrix heatmap defining three clusters (k = 3) and their correlation area; **(D)** PCA diagram of HCC samples in cluster A, B, and C. **(E)** Complex heat maps show clinical correlations among the three clusters; **(F)** Survival analysis of three PRGclusters.

PRGclusters, with PRGcluster C showing the poorest OS (Figure 3F).

Additionally, we conducted the GSVA analysis to identify distinct pathways associated with PRGclusters A, B, and C (Figures 4A–C). The ssGSEA were utilized to assess the immune cell infiltrations in three PRGclusters. The boxplot showed that PRGcluster C was enriched in activated CD4 T cells, activated dendritic cells, CD56 bright nature killer cells, immature B cells, immature dendritic cells, MDSCs, macrophages, natural killer cells, plasmacytoid dendritic cells, regulatory T cells, T follicular helper cells, and type 2 T helper cells. While, PRGcluster A was enrich in eosinophils (Figure 4D).

Generation of PRG signatures in HCC

We conducted a differential gene expression analysis of three PRGclusters, comparing them in pairs three times among the three subtypes. We used a Venn diagram to successfully identify 153 DEGs exhibiting intersection across these three clusters (Figure 5A). The potential functions and pathways governed by these 153 DEGs were unraveled using GO and KEGG enrichment analyses performed using the "ClusterProfiler" packages. The GO results unveiled that these DEGs were involved in chromosome segregation, wound healing, and positive regulation of the cell cycle process in the biological process (BP). Within the Cellular Component (CC) category, they were prominently associated with chromosomal regions, collagen-containing extracellular matrices, and nuclear chromosomes. The Molecular Function (MF) exhibited closely related to integrin binding, platelet–derived growth factor binding, and single–stranded DNA binding (Figure 5B). Furthermore, the KEGG pathway analysis demonstrated their participation in processes such as Phagosome, PI3K-Akt signaling pathway, cell adhesion molecules, ECM-receptor interaction, Proteoglycans in cancer, and Cell cycle (Figure 5C).

To further analyze the important roles, univariate Cox regression was performed to identify the relationship between the 153 PRGcluster-related DEGs and the prognosis in HCC. Subsequently, patients were categorized into two major gene clusters, denoted as genecluster A and genecluster B (Figures 5D, E). The Kaplan–Meier analysis revealed that patient in genecluster B exhibited a more favorable OS rate compared to those in genecluster A (Figure 5F). A complex genecluster-based heatmap was developed by combining the gender, age, HCC clinical stage, PRGcluster, genecluster in TCGA and GSE 76427 (Figure 5G). Moreover, the analyzing the transcriptomic profile from the heatmap was analyzed that revealed the upregulation in most genes of genecluster A, whereas those in genecluster B predominantly exhibited downregulation. The DGEs analysis between genecluster A and B showed that CASP8, FADD, CASP6, NLRP3, PSTPIP2, TNFAIP3, CASP7, PARP1, GSDMD, MLKL, IRF1, AIM2, ZBP1, CASP1, RIPK1, RIPK3, TRADD, MEFV, PYCARD, NLRC4 were upregulated in genecluster A (Figure 5H).

Construction of prognostic PANoptosis risk scoring model

The HCC patients were randomly divided into a training set (243 samples) and a testing set (242 samples) to explore the

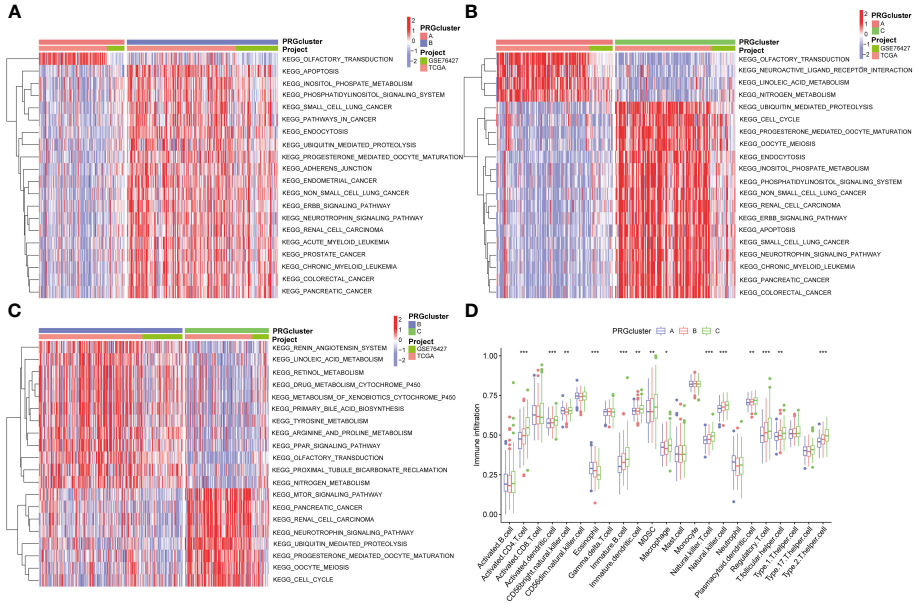

FIGURE 4
GSVA results between three PRGclusters and relationship of tumor microenvironment in three PRGclusters. **(A–C)** The GSVA heat map showed the differences in pathways in the three clusters; **(D)** The differential analyses between immune cells and the scale of fraction for PRGcluster A, B and C. *p<0.05, **p<0.01, ***p<0.001.

prognosis related PRG-related DEGs. A univariate Cox regression analysis was performed using the 153 DEPRGs along with survival data within the training datasets. Out of these, 93 DEPRGs were exhibited significant associations with prognosis (p< 0.05). To enhance the precision of gene selection for model construction, we adopted a systematic approach. Specifically, we randomly sampled 80% of the training set specimens for LASSO regression analysis, incorporating tenfold cross-validation and executing 1000 iterations. Subsequently, this rigorous methodology enabled the identification of a refined subset comprising 4 significant genes crucial for model refinement. (Figures 6A, B). Subsequently, we performed a multivariate Cox regression analysis using these four significant genes, and identifying the most pivotal genes for prognosis—CTSC, CDCA8, G6PD, and CXCL9The PANoptosis

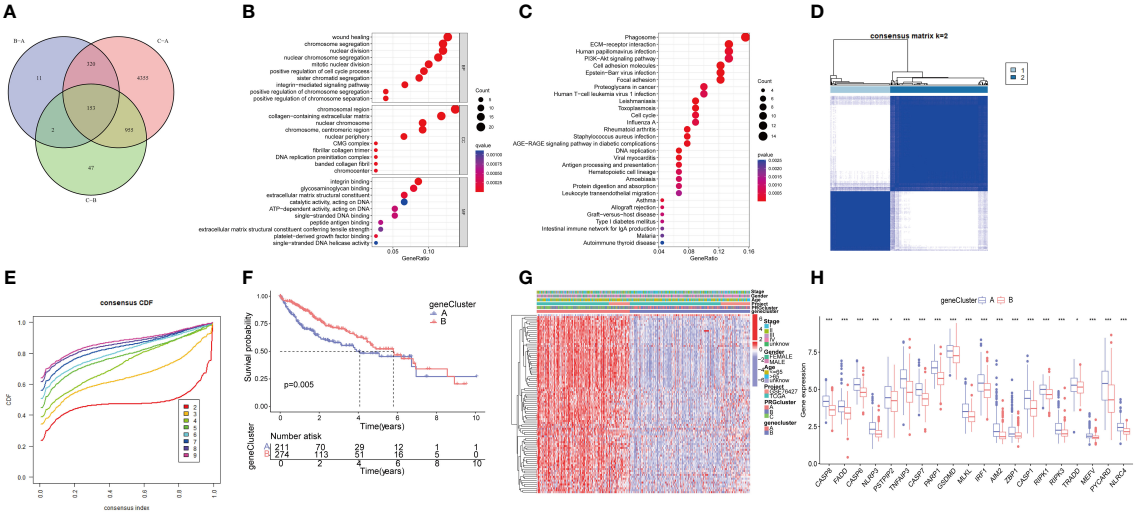

FIGURE 5
Functional enrichment analysis of PRGs, and identified two genecluster based on 153 DEGs. **(A)** The Venn diagram shows the intersection of three PRGclusters; **(B)** Analysis of BP, CC, and MF terms of GO enrichment demonstrated the possible function of the 153 DEGs; **(C)** Kyoto Encyclopedia of Genes and Genomes (KEGG) pathway enrichment analysis revealed the possible pathways; **(D)** Unsupervised cluster analysis of 153 DEGs developed two geneclusters (k = 2); **(E)** Consensus matrix heatmap defining two clusters and their correlation area; **(F)** Survival analysis of two geneclusters. **(G)** A complex heat map illustrated the expression patterns; **(H)** Expression of PRGs between genecluster A and genecluster B. *p<0.05, ***p<0.001. DEGs, differential expressed genes.

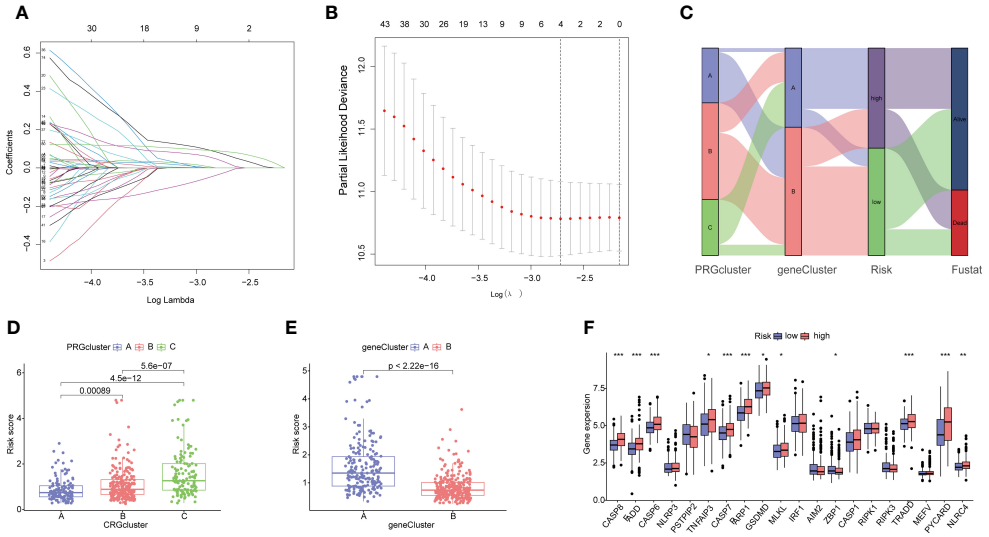

FIGURE 6
Identification of 4 genes for estimating the risk score and the relationship between molecular classifications, PRGs expression levels and the risk score. **(A, B)** The Least absolute shrinkage and selection operator (LASSO) regression analysis and partial likelihood deviance on the prognostic genes; **(C)** Sankey plot showed the correlation between PRGclusters, geneclusters, risk groups and survival status in HCC patients; **(D)** Boxplots indicate the differences in risk scores in three PRGclusters and **(E)** two geneclusters. **(F)** The differential analysis of PRGs expression in high- and low-risk groups. *p<0.05, **p<0.01, ***p<0.001.

Risk scoring system was constructed based on the following formula in the training sets: Risk score=Exp (CTSC)× (0.215) + Exp (CDCA8) × (0.232) + Exp(G6PD) × (0.138) + Exp (CXCL9) × (-0.196). All set files were combined by the training group and testing group files. The HCC patients were subsequently categorized into high- and low-risk groups based on the median Risk score for each group. The Sankey diagram shows the distribution of PRGs risk scores with three PRGcluster, two geneclusters, and HCC patients survival status (Figure 6C). The boxplot showed that PRGcluster C and genecluster A had higher risk scores (Figures 6D, E). The differential expression analysis between high- and low-risk group demonstrated that CASP8, FADD, CASP6, TNFAIP3, CASP7, PARP1, GSDMD, MLKL, ZBP1, TRADD, PYCARD, and NLRC4 were upregulated in high-risk group (Figure 6F).

Validation of prognostic PANoptosis risk scoring model

The KM analysis revealed that patients with low-risk had a better survival rate than those with high-risk in both total, training, and testing sets (P< 0.05) (Figures 7A–C). Additionally, we utilized the ROC curves to assess the prediction efficiency of the risk score. The AUCs for 1-, 3-, and 5-year survival rates in the training set were 0.696, 0.706, and 0.603, respectively. In total sets, the AUCs for 1-, 3-, and 5-year survival rates was 0.735, 0.706, 0.638, respectively. In testing sets, the AUCs of 1-, 3-, and 5-year survival rates were 0.771, 0.697, and 0.708, respectively (Figures 7D–F). These results indicated a favorable predictive performance for the survival of HCC patients. We next constructed a nomogram with using risk score, clinical stage, gender, and age (Figure 7G). the calibration curves indicated a relative link between observed and nomogram-predicted OS of HCC patients (Figure 7H), confirming the validity of the nomogram model for predicting the survival of HCC patients.

The gene expression differences for CTSC, CDCA8, G6PD, and CXCL9 between high- and low-risk group in all set, training set, and testing set are depicted in Figures 8A–C. The heatmap visually represented that CTSC, CDCA8, and G6PD exhibited higher expression levels in the high-risk groups, whereas CXCL9 showed lower expression levels. We observed an inverse correlation between risk score and survival time, as well as a positive association between risk score and the death rate across all sets—total, training, and testing. These findings underscore that HCC patients with higher risk scores had poorer survival outcomes (Figures 8D–I).

Relationship between signature and TME

The association analysis between immune cell abundance and the risk score showed that neutrophils and macrophages M2 were positively correlated with risk score, whereas CD8 T cells, macrophages M1, and naïve B cells were negatively related with risk score (Supplementary Figure 2). Furthermore, Figure 9A demonstrates the correlation between immune cells and the four risk genes. The CTSC displayed significant associations with neutrophils, macrophages M2, and CD4 memory resting T cells. In the low-risk group, the Stromal Score, Immune Score, and ESTIMATE score were significantly higher compared to the high-risk group (Figure 9B).

Cancer stem cells (CSCs) were thought to play an important role in the recurrence, metastasis, and identifying therapeutic target due to their differentiation and self-renewal capacity l (31). A correlation analysis between the risk score and stem cells unveiled

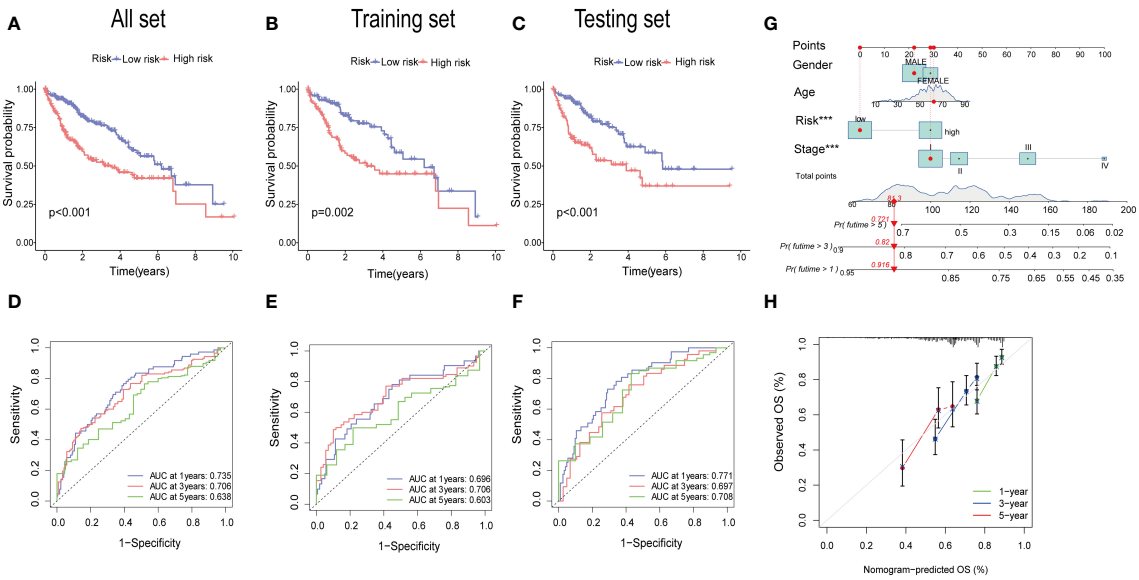

FIGURE 7
Validation of the prognostic value of the signatures. **(A–C)** K-M survival curve of all sets, testing set, and training set. **(D–F)** The ROS for 1-year, 3-year, and 5-year OS prediction of all sets, testing set, and training set. **(G)** The nomogram of the risk score and clinical features (age, gender, and stage) for predicting the survival of HCC patients. **(H)** The calibration curves showed the accuracy of the nomogram in the 1st, 3rd, and 5th years.

a positive linear correlation between the risk score and stem cell content (R=0.3, p<.001) (Figure 9C).

Furthermore, we explored the disparity in tumor somatic mutations between the high- and low-risk groups using "maftools". The top six mutated genes were TP53, CTNNB1, TTN, MUC16, PCLO, and ALB in both high- and low-risk groups (Figures 9D, E). In addition, we observed that patients with high TMB displayed a poorer overall survival rate (Figure 9F). The combination of TMB and risk score demonstrated that low risk plus low TMB had the best OS (Figure 9G).

Drugs susceptibility analysis

We next investigated the predictive therapeutic effects in patients with HCC by assessing the relationship between the two

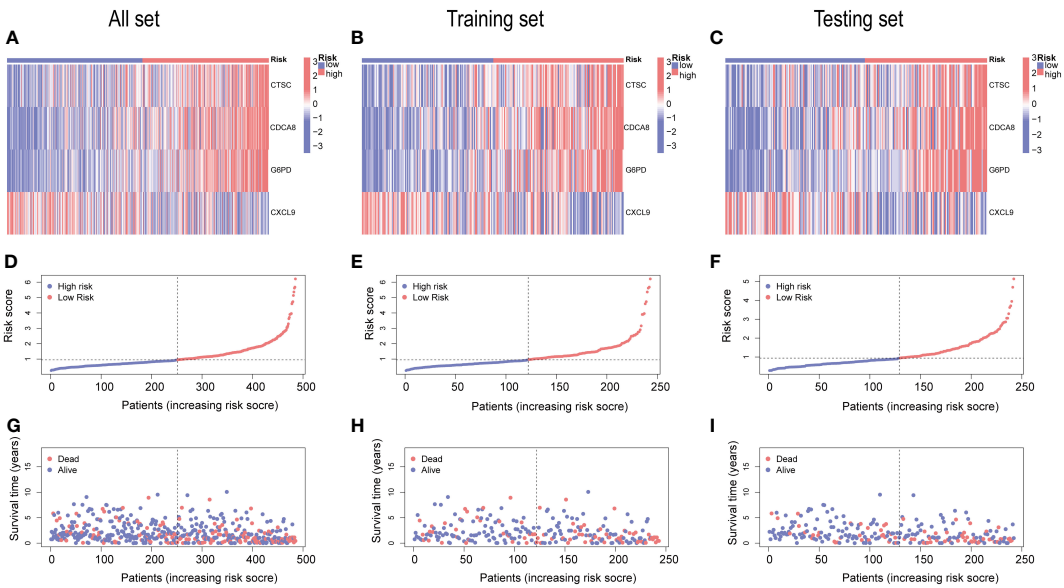

FIGURE 8
An analysis of risk gene expression and the distribution of risk scores, survival status of HCC patients. **(A–C)** Heatmap of four risk genes across different risk scores in the All, training, and testing sets, respectively. **(D–F)** Exhibition of PRGs risk score model of the All, training, and testing sets, respectively. **(G–I)** Survival status between low-and high-risk groups in the All, training, and testing sets, respectively.

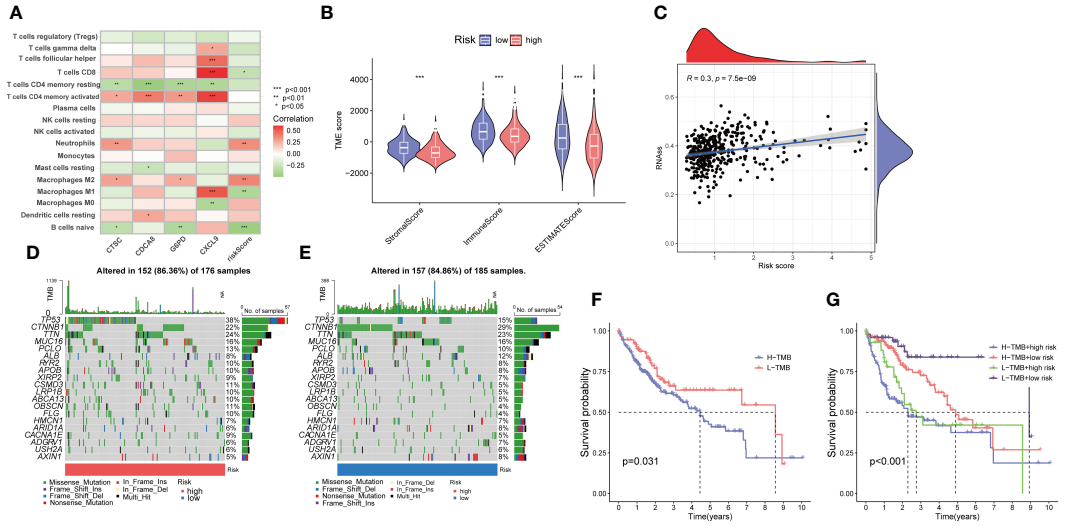

FIGURE 9
Evaluation of the tumor microenvironment, and tumor mutation burden (TMB) in low- and high-risk groups. **(A)** Correlation between the four risk genes and the abundance of immune cells. **(B)** Comparison of ESTIMATE scores, stromal scores, and immune scores between the low- and high-risk groups. **(C)** Correlation between the stem cell content and the PANoptosis risk score. **(D, E)** The frequency of somatic gene mutations in the high- and low-risk groups, respectively. **(F, G)** The Kaplan-Meier curve of the tumor mutation burden and risk scores versus the overall survival. *p<0.05, **p<0.01, ***p<0.001

risk groups and drug sensitivity. Our analysis revealed significant differences in drug responses between the high- and low-risk groups, with 56 drugs exhibiting noteworthy distinctions. Among them 16 drugs had lower IC50 in high-risk groups, such as Paclitaxel, Sepantronium, and Tozasertib. Low-risk group were more sensitive to Oxaliplatin, sorafenib, irinotecan (Supplementary Table 4).

Validation of the expression levels signature genes

GSE14520 was used to validated the mRNA expression and diagnosis probability. The results showed that CTSC, CDCA8, and G6PD were upregulated in HCC tissues, whereas CXCL9 was downregulated (Figures 10A–D). The AUC value of CTSC, CDCA8, G6PD, and CXCL9genes were 0.656, 0.858, 0.882, 0.621, respectively and the model AUC value reached to 0.92, suggesting our signature had higher quality of prediction (Figures 10E, F). In addition, we used RT-PCR to validated the mRNA expression of signature genes between adjacent tumor tissue and HCC, and normal liver cell THLE3 and liver cancer cell line of HCCLM3, MHCC-97H, SUN449, HepG2, and Huh7. Compared with the adjacent tumor tissue and most liver cancer cells lines, a significant increase expression of G6PD, CDCA8, and CTSC in HCC tissues and liver cancer cells was observed, whereas CXCL9 was significant downregulated (Figures 10G–N). However, the mRNA expression of G6PD and CDCA8 showed no significant differences between THLE3 and HepG2 (Figures 10K, M). IHC and western blotting further confirmed the higher expression of CTSC in HCC tissues compared to the adjacent tumor tissues (Figures 10O–R).

Effects of CTSC on the proliferation and migration of SUN-449 cell

We designed three siRNA to study the impact of CTSC downregulation in SUN449 cells due to the upregulated expression of CTSC. qRT-PCR confirmed the CTSC effectiveness of downregulation following siRNA interference (Figure 11A). The results of Transwell and Wound-healing assays indicated the inhibition CTSC attenuated the migratory capabilities of SUN449 cell (Figures 11B–E). The EdU assay revealed a reduced proportion of EdU-positive cells upon the inhibition of CTSC in SUN449 cells, indicating that CTSC fosters the proliferation of HCC cells (Figure 11F). qRT-PCR result showed that inhibition of CTSC could increase the mRNA expression of CASP3, CASP7, GSDMD, CASP1, MLKL, RIPK3(Figures 11G–L).

Discussion

HCC is a common fatal malignancy of the digestive system whose global burden has surged significantly from 1990 to 2019, posing substantial threats to human life, health, and the global economy (32). Despite previous efforts to diagnose and treat patients with HCC, a majority of them are diagnosed at advanced stages, rendering them ineligible for surgical resection and resulting in unfavorable prognoses. Therefore, it is imperative to elucidate the mechanism contributing to the pathogenesis of HCC to explore innovative approaches for diagnosis and treatment. PANoptosis, a component of the host's innate immune response, has been identified as a novel mechanism governing inflammatory programmed cell death, encompassing pyroptosis, apoptosis, and necroptosis (6). Previous studies have demonstrated the significant

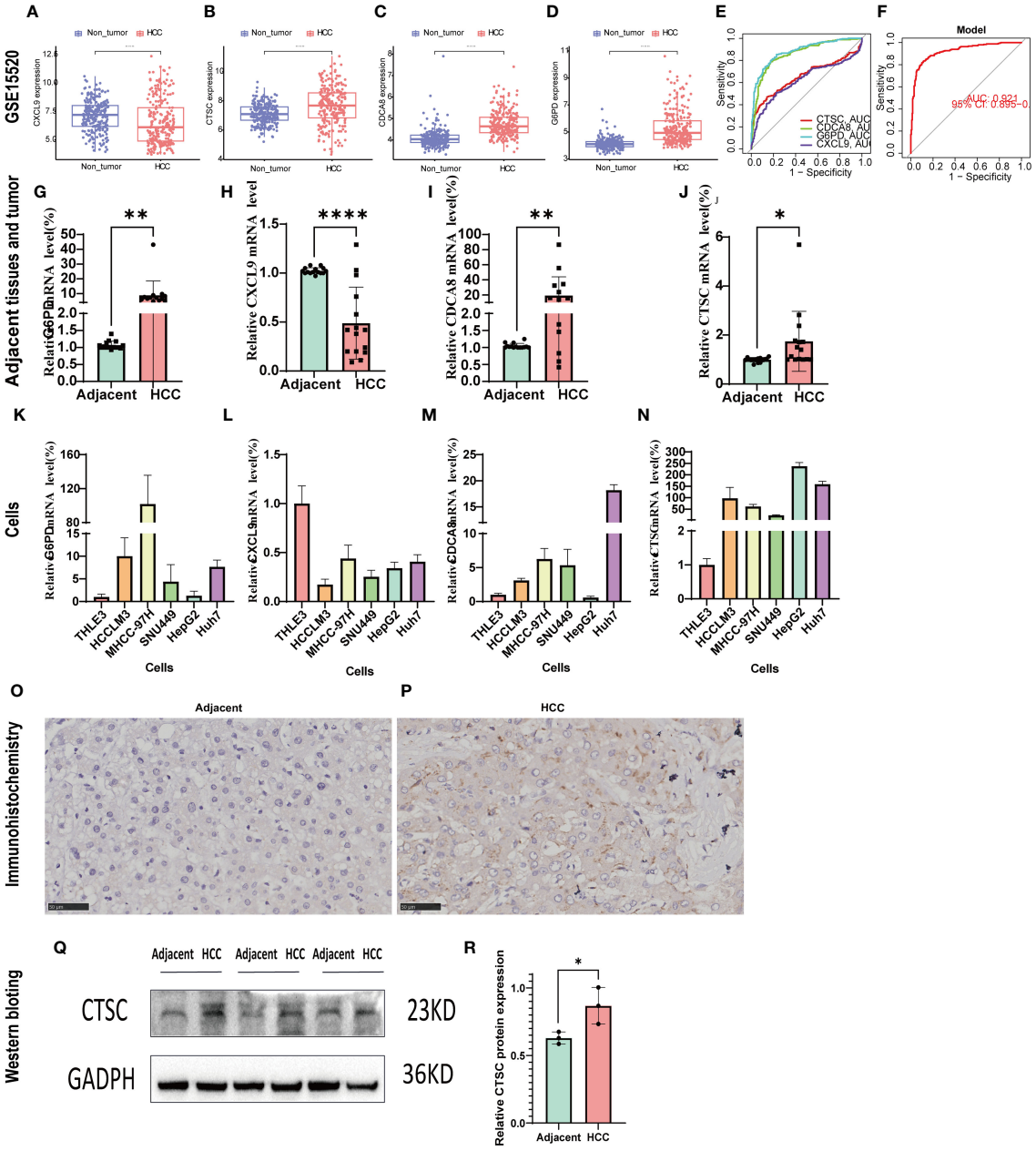

FIGURE 10
Validation of the signature genes with GSE14520, qRT-PCR, and IHC. **(A–D)** The expression of CXCL9, CTSC, CDCA8, G6PD between HCC and normal tissues in GSE14520; **(E)** The ROC results of 4 marker genes in GSE14520. The AUC value of CXCL9, CTSC, CDCA8, G6PD was 0.656,0.858,0.882,0.621, respectively. **(F)** ROC results of the 4-gene-based model based on 3-fold cross-validation in GSE14520. The AUC value as 0.921. AUC, area under curve; ROC, receiver operating characteristic; DCA, Decision curve analysis. **(G–J)** qRT-PCR confirmed the 4 marker genes expression between HCC tissues and adjacent tumor tissues; **(K–N)** qRT-PCR validated the 4 marker genes expression between HCC cells (HCCLM3, MHCC-97H, SUN449, HepG2, Huh7) and normal liver cell (THLE3). **(O, P)** CTSC representative IHC stained images in adjacent tissues and HCC tissue. **(Q, R)** Western blot analysis the protein expression in adjacent tumor tissues and HCC tissue. *p < 0.05; **p < 0.01; ****p < 0.0001.

role of PANoptosis in tumorigenesis and anti-tumor therapies (16). We identified a valid signature to assess the treatment and prognosis of HCC and developed a signature based on the concept of PANoptosis for HCC patients.

In our study, we used 29 PRGs to evaluate their somatic mutations, CNVs, DEGs. Our findings indicated that the majority of PRGs were significantly upregulated in HCC, with only NLRP3, AIM2, and MEFV demonstrating downregulation in HCC. Notably, NLRP3 and AIM2 were significantly correlated with HCC prognosis. Previous research has confirmed the downregulation of AIM2 expression in human HCC tissues compared to adjacent normal tissues. Furthermore, we revealed that patients with HCC with higher AIM2 expression exhibited improved overall survival rates (33), consistent with our analysis. Regarding NLRP3, it plays dual roles in HCC. On one hand, the NLRP3 inflammasome inhibits HCC development via pyroptosis, while on the other

10.3389/fimmu.2024.1323199

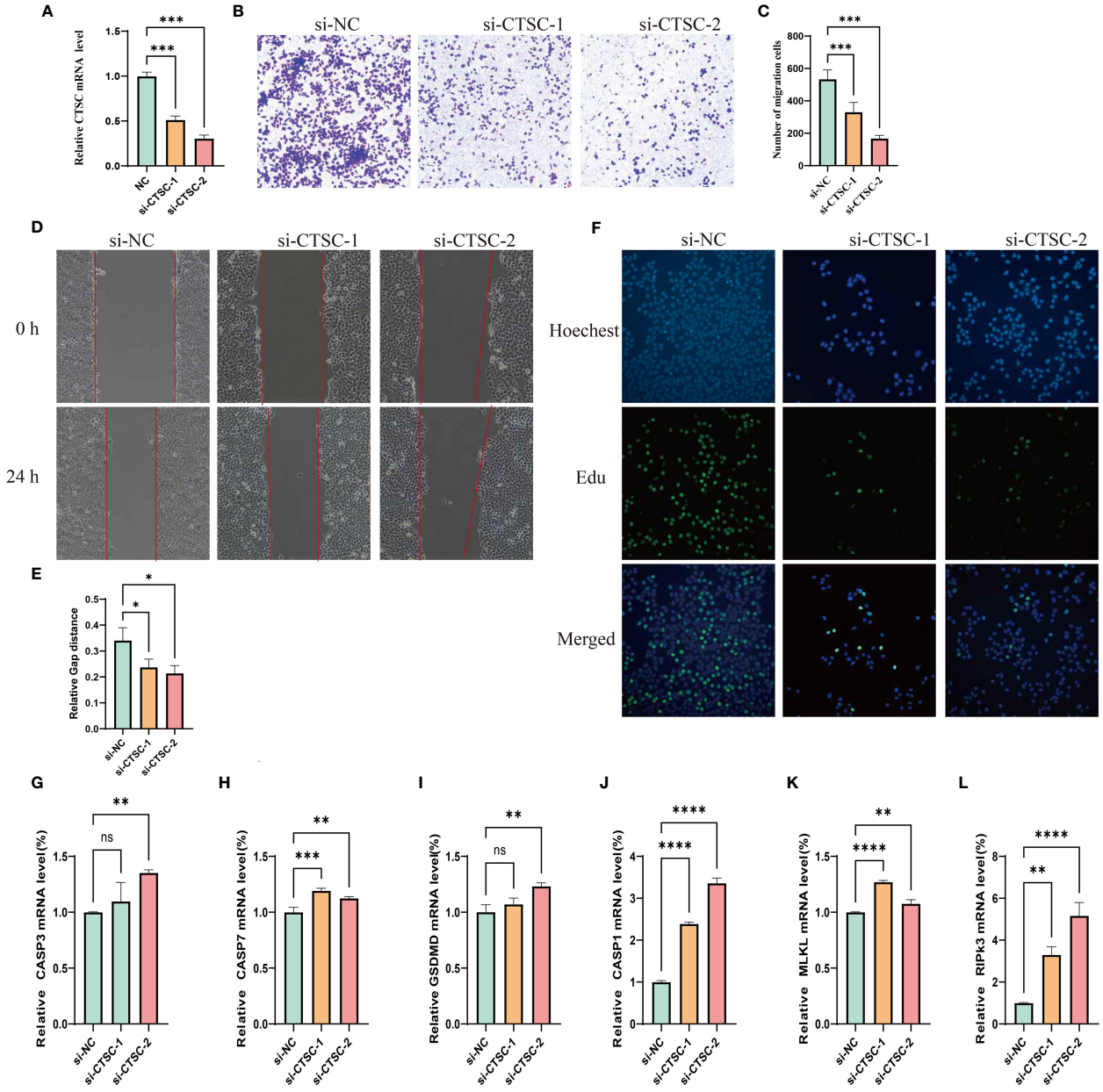

FIGURE 11
Cell model validation of CTSC in SUN-449 cell transfected with siCTSC and vector. **(A)** Relative CTSC mRNA level after being knocked down. **(B, C)** Transwell assays were employed to assess the ability of SUN-449 cell to migrate after CTSC was knocked down for 24 h; **(D, E)** Representative images and quantitative analysis of the results from the wound healing assay; **(F)** EdU assay was conducted between the si-NC and CTSC knockdown SUN-449 cells; **(G–L)** The mRNA expression of CASP3, CASP7, GSDMD, CASP1, MLKL, RIPK3 after CTSC was knocked down. *p < 0.05; **p < 0.01; ***p < 0.001; ****p < 0.0001. ns, not significant.

hand, it promotes HCC growth through the mediation of different signaling pathways (34). Additionally, we identified that 14 PRGs were significantly associated with the survival rate of HCC patients. Collectively, these results suggest that PANoptosis may indeed play a pivotal role in the context of HCC.

We initiated our study by conducting a comprehensive clustering analysis to identify the molecular subtype of PANoptosis. All HCC patients were categorized into three distinct PRGclusters. Notably, although PRGcluster C exhibited an overall high expression of most PRGs, it displayed experienced a significantly worse prognosis. Thus, higher expression levels of PRGs could be associated with a lower rate of survival. Additionally, PRGcluster C exhibited heightened immune infiltration, characterized by the presence of various immune cells such as activated CD4 T cells, immature dendritic cells, MDSCs, macrophages, natural killer cells, and regulatory T cells. Previous studies has indicated that certain components within TME, including dendritic cells, macrophages, and natural killer cells, can promote tumor proliferation, invasion, metastasis, and hinder anti-cancer immune responses (35–37). This finding implies that the elevated expression of PRGs could lead to increased immune cell infiltration and subsequently result in a poorer survival rates.

Furthermore, we identified 153 DEGs related to PANoptosis among the three PRGclusters, and subsequently categorized patients into two geneclusters. Notably, geneCluster A exhibited higher PRG expression levels and a worse survival prognosis. Altogether, these findings provide valuable insights into the underlying biology of these specific tumor types and offer potential avenues for subgroup screening in HCC.

To improve the prognosis prediction and characterization capabilities of each patient with HCC, LASSO and multivariate Cox regression analyses were employed to construct a novel prognostic signature to better predict HCC prognosis. High-risk groups were characterized by elevated expression levels of most PRGs and poorer prognoses. Furthermore, PRGcluster C and geneCluster A, both associated with reduced survival rates, displayed higher risk scores. This reinforcing the correlation between higher risk scores in our established signature and unfavorable prognostic outcomes. Our risk model has practical applications in treatment personalization, increased surveillance frequency, and patient prognosis prediction. Specifically, high-risk patients may benefit from aggressive therapies, while more frequent monitoring and surveillance can aid in early disease detection. Moreover, our analysis encompassing ROC curves, nomograms, and calibration plots underscored the superior predictive performance and accuracy of the constructed signature. The 1-,3-,5-year AUC was 0.735, 0.706, 0.638 in the present model, while another study PANoptosis-related gene signature model showed 1-,3-,5-year AUC was 0.707, 0.622, and 0.562, respectively. This indicating that the efficiency of diagnosis of our model was superior than previous prognostic model (38).

Four risk gene (G6PD, CTSC, CDCA8, *and* CXCL9) were identified and utilized to calculate the risk score in our study. These four risk genes have been previously associated with various types of malignant tumors, including HCC. G6PD has been recognized as a prognostic signature and a potential treatment target for different tumors (39). Zeng et al. reported that the expression of G6PD in HCC tissues was upregulated compared to the corresponding adjacent normal tissues (39). In our qRT-PCR analysis, we confirmed the elevated expression of *G6PD* in HCC tissues and HCC cell lines. *G6PD* is known to promote HCC cell proliferation, invasion, migration and inhibit ferroptosis. Knockdown *G6PD* or inhibit it with smilax China root extract could suppresses HCC cell growth, tumorigenesis and metastasis (39–41). CDCA8, a crucial regulator of mitosis, is upregulated in numerous cancer types. A high expression of CDCA8 has been associated with higher AFP, larger tumor size, pathological status, T stage, and poor prognosis in HCC. Silencing CDCA8 could suppresses tumor growth, proliferation, and stemness of HCC by inactivating AKT/β–Catenin Signaling, and regulating the CDK1/cyclin B1 signaling axis (42–45). CXCL9, a specific ligand for CXCR3, facilitates tumor-suppressive lymphocytic infiltration in certain solid tumors coupled with its two family members CXCL10 and CXCL11 (46). Increasing evidence has demonstrated that CXCL9 is closely correlated with the prognosis of certain solid tumor patients, such as colorectal cancer lung cancer, and HCC (47). Ding et al. revealed that CXCL9 binding to CXCR3 promotes metastasis and invasion of CD133+ liver cancer cells via the p-ERK1/2-MMP2/MMP9 pathway (48). In addition, increasing the expression of CXCL9 with rhCXCL9 has been reported to enhance the HCC invasion ability by upregulating the PREX2 (49).

Cathepsin C(CTSC), a lysosomal cysteine protease abundantly expressed in multiple tissues and belonging to the papain superfamily, plays a pivotal role in numerous tumor biological processes. Moreover, CTSC regulates breast cancer lung metastases by modulating neutrophil infiltration and the formation of neutrophil extracellular traps (50). Silencing CTSC has the capacity to promote apoptosis, thereby restraining the growth of colorectal cancer. Furthermore, it can enhance colorectal cancer metastasis by modulating immune escape through the upregulation of CSF1 (51, 52). An earlier study has documented the pivotal role of cathepsin C in regulating pyroptosis and lysosome-mediated cell death within cathepsin C-deficient mouse splenocytes (53). For HCC, CTSC collaborates with the TNF-α/p38 MAPK Signaling Pathway to enhance proliferation and metastasis (54). In addition, our results also showed that inhibition CTSC could attenuated HCC cells metastasis and proliferation, confirming the previous results. This indicated that CTSC could be a target for HCC therapy.

Immunoreactivity plays a critical role in the development of tumors and offers a promising target for potential cancer therapies (55). Our risk score was negatively correlated with CD8 T cells, macrophages M1, and naïve B cells, and positively correlated with neutrophils, macrophages M2. A higher number of CD8+ T cell, macrophages M1, cases were positively associated with better OS and DFS in HCC patients, whereas macrophages M2 were related to a poor prognosis and outcome of HCC (56–59). This is consistent with our finding that the low-risk group had a better prognosis, as shown in our previous overall survival analysis. In the present study, we also explore the correlation among risk genes, risk score, and immune cells. The results showed that high-risk group associated with a lower Stromal Score, Immnune Score, and ESTIMATE score, and higher TMB. This suggests that our signature could predict the TME composition. These result of our study was aligned with a previous study based on cuproptosis-related genes (60). However, another model based on the immune-related gene was on the contrast, namely high-risk group have a higher Stromal Score, Immnune Score, and ESTIMATE score (61). CSCs, as a driver of tumor progression and growth, contribute to metastasis, recurrence, and drug resistance (62). A previous study indicated that a high immune score is indicative of improved chemotherapy and immunotherapy efficacy (63). In our research, we found the low-risk group displayed higher immune and lower stem cell content, implying a more favorable anti-tumor treatment. We found that TP53 and CTNNB1 genes were the most frequently mutated genes in both groups, which was consistent with previous study (64). Mutations in TP53 gene is regarded as a major driver of HCC, and higher mutation rate of TP53 was associated with poor overall survival (65). In our study, we found that high-risk group have higher mutation frequency of TP53 and poor prognosis, compared to low-risk group. Our study showed that Oxaliplatin, irinotecan, and sorafenib was more sensitivity in low-risk group, consistent with previous studies (66–68) supporting our risk model possesses the potential to predict the effectiveness of drugs treatment. In addition, one person can be stratified into high- or low-risk group

and matching the most suitable personalized medicine through prediction based on based on the expression of risk gene of the person, then increasing the treatment effectiveness.

Nonetheless, our study had certain limitations. Firstly, the majority of our analyses relied on publicly available datasets and all samples were obtained retrospectively, which could have introduce cases selection bias and thus affected the accuracy of our finding. Hence, it is imperative to conduct well-designed prospective studies in order to validate the robustness and applicability of our findings. Secondly, although we conducted expression validation at both tissue and HCC cell levels, the sample size was relatively limited. We plane to are committed to expanding our sample collection efforts to assess this signature in the context of immunotherapy in the future. Thirdly, some crucial clinical variables such as surgical interventions, neoadjuvant chemotherapy, and tumor markers were not included in our study. Fourthly, although we have performed qRT-PCR to validate the relationship between CTSC and PANoptosis marker gene, more research, including Western blotting and IHC need conducted to confirm the result. Finally, although our prognostic model has some benefits, it has some barrier to clinical implementation. For example, the data availability and quality, and cost-effectiveness due to additional tests, monitoring. Consequently, our findings' validity is relies on the inclusion of clinical cases.

Conclusion

In conclusion, we have developed a pivotal PANoptosis-based molecular clustering approach and prognostic signature with multifaceted capabilities, including survival prediction, TMB assessment, and clinical therapy guidance. Our study has the potential to advance our understanding of PANoptosis in HCC and contribute to the development of more effective personalized immunotherapy or targeted therapy. Nonetheless, it is imperative to acknowledge the inherent limitations of this study, and further experiments and clinical case validations are warranted to substantiate our findings.

Data availability statement

The datasets presented in this study can be found in online repositories. The names of the repository/repositories and accession number(s) can be found in the article/Supplementary Material.

Ethics statement

The studies involving humans were approved by The Medical Ethics Committee of LiuZhou People's Hospital Affiliated to Guangxi Medical University. The studies were conducted in accordance with the local legislation and institutional requirements. The participants provided their written informed consent to participate in this study. The animal studies were approved by The Medical Ethics Committee of LiuZhou People's Hospital Affiliated to Guangxi Medical University, and all patients provided written informed consent in accordance with the Declaration of Helsinki. The studies were conducted in accordance with the local legislation and institutional requirements. Written informed consent was obtained from the owners for the participation of their animals in this study. Written informed consent was obtained from the individual(s) for the publication of any potentially identifiable images or data included in this article.

Author contributions

GO: Data curation, Formal analysis, Validation, Writing – original draft, Funding acquisition, Project administration, Software, Writing – review & editing. QL: Validation, Formal analysis, Software, Writing – original draft. YW: Writing – original draft. WD: Writing – review & editing, Project administration. HD: Validation, Writing – review & editing, Project administration. YLL: Software, Writing – review & editing. JL: Writing – review & editing, Software. ML: Writing – review & editing, Software. SWL: Data curation, Writing – review & editing. SL: Data curation, Writing – review & editing. YYL: Writing – review & editing, Data curation. GP: Funding acquisition, Writing – review & editing, Data curation. JY: Writing – review & editing, Writing – original draft. TG: Data curation, Writing – original draft, Writing – review & editing.

Funding

The author(s) declare financial support was received for the research, authorship, and/or publication of this article. This work was supported in part by Guangxi Key Laboratory of Early Prevention and Treatment for Regional High Frequency Tumor (NO. GKE-KF202303), Guangxi Key Research and Development Plan (No. Guike AB23026016), Liuzhou Science and Technology Project (2021CBC0101).

Acknowledgments

We express our sincere gratitude to the reviewers for their helpful comments on the present article, as well as the researcher providing the data sets of TCGA. We thank Bullet Edits Limited for the linguistic editing and proofreading of the manuscript.

Conflict of interest

The authors declare that the research was conducted in the absence of any commercial or financial relationships that could be construed as a potential conflict of interest.

Publisher's note

All claims expressed in this article are solely those of the authors and do not necessarily represent those of their affiliated organizations, or those of the publisher, the editors and the reviewers. Any product that may be evaluated in this article, or claim that may be made by its manufacturer, is not guaranteed or endorsed by the publisher.

Supplementary material

The Supplementary Material for this article can be found online at: https://www.frontiersin.org/articles/10.3389/fimmu.2024.1323199/full#supplementary-material

References

1. Sung H, Ferlay J, Siegel RL, Laversanne M, Soerjomataram I, Jemal A, et al. Global cancer statistics 2020: GLOBOCAN estimates of incidence and mortality worldwide for 36 cancers in 185 countries. *CA: Cancer J Clin.* (2021) 71:209–49. doi: 10.3322/caac.21660

2. Llovet JM, Kelley RK, Villanueva A, Singal AG, Pikarsky E, Roayaie S, et al. Hepatocellular carcinoma. *Nat Rev Dis Primers.* (2021) 7:6. doi: 10.1038/s41572-020-00240-3

3. Chakraborty E, Sarkar D. Emerging therapies for hepatocellular carcinoma (HCC). *Cancers.* (2022) 14:2798. doi: 10.3390/cancers14112798

4. Jemal A, Ward EM, Johnson CJ, Cronin KA, Ma J, Ryerson B, et al. Annual report to the nation on the status of cancer, 1975-2014, featuring survival. *J Natl Cancer Inst.* (2017) 109:djx030. doi: 10.1093/jnci/djx030

5. García-Pras E, Fernández-Iglesias A, Gracia-Sancho J, Pérez-del-Pulgar S. Cell death in hepatocellular carcinoma: pathogenesis and therapeutic opportunities. *Cancers.* (2021) 14:48. doi: 10.3390/cancers14010048

6. Wang Y, Kanneganti T-D. From pyroptosis, apoptosis and necroptosis to PANoptosis: A mechanistic compendium of programmed cell death pathways. *Comput Struct Biotechnol J.* (2021) 19:4641–57. doi: 10.1016/j.csbj.2021.07.038

7. Pandian N, Kanneganti T-D. PANoptosis: A unique innate immune inflammatory cell death modality. *J Immunol.* (2022) 209:1625–33. doi: 10.4049/jimmunol.2200508

8. Samir P, Malireddi RKS, Kanneganti T-D. The PANoptosome: A deadly protein complex driving pyroptosis, apoptosis, and necroptosis (PANoptosis). *Front Cell Infect Microbiol.* (2020) 10:238. doi: 10.3389/fcimb.2020.00238

9. Shi C, Cao P, Wang Y, Zhang Q, Zhang D, Wang Y, et al. PANoptosis: A cell death characterized by pyroptosis, apoptosis, and necroptosis. *J Inflamm Res.* (2023) 16:1523–32. doi: 10.2147/JIR.S403819

10. Nicolè L, Sanavia T, Cappellesso R, Maffeis V, Akiba J, Kawahara A, et al. Necroptosis-driving genes RIPK1, RIPK3 and MLKL-p are associated with intratumoral CD3+ and CD8+ T cell density and predict prognosis in hepatocellular carcinoma. *J Immunother Cancer.* (2022) 10:e004031. doi: 10.1136/jitc-2021-004031

11. Zou Z, Zhao M, Yang Y, Xie Y, Li Z, Zhou L, et al. The role of pyroptosis in hepatocellular carcinoma. *Cell Oncol (Dordrecht).* (2023) 46(4):811–23. doi: 10.1007/s13402-023-00787-9

12. Yang Y, Zhang Y, Cao J, Su Z, Li F, Zhang P, et al. FGFR4 and EZH2 inhibitors synergistically induce hepatocellular carcinoma apoptosis *via* repressing YAP signaling. *J Exp Clin Cancer Res: CR.* (2023) 42:96. doi: 10.1186/s13046-023-02659-4

13. Wheeler DA, Roberts LR. Comprehensive and integrative genomic characterization of hepatocellular carcinoma. *Cell.* (2017) 169:1327–1341.e23. doi: 10.1016/j.cell.2017.05.046

14. Grinchuk OV, Yenamandra SP, Iyer R, Singh M, Lee HK, Lim KH, et al. Tumor-adjacent tissue co-expression profile analysis reveals pro-oncogenic ribosomal gene signature for prognosis of resectable hepatocellular carcinoma. *Mol Oncol.* (2018) 12:89–113. doi: 10.1002/1878-0261.12153

15. Leek JT, Johnson WE, Parker HS, Jaffe AE, Storey JD. The sva package for removing batch effects and other unwanted variation in high-throughput experiments. *Bioinformatics.* (2012) 28:882–3. doi: 10.1093/bioinformatics/bts034

16. Wang X, Sun R, Chan S, Meng L, Xu Y, Zuo X, et al. PANoptosis-based molecular clustering and prognostic signature predicts patient survival and immune landscape in colon cancer. *Front Genet.* (2022) 13:955355. doi: 10.3389/fgene.2022.955355

17. Ritchie ME, Phipson B, Wu D, Hu Y, Law CW, Shi W, et al. limma powers differential expression analyses for RNA-sequencing and microarray studies. *Nucleic Acids Res.* (2015) 43:e47. doi: 10.1093/nar/gkv007

18. Wilkerson MD, Hayes DN. ConsensusClusterPlus: a class discovery tool with confidence assessments and item tracking. *Bioinformatics.* (2010) 26:1572–3. doi: 10.1093/bioinformatics/btq170

19. Wickham H, Chang W, Wickham MH. Package 'ggplot2.' *Create elegant data visualisations using the grammar of graphics Version* (2016). Available at: https://search.r-project.org/CRAN/refmans/ggplot2/html/ggplot2-package.html.

20. Hänzelmann S, Castelo R, Guinney J. GSVA: gene set variation analysis for microarray and RNA-Seq data. *BMC Bioinf.* (2013) 14:7. doi: 10.1186/1471-2105-14-7

21. Liberzon A, Birger C, Thorvaldsdóttir H, Ghandi M, Mesirov JP, Tamayo P. The Molecular Signatures Database (MSigDB) hallmark gene set collection. *Cell Syst.* (2015) 1:417–25. doi: 10.1016/j.cels.2015.12.004

22. Yu G, Wang L-G, Han Y, He Q-Y. clusterProfiler: an R package for comparing biological themes among gene clusters. *OMICS.* (2012) 16:284–7. doi: 10.1089/omi.2011.0118

23. Tibshirani R. The lasso method for variable selection in the Cox model. *Stat Med.* (1997) 16:385–95. doi: 10.1002/(sici)1097-0258(19970228)16:4<385::aid-sim380>3.0.co;2-3

24. Guan M, Jiao Y, Zhou L. Immune infiltration analysis with the CIBERSORT method in lung cancer. *Dis Markers.* (2022) 2022:3186427. doi: 10.1155/2022/3186427

25. Scire J, Huisman JS, Grosu A, Angst DC, Lison A, Li J, et al. estimateR: an R package to estimate and monitor the effective reproductive number. *BMC Bioinf.* (2023) 24:310. doi: 10.1186/s12859-023-05428-4

26. Yoshihara K, Shahmoradgoli M, Martínez E, Vegesna R, Kim H, Torres-Garcia W, et al. Inferring tumour purity and stromal and immune cell admixture from expression data. *Nat Commun.* (2013) 4:2612. doi: 10.1038/ncomms3612

27. Yi M, Nissley DV, McCormick F, Stephens RM. ssGSEA score-based Ras dependency indexes derived from gene expression data reveal potential Ras addiction mechanisms with possible clinical implications. *Sci Rep.* (2020) 10:1–16. doi: 10.1038/s41598-020-66986-8

28. Mayakonda A, Lin D-C, Assenov Y, Plass C, Koeffler HP. Maftools: efficient and comprehensive analysis of somatic variants in cancer. *Genome Res.* (2018) 28:1747–56. doi: 10.1101/gr.239244.118

29. Astivia OLO, Zumbo BD. Population models and simulation methods: The case of the Spearman rank correlation. *Br J Math Stat Psychol.* (2017) 70:347–67. doi: 10.1111/bmsp.12085

30. Maeser D, Gruener RF, Huang RS. oncoPredict: an R package for predicting in vivo or cancer patient drug response and biomarkers from cell line screening data. *Brief Bioinform.* (2021) 22:bbab260. doi: 10.1093/bib/bbab260

31. Yang L, Shi P, Zhao G, Xu J, Peng W, Zhang J, et al. Targeting cancer stem cell pathways for cancer therapy. *Signal Transduct Target Ther.* (2020) 5:8. doi: 10.1038/s41392-020-0110-5

32. Yang J, Pan G, Guan L, Liu Z, Wu Y, Liu Z, et al. The burden of primary liver cancer caused by specific etiologies from 1990 to 2019 at the global, regional, and national levels. *Cancer Med.* (2022) 11:1357–70. doi: 10.1002/cam4.4530

33. Zheng P, Xiao W, Zhang J, Zheng X, Jiang J. The role of AIM2 in human hepatocellular carcinoma and its clinical significance. *Pathol Res Pract.* (2023) 245:154454. doi: 10.1016/j.prp.2023.154454

34. Tang Y-L, Tao Y, Zhu L, Shen J-L, Cheng H. Role of NLRP3 inflammasome in hepatocellular carcinoma: A double-edged sword. *Int Immunopharmacol.* (2023) 118:110107. doi: 10.1016/j.intimp.2023.110107

35. Hinshaw DC, Shevde LA. The tumor microenvironment innately modulates cancer progression. *Cancer Res.* (2019) 79:4557–66. doi: 10.1158/0008-5472.CAN-18-3962

36. Hao X, Sun G, Zhang Y, Kong X, Rong D, Song J, et al. Targeting immune cells in the tumor microenvironment of HCC: new opportunities and challenges. *Front Cell Dev Biol*. (2021) 9:775462. doi: 10.3389/fcell.2021.775462

37. Kotsari M, Dimopoulou V, Koskinas J, Armakolas A. Immune system and hepatocellular carcinoma (HCC): new insights into HCC progression. *Int J Mol Sci*. (2023) 24:11471. doi: 10.3390/ijms241411471

38. Wei Y, Lan C, Yang C, Liao X, Zhou X, Huang X, et al. Robust analysis of a novel PANoptosis-related prognostic gene signature model for hepatocellular carcinoma immune infiltration and therapeutic response. *Sci Rep*. (2023) . 13:14519. doi: 10.1038/s41598-023-41670-9

39. Zeng T, Li B, Shu X, Pang J, Wang H, Cai X, et al. Pan-cancer analysis reveals that G6PD is a prognostic biomarker and therapeutic target for a variety of cancers. *Front Oncol*. (2023) 13:1183474. doi: 10.3389/fonc.2023.1183474

40. Cao F, Luo A, Yang C. G6PD inhibits ferroptosis in hepatocellular carcinoma by targeting cytochrome P450 oxidoreductase. *Cell Signal*. (2021) 87:110098. doi: 10.1016/j.cellsig.2021.110098

41. Kanwal L, Ali S, Rasul A, Tahir HM. Smilax China root extract as a novel Glucose- 6-phosphate dehydrogenase inhibitor for the treatment of hepatocellular carcinoma. *Saudi J Biol Sci*. (2022) 29:103400. doi: 10.1016/j.sjbs.2022.103400

42. Wu H, Liu S, Wu D, Zhou H, Sui G, Wu G. Cell division cycle-associated 8 is a prognostic biomarker related to immune invasion in hepatocellular carcinoma. *Cancer Med*. (2023) 12:10138–55. doi: 10.1002/cam4.5718

43. Shuai Y, Fan E, Zhong Q, Chen Q, Feng G, Gou X, et al. CDCA8 as an independent predictor for a poor prognosis in liver cancer. *Cancer Cell Int*. (2021) 21:159. doi: 10.1186/s12935-021-01850-x

44. Jeon T, Ko MJ, Seo Y-R, Jung S-J, Seo D, Park S-Y, et al. Silencing CDCA8 suppresses hepatocellular carcinoma growth and stemness *via* restoration of ATF3 tumor suppressor and inactivation of AKT/β–catenin signaling. *Cancers*. (2021) 13:1055. doi: 10.3390/cancers13051055

45. Cui Y, Jiang N. CDCA8 facilitates tumor proliferation and predicts a poor prognosis in hepatocellular carcinoma. *Appl Biochem Biotechnol*. (2024) 196(3):1481–92. doi: 10.1007/s12010-023-04603-w

46. Seitz S, Dreyer TF, Stange C, Steiger K, Bräuer R, Scheutz L, et al. CXCL9 inhibits tumour growth and drives anti-PD-L1 therapy in ovarian cancer. *Br J Cancer*. (2022) 126:1470–80. doi: 10.1038/s41416-022-01763-0

47. Ding Q, Lu P, Xia Y, Ding S, Fan Y, Li X, et al. CXCL9: evidence and contradictions for its role in tumor progression. *Cancer Med*. (2016) 5:3246–59. doi: 10.1002/cam4.934

48. Ding Q, Xia Y, Ding S, Lu P, Sun L, Liu M. An alternatively spliced variant of CXCR3 mediates the metastasis of CD133+ liver cancer cells induced by CXCL9. *Oncotarget*. (2016) 7:14405–14. doi: 10.18632/oncotarget.7360

49. Lan X, Xiao F, Ding Q, Liu J, Liu J, Li J, et al. The effect of CXCL9 on the invasion ability of hepatocellular carcinoma through up-regulation of PREX2. *J Mol Histol*. (2014) 45:689–96. doi: 10.1007/s10735-014-9593-0

50. Xiao Y, Cong M, Li J, He D, Wu Q, Tian P, et al. Cathepsin C promotes breast cancer lung metastasis by modulating neutrophil infiltration and neutrophil extracellular trap formation. *Cancer Cell*. (2021) 39:423–437.e7. doi: 10.1016/j.ccell.2020.12.012

51. Dang Y-Z, Chen X-J, Yu J, Zhao S-H, Cao X-M, Wang Q. Cathepsin C promotes colorectal cancer metastasis by regulating immune escape through upregulating CSF1. *Neoplasma*. (2023) 70:123–35. doi: 10.4149/neo_2023_220726N757

52. Khaket TP, Singh MP, Khan I, Kang SC. *In vitro* and in *vivo* studies on potentiation of curcumin-induced lysosomal-dependent apoptosis upon silencing of cathepsin C in colorectal cancer cells. *Pharmacol Res*. (2020) 161:105156. doi: 10.1016/j.phrs.2020.105156

53. Fløyel T, Frørup C, Størling J, Pociot F. Cathepsin C regulates cytokine-induced apoptosis in β-cell model systems. *Genes (Basel)*. (2021) 12:1694. doi: 10.3390/genes12111694

54. Zhang G-P, Yue X, Li S-Q. Cathepsin C interacts with TNF-α/p38 MAPK signaling pathway to promote proliferation and metastasis in hepatocellular carcinoma. *Cancer Res Treat: Off J Korean Cancer Assoc*. (2020) 52:10–23. doi: 10.4143/crt.2019.145

55. Wang D-R, Wu X-L, Sun Y-L. Therapeutic targets and biomarkers of tumor immunotherapy: response versus non-response. *Signal Transduct Target Ther*. (2022) 7:331. doi: 10.1038/s41392-022-01136-2

56. Dong P, Ma L, Liu L, Zhao G, Zhang S, Dong L, et al. $CD86^+/CD206^+$, diametrically polarized tumor-associated macrophages, predict hepatocellular carcinoma patient prognosis. *Int J Mol Sci*. (2016) 17:320. doi: 10.3390/ijms17030320

57. Sachdeva M, Arora SK. Prognostic role of immune cells in hepatocellular carcinoma. *EXCLI J*. (2020) 19:718–33. doi: 10.17179/excli2020-1455

58. Li J-Q, Yu X-J, Wang Y-C, Huang L-Y, Liu C-Q, Zheng L, et al. Distinct patterns and prognostic values of tumor-infiltrating macrophages in hepatocellular carcinoma and gastric cancer. *J Transl Med*. (2017) 15:37. doi: 10.1186/s12967-017-1139-2

59. Atanasov G, Dino K, Schierle K, Dietel C, Aust G, Pratschke J, et al. Immunologic cellular characteristics of the tumour microenvironment of hepatocellular carcinoma drive patient outcomes. *World J Surg Oncol*. (2019) 17:97. doi: 10.1186/s12957-019-1635-3

60. Peng X, Zhu J, Liu S, Luo C, Wu X, Liu Z, et al. Signature construction and molecular subtype identification based on cuproptosis-related genes to predict the prognosis and immune activity of patients with hepatocellular carcinoma. *Front Immunol*. (2022) 13:990790. doi: 10.3389/fimmu.2022.990790

61. Wang L, Wang L, He P. Comprehensive analysis of immune-related gene signature based on ssGSEA algorithms in the prognosis and immune landscape of hepatocellular carcinoma. *Front Genet*. (2022) 13:1064432. doi: 10.3389/fgene.2022.1064432

62. Walcher L, Kistenmacher A-K, Suo H, Kitte R, Dluczek S, Strauß A, et al. Cancer stem cells—Origins and biomarkers: perspectives for targeted personalized therapies. *Front Immunol*. (2020) 11:1280. doi: 10.3389/fimmu.2020.01280

63. Dai G-P, Wang L-P, Wen Y-Q, Ren X-Q, Zuo S-G. Identification of key genes for predicting colorectal cancer prognosis by integrated bioinformatics analysis. *Oncol Lett*. (2020) 19:388–98. doi: 10.3892/ol.2019.11068

64. Kumar S, Nadda N, Quadri A, Kumar R, Paul S, Tanwar P, et al. Assessments of TP53 and CTNNB1 gene hotspot mutations in circulating tumour DNA of hepatitis B virus-induced hepatocellular carcinoma. *Front Genet*. (2023) 14:1235260. doi: 10.3389/fgene.2023.1235260

65. Woo HG, Wang XW, Budhu A, Kim YH, Kwon SM, Tang Z, et al. Association of *TP53* mutations with stem cell-like gene expression and survival of patients with hepatocellular carcinoma. *Gastroenterology*. (2011) 140:1063–1070.e8. doi: 10.1053/j.gastro.2010.11.034

66. Keating GM. Sorafenib: a review in hepatocellular carcinoma. *Target Oncol*. (2017) 12:243–53. doi: 10.1007/s11523-017-0484-7

67. Lai Z, Huang Y, Wen D, Lin X, Kan A, Li Q, et al. One day versus two days of hepatic arterial infusion with oxaliplatin and fluorouracil for patients with unresectable hepatocellular carcinoma. *BMC Med*. (2022) 20:415. doi: 10.1186/s12916-022-02608-6

68. Liu Q, Hua S, Wang X, Chen F, Gou S. The introduction of immunosuppressor (TDO inhibitor) significantly improved the efficacy of irinotecan in treating hepatocellular carcinoma. *Cancer Immunol Immunother*. (2021) 70:497–508. doi: 10.1007/s00262-020-02697-3

frontiers | Frontiers in Immunology

TYPE Original Research
PUBLISHED 25 July 2024
DOI 10.3389/fimmu.2024.1374465

OPEN ACCESS

EDITED BY
Yongqian Shu,
Nanjing Medical University, China

REVIEWED BY
Young-im Kim,
National Institutes of Health (NIH), United States
Li-Da Wu,
Nanjing Medical University, China

*CORRESPONDENCE
Song-Mei Liu
smliu@whu.edu.cn

†These authors have contributed equally to this work

RECEIVED 22 January 2024
ACCEPTED 11 July 2024
PUBLISHED 25 July 2024

CITATION
Xu S, Zhang Y, Yang Y, Dong K, Zhang H, Luo C and Liu S-M (2024) A m^{6}A regulators-related classifier for prognosis and tumor microenvironment characterization in hepatocellular carcinoma.
Front. Immunol. 15:1374465.
doi: 10.3389/fimmu.2024.1374465

A m^{6}A regulators-related classifier for prognosis and tumor microenvironment characterization in hepatocellular carcinoma

Shaohua Xu[1,2†], Yi Zhang[1†], Ying Yang[1†], Kexin Dong[1], Hanfei Zhang[1], Chunhua Luo[2] and Song-Mei Liu[1*]

[1]Department of Clinical Laboratory, Center for Gene Diagnosis & Program of Clinical Laboratory, Zhongnan Hospital of Wuhan University, Wuhan, China, [2]The First College of Clinical Medical Science, China Three Gorges University, Yichang, China

Background: Increasing evidence have highlighted the biological significance of mRNA N^6-methyladenosine (m^{6}A) modification in regulating tumorigenicity and progression. However, the potential roles of m^{6}A regulators in tumor microenvironment (TME) formation and immune cell infiltration in liver hepatocellular carcinoma (LIHC or HCC) requires further clarification.

Method: RNA sequencing data were obtained from TCGA-LIHC databases and ICGC-LIRI-JP databases. Consensus clustering algorithm was used to identify m^{6}A regulators cluster subtypes. Weighted gene co-expression network analysis (WGCNA), LASSO regression, Random Forest (RF), and Support Vector Machine-Recursive Feature Elimination (SVM-RFE) were applied to identify candidate biomarkers, and then a m^{6}Arisk score model was constructed. The correlations of m^{6}Arisk score with immunological characteristics (immunomodulators, cancer immunity cycles, tumor-infiltrating immune cells (TIICs), and immune checkpoints) were systematically evaluated. The effective performance of nomogram was evaluated using concordance index (C-index), calibration plots, decision curve analysis (DCA), and receiver operating characteristic curve (ROC).

Results: Two distinct m^{6}A modification patterns were identified based on 23 m^{6}A regulators, which were correlated with different clinical outcomes and biological functions. Based on the constructed m^{6}Arisk score model, HCC patients can be divided into two distinct risk score subgroups. Further analysis indicated that the m^{6}Arisk score showed excellent prognostic performance. Patients with a high m^{6}Arisk score was significantly associated with poorer clinical outcome, lower drug sensitivity, and higher immune infiltration. Moreover, we developed a nomogram model by incorporating the m^{6}Arisk score and clinicopathological features. The application of the m^{6}Arisk score for the prognostic stratification of HCC has good clinical applicability and clinical net benefit.

Conclusion: Our findings reveal the crucial role of m^{6}A modification patterns for predicting HCC TME status and prognosis, and highlight the good clinical applicability and net benefit of m^{6}Arisk score in terms of prognosis, immunophenotype, and drug therapy in HCC patients.

KEYWORDS

N^6-methyladenosine, WGCNA, SVM-RFE, LASSO, consensus clustering algorithm, TIICs, DCA

1 Introduction

Hepatocellular carcinomas (HCC, accounting for 90% of liver cancer) is one of the most frequent fatal malignancies and ranks fourth among cancer-related mortality worldwide (1). Despite recent great advances in treatment interventions, 5-year overall survival (OS) for HCC patients remains poor and unsatisfactory, with only 5% to 15% of early-stage patients qualifying for surgical excision (2). HCC is insidious and develops rapidly, and patients are usually diagnosed at an advanced stage. The treatment strategies that are currently available for more than 90% of liver cancer patients mainly include chemotherapy, immunotherapy, natural compounds, and nanotechnology (2). However, the clinical benefit of these therapies remains unsatisfactory, mainly due to the lack of effective pre-treatment predictive biomarkers. Besides, treatment of regional resection and liver transplantation is still limited, and the recurrence rate after regional resection is high. Therefore, it is imperative to identify novel reliable biomarkers and therapeutic targets that enable early diagnosis and treatment response prediction for HCC patients.

Although the risk factors for liver carcinogenesis are well defined (including hepatitis B and C viruses, fatty liver, alcoholic cirrhosis, diabetes, obesity, etc), the underlying molecular mechanisms remain ambiguous. Extensive evidence shows that epigenetic mechanisms is implicated in multiple aspects of cancer biology, from driving primary tumor growth and invasion to modulating the immune response within the tumor microenvironment (TME). The complex bidirectional dynamic cross-talk between cancer cells and their microenvironment has been identified as a key factor that drives tumor initiation, growth, progression, malignant conversion, invasion, metastasis, drug resistance and patient prognosis (3–5). TME is a complex and evolving multi-layered cellular environment composed of stroma, vascular, and innate/adaptive immune cells, as well as a community of malignant clones (6). N^6-methyladenosine (m^{6}A) methylation is one of the most common types of modifications in eukaryotic messenger RNA (mRNA). Similar to modifications in DNA or proteins, it is regulated by various types of regulators, including methyltransferases (“ writers “), RNA-binding proteins (“ readers “), and demethylases (“ erasers “). Dysregulation of m^{6}A regulatory factors is associated with malignant tumor progression and TME-specific immunomodulation abnormalities (7, 8). Nonetheless, the role of m6A regulators in TME heterogeneity and immune cell infiltration in HCC remains to be further investigated. Therefore, it is crucial to comprehensively understand the relationship between RNA methylation modification patterns and genetic alterations underlying cancer cell heterogeneity.

Cancer is both a genetic and epigenetic disease. Gene mutations and epigenetic alterations have been identified as significant contributors to human carcinogenesis. Unlike genetic mutations, epigenetic modifications refer to heritable changes that mediate gene expression without altering the genetic DNA sequence (9). Extensive evidence shows that epigenetic mechanisms is implicated in multiple aspects of cancer biology, from driving primary tumor growth and invasion to modulating the immune response within the TME. Epigenetics-based diagnostic and prognostic tools also greatly contribute to the development of precision oncology. Recent studies have reported that abnormal decreases or increases in the overall abundance of m^{6}A in some types of cancer may be associated with cancer progression and clinical outcomes. It has been reported that the overall abundance and expression level of m^{6}A in mRNA or total RNA in human gastric cancer and liver cancer tissues are significantly increased, and are closely related to the expression level of m^{6}A methylation regulatory enzymes (10, 11). It has also been reported that the overall abundance of m^{6}A is significantly reduced in more advanced human bladder cancer tissues and is associated with poor prognosis in bladder cancer patients (12). Another study showed that m^{6}A abundance is associated with therapeutic drug response and may be an epigenetic driver of chemotherapy resistance (13). Together, these results suggest that m^{6}A modification regulators have different potential in prognosis stratification and the development of new therapeutic strategies across various cancers. Due to immune evasion and heterogeneity in the TME, only a minority of patients respond favorably to immunotherapy. At this point, better stratification is urgently needed for HCC patients to enhance treatment efficacy. Therefore, comprehensive investigation of m^{6}A modification and its biological roles in HCC may contribute to improving prognosis prediction and personalized precision treatment approaches for HCC.

In this study, we first profiled the expression of 23 m^{6}A regulators and identified two distinct m^{6}A regulator-mediated modification patterns based on TCGA-LIHC cohort. We then constructed a novel m^{6}A-risk scoring system to quantify the m^{6}A

modification patterns in individual tumors and to predict the clinical response of HCC patients to common chemotherapy or targeted drugs. Additionally, we comprehensively evaluated the association between m^{6}A modification patterns and TME cell-infiltrating characteristics.

2 Materials and methods

2.1 Data source and preprocessing

RNA-sequencing data (counts value) with corresponding complete clinical information of HCC were obtained from TCGA-LIHC program (https://portal.gdc.cancer.gov/repository) and ICGC-LIRI-JP database (https://dcc.icgc.org). The annotation file of GRCh38 (version 36) was downloaded from GENCODE to identify the length of each mRNA. Subsequently, RNA-sequencing data in counts format was transformed into transcripts per kilobase million (TPM) format and further subjected to log2 transformation for normalization. In addition, somatic mutation data and CNV files were retrieved from the TCGA-LIHC program. Samples lacking clinicopathological information or survival outcomes were excluded from further analysis. Ultimately, 23 acknowledged m^{6}A regulator genes, including 8 writers, 13 readers, and 2 erasers, were identified from previous studies (14–16).

2.2 Unsupervised clustering of m^{6}A regulator genes

Consensus unsupervised clustering analysis was employed for identifying distinct m^{6}A regulator modification patterns in the TCGA-LIHC cohort by the k-means algorithms, which is available in the "ConsensusClusterPlus" R package (17, 18). The "ConsensusClusterPlus" package provides quantitative stability evidence to determine a cluster count and cluster membership in an unsupervised analysis. The quantity and stability of clusters were determined by consensus clustering algorithm, and conducted for 1,000 iterations (18). The cumulative distribution function (CDF) curves were used to determine the optimal number of clusters, indexed by k-means algorithms value from 2 to 9. Ultimately, based on the clustering effect, the clustering stability was higher when k = 2.

2.3 Differentially expressed genes analysis

The expression profile data from TCGA-LIHC cohorts were preprocessed by R software (V.4.0.5). The differential expression analysis between two distinct m^{6}A cluster subtypes were performed using the "DESeq2" R package (19) (V.1.38.3). Genes with |log2FoldChange| > 1 and P adj < 0.001 were regarded as statistically significant. Furthermore, Gene ontology (GO) and Kyoto Encyclopedia of Genes and Genomes (KEGG) pathway enrichment analyses were performed for DEGs using the "clusterProfiler" R package. GO categories comprised biological processes (BP), molecular functions (MF), and cellular components (CC). The p-value was adjusted using the Benjamini–Hochberg (BH) approach or False Discovery Rate (FDR) for multiple testing corrections. The results satisfied FDR < 0.05 were regarded as statistically significant.

2.4 Gene set enrichment analysis

This analysis aimed to discern potentially relevant gene expression signatures between distinct m^{6}A cluster subtypes utilizing the 'clusterProfiler' package (V.4.6.0). The reference gene set for GSEA analysis, 'c2.cp.kegg.v7.4.symbols.gmt,' was obtained from MSigDB database (http://software.broadinstitute.org/gsea/msigdb/index.jsp). Differential expression analysis between the two cluster subtypes was conducted using "DEseq2" package (V.1.38.3). Subsequently, all genes were ranked from high to bottom according to log2-fold change, and this sorted gene set was used for GSEA analysis. For achieving a normalized enrichment score (NES) for each analysis, a permutation test with 1,000 iterations were performed. The pathways meeting the criteria of |NES| > 1, p-value < 0.05, and q-value < 0.05 were regarded as significant enrichment.

2.5 Gene set variation analysis

This analysis was performed to assess the variation of hallmark pathway activity in distinct m^{6}A cluster subtypes via 'GSVA' package (V.1.38.0) in an unsupervised manner (20). In this study, the gene set 'h.all.v7.4.symbols.gmt' was selected as the background gene set for GSVA analysis, which was downloaded from MSigDB database (21). The 'limma' R package was utilized to analyze the differences in hallmark pathways between two m^{6}A cluster subtypes. The criteria for screening significant difference were as follows: |t-value| >2 and p-values < 0.05. The pathway with a t-value > 0 was thought to be activated in the m^{6}A cluster B, and conversely, the pathway with a t-value < 0 was considered to be activated in the m^{6}A cluster A.

2.6 Weighted gene co-expression network analysis

WGCNA R package was utilized to construct an unsigned weighted co-expression network to identify m^{6}A cluster-related gene modules. First of all, TCGA-LIHC expression data in TPM format were evaluated for availability and genes were screened using the lowest median absolute deviation (MAD) for further analysis. The Pearson's correlation matrices between all included genes were calculated, and then transformed into an unsigned weighted adjacency matrix using a power function. The power β was estimated by soft-threshold of 0.85 to obtain a network with scale-free topology. Furthermore, a topological overlap measure (TOM) matrix was generated to estimate the connectivity property of nodes in the network. The node in the networks represented a

coding gene in the modules and an edge connecting two genes indicated a strong correlation. Average linkage hierarchical clustering was used to construct a clustering dendrogram of the TOM matrix. Dynamic tree-cutting algorithm was used to obtain appropriate modules of co-expressed genes with deep split = 2 and the minimum gene module size of 40, and the height cutting threshold of merging similar modules was set to 0.3. Genes outside of each module were denoted with color "grey". The association between module Eigengenes (ME) values with clinicopathological characteristics was assessed by Pearson's correlation, and the modules with the strongest association with m^6A cluster were selected for further analysis.

2.7 Identification of optimal feature gene biomarkers

To identify the optimal feature gene variables with the superior discriminative power, three machine-learning algorithms were implemented to predict disease status, including LASSO (least absolute shrinkage and selection operator) regression, SVM-RFE (support vector machine-recursive feature elimination), and RF (random forest classifier). LASSO regression analysis was performed using the 'glmnet' R package (22), and SVM-RFE using the 'e1071' R package (23). In the LASSO regression analysis, the response type was configured as binomial, and the alpha parameter was set to 1. Meanwhile, SVM-RFE model was compared by the average mis-judgement rates of their 10-fold cross-validations (24). The final importance of features was based on the average importance of each feature variable in each iteration. In the RF algorithm, the importance ranking of each gene, and the error rate and accuracy rate of the combination in each iteration were obtained using the RFE method. The feature genes were the corresponding genes in the optimal combination with the lowest error rate. The overlapping genes between the three machine-learning algorithms were regarded as optimal diagnostic biomarkers. The accuracy of the overlapping genes for diagnosis was evaluated using the receiver operating characteristic curve (ROC) in TCGA-LIHC dataset, and the expression levels of candidate genes were further validated in the ICGC-LIRI-JP dataset.

2.8 Construction of m^6Arisk score model for HCC prognosis

The overlapping feature genes obtained above were first subjected to univariate Cox regression to obtain the OS related DEGs. Followed by least absolute shrinkage and selection operator (LASSO) penalties regression, we identified the most powerful prognostic DEGs and their correlative coefficients using "glmnet" R package. Meanwhile, the "caret" R package was utilized to randomly divide the TCGA-LIHC cohort (n = 371) with a ratio of 1:1, with 50% of the data used for training and 50% for validation. Next, the independent prognostic feature genes were identified using multivariate Cox regression analysis to construct a m^6A related prognostic risk score model in the training set. Then, the m^6Arisk scores were calculated using the formula: m^6Arisk-score = Σ (gene expression * risk coefficient). Based on the median of risk score, the training set and testing set were stratified into low- and high-risk groups, respectively. Finally, survival analysis and receiver operating characteristic (ROC) curve analysis were carried out for the two risk groups using the "survminer" and "survivalROC" R packages, respectively.

2.9 The immunological characteristics of the tumor microenvironment

To confirm the role of m^6Arisk score in modulating cancer immunity in HCC, we analyzed the correlation between m^6Arisk and the immunological characteristics of TME. The immunological characteristics included the activity of the cancer immunity cycle, infiltration level of tumor-infiltrating immune cells (TIICs), and the expression of immunomodulators and inhibitory immune checkpoints. The cancer immunity cycle consists of seven steps that reflect the anticancer immune response and determine the fate of the tumor cells (25) (Supplementary Table S12). The immunomodulators comprise major histocompatibility complex (MHC), receptors, chemokines, and immune stimulators (26) (Supplementary Table S17). In this study, the activities of the cancer immunity cycle were also quantified using a single sample gene set enrichment analysis (ssGSEA) as previously reported (27). Moreover, to avoid the calculation error of different algorithms and marker gene sets, six independent algorithms [including Cibersort (28), MCP-counter (29), quanTIseq (30), TIMER (31), xCell (32), and TISIDB (33)] were used to comprehensively calculate TIICs infiltration level in TME (Supplementary Table S7). Thereafter, the effector genes of TIICs and inhibitory immune checkpoints were also identified and collected from previous studies (34) (Supplementary Tables S18, S19).

2.10 Somatic mutation analysis

For genomic layer analysis, the mutation annotation format (MAF) data of HCC patients was derived from the TCGA-LIHC database (http://tcga-data.nci.nih.gov/tcga/) and analyzed using the "maftools" R package (35). The mutation profile was visualized using a waterfall plot, which displays the mutation types and frequencies of the top driver genes. Fisher's exact test was conducted to compare the differential mutation patterns between the two distinct m^6Arisk score groups. Genes with a *p*-value less than 0.05 were considered statistically significant and were visualized in a forest plot. In addition, a lollipop diagram was drawn to indicate the mutation types of the most frequently mutated gene in order to provide insight into the molecular alterations associated with hepatocellular carcinoma (HCC) development. Furthermore, the exclusivity and co-occurrence of mutations for the top 20 mutated genes were analyzed. The prognostic value of TMB and the combination of TMB and m^6Arisk scores were comprehensively evaluated. Additionally, the relationship between the m^6Arisk scores and the cancer stem cell

(CSC) index was evaluated to investigate their potential association in tumor progression and treatment resistance.

2.11 Prediction of therapeutic response by m^{6}Arisk score

The T cell receptor (TCR) repertoire is a well-characterized immune trait that plays a key role in the selective activation of the adaptive immune system (36, 37), tightly linked to the immune status and anti-tumor immune response. In this study, we obtained the TCR Shannon diversity index and richness of the TCGA-LIHC cohort from previous literature (36) and investigated their differences between the two distinct m^{6}Arisk scores groups. The Tumor Inflammation Signature (TIS) is a transcriptome-based algorithm consisting of 18 genes that measures a pre-existing but suppressed adaptive immune response within the tumor (38). We computed the TIS score of each patient as previously reported (39) in TCGA-LIHC dataset to speculate on the association between m^{6}Arisk scores and the adaptive immune response. Imunophenoscore (IPS), a machine learning-based scoring scheme that represents the determinants of immunogenicity, has been proven to be tightly linked to the survival of multiple cancer and is a promising predictor of response to immunotherapy (26). We obtained the IPS of HCC from the Cancer Immunome Atlas (TCIA) (https://tcia.at/home) and compared them between the two m^{6}Arisk-score groups to predict the immunotherapeutic sensitivities.

Moreover, to explore the potential clinical applications of the m^{6}Arisk score in treatment decisions, we utilized the "oncoPredict" R package (40) to infer the semi-inhibitory concentration (IC50) values of commonly used targeted/chemotherapy drugs. We then performed a correlation analysis between the IC50 values and the m^{6}Arisk-score groups using the Wilcoxon test. The drugs and their target information were derived from DrugBank (https://go.Drugbank.com/). This analysis aimed to investigate the relationship between m^{6}Arisk score and the response to specific drugs, providing insights into personalized treatment strategies.

2.12 Establishment and validation of a nomogram scoring system

The m^{6}Arisk scores and common clinical variables (including age, gender, and TNM stages) were incorporated to establish a nomogram scoring system using the "rms" R package (41). In this study, the time-dependent ROC curves of nomogram and clinical prognostic variables at 1-, 3-, and 5-year were generated, and the corresponding time-dependent area under the curves (AUCs) was calculated to evaluate the discrimination of nomogram. The calibration curves and the decision curve analysis (DCA) of 1-, 3-, and 5-year were plotted to assess the prediction accuracy and clinical net benefit of nomogram, respectively (42, 43). In addition, concordance index (C-index) was also performed to assess the prediction efficiency and accuracy of nomogram. A C-index score around 0.70 indicates a good model, whereas a score around 0.50 suggests random background.

2.13 Clinical sample collection, RNA isolation, and qPCR

Twenty-eight pairs of fresh-frozen tissues (HCC tissues and adjacent tissues) were collected from the Zhongnan Hospital of Wuhan University and approved by the ethics committee (Approval Number 2017058). Written informed consent was obtained from all the participants. Complementary DNA (cDNA) was synthesized from total RNA using the Prime Script RT Reagent Kit (Vazyme, R333-01, China). The SYBR Prime Script RT-PCR kit (Vazyme, Q712-02, China) was used for qPCR on a CFX96 instrument (Bio-Rad, America). Gene expression levels were calculated with the $2^{-\Delta\Delta ct}$ strategy and normalized to the "housekeeping" gene β-actin. The primer sequences were integrated into Supplementary Table S20.

2.14 Statistical analysis

All statistical analyses and graphical plotting were performed using R software (version 4.0.5.) Unless stated otherwise, P <0.05 (two-sided) was considered statistically significant.

3 Results

3.1 Landscape of genetic variation of 23 m^{6}A regulators in LIHC

In this study, we identified 23 m^{6}A RNA methylation regulatory genes (including eight "writers," thirteen "readers," and two "erasers") from the published literature, and systematically investigated the roles of them in LIHC. The workflow for this study is shown in Figure 1A. Additionally, the significantly enriched biological processes of the 23 m^{6}A regulators were summarized using the Metascape database, as depicted in Figure 1B. These processes primarily revolve around mRNA stability, mRNA transport, mRNA metabolic processes, mRNA modification, and ncRNA processing. Figure 1C illustrates the dynamic reversible process of the m^{6}A regulators, showcasing their ability to recognize, remove, and add m^{6}A-modified sites. These analyses provided insights into the regulatory complexity and functional implications of m^{6}A RNA methylation in gene expression and RNA metabolism. The somatic mutations analysis of 23 m^{6}A regulators demonstrated that a total of 42 of the 371 (11.3%) TCGA-LIHC samples experienced genetic alterations of m^{6}A regulators, primarily including missense mutations and splice site (Figure 1D). Moreover, the CNA analysis revealed CNV alterations were prevalent in the 23 m^{6}A regulators, with most of the alterations being focused on gene amplification (such as *VIRMA*, *METTL3*, *HNRNPC*, *IGF2BP2*, and *YTHDF3*), whereas *WTAP*, *YTHDF2*, and *ZC3H13* showed the highest deletion frequency (Figure 1E). Further investigation of the expression profiles of the 23 m^{6}A regulators indicated that most of the m^{6}A writers

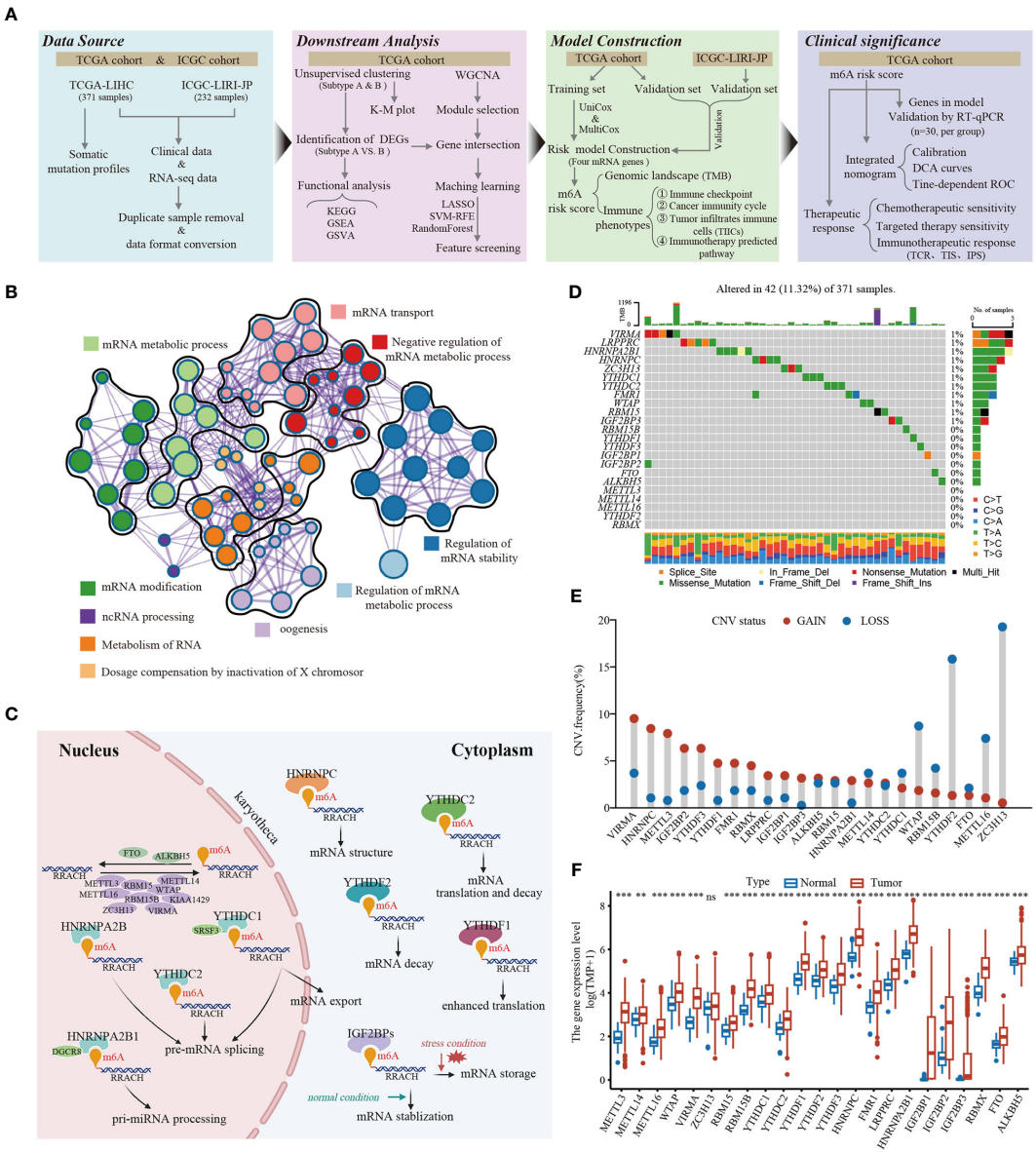

FIGURE 1
The landscape of genetic and transcriptional alterations of m6A regulators in HCC. **(A)** The schematic workflow of this study. K-M plot, Kaplan-Meier plot; GSEA, gene set enrichment analysis; GSVA, gene set variation analysis; WGCNA, weighted gene co-expression network analysis; ROC, receiver operating characteristic; LASSO, least absolute shrinkage and selection operator; SVM-RFE, support vector machine recursive feature elimination; UniCox, univariate Cox; MultiCox, multivariate Cox; DCA, decision curve analysis, TCR, T cell receptor; TIS, Tumor Inflammation Signature; IPS, Imunophenoscore. **(B)** The enrichment network of 23 m^{6}A regulators visualized by Metascape (https://metascape.org/), showed the similarity of enrichment terms within and between clusters. **(C)** The regulation mechanism of m^{6}A "writer," "eraser," and "reader" proteins on RNA metabolism. **(D)** Mutation frequencies of 23 m^{6}A regulators in 371 HCC patients from TCGA-LIHC cohort. **(E)** Frequencies of copy number variant (CNV) of the 23 m^{6}A regulators. **(F)** The differential expression levels of 23 m^{6}A regulators between tumor and normal tissues. ** $P < 0.01$; *** $P < 0.001$; ns, No significance.

(*METTL3/14/16*, *WTAP*, *VIRMA*, and *RBM15/15B*), readers (*YTHDC1/2*, *YTHDF1/2/3*, *HNRNPC*, *FMR1*, *LRPPRC*, *HNRNPA2B1*, *IGF2BP1/2/3*, and *RBMX*), and erasers (*FTO* and *ALKBH5*) were markedly upregulated in the tumor tissues (Figure 1F). The survival analysis revealed that most of the m^{6}A regulators were significantly correlated with LIHC prognoses (Supplementary Figure S1). Taken together, these results demonstrate that m^{6}A regulators may act as diagnostic biomarkers and prognostic predictors for LIHC.

3.2 Identification of m^{6}A modification subtypes and function enrichment analysis

Figure 2A presented the interactions and interconnections among the 23 m^{6}A regulators and their prognostic value in TCGA-LIHC patients. Most of these genes were risk factors and were significantly positively correlated with each other (p<0.001). The results suggested that the cross-talk between these m^{6}A regulators probably play important roles in the formation of

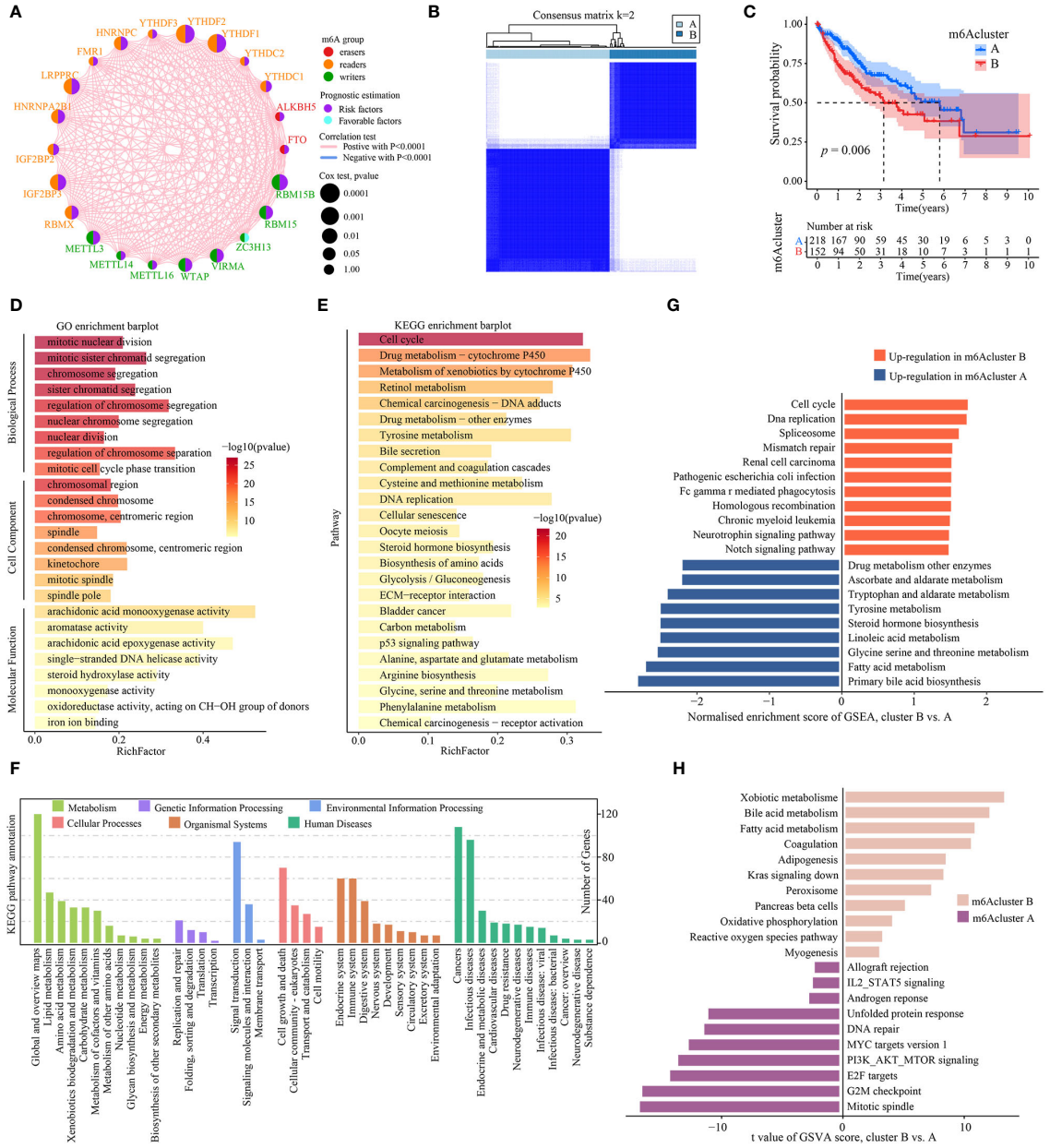

FIGURE 2
Identification and functional enrichment analysis of m^{6}A cluster subtypes. **(A)** The interaction analysis of expression on 23 m^{6}A regulators in TCGA-LIHC. Different colored circles represent different modification types of m6A regulators. The size of the circle represents the prognostic effect of each m^{6}A regulator and scaled by *p* value. Connecting lines represent interactions between each other. **(B)** The consensus score matrix of 371 samples (k = 2). **(C)** Kaplan-Meier curves for estimating the overall survival between subtypes of m^{6}A cluster. **(D)** GO enrichment and **(E)** KEGG enrichment analyses of the DEGs (|log2FoldChange| > 1, *P*-adj < 0.001) between m6A cluster B and A. The top 25 enriched terms are shown. The color of the bars denotes the negative logarithm of the p-value of the hypergeometric test. **(F)** The bar charts showing KEGG pathway annotation. The color indicates the category A of annotation terms. The horizontal coordinate presents the category B of annotation terms, and the ordinate denotes the number of genes (hits) of category B. **(G)** Bar charts showing the top 10 KEGG pathway terms enriched by GSEA. Red and blue represent the upregulated pathway terms in m^{6}A cluster B and A, respectively. **(H)** The GSVA score of hallmark pathway activities curated from MSigDB in distinct m^{6}A modification patterns. T values are from two-sided unpaired limma-moderated t test (linear models), corrected for effects from the patient of origin.

different modification patterns and was implicated in the pathogenesis and progression of tumor. To further explore the modification patterns of m^{6}A regulators, unsupervised clustering algorithms based on the expression profiles of 23 m^{6}A regulators were applied to construct m^{6}A subtypes. As shown in Figure 2B and Supplementary Figure S2, the consensus score matrix revealed that k = 2 appeared to be an optimal choice for ensuring the least crossover between TCGA-LIHC samples. Next, Kaplan-Meier survival curves showed that m^{6}A cluster A presented significantly better prognoses than cluster B (P = 0.006; Figure 2C).

Next, the representative DEGs (|log2FoldChange| > 1, *P*-adj < 0.001) between m^{6}Acluster were identified to explore the

underlying biological functions (Supplementary Table S1). GO analysis revealed that the DEGs had a significant enrichment in a number of cell cycle biological processes, including mitotic nuclear division, mitotic sister chromatid segregation, nuclear chromosome segregation, regulation of chromosome segregation, and nuclear division (Figure 2D, Supplementary Table S2). KEGG analysis indicated that cell cycle and metabolic pathways such as DNA replication, cellular senescence, bile secretion, Glycolysis/Gluconeogenesis, biosynthesis of amino acids were significantly enriched, as well as cancer-related pathways such as ECM-receptor interaction and p53 signaling pathway (Figure 2E, Supplementary Table S3). KEGG pathway annotation results revealed that many cancer-related pathways were identified, including those with functions in the immune and endocrine system, signaling transduction, DNA/RNA replication and repair, cell growth and death, and metabolism (Figure 2F). To explore the underlying biological mechanism of distinct m^{6}Acluster subtypes, GSEA and GSVA analyses were conducted. The GSEA analysis also prompted that signaling transduction/cell cycle-related pathways were highly activated in m^{6}Acluster B while metabolism biological processes were highly activated in m^{6}Acluster A (Figure 2G, Supplementary Table S4). In addition, a direct comparison of hallmark pathway expression using GSVA revealed a strong enrichment of signaling transduction and metabolism in m^{6}Acluster B versus A, such as fatty acid and bile acid metabolism, oxidative phosphorylation, IL2-STAT5 signaling, MYC targets, PI3K-AKT-mTOR signaling, E2F targets, and G2M checkpoint (Figure 2H, Supplementary Table S5). All above results demonstrated that m^{6}Acluster subtypes was correlated with dysregulation of signaling transduction and metabolism, which may be implicated in the poor prognosis of TCGA-LIHC patients.

3.3 Weighted gene co-expression network construction and selection of feature genes

To identify m^{6}Acluster-related modules, WGCNA was constructed based on the expression profiles of TCGA-LIHC and clinical trait. Here, we selected the top 5000 genes with the lowest median absolute deviation (MAD) to build a co-expression network. A dendrogram of 344 samples with complete clinical information was clustered using the average linkage method and Pearson's correlation method, and no discrete samples were found (Figure 3A). Next, the power value of $\beta = 7$ (scale-free topology fitting index $R^2 = 0.85$) was selected as the soft threshold to construct a scale-free network with high average connectivity (Supplementary Figures S3A, S3B). After merging the similar modules using two settings: clustering height = 0.3 and min module size = 40, six modules were identified for subsequent analysis (Figure 3B, Supplementary Figure S3C). Through the transcription correlation study within modules, there was no substantial linkage between modules (Supplementary Figure S3D). The relevance between ME (Module Eigengene) and clinical features (m^{6}Acluster, fu-time, fu-stat, age, gender, grade, and stage) was evaluated based on module-trait relationships (MTRs). The module-trait relationship results indicated that the MEblue (r = 0.73, P = 9e-59), the MEbrown (r = 0.42, P = 5e-16), the MEred (r = 0.35, P = 3e-11), the MEgreen (r = -0.39, P = 8e-14) are significantly associated with m^{6}Acluster (Figure 3C). Moreover, the MEblue and MEgreen were significantly related to other clinical features, and the two modules showed an inverse correlation trend. Considering the high correlation with m^{6}Acluster, we selected the MEblue module as the target module for the subsequent study. The scatterplot of GS versus MM indicated that significant correlation existed in the module membership (MM) and gene significance (GS) of the MEblue (cor = 0.48, P = 1.6e-58) module (Supplementary Figure S3E).

Here, the differentially expressed genes (DEGs) (|log2FoldChange| > 1, P-adj < 0.001) between different cohorts were illustrated by the volcano plot. As shown in Figures 3D and 3E, a total of 3081 DEGs (2609 up-regulation and 472 down-regulation) were identified between tumor and tumor-adjacent tissues, and 910 DEGs (737 up-regulation and 173 down-regulation) between m^{6}Acluster A and cluster B. Then, 343 overlapping genes were obtained by intersecting the blue module genes and the differential genes using a Venn diagram (Figure 3F). To identify key feature genes, the 343 candidate genes were submitted into LASSO regression algorithm, SVM-RFE algorithm, and RF model. LASSO regression analyses with a 10-fold cross-validation identified thirty-five gene signatures (Figure 3G). An eleven-gene signature was identified by SVM-RFE algorithm with a 10-fold cross-validation accuracy of 0.962 (Figure 3H). The RF model algorithm sorted sixteen gene signatures with MeanDecreaseGini scores greater than 2.5 (Figure 3I). To obtain a robust feature gene for m^{6}Acluster, we intersected the genes screened out by the above three algorithms and identified three key feature genes: *IGF2BP2*, *MAPRE1*, and *ACTL6A*, as shown in Figure 3J. The ROC curves of *IGF2BP2*, *MAPRE1*, and *ACTL6A* revealed the probability of them as valuable biological markers with AUCs higher then 0.7 (Figure 3K), indicating that the three diagnostic markers had a higher diagnostic value. Furthermore, our PCR results demonstrated that the expression levels of *ACTL6A*, *MAPRE1*, and *IGF2BP2* were upregulated in HCC tissues compared to adjacent tissues (p < 0.01, as shown in Supplementary Figure S4).

3.4 Construction and evaluation of m^{6}Arisk scoring model

To explore potentially valuable prognostic genes more broadly, we included overlapping genes that appeared in any two algorithms for subsequent analysis. Overall, 11 out of thirteen genes were found to affect prognosis based on univariate Cox analysis (Figure 4A, Supplementary Table S6). Next, we performed LASSO and multivariate Cox regression analysis for eleven prognostic genes to further select optimum prognostic signature. Followed by LASSO analysis, seven best candidate DEGs (*SRD5A2*, *IGF2BP2*, *ZSWIM5*, *PAK1*, *ACTL6A*, *PRKCD*, *LRRC1*) were retained according to the minimum partial likelihood deviance (Figures 4B, C). Subsequently, the seven candidate DEGs underwent multivariate Cox analysis, resulting in the retention of four genes (*SRD5A2*, *IGF2BP2*, *ZSWIM5*, *PRKCD*) according to the Akaike information criterion

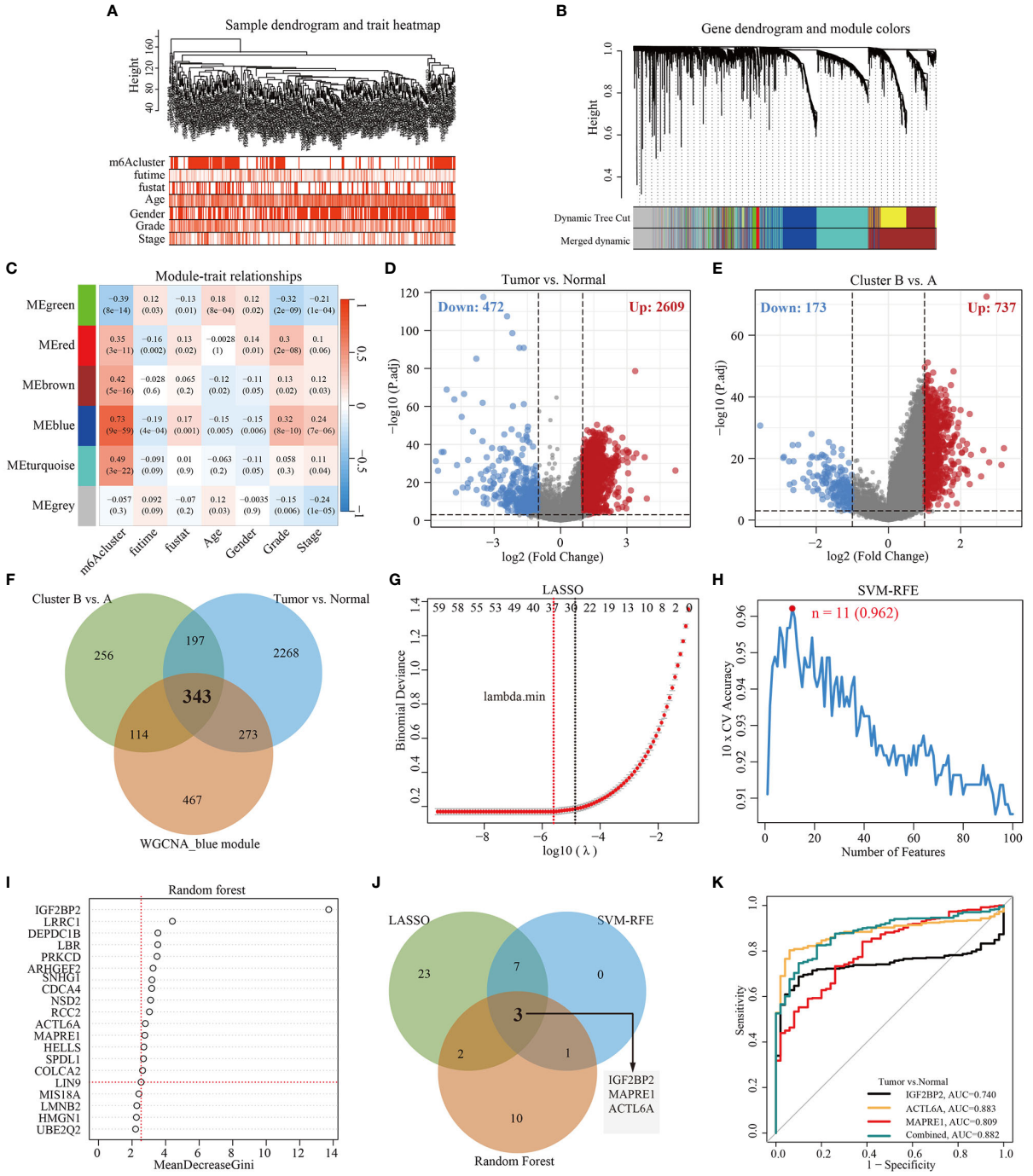

FIGURE 3
Construction of WGCNA and selection of feature genes. **(A)** Clustering dendrogram of 344 samples with clinical trait heatmap in TCGA-LIHC database. **(B)** Gene clustering dendrograms showing the original and combined modules, various colors represent different modules. **(C)** The relationship of seven traits (including m6Acluster and clinicopathology) and six modules, red and blue represents positive and negative correlations, respectively. Each cell contains the corresponding correlation value and *p*-value. **(D)** Volcano plot of DEGs between tumor and normal tissues. **(E)** Volcano plot of DEGs between cluster B and cluster A. **(F)** Venn diagram demonstrating 343 overlapping genes between the WGCNA blue module gene and the identified DEGs. **(G)** Cross-validation for selecting the optimal tuning parameter log (λ) in LASSO regression algorithm. **(H)** Eleven feature genes were identified by SVM-RFE algorithm with a 10-fold cross-validation accuracy of 0.962. **(I)** Gene importance scores in RF model. MeanDecreaseGini score greater than 2.5 was selected for the inclusion threshold of feature genes. **(J)** Venn diagram demonstrating three diagnostic markers shared by three algorithms (LASSO, SVM-RFE, and Random Forest). **(K)** Performance of three biomarker genes in discriminating tumor from normal controls based on TCGA-LIHC database.

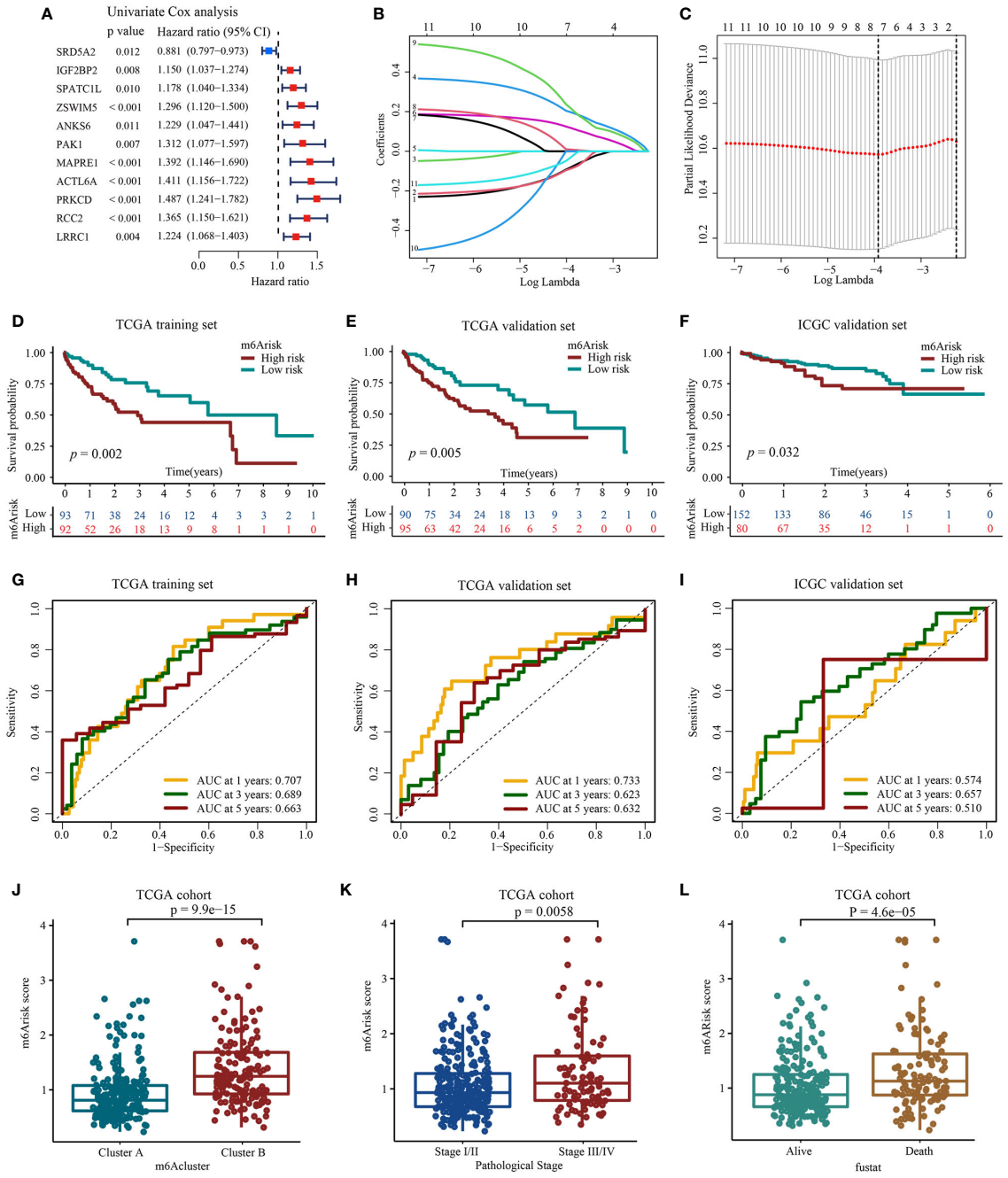

FIGURE 4
Construction and evaluation of prognostic signature using m^{6}A-related candidate genes. **(A)** Univariate Cox regression analysis. **(B, C)** LASSO regression analysis and optimal parameter (lambda) selection of the eleven prognostic genes by using 10-fold cross-validation. Dotted vertical lines represents the optimal values selected by the minimum criteria (right) and the 1- standard error (SE) of the minimum criteria (left). **(D)** Development of m^{6}Arisk model in TCGA-LIHC training set **(E)** Validation of the m^{6}Arisk model in TCGA-LIHC internal validation set. **(F)** Validation of the m^{6}Arisk model in external independent validation sets: ICGC-LIRI-JP. **(G–I)** The predictive accuracy of m^{6}Arisk model for survival. **(J)** Differences in m^{6}Arisk score between two distinct m6Acluster subtypes. **(K)** Differences in m^{6}Arisk score between HCC patients with AJCC stages III–IV and stages I-II. AJCC, American Joint Committee on Cancer. **(L)** Differences in m^{6}Arisk score between HCC patients who had deceased and HCC patients who were alive.

(AIC) value. Consequently, the m^{6}Arisk score model was developed according to RNA-expression profiles using the following formula: Risk score = (−0.1430* expression of *SRD5A2*) + (0.2223*expression of *IGF2BP2*) + (0.2784* expression of *ZSWIM5*) + (0.4081* expression of *PRKCD*). As shown in Supplementary Figure S4, HCC tissues exhibited decreased *SRD5A2* expression levels ($p < 0.01$), while *ZSWIM5*, *PRKCD*, and *IGF2BP2* expression levels ($p < 0.01$) were upregulated compared to adjacent tissues.

After the construction of m^{6}Arisk score model, we performed evaluation and validation analysis of the risk model. In the TCGA-LIHC training dataset, 185 patients were divided into high m^{6}Arisk score group (n=92) and low m^{6}Arisk score group (n=93) using the

median m^{6}Arisk score as the risk cutoff. As shown in Figures 4D, G, individuals with elevated m^{6}Arisk scores experienced notably shorter overall survival (OS) times compared to those with lower m^{6}Arisk scores. The area under the curve (AUC) values for the m^{6}Arisk scoring model were 0.707, 0.689, and 0.663 for the 1-year, 3-year, and 5-year OS periods, respectively. The predictive accuracy of the m^{6}Arisk scoring model was well validated in TCGA-LIHC internal validation cohort, with AUC values of 0.733, 0.623, and 0.632 for 1-, 3-, and 5-year OS, respectively (Figures 4E, H). In addition, we further verified the predictive capacity of the m^{6}Arisk scoring model in external ICGC-LIRI-JP cohort (Figures 4F, I). As shown in Figure 4J, a significant difference in the distribution of m^{6}Arisk scores was observed between m^{6}Acluster A and B. The risk scores of the patients in m^{6}Acluster B were substantially higher than those of the patients in m^{6}Acluster A. We also determined the relationship between m^{6}Arisk score and clinicopathological features of HCC patients. HCC patients diagnosed with AJCC stages III–IV had significantly higher m^{6}Arisk scores than those diagnosed with stage I-II (Figure 4K). Similarly, the m^{6}Arisk score of patients who died was significantly higher than that of patients who survived (Figure 4L). These results indicate that the m^{6}Arisk scoring model may serve as a powerful indicator for the prognosis of liver cancer patients.

3.5 The m^{6}Arisk score significantly correlates with tumor immune phenotypes of HCC

Here, we investigated the existence of immune heterogeneity in different m^{6}Arisk score groups, and the association between the m^{6}Arisk score and various immune characteristics (expression of immunomodulator and TIIC effector genes, immunotherapy-related characteristics, and immune checkpoints). As shown in Figure 5A, Supplementary Table S7, we first investigated the infiltration level of Tumor infiltrates immune cells (TIICs) using six independent algorithms. The result indicated that the m^{6}Arisk score was positively correlated with the infiltration level of CD8+ T cells, dendritic cells, and macrophages under different algorithms (Figure 5B; Supplementary Table S8). As expected, m^{6}Arisk score was also found to be positively correlated with the effector genes of these TIICs (Supplementary Figures S5A, S5B). We also analyzed the correlations between m^{6}Arisk score and the immunotherapy predicted pathways signatures (Supplementary Tables S9–S11). As shown in Figures 5C, E, the m^{6}Arisk score was positively correlated with a majority of the immunotherapy predicted-related pathways, including IFN-Gamma signature, base-excision repair, cell cycle, Fanconi anemia pathway, p53 signaling pathway, MicroRNAs in cancer, proteasome, and pyrimidine metabolism.

In addition, the activities of a portion of the cancer immunity cycle were also found to be upregulated in the high-m^{6}Arisk score group, including the release of cancer cell antigens (Step 1) and trafficking of immune cells to tumors (Step 4, mainly those that exert antitumor immunity), such as CD8 T cell recruiting, NK cell recruiting, and MDSC recruiting (Figure 5D, Supplementary Table S12). The activities of the cancer immunity cycle are a direct comprehensive performance of the functions of the chemokine system and other immunomodulators (25, 27). The elevated activity of these steps might increase the infiltration levels of effector TIICs in the TME. Interestingly, the activity of infiltration of immune cells to tumors (Step 5) and recognition of cancer cells by T cells (Step 6) was upregulated in the low-m^{6}Arisk score group. Moreover, the correlation analysis indicated that m^{6}Arisk score demonstrated a predominantly positive correlation with the critical steps of cancer-immunity cycle (Step 1 and Step 4) and the enrichment scores of immunotherapy-predicted pathways gene signatures, including the interferon-γ signature, base-excision repair, cell cycle, DNA replication, homologous recombination, the p53 signaling pathway, and others (Figure 5E, Supplementary Table S11).

In addition, the enrichment scores for several immunosuppressive oncogenic pathways (such as radiotherapy-predicted pathways and EGFR ligands) were significantly higher in the high-m6Arisk group (Figure 5F; Supplementary Tables S13, S14). Previous studies have found that inhibiting these oncogenic pathways promoted the formation of an inflamed tumor microenvironment (TME), thereby reactivating cancer immunity. We also examined the relationship between known biological signatures and the m^{6}Arisk score through Spearman analysis. A heatmap of the correlation matrix demonstrated that the m^{6}Arisk score was markedly positively correlated with the immune activation process and DNA repair signatures (Figure 5G, Supplementary Tables S15, S16). Consistently, a significant proportion of immune checkpoint genes were observed to be highly expressed in the high-risk score group within this study, such as CD27, CD28, CD40, CTLA4, CD44, CD48, NRP1, CD276, LAG3, TNFSF4, PDCD1 (PD-1), and TIGIT (Figure 5H). Similarly, another heatmap was drawn to show the mRNA expression profiles of immunomodulator genes including chemokine, immune inhibitor, immune stimulator, MHC, and receptor in two m^{6}Arisk score groups (Supplementary Figure S5C). The m^{6}Arisk score positively correlated with the mRNA expression profiles of immunomodulator genes. Most MHC molecules were upregulated in the high-m^{6}Arisk group, suggesting that antigen presentation and processing capacity were upregulated in the high-m^{6}Arisk group. The chemokines, including *CCL4*, *CCL5*, *CCL8*, *CCL20*, *CCL26*, *CXCL1*, *CXCL3*, *CXCL5*, *CXCL9*, *CXCL11*, *CXCL16*, and paired receptors including *CCR1*, *CCR5*, *CXCR3*, *CXCR4*, and *CXCR6*, were positively correlated with m^{6}Arisk score. These chemokines and receptors promote the recruitment of effector TIICs such as CD8+ T cells and antigen-presenting cells. However, given the complex and diverse functions of the chemokine system, although the relationship between m6Arisk score and individual chemokines is not sufficient to clarify the overall immune effect of m6Arisk in TME, it also reflects that the high score of m6Arisk is closely related to the development of inflammatory TME to some extent.

3.6 Genomic alterations between different m^{6}Arisk score groups

To give a hint of m6Arisk-related mechanisms for OS classification of HCC from genomic layer, available somatic mutations of the TCGA-LIHC dataset were acquired, and the distribution differences in the high- and low-m6Arisk groups

10.3389/fimmu.2024.1374465

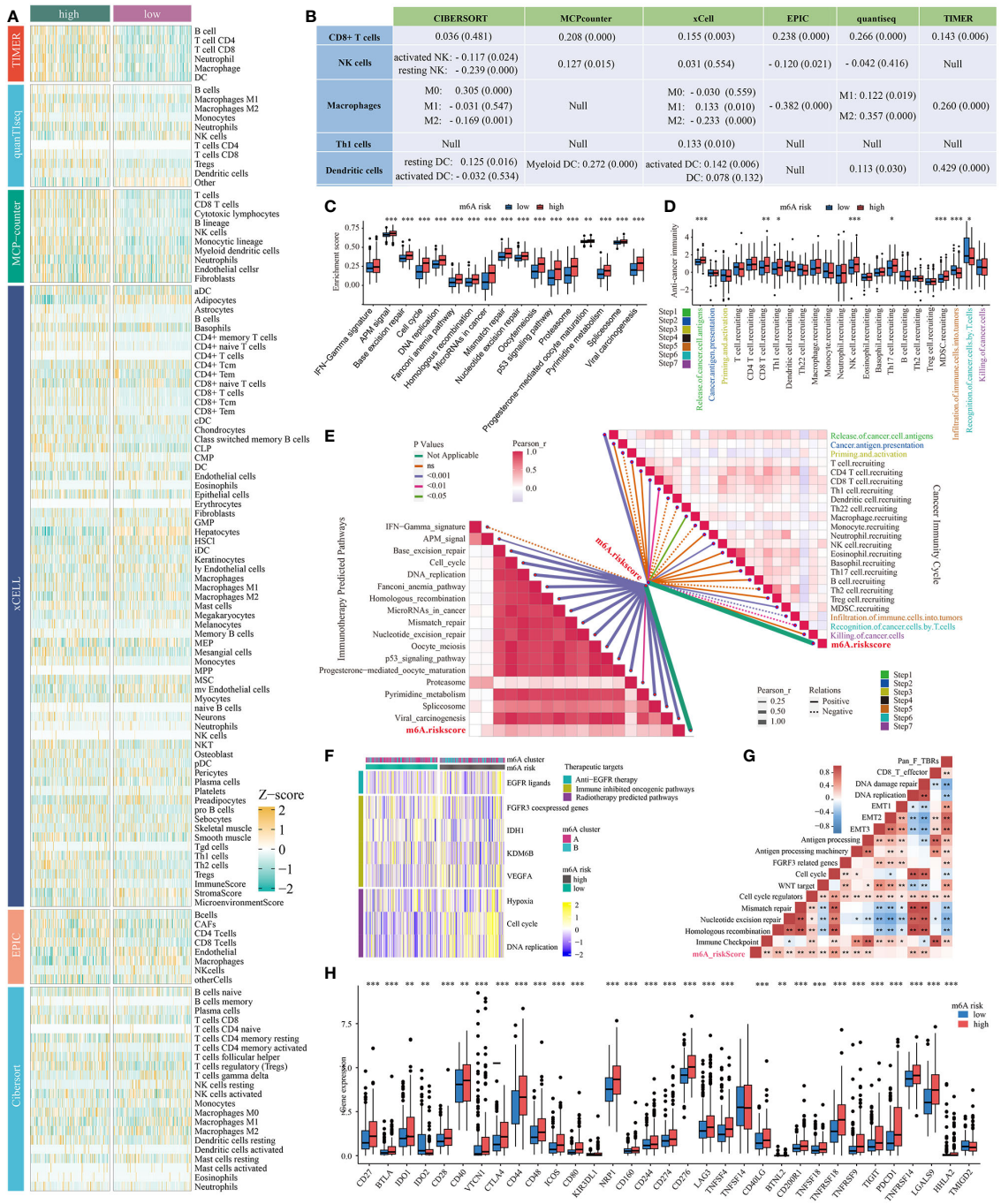

FIGURE 5
Correlation between the m^{6}Arisk score and immune phenotypes. **(A)** Six independent algorithms including CIBERSORT, MCP-counter, xCell, EPIC, quantiseq, and TIMER, further verified the stability and robustness of the ssGSEA results. **(B)** Correlation between m6Arisk score and the infiltration levels of five types of TIICs (CD8+ T cells, NK cells, macrophages, Th1 cells, and dendritic cells). **(C)** Differences in the enrichment scores of immunotherapy-predicted pathways between the two m6Arisk groups in TCGA-LIHC cohort. The enrichment scores were calculated using ssGSEA algorithms. **(D)** Differences in the various steps of the cancer immunity cycle between the two m6Arisk groups in TCGA-LIHC cohort. **(E)** Pearson's correlation analysis of the m^{6}Arisk score with cancer immunity cycle activity (top right) and immunotherapy-predicted pathways (bottom left) based on TCGA-LIHC cohort. The color of the line represents the size of the *P* value, and the thickness of the line represents the size of the r value. The solid and dotted lines represent positive and negative correlations, respectively. **(F)** Correlations between m^{6}Arisk scores and the enrichment scores of several therapeutic signatures such as targeted therapy and radiotherapy. **(G)** Correlations between m^{6}Arisk scores and the known biological gene signatures using Spearman analysis. The color presented the Spearman correlation coefficient. **(H)** Difference analysis of immune checkpoints effect genes between high- and low-m^{6}Arisk groups in TCGA-LIHC cohort. * $P < 0.05$; ** $P < 0.01$; *** $P < 0.001$. ns, No significance.

were analyzed by the package "maftools". Figures 6A, B showed the top 20 genes with the highest mutation frequencies in the two m^{6}Arisk-score groups. The summary of the mutation information, along with statistical calculations, is presented in Supplementary Figures S6A, S6B. *TP53* (35%) and *TNN* (26%) were the most frequently mutated genes in the high- and low-m^{6}Arisk patients, respectively, with *TP53* having the highest frequency. The Forest plot (Figure 6C) illustrates genes with significant differences in mutation frequency between the two m^{6}Arisk score groups, including *TP53*, *RB1*, *PCDHB1*, *SMCHD1*, *ZC3H6*, *SPEG*, *DNAH17*, *SPAG17*, and *DOCK2*. As *TP53* was the most frequently mutated gene, a lollipop diagram (Figure 6D) was created to illustrate the specific mutation sites of *TP53*, with a higher number of missense mutations observed in the high-m^{6}Arisk group. Furthermore, the associations of exclusivity and co-occurrence across mutated genes from the high- and low-m^{6}Arisk score groups are shown in Figure 6E, with green representing co-occurrence and brown representing mutual exclusion. Here, the tumor mutation burden (TMB) quantification results demonstrated an elevated level in the high-m6Arisk group, although in a non-significant mode (Supplementary Figure S6C), and HCC patients with a lower TMB score presented a better overall survival (OS) (Figure 6F). This finding suggests the presence of heterogeneity and complexity among cancer patients, which is consistent with existing literature reports (44). To further investigate, we categorized all HCC patients into four subgroups based on TMB and m^{6}Arisk score: high-TMB and high-m^{6}Arisk, low-TMB and high-m^{6}Arisk, high-TMB and low-m^{6}Arisk, and low-TMB and low-m^{6}Arisk. Survival curves were plotted for each subgroup, and it was observed that the high-TMB and high-m^{6}Arisk score group exhibited the worst prognosis among them (Figure 6G). We then assessed the potential correlation between the m^{6}Arisk score and the cancer stem cell (CSC) index in HCC. As shown in Figure 6H, a positive linear correlation between the m^{6}Arisk score and CSC index was observed ($R = 0.14$, $P < 0.01$). The results suggest that HCC cells with a higher m^{6}Arisk score may have more pronounced stem cell properties and a lower degree of cell differentiation.

3.7 The m^{6}Arisk score predicts therapeutic responses in HCC

Here, we firstly estimated the T cell receptor (TCR) repertoire for HCC patients and HCC patients (TCGA-LIHC cohorts) in the high-m^{6}Arisk score group exhibited a significantly higher TCR richness and diversity, indicating that they possessed greater tumor immune potential (Figure 7A). Besides, the Tumor Inflammation Signature (TIS), an 18-gene index that measures adaptive immune resistance within tumors, was utilized to evaluate the immune potential of the two risk groups. As shown in Figure 7B, patients in the two m^{6}Arisk score groups exhibited a non-significant TIS score, indicating no significant difference in anti-tumor immune potential. Imunophenoscore (IPS) is a recognized indicator of patients' response to immunotherapy, and no significant differences were observed between the two m^{6}Arisk score groups, suggesting no difference in response to immune checkpoint blockade (ICB) between the two groups (Figure 7C). These results suggest that the m6Arisk score may not help identify effective anti-tumor immunotherapy precision medicine therapies.

We subsequently investigated whether the m^{6}Arisk score could accurately guide precision treatments by assessing the differences in anticancer drug sensitivity between the two m^{6}Arisk score subgroups, aiming to identify potential individualized therapy modalities for LIHC patients. The IC50 values demonstrated that LIHC patients with a lower m^{6}Arisk score exhibited a higher sensitivity to common chemotherapeutic drugs, including vincristine, vinblastine, pevonedistat, paclitaxel, osimertinib, navitoclax, docetaxel, vinorelbine, and 5-fluorouracil (Figure 7D). Additionally, LIHC patients with lower m^{6}Arisk score also showed higher sensitivity to several targeted drugs, such as alpelisib, bortezomib, cediranib, ibrutinib, axitinib, crizotinib, buparlisib, dasatinib, and ruxolitinib (Figure 7E). In contrast, patients with a high m^{6}Arisk score exhibited relatively high sensitivity to the chemotherapy drug mitoxantrone (Figure 7D) and the targeted drug selumetinib (Figure 7E). These results demonstrate that the m^{6}Arisk score may contribute to identifying effective antitumor agents and precision medicine therapies for LIHC treatment.

3.8 Construction and validation of a nomogram

To assess whether the m^{6}Arisk scores predicting model was an independent predictor in HCC (TCGA-LIHC cohorts), univariate and multivariate Cox regression analyses were conducted. As shown in Figures 8A, B, the HR of m^{6}Arisk scores in univariate and multivariate analysis was 1.573 (95%CI: 1.314-1.883; $p<0.001$) and 1.485 (95%CI: 1.223-1.803; $p<0.001$), suggesting that m^{6}Arisk scores could be used as an independent prognostic indicator compared with the other clinical features (age, gender, AJCC stage, and TNM stage). To facilitate the clinical feasibility of the m^{6}Arisk score, a nomogram was constructed by integrating the m^{6}Arisk score and clinicopathological features to predict overall survival (OS) at 1-, 3-, and 5- years. As shown in Figure 8C, the predictors included the m^{6}Arisk score and TNM stage, which had the greatest influence on OS. We subsequently validated the predictive capability and accuracy of this nomogram by concordance index (C-index), calibration curve, and decision curve analysis (DCA). The C-index of the nomogram was 0.680 (95% CI: 0.562–0.779) in the TCGA-LIHC cohort (Figure 8D) and 0.733 (95% CI: 0.553–0.859) in external validation cohort (Supplementary Figure S7A), indicating that the nomogram had a relatively good discriminatory power. Similarly, the calibration plots show an ideal consistency between the actual observations and the nomogram predictions of the 1-, 3-, and 5-year OS in both the TCGA-LIHC cohort and external validation cohort (Figure 8E, Supplementary Figure S7B). The ROC analysis revealed that the AUC values of the constructed nomogram for predicting 1-, 3-, and 5-year OS were 0.742, 0.704, and 0.713, respectively, further demonstrating the predictive capability of the nomogram

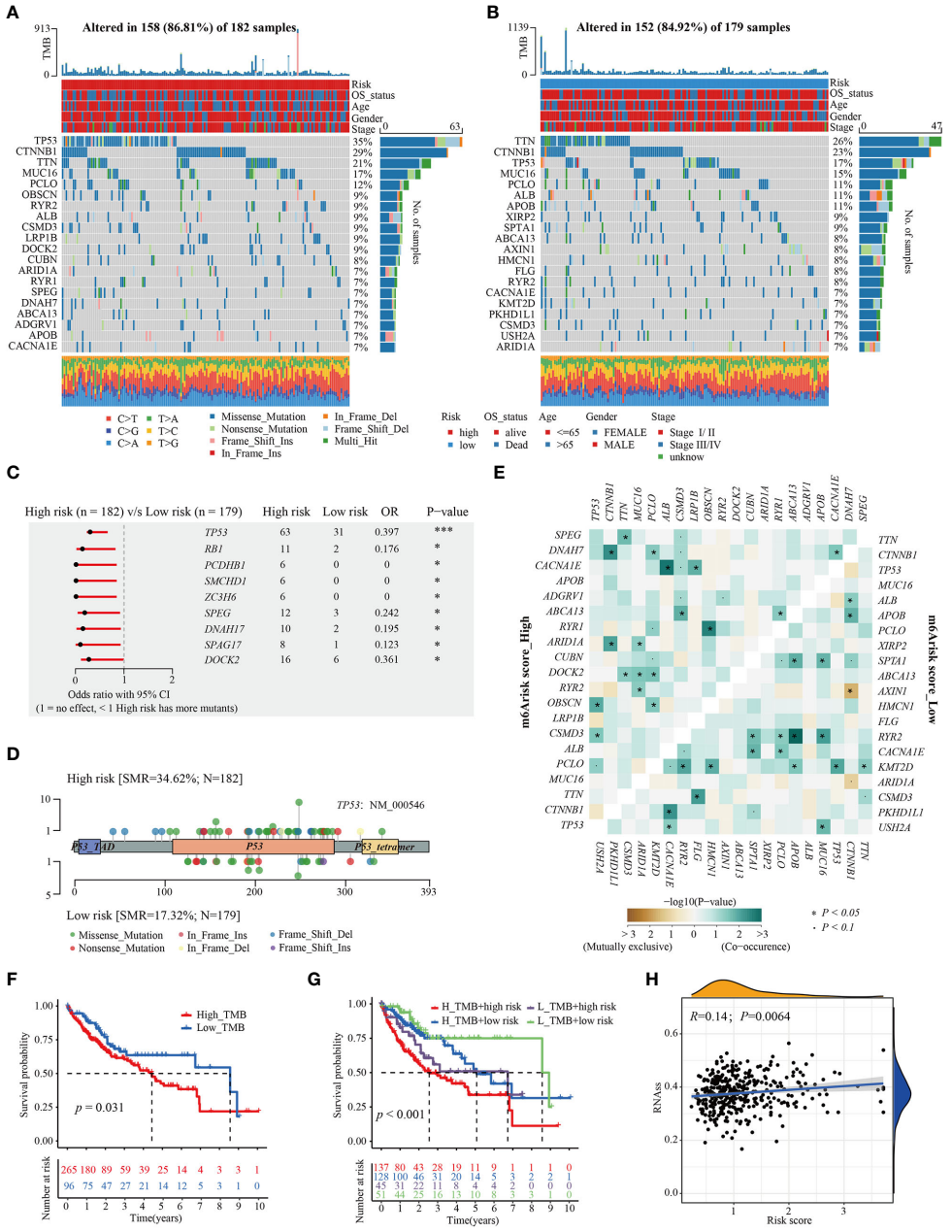

FIGURE 6
Distinctive genomic mutation patterns between the m6Arisk score groups. **(A, B)** Waterfall plots depicting the somatic mutation landscapes of the top 20 most frequently mutated genes in the high- and low-m^{6}Arisk score groups. **(C)** Forest plot displaying the common driver genes mutating significantly differentially in the high- and low- m6Arisk score groups. **(D)** Lollipop diagram visualizing the differential mutation site for TP53 between the two distinct m6Arisk score groups. **(E)** The mutual exclusivity and co-occurrence of mutations in the most frequently mutated genes of the high- and low-m6Arisk score groups. **(F)** Kaplan-Meier curves of TMB in the high- and low-m^{6}Arisk score groups. **(G)** Kaplan-Meier curves for HCC patients in the whole TCGA-LIHC cohort stratified by both TMB and m^{6}Arisk score. TMB, tumor mutation burden. **(H)** Relationships between m^{6}Arisk score and cancer stem cell (CSC) index. ***$P < 0.001$, *$P < 0.05$.

(Figures 8F–H). As showed in Figures 8I–K, nomogram incorporating the m^{6}Arisk model yielded a relatively better net benefits than other clinical traits in predicting 1-, 3-, and 5-year OS for HCC patients in the TCGA-LIHC cohort, suggesting that the nomogram had a relatively good prognostic accuracy and clinical applicability. The ROC and decision curve (DCA) analysis indicated that the proposed nomogram had a similar performance in the ICGC-LIRI-JP cohort (Supplementary Figures S7C–S7H).

4 Discussion

Hepatocellular carcinoma (HCC) remains a major health challenge with a growing incidence worldwide today, characterized by high recurrence rates and heterogeneity (45). The existing prognostic staging system still has some limitations in evaluating clinical prognosis and individual treatment for HCC patients. How to control its progression and improve the survival

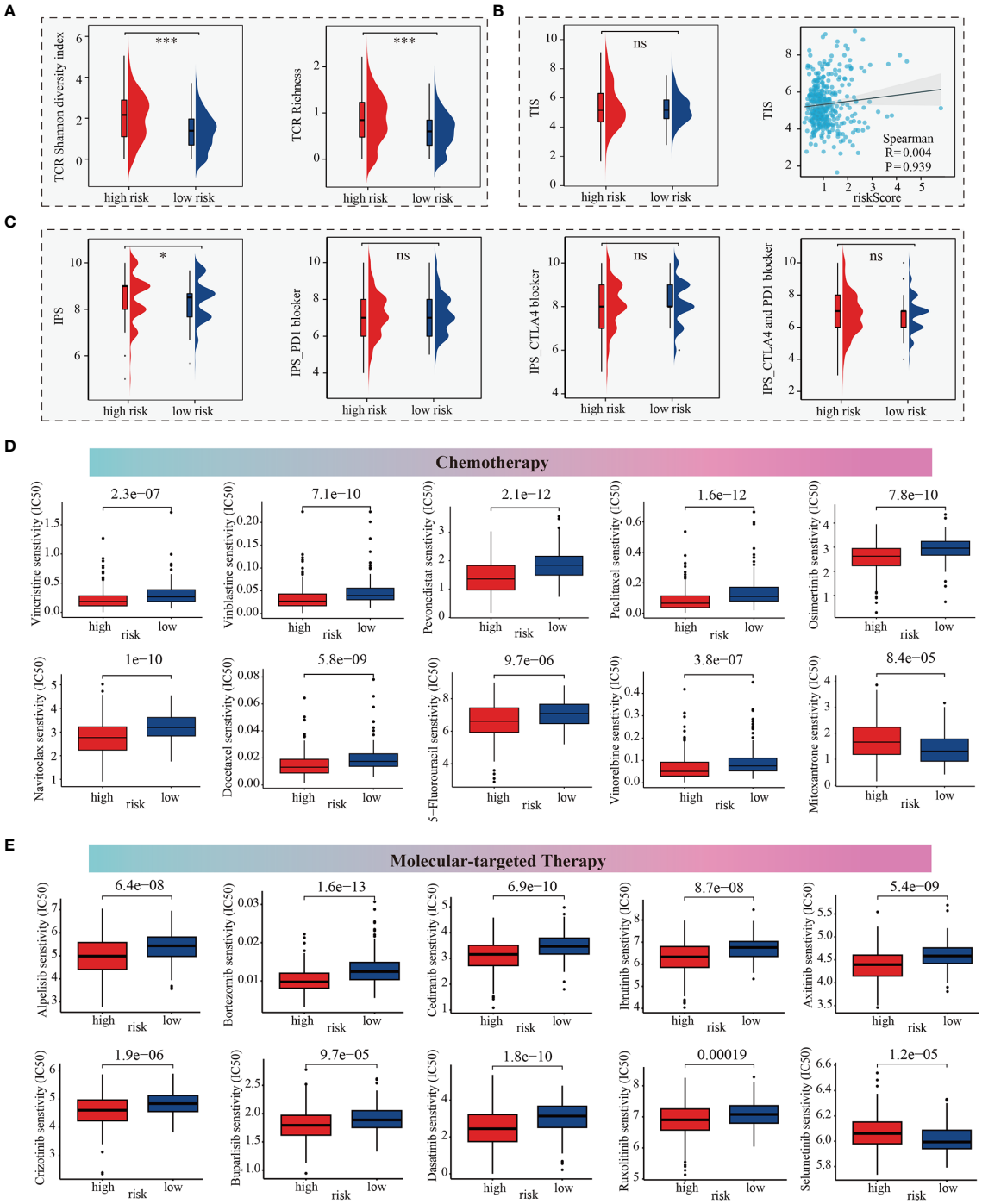

FIGURE 7
m^{6}Arisk score based prediction of treatment response. **(A)** TCR repertoire analysis illustrating significantly higher levels of TCR richness and diversity in the high-m^{6}Arisk score group based on the TCGA-LIHC cohort. **(B)** Comparison of TIS between the two distinct m^{6}Arisk score groups based on the TCGA-LIHC cohort. **(C)** IPS comparison of the high- and low- m^{6}Arisk score groups based on the TCGA-LIHC cohort. **(D)** Boxplots depicting differential sensitivities of common chemotherapeutic drugs between the two distinct m^{6}Arisk score groups. **(E)** Differential sensitivities of common molecular-targeted therapeutic drugs between the distinct m^{6}Arisk score groups. *, P <0.05; ***, P <0.001; ns, No significance.

rate of patients remains an urgent issue to be solved in the current treatment of liver cancer. Accumulating evidence demonstrates that hepatocellular carcinogenesis is regulated by complex genetic and epigenetic mechanisms, and influenced by immune cell infiltration and the tumor microenvironment (46–49). A study using whole-genome and -exome sequencing analysis has shown that epigenetic regulation is the most unusual differential modifier in HCC. As the most predominant epigenetic modification, RNA methylation modification plays an indispensable and pleiotropic biological role in malignant transformation and cancer progression. N^6-methyladenosine modification affects gene expression by regulating RNA processing, decay, and translation, and abnormal

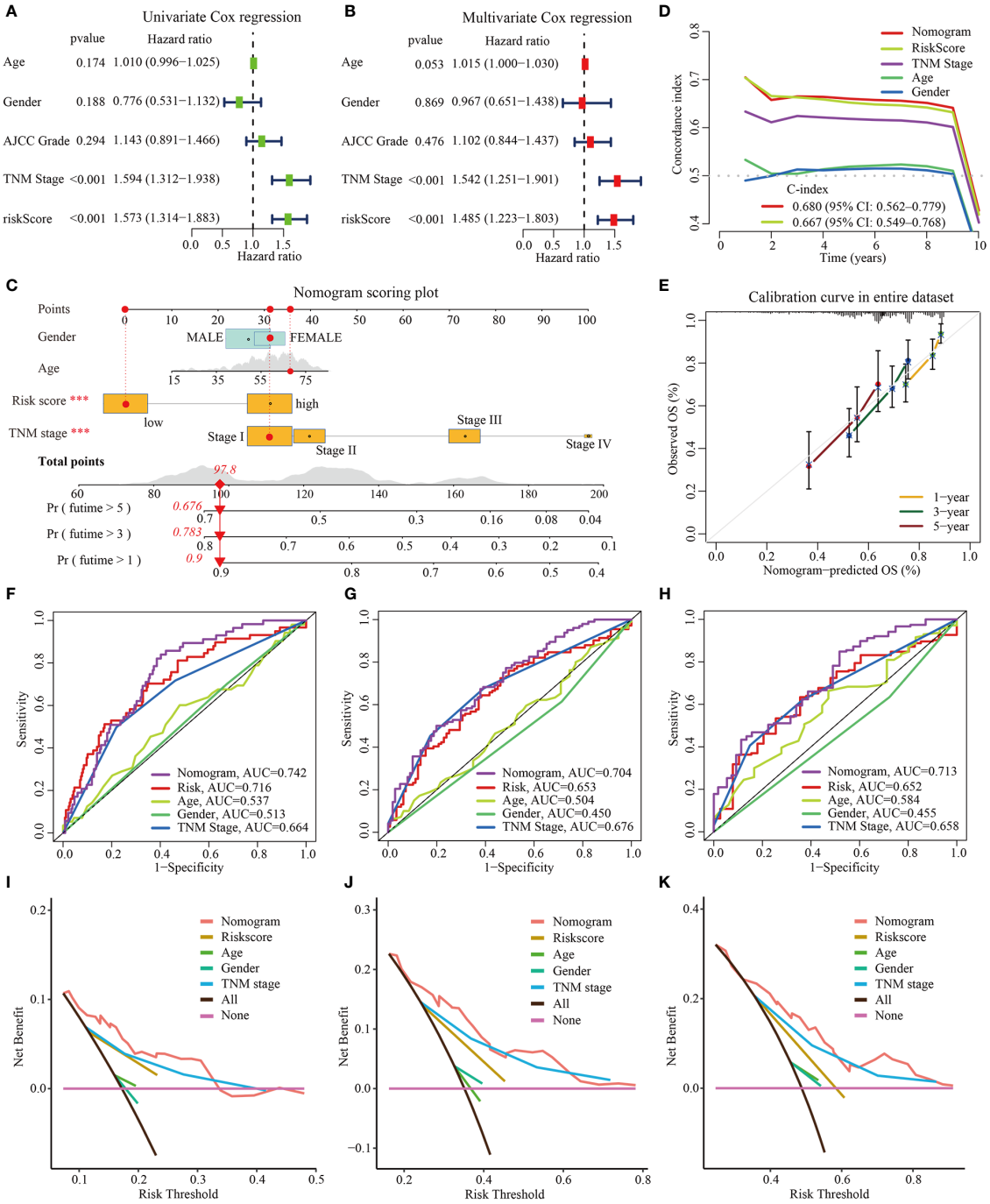

FIGURE 8
Construction and validation of nomogram based on TCGA-LIHC dataset. **(A, B)** Univariate and multivariate Cox regression analysis for m6Arisk score, respectively. **(C)** The established nomogram for predicting the 1-, 3-, and 5-year OS of HCC patients. The red arrow signifies an example to visualize the assessment of risk for 1-, 3-, and 5-year OS. **(D)** C-indexes for the generated nomogram and single variables in predicting OS of HCC patients. The C-index was estimated by truncating the follow-up time to 1 to 10 years and plotting it on the X-axis as the truncation year. **(E)** Calibration curves of the nomogram in terms of the agreement between predicted and observed outcomes. **(F–H)** The ROC curves of the nomograms and clinical characteristics for predicting 1-year, 3-year, and 5-year OS in HCC patients. **(I–K)** The DCA curves of the nomograms and clinical characteristics for predicting 1-year, 3-year, and 5-year OS in HCC patients. OS, overall survival; DCA, decision curve analysis; ROC, receiver operating curve.

expression of the m^{6}A methylase complexes is strongly associated with various human cancers (8, 50–52), including HCC.

Recent studies have shown the impact of m^{6}A RNA modification on various inflammatory development of cancer. Inflammation predisposes patients to cancer, especially affecting the composition of the tumor microenvironment and the plasticity of tumor cells, including surrounding stromal and inflammatory cells (53). m^{6}A dysregulation may lead to aberrant expression of

oncogenic or the tumor-suppressive genes, contributing to HCC initiation and progression. m^{6}A dysregulation may also contribute to epigenetic alterations in HCC cancer cells, and may affect cancer stem cell potential, thereby impacting tumor growth and therapy resistance (54). Besides, another study indicated that the construction of polygenic risk prediction model based on m^{6}A related genes has good clinical predictive ability and accuracy in predicting the survival and prognosis of glioma patients, and is an independent risk factor for glioma. These results suggest that the construction of polygenic risk prediction models based on m^{6}A associated genes has different potential in the stratification of cancer prognosis and the development of new treatment strategies. Thus, comprehensively investigating m^{6}A modification in HCC and its biological roles may facilitate improved prognostic predictions and individual precise treatment modalities for HCC. In this study, we identified two distinct m^{6}A modification patterns in HCC, each being associated with immunological properties, therapeutic response, and prognoses. Finally, we further developed an m^{6}Arisk score model to quantify the m^{6}Arisk subtype in HCC patients and independently validated this model using the ICGC-LIRI-JP cohorts.

In this study, we found that these m^{6}A regulatory genes present a tight and highly interconnected molecular interaction network, which are mainly involved in mRNA stability, mRNA transport, and mRNA metabolism. Analysis of copy number alterations (CNA) and expression profiles revealed a significant abnormal imbalance in the expression levels of m^{6}A writers, readers, and erasers between tumor and normal tissues. In theory, these imbalances could lead to aberrant m^{6}A modification patterns, ultimately contributing to HCC formation and progression. Furthermore, based on the expression profiles of 23 m^{6}A regulators, we identified two independent m^{6}A modification patterns in the TCGA-LIHC cohort using the consensus unsupervised clustering algorithm. Subsequent survival analysis revealed significantly worse prognoses for HCC patients in m^{6}Acluster B compared to those in m^{6}Acluster A. Additionally, we observed that cluster-specific DEGs were also associated with cell cycle and metabolic pathways, as well as cancer-related pathways, such as ECM-receptor interaction and p53 signaling pathway. These findings provide further insights into the potential biological mechanisms underlying the distinct m^{6}A modification patterns and their implications in HCC development and progression.

Moreover, we identified modules significantly correlated with clinical features and m^{6}Acluster subtypes in the subsequent WGCNA based on TCGA-LIHC cohort. To screen potential prognostic biomarkers, we performed three different algorithms (LASSO, SVM-RFE and RF) on the above overlapping 343 DEGs. We also developed a robust m^{6}Arisk score model based on the expression of four m^{6}A-related genes. Our results indicated that the m^{6}Arisk score performed well in predicting the prognoses of HCC patients. Particularly, a high m^{6}risk score was significantly associated with poorer clinical outcomes and lower drug sensitivity. In clinical practice, the TNM stage is a conventional reference for evaluating clinical outcomes and treatment decisions. Surprisingly, multi-Cox regression analysis further validated the superiority of the established m^{6}Arisk score model in predicting OS in HCC patients, independent of other clinical features such as age, gender, and TMN stage. Finally, by integrating the m^{6}Arisk score and clinical features, we developed a quantitative nomogram that enhances the clinical operability of m^{6}Arisk score. The prognostic model can be used for stratifying the prognosis of HCC patients and provides new ideas for targeted therapies. Moreover, the patients in the high- and low-m^{6}Arisk score groups presented distinct clinicopathological features, mutation patterns, immune cell infiltration and immune checkpoint characteristics.

With in-depth research on tumor immunology, immunotherapy has emerged as a promising strategy for tumor treatment. Immune checkpoint blockade (ICB) is currently the most successful and common immunotherapy strategy (55, 56). Currently, PD-1/PD-L1 monoclonal antibodies have become important targeted therapeutic drugs for a variety of tumor immunotherapy. Thus, the therapy immunotherapy strategies targeting m6A methylation provide direction for a direction for improving the therapeutic efficacy of immune checkpoint inhibits. Previous studies have shown that epigenetic-based targeted therapies and immunotherapies work better in clinical tries (57). A study on HCC stem cells found that knockdown AMD1 leaded decreased FTO to regulate m6A methylation levels, which reduced the resistance of HCC cells to sorafenib. They also verified the specific inhibitor of AMD1 may be an effective alternative agent for the treatment of HCC in combination with sorafenib (58). In a similar study of lung cancer, targeting the m6A methylation regulatory enzyme could inhibit cancer cell growth or increase the sensitivity of anti-cancer drugs (59). In glioblastoma, reversing temozolomide resistance conferred by m6A methylation could aid in the development of new therapeutic interventions (60). Another study showed that targeted m6A therapy mediated by knockdown of ALKBH5 expression participated in and promoted angiogenesis, which may also play a role in HCC, providing a new avenue for combined immunotherapy (61). Although clinical immunotherapy (such as anti-PD-1, anti-PD-L1, and anti-CTLA-4) for HCC has been widely used for HCC worldwide (62, 63), only a minority of patients benefited from immunotherapy. Therefore, there is an urgent need for more effective biomarkers to assess whether patients with HCC benefit from tumor immunotherapy. In this study, our findings indicated that high-m^{6}Arisk group appeared to coexist with high expression levels of common immune checkpoint molecules (such as CTLA-4, PDCD1(PD-1), and TIGIT), indirectly suggesting that m^{6}Arisk score may be a better predictor of immunotherapy in HCC patients. The upregulation of immune checkpoints such as PD-L1/PD-1 is a critical characteristic of an inflamed TME, which is driven by pre-infiltrating tumor infiltrating immune cells (TIICs) (64). These immune checkpoints suppress pre-existing cancer immunity to avoid an excessive immune response, but also lead to immune evasion. Here, the expression of immune checkpoints (such as CTLA-4, PDCD1(PD-1), and TIGIT) was significantly upregulated in the high-m^{6}Arisk group, which might be attributed to the upregulation of pre-existing TIICs. These results suggested that the HCC patients with high-m^{6}Arisk score were more sensitive to immune checkpoint blockade (ICB). However, in this study, immunophenotypic scores (IPS) showed no

significant difference in response to ICB between the two m^{6}Arisk score groups. This might be due to the complexity and multiple functions of the TME system, the relationship between m^{6}Arisk and individual immune checkpoints was insufficient to clarify the overall immunological effect of m^{6}Arisk in TME.

Moreover, we also observed a positive correlation of m^{6}Arisk score with the infiltration level of CD8$^+$ T cells under different algorithms. A growing number of studies have evaluated the contribution of cytotoxic cells, especially CD8$^+$ T cells. The cancer immunity cycle represents the immune response of our body to cancer. The activities of the cancer immunity cycle are a direct reflection of the final effect of complex immunomodulatory interactions in tumor microenvironment (TME). In this study, we noted that m^{6}Arisk score presented a positive correlation with the activities of a portion of the cancer immunity cycle. For example, the release of cancer cell antigens (Step 1) and trafficking of immune cells to tumors (Step 4, mainly those that exert antitumor immunity), such as CD8 T cell recruiting, NK cell recruiting, and MDSC recruiting, was significantly upregulated in the high-m^{6}Arisk group. Consequently, the infiltration levels of several effector TIICs, such as CD8+ T cells, dendritic cells, and macrophages, were also significantly increased in the high-m^{6}Arisk group, which had been validated in six different algorithms. Therefore, the high m^{6}Arisk-score reflected an inflammatory phenotype in TME. Meanwhile, m^{6}Arisk score was positively correlated with the enrichment scores of immunotherapy-predicted pathways.

Besides, our findings further indicated that HCC patients with a high m^{6}Arisk score were more sensitive to some common chemotherapy and molecular-targeted drugs, suggesting that the m^{6}Arisk score might contribute to guiding personalized treatment for patients. However, the drug mechanisms and their effects on HCC progression need to be further studied. Additionally, we developed a nomogram model by incorporating the m^{6}Arisk score and clinicopathological features, and further validated and evaluated the predictive capability and accuracy of this model in external verification cohort. These results suggested that the application of the m^{6}Arisk score for the prognostic stratification of HCC has good clinical applicability and clinical net benefit.

Finally, it's worth noting that despite its intriguing and promising findings, this study has several limitations. First, this study is a retrospective study based on public online databases (TCGA-LIHC and ICGC-LIRI-JP), which may have inherent selection bias. Second, although our results were generalized and robust in validation cohorts, the batch effects from different cohorts should be considered. Third, although we highlighted the predictive power of m^{6}Arisk scores for HCC TME status and prognosis, we did not identify the molecular mechanisms involved.

5 Conclusion

In our study, our findings reveal the crucial role of m^{6}A modification patterns for predicting HCC TME status and prognosis, and highlight the good clinical applicability and net benefit of m^{6}Arisk score in terms of prognosis, immunophenotype, and drug therapy in HCC patients.

Data availability statement

The original contributions presented in the study are included in the article/Supplementary Materials, further inquiries can be directed to the corresponding author/s.

Ethics statement

Twenty-eight pairs of fresh-frozen tissues (HCC tissues and adjacent tissues) were collected from the Zhongnan Hospital of Wuhan University and approved by the ethics committee (Approval Number 2017058). Written informed consent was obtained from all the participants. The studies were conducted in accordance with the local legislation and institutional requirements. The participants provided their written informed consent to participate in this study.

Author contributions

SX: Data curation, Investigation, Methodology, Software, Visualization, Writing – original draft, Writing – review & editing. YZ: Methodology, Validation, Writing – review & editing. YY: Methodology, Validation, Writing – review & editing. KD: Methodology, Validation, Software, Writing – review & editing. HZ: Methodology, Software, Validation, Writing – review & editing. CL: Methodology, Writing – review & editing. S-ML: Conceptualization, Funding acquisition, Writing – review & editing.

Funding

The author(s) declare financial support was received for the research, authorship, and/or publication of this article. This work was supported by the National Natural Science Foundation of China (81772276) and Hubei Provincial Natural Science Fund for Creative Research Groups (2019CFA018).

Conflict of interest

The authors declare that the research was conducted in the absence of any commercial or financial relationships that could be construed as a potential conflict of interest.

Publisher's note

Supplementary material

The Supplementary Material for this article can be found online at: https://www.frontiersin.org/articles/10.3389/fimmu.2024.1374465/full#supplementary-material

References

1. Llovet JM, Kelley RK, Villanueva A, Singal AG, Pikarsky E, Roayaie S, et al. Hepatocellular carcinoma. *Nat Rev Dis Primers*. (2021) 7:6. doi: 10.1038/s41572-020-00240-3

2. Anwanwan D, Singh SK, Singh S, Saikam V, Singh R. Challenges in liver cancer and possible treatment approaches. *Biochim Biophys Acta Rev Cancer*. (2020) 1873:188314. doi: 10.1016/j.bbcan.2019.188314

3. Hanahan D, Coussens LM. Accessories to the crime: functions of cells recruited to the tumor microenvironment. *Cancer Cell*. (2012) 21:309–22. doi: 10.1016/j.ccr.2012.02.022

4. Junttila MR, de Sauvage FJ. Influence of tumour micro-environment heterogeneity on therapeutic response. *Nature*. (2013) 501:346–54. doi: 10.1038/nature12626

5. McAllister SS, Weinberg RA. The tumour-induced systemic environment as a critical regulator of cancer progression and metastasis. *Nat Cell Biol*. (2014) 16:717–27. doi: 10.1038/ncb3015

6. Grivennikov SI, Greten FR, Karin M. Immunity, inflammation, and cancer. *Cell*. (2010) 140:883–99. doi: 10.1016/j.cell.2010.01.025

7. Fu Y, Dominissini D, Rechavi G, He. C. Gene expression regulation mediated through reversible m(6)A RNA methylation. *Nat Rev Genet*. (2014) 15:293–306. doi: 10.1038/nrg3724

8. Delaunay S, Frye M. RNA modifications regulating cell fate in cancer. *Nat Cell Biol*. (2019) 21:552–9. doi: 10.1038/s41556-019-0319-0

9. Bird A. DNA methylation patterns and epigenetic memory. *Genes Dev*. (2002) 16:6–21. doi: 10.1101/gad.947102

10. Wang Q, Chen C, Ding Q, Zhao Y, Wang Z, Chen. J, et al. METTL3-mediated m(6)A modification of HDGF mRNA promotes gastric cancer progression and has prognostic significance. *Gut*. (2020) 69:1193–205. doi: 10.1136/gutjnl-2019-319639

11. Hou J, Zhang H, Liu J, Zhao Z, Wang J, Lu. Z, et al. YTHDF2 reduction fuels inflammation and vascular abnormalization in hepatocellular carcinoma. *Mol Cancer*. (2019) 18:163. doi: 10.1186/s12943-019-1082-3

12. Gu C, Wang Z, Zhou N, Li G, Kou Y, Luo. Y, et al. Mettl14 inhibits bladder TIC self-renewal and bladder tumorigenesis through N(6)-methyladenosine of Notch1. *Mol Cancer*. (2019) 18:168. doi: 10.1186/s12943-019-1084-1

13. Yan F, Al-Kali A, Zhang Z, Liu J, Pang J, Zhao. N, et al. A dynamic N(6)-methyladenosine methylome regulates intrinsic and acquired resistance to tyrosine kinase inhibitors. *Cell Res*. (2018) 28:1062–76. doi: 10.1038/s41422-018-0097-4

14. Han SH, Choe J. Diverse molecular functions of m(6)A mRNA modification in cancer. *Exp Mol Med*. (2020) 52:738–49. doi: 10.1038/s12276-020-0432-y

15. Wang T, Kong S, Tao M, Ju S. The potential role of RNA N6-methyladenosine in Cancer progression. *Mol Cancer*. (2020) 19:88. doi: 10.1186/s12943-020-01204-7

16. Zhao Y, Shi Y, Shen H, Xie W. m(6)A-binding proteins: the emerging crucial performers in epigenetics. *J Hematol Oncol*. (2020) 13:35. doi: 10.1186/s13045-020-00872-8

17. Seiler M, Huang CC, Szalma S, Bhanot G. ConsensusCluster: a software tool for unsupervised cluster discovery in numerical data. *OMICS*. (2010) 14:109–13. doi: 10.1089/omi.2009.0083

18. Wilkerson MD, Hayes DN. ConsensusClusterPlus: a class discovery tool with confidence assessments and item tracking. *Bioinformatics*. (2010) 26:1572–3. doi: 10.1093/bioinformatics/btq170

19. Love MI, Huber W, Anders S. Moderated estimation of fold change and dispersion for RNA-seq data with DESeq2. *Genome Biol*. (2014) 15:550. doi: 10.1186/s13059-014-0550-8

20. Hanzelmann S, Castelo R, Guinney J. GSVA: gene set variation analysis for microarray and RNA-seq data. *BMC Bioinf*. (2013) 14:7. doi: 10.1186/1471-2105-14-7

21. Liberzon A, Birger C, Thorvaldsdottir H, Ghandi M, Mesirov JP, Tamayo P. The Molecular Signatures Database (MSigDB) hallmark gene set collection. *Cell Syst*. (2015) 1:417–25. doi: 10.1016/j.cels.2015.12.004

22. Engebretsen S, Bohlin J. Statistical predictions with glmnet. *Clin Epigenet*. (2019) 11:123. doi: 10.1186/s13148-019-0730-1

23. Sanz H, Valim C, Vegas E, Oller JM, Reverter F. SVM-RFE: selection and visualization of the most relevant features through non-linear kernels. *BMC Bioinf*. (2018) 19:432. doi: 10.1186/s12859-018-2451-4

24. Qiu J, Peng B, Tang Y, Qian Y, Guo P, Li M, et al. CpG methylation signature predicts recurrence in early-stage hepatocellular carcinoma: results from a multicenter study. *J Clin Oncol*. (2017) 35:734–42. doi: 10.1200/JCO.2016.68.2153

25. Chen DS, Mellman I. Oncology meets immunology: the cancer-immunity cycle. *Immunity*. (2013) 39:1–10. doi: 10.1016/j.immuni.2013.07.012

26. Charoentong P, Finotello F, Angelova M, Mayer C, Efremova M, Rieder D, et al. Pan-cancer immunogenomic analyses reveal genotype-immunophenotype relationships and predictors of response to checkpoint blockade. *Cell Rep*. (2017) 18:248–62. doi: 10.1016/j.celrep.2016.12.019

27. Xu L, Deng C, Pang B, Zhang X, Liu W, Liao G, et al. TIP: A web server for resolving tumor immunophenotype profiling. *Cancer Res*. (2018) 78:6575–80. doi: 10.1158/0008-5472.CAN-18-0689

28. Newman AM, Liu CL, Green MR, Gentles AJ, Feng W, Xu Y, et al. Robust enumeration of cell subsets from tissue expression profiles. *Nat Methods*. (2015) 12:453–7. doi: 10.1038/nmeth.3337

29. Becht E, Giraldo NA, Lacroix L, Buttard B, Elarouci N, Petitprez F, et al. Estimating the population abundance of tissue-infiltrating immune and stromal cell populations using gene expression. *Genome Biol*. (2016) 17:218. doi: 10.1186/s13059-016-1070-5

30. Finotello F, Mayer C, Plattner C, Laschober G, Rieder D, Hackl H, et al. Molecular and pharmacological modulators of the tumor immune contexture revealed by deconvolution of RNA-seq data. *Genome Med*. (2019) 11:34. doi: 10.1186/s13073-019-0638-6

31. Li T, Fu J, Zeng Z, Cohen D, Li J, Chen Q, et al. TIMER2.0 for analysis of tumor-infiltrating immune cells. *Nucleic Acids Res*. (2020) 48:W509–W14. doi: 10.1093/nar/gkaa407

32. Aran D, Hu Z, Butte AJ. xCell: digitally portraying the tissue cellular heterogeneity landscape. *Genome Biol*. (2017) 18:220. doi: 10.1186/s13059-017-1349-1

33. Ru B, Wong CN, Tong Y, Zhong JY, Zhong SSW, Wu WC, et al. TISIDB: an integrated repository portal for tumor-immune system interactions. *Bioinformatics*. (2019) 35:4200–2. doi: 10.1093/bioinformatics/btz210

34. Auslander N, Zhang G, Lee JS, Frederick DT, Miao B, Moll T, et al. Robust prediction of response to immune checkpoint blockade therapy in metastatic melanoma. *Nat Med*. (2018) 24:1545–9. doi: 10.1038/s41591-018-0157-9

35. Mayakonda A, Lin DC, Assenov Y, Plass C, Koeffler HP. Maftools: efficient and comprehensive analysis of somatic variants in cancer. *Genome Res*. (2018) 28:1747–56. doi: 10.1101/gr.239244.118

36. Sayaman RW, Saad M, Thorsson V, Hu D, Hendrickx W, Roelands J, et al. Germline genetic contribution to the immune landscape of cancer. *Immunity*. (2021) 54:367–86.e8. doi: 10.1016/j.immuni.2021.01.011

37. Han Y, Li H, Guan Y, Huang J. Immune repertoire: A potential biomarker and therapeutic for hepatocellular carcinoma. *Cancer Lett*. (2016) 379:206–12. doi: 10.1016/j.canlet.2015.06.022

38. Danaher P, Warren S, Lu R, Samayoa J, Sullivan A, Pekker I, et al. Pan-cancer adaptive immune resistance as defined by the Tumor Inflammation Signature (TIS): results from The Cancer Genome Atlas (TCGA). *J Immunother Cancer*. (2018) 6:63. doi: 10.1186/s40425-018-0367-1

39. Tan L, Qin Y, Xie R, Xia T, Duan X, Peng L, et al. N6-methyladenosine-associated prognostic pseudogenes contribute to predicting immunotherapy benefits and therapeutic agents in head and neck squamous cell carcinoma. *Theranostics*. (2022) 12:7267–88. doi: 10.7150/thno.76689

40. Maeser D, Gruener RF, Huang RS. oncoPredict: an R package for predicting *in vivo* or cancer patient drug response and biomarkers from cell line screening data. *Brief Bioinform*. (2021) 22(6):bbab260. doi: 10.1093/bib/bbab260

41. Iasonos A, Schrag D, Raj GV, Panageas KS. How to build and interpret a nomogram for cancer prognosis. *J Clin Oncol*. (2008) 26:1364–70. doi: 10.1200/JCO.2007.12.9791

42. Fitzgerald M, Saville BR, Lewis RJ. Decision curve analysis. *JAMA*. (2015) 313:409–10. doi: 10.1001/jama.2015.37

43. Kerr KF, Brown MD, Zhu K, Janes H. Assessing the clinical impact of risk prediction models with decision curves: guidance for correct interpretation and appropriate use. *J Clin Oncol*. (2016) 34:2534–40. doi: 10.1200/JCO.2015.65.5654

44. Zhang Y, Yang Z, Tang Y, Guo C, Lin D, Cheng L, et al. Hallmark guided identification and characterization of a novel immune-relevant signature for prognostication of recurrence in stage I–III lung adenocarcinoma. *Genes Dis*. (2022) 10(4):1657–74. doi: 10.1016/j.gendis.2022.07.005

45. Llovet JM, Zucman-Rossi J, Pikarsky E, Sangro B, Schwartz M, Sherman M, et al. Hepatocellular carcinoma. *Nat Rev Dis Primers*. (2016) 2:16018. doi: 10.1038/nrdp.2016.18

46. Braghini MR, Lo Re O, Romito I, Fernandez-Barrena MG, Barbaro B, Pomella S, et al. Epigenetic remodelling in human hepatocellular carcinoma. *J Exp Clin Cancer Res*. (2022) 41:107. doi: 10.1186/s13046-022-02297-2

47. Ozen C, Yildiz G, Dagcan AT, Cevik D, Ors A, Keles U, et al. Genetics and epigenetics of liver cancer. *N Biotechnol*. (2013) 30:381–4. doi: 10.1016/j.nbt.2013.01.007

48. Pea A, Jamieson NB, Braconi C. Biology and clinical application of regulatory RNAs in hepatocellular carcinoma. *Hepatology*. (2021) 73 Suppl 1:38–48. doi: 10.1002/hep.31225

49. Han TS, Ban HS, Hur K, Cho HS. The epigenetic regulation of HCC metastasis. *Int J Mol Sci*. (2018) 19(12):3978. doi: 10.3390/ijms19123978

50. Liang W, Lin Z, Du C, Qiu D, Zhang Q. mRNA modification orchestrates cancer stem cell fate decisions. *Mol Cancer*. (2020) 19(1):38. doi: 10.1186/s12943-020-01166-w

51. Yang S, Wei J, Cui YH, Park G, Shah P, Deng Y, et al. m(6)A mRNA demethylase FTO regulates melanoma tumorigenicity and response to anti-PD-1 blockade. *Nat Commun*. (2019) 10:2782. doi: 10.1038/s41467-019-10669-0

52. Barbieri I, Kouzarides T. Role of RNA modifications in cancer. *Nat Rev Cancer*. (2020) 20:303–22. doi: 10.1038/s41568-020-0253-2

53. Zhang S, Meng Y, Zhou L, Qiu L, Wang H, Su D, et al. Targeting epigenetic regulators for inflammation: Mechanisms and intervention therapy. *MedComm (2020)*. (2022) 3:e173. doi: 10.1002/mco2.173

54. Qiu L, Jing Q, Li Y, Han J. RNA modification: mechanisms and therapeutic targets. *Mol BioMed*. (2023) 4:25. doi: 10.1186/s43556-023-00139-x

55. Topalian SL, Taube JM, Pardoll DM. Neoadjuvant checkpoint blockade for cancer immunotherapy. *Science*. (2020) 367. doi: 10.1126/science.aax0182

56. Ribas A, Wolchok JD. Cancer immunotherapy using checkpoint blockade. *Science*. (2018) 359:1350–5. doi: 10.1126/science.aar4060

57. Cheng Y, Zhang T, Xu Q. Therapeutic advances in non-small cell lung cancer: Focus on clinical development of targeted therapy and immunotherapy. *MedComm (2020)*. (2021) 2:692–729. doi: 10.1002/mco2.105

58. Bian X, Shi D, Xing K, Zhou H, Lu L, Yu D, et al. AMD1 upregulates hepatocellular carcinoma cells stemness by FTO mediated mRNA demethylation. *Clin Transl Med*. (2021) 11:e352. doi: 10.1002/ctm2.352

59. Khan RIN, Malla WA. m6A modification of RNA and its role in cancer, with a special focus on lung cancer. *Genomics*. (2021) 113:2860–9. doi: 10.1016/j.ygeno.2021.06.013

60. Li F, Chen S, Yu J, Gao Z, Sun Z, Yi Y, et al. Interplay of m6 A and histone modifications contributes to temozolomide resistance in glioblastoma. *Clin Transl Med*. (2021) 11:e553. doi: 10.1002/ctm2.553

61. Zhao Y, Hu J, Sun X, Yang K, Yang L, Kong L, et al. Loss of m6A demethylase ALKBH5 promotes post-ischemic angiogenesis via post-transcriptional stabilization of WNT5A. *Clin Transl Med*. (2021) 11:e402. doi: 10.1002/ctm2.402

62. Wu X, Gu Z, Chen Y, Chen B, Chen W, Weng L, et al. Application of PD-1 blockade in cancer immunotherapy. *Comput Struct Biotechnol J*. (2019) 17:661–74. doi: 10.1016/j.csbj.2019.03.006

63. Sangro B, Sarobe P, Hervas-Stubbs S, Melero I. Advances in immunotherapy for hepatocellular carcinoma. *Nat Rev Gastroenterol Hepatol*. (2021) 18:525–43. doi: 10.1038/s41575-021-00438-0

64. Spranger S, Spaapen RM, Zha Y, Williams J, Meng Y, Ha TT, et al. Up-regulation of PD-L1, IDO, and T(regs) in the melanoma tumor microenvironment is driven by CD8(+) T cells. *Sci Transl Med*. (2013) 5:200ra116. doi: 10.1126/scitranslmed.3006504

frontiers | Frontiers in Immunology

TYPE Original Research
PUBLISHED 25 November 2024
DOI 10.3389/fimmu.2024.1423194

OPEN ACCESS

EDITED BY
Susan (krum) Miranda,
University of Tennessee Health Science Center (UTHSC), United States

REVIEWED BY
Meng Jia,
University of Pennsylvania, United States
Jeong A Park,
Inha University Hospital, Republic of Korea

*CORRESPONDENCE
Si-shan Bian
sdszyybss@163.com

RECEIVED 25 April 2024
ACCEPTED 07 November 2024
PUBLISHED 25 November 2024

CITATION
Wu A, Yang Z-k, Kong P, Yu P, Li Y-t, Xu J-l, Bian S-s and Teng J-w (2024) Exploring osteosarcoma based on the tumor microenvironment.
Front. Immunol. 15:1423194.
doi: 10.3389/fimmu.2024.1423194

Exploring osteosarcoma based on the tumor microenvironment

Ao Wu[1], Zhi-kai Yang[2], Peng Kong[3], Peng Yu[1], You-tong Li[1], Jia-le Xu[1], Si-shan Bian[4]* and Jia-wen Teng[4]

[1]The First Clinical College of Shandong University of Traditional Chinese Medicine, Jinan, Shandong, China, [2]Hand and Foot Orthopaedic Department, Changle County People's Hospital, Weifang, Shandong, China, [3]Department of Minimally Invasive Orthopedics, Affiliated Hospital of Shandong Traditional Chinese Medicine University, Jinan, Shandong, China, [4]Department of Traumatology and Orthopaedics, Affiliated Hospital of Shandong University of Traditional Chinese Medicine, Jinan, Shandong, China

Osteosarcoma is a cancerous bone tumor that develops from mesenchymal cells and is characterized by early metastasis, easy drug resistance, high disability, and mortality. Immunological characteristics of the tumor microenvironment (TME) have attracted attention for the prognosis and treatment of osteosarcoma, and there is a need to explore a signature with high sensitivity for prognosis. In the present study, a total of 84 samples of osteosarcoma were acquired from the UCSC Xena database, analyzed for immune infiltration and classified into two categories depending on their immune properties, and then screened for DEGs between the two groups and analyzed for enrichment, with the majority of DEGs enriched in the immune domain. To further analyze their immune characteristics, the immune-related genes were obtained from the TIMER database. We performed an intersection analysis to identify immune-related differentially expressed genes (IR-DEGs), which were analyzed using a univariate COX regression, and LASSO analysis was used to obtain the ideal genes to construct the risk model, and to uncover the prognostic distinctions between high-risk scoring group and low-risk scoring group, a survival analysis was conducted. The risk assessment model developed in this study revealed a notable variation in survival analysis outcomes between the high-risk and low-risk scoring groups, and the conclusions reached by the model are consistent with the findings of previous scholars. They also yield meaningful results when analyzing immune checkpoints. The risk assessment model developed in this study is precise and dependable for forecasting outcomes and analyzing characteristics of osteosarcoma.

KEYWORDS

osteosarcoma, tumor microenvironment, immune-related genes, immunotherapy, immunization checkpoints

1 Introduction

Osteosarcoma(OS) originates from bone tissue and is a malignant tumor with local invasion and rapid infiltrative metastasis, prevalent in children and adolescents (1, 2). Osteosarcoma has a high disability rate. Currently, surgery combined with chemotherapy is the universal treatment for osteosarcoma, but the survival rate of patients after 5 years is still relatively poor (3). Consequently, there is a pressing requirement to develop novel evaluation methods to enhance the effectiveness of treatment. Immunotherapy has emerged as the most promising treatment in the past few decades.

The immune system plays a role in every phase of tumor formation and advancement. Thus, dysfunction in the immune system plays a significant role in the onset of tumors. When the immune system interplays with the tumor microenvironment, the T cells associated with the anti-tumor immune response will be activated, and they will up-regulate the expression of various inhibitory receptors on their cell surfaces and bind to the corresponding ligands expressed on the exterior of the tumor cells, resulting in the suppression of the immune response, i.e., the intensity of the anti-tumor immune response will be weakened, and ultimately, the tumor cells will be able to achieve immune escape. The goal of immune checkpoint blockade (ICB) therapy is to enhance the functionality of T cells by disrupting the interaction between these receptors and their ligands, thereby enabling more efficient eradication of cancer cells through the immune system. An increasing body of clinical research has shown the efficacy of immune checkpoint blockade (ICB) therapy in the treatment of many kinds of tumor types (4–6). These trials have facilitated the study of the osteosarcoma tumor microenvironment(TME). TME and tumor clinical presentation, prognosis, and response to immunotherapy are closely related (7, 8), and TME is considered a key factor in OS progression (9). Enhanced comprehension of the immune system's role in osteosarcoma and the tumor microenvironment (TME) contributes to the advancement of immunotherapy for this condition.

In this study, osteosarcoma samples were obtained from an online database and the samples were immuno-scored, divided into two groups, and analyzed for further analysis of immune-related differential genes between the two groups. A comprehensive immune profile was constructed based on the correlation between the expression levels, prognostic value, and immune infiltration levels of these genes. This study may assist in immunological precision therapy.

2 Materials and methods

2.1 Data acquisition

TARGET-OS fragment per kilobase of transcript per million mapped reads (FPKM) values (https://gdc-hub.s3.us-east-1.amazonaws.com/download/TARGET-OS.htseq_fpkm.tsv.gz) was obtained from UCSC Xena web platform(https://xenabrowser.net/datapages/) for downstream analysis, and Counts values(https://gdc-hub.s3.us-east-1.amazonaws.com/download/TARGET-OS.htseq_counts.tsv.gz) were obtained for differential analysis.

Eighty-eight osteosarcoma samples were initially retrieved from the UCSC Xena web platform; samples with no or incomplete clinical information were excluded, for a total of 84 osteosarcoma samples. The clinical characteristics of 84 patients with osteosarcoma are shown in Supplementary Table S1. In addition, we obtained the set of immune-related genes from the TIMER database for subsequent analyses(Supplementary Table S2). The somatic mutation data and the copy number variation (CNV) profile were obtained from TCGA (https://portal.gdc.cancer.gov/).

2.2 Immune assessment, clustering, and comparison of immune properties

The tumor samples were scored using the ESTIMATE algorithm to obtain StromalScore, ImmuneScore, ESTIMATEScore, and TumorPurity (10), and the samples were divided into two groups, named high and low, based on the average of the above four data sets. Survival analysis was conducted to investigate the correlation between the four parameters and overall survival (OS).

Subsequently, the abundance of 30 immune cells in the tumor samples was assessed using the ssGSEA algorithm (11), and the tumor samples were consistently clustered to obtain immune subtype groupings. An examination was conducted to explore variations in various attributes among clinical phenotypes. Clinical characteristics, including gender, age, survival time, survival status, whether metastatic or not, and previously obtained immune subtype groupings, were visualized using a heatmap, and a box plot was created to assess the levels of immune infiltration among different immune subtypes. In addition, box plots of the four scores obtained from the previous ESTIMATE algorithm were compared according to the immune subtype groupings. To assess the tumor mutational burden (TMB), we examined the total count of unique genes without synonymous somatic mutations per megabase (Mb) in each sample. Truncating mutations comprised frame-shift deletions or insertions, nonsense mutations, and splice-site mutations. In addition, non-truncating mutations encompass in-frame deletions or insertions, missense mutations, and nonstop mutations. We identified mutational differences between the two groups based on immunological grouping. Subsequently, differently expressed genes (DEGs) were identified through comparative analysis of immune subtype classifications utilizing the limma package in R software version 4.3.2, with a significance threshold set at $P<0.05$ and $|logFC|>1$. Volcano plots were generated to visualize differentially expressed genes (DEGs), which were further subjected to gene ontology (GO) function annotation and Kyoto Encyclopedia of Genes and Genomes (KEGG) pathway analysis. Pathway differences between immune subtypes were analyzed using GSEA. GO and KEGG analyses were obtained from the DAVID Database (https://david.ncifcrf.gov/) and then visualized using the R software ggplot2 package, and GSEA results were analyzed using the R software clusterProfiler package and the GseaVis package.

2.3 Assessment of immune-related DEGs

Immune-related differentially expressed genes (IR-DEGs) were identified by intersecting differentially expressed genes (DEGs) with immune-related genes. The IR-DEGs were imported into the STRING platform for protein-protein interaction (PPI) analysis, and the IR-DEGs were analyzed for their functions using GO functional annotation and KEGG pathway analysis. The intersecting genes were also analyzed for GSEA enrichment using the above methods. Finally, the MCC algorithm in Cytoscape software version 3.10.1 was used to obtain the top ten genes. Next, we explored the overall survival and immune infiltration among various immune subtypes based on the top ten genes.

2.4 Risk model construction

By setting the significance level at $P < 0.05$, the univariate Cox regression analysis was conducted to explore the IR-DEGs and identify genes related to survival outcomes. Next, the study utilized Least Absolute Shrinkage and Selection Operator (LASSO) estimation for survival modeling of genes showing significant correlations with survival to identify potential candidate genes. Following this, the sample's risk score was computed based on the selected candidate gene. The samples are divided into training sets and test sets on average. The grouping is strictly randomly followed, and there is no statistical difference between the two groups. Calculate the prognosis of the training set, test set, and all groups, and present with the ROC curve.

2.5 Prognosis of features

We first assessed tumor immune escape and immune checkpoint blockade responses using the Tumor Immune Dysfunction and Exclusion (TIDE) online website (http://tide.dfci.harvard.edu/), followed by risk scoring to divide the sample into a high-risk scoring group and a low-risk scoring group, and then TIDE values were calculated between the two groups, with higher TIDE scores associated with poorer immune checkpoint blockade therapy. The differences in immune checkpoint-related genes between the two groups were subsequently calculated and represented by a scatter plot. The samples were categorized based on the high and low levels of candidate genes, and then the disparity in immune checkpoint-related genes was computed between the two sets. This dissimilarity was visually depicted through a scatter plot to investigate the potential connection between the candidate genes and immune checkpoint genes. The immune infiltration of all samples was calculated using CIBERSORT to screen for differential immune cells between the high-risk scoring group and the low-risk scoring group, and the expression of candidate genes in the differential immune cells was calculated. MicroenvironmentScore was calculated for all samples using the xCell (https://xcell.ucsf.edu/) online site. Differences in MicroenvironmentScore between the high-risk scoring group and the low-risk scoring group were calculated and visualized in a boxplot.

3 Results

3.1 A holistic landscape of immunological features

Based on the tumor stroma and immune characteristics of osteosarcoma, the acquired osteosarcoma samples were analyzed using the ESTIMATE algorithm to reveal the level of immune infiltration of tumor samples in osteosarcoma. StromalScore, ImmuneScore, ESTIMATEScore, and TumorPurity were calculated and analyzed in the tumor samples (Supplementary Table S3). The scores were grouped according to their median (median of StromalScore, ImmuneScore, ESTIMATEScore, and TumorPurity were 488.57, 424.86, 1095.16, and 0.72 in that order), and were named as high and low groupings, respectively. These scores reflect the different compositions of the tumor microenvironment, assessing the degree of stromal and immune cell infiltration, and by grouping them, it is possible to understand the biology of the tumor better and to explore its relationship with tumor prognosis by performing a Kaplan-Meier curve analysis based on survival time and status (Figures 1A–D). In StromalScore, ImmuneScore, and ESTIMATEScore, high grouping was significantly associated with high survival, while low TumorPurity was associated with high survival. Of these, ImmuneScore was most significantly associated with survival. The data obtained from the above suggests that osteosarcoma can be analyzed prognostically based on ImmuneScore, followed by ssGSEA analysis.

The impact of immunity on osteosarcoma was explored using ssGSEA (Supplementary Table S4). Subsequently, unsupervised clustering was performed on the ssGSEA results, and the number of clusters with the highest average within-group concordance was 2 (Figure 2B). Therefore, based on their immune characteristics, the samples were categorized into two groups, and the 30 immune cells were subsequently displayed along with clinical characteristics including gender, age, survival time, survival status, and whether the tumor has metastasized or not (Figure 2A). There are noticeable variations in immunological features observed between the clustered groups. Groups with rich immune profiles were named high immune groups, therefore, groups with lower immune profiles were named low immune groups (Supplementary Table S5). Tumour metastasis was more frequent in the low-immunity group than in the high-immunity group. To further investigate the relationship between immune groupings and the levels of TME, immune activation, and tumor cell infiltration, several analyses of osteosarcoma TME were performed. As expected, StromalScore, ImmuneScore, and ESTIMATEScore were higher and TumorPurity was lower in the hyperimmune group (Figures 2C–F), suggesting that the hyperimmune group was associated with higher survival. Immune checkpoints and immune cell abundance were also significantly higher in the hyperimmune group (Figure 2G). Subsequent Principal Component Analysis (PCA) was performed and the immune characteristics differed significantly between the two groups (Figure 2H), therefore, we hypothesized that the immune groupings found above could well distinguish the immune and genetic characteristics of the samples.

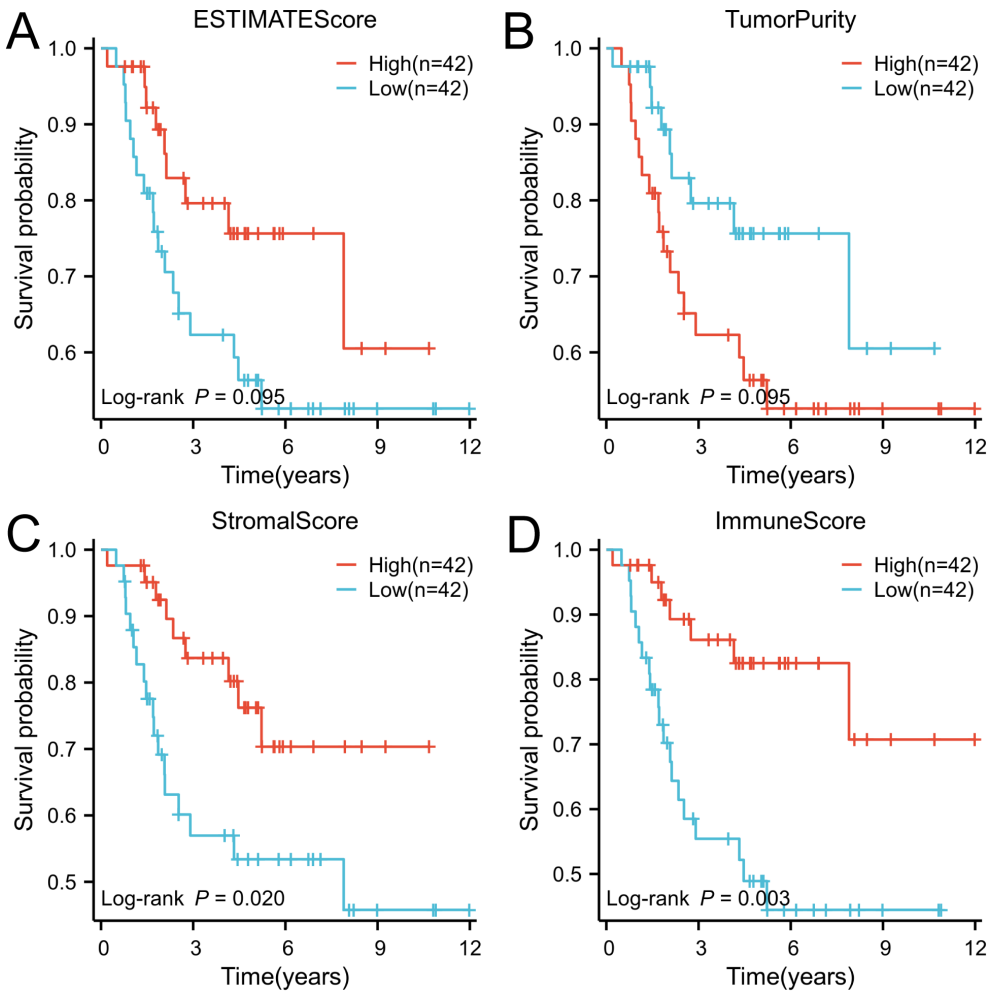

FIGURE 1
The ESTIMATE algorithm was utilized to conduct survival analysis on patient groups categorized based on high and low immune scores, and the results were visually represented through Kaplan-Meier (K-M) curves. **(A)** ESTIMATE score, **(B)** Tumor purity score, **(C)** Stromal score, and **(D)** Immune score.

3.2 Mutation analysis

The analysis of gene mutations revealed a notably elevated mutation rate in the low immunity group, with TP53 being identified as the gene exhibiting the highest frequency of mutations (Figure 3A). Tumor Mutation Burden (TMB) analysis was carried out (Supplementary Table S6) and visualized using scatter plots (Figure 3B). Following this, an analysis of TMB in the high and low-immunity cohorts demonstrated a variation in TMB levels between the two groups, with TMB showing an elevation in the low-immunity cohort (Figure 3C). We hypothesized that this may be related to the poorer prognosis of the low-immunity group.

3.3 Screening and evaluation of differentially expressed genes

The examination of gene expression variations between immune subtypes identified a pool of 836 differentially expressed genes for subsequent scrutiny (Supplementary Table S7), with 697 genes showing up-regulation (83.37%) and 139 genes demonstrating down-regulation (16.63%) (Figure 4A). Enrichment analyses of DEGs by GO annotation and KEGG pathway enrichment analyses identified 497 biological processes (BPs), 94 cell components (CCs), 118 molecular functions (MFs), and 69 KEGG pathways (Figures 4C, D). The DEGs were also analyzed for GSEA enrichment (Figure 4B).

As shown in the figure, the top ten biological processes were filtered according to P-value, most of which were related to immunity, including immune response, inflammatory response, innate immune response, neutrophil chemotaxis, and adaptive immune response. In addition, KEGG pathways are also related to immunity, including Phagosome, Antigen processing and presentation, B cell receptor signaling pathway Th17 cell differentiation, etc. In summary, DEGs and immunity are closely related, subsequently, GSEA enrichment analysis of DEGs was performed to further investigate the pathway differences between immune subtypes, based on P<0.05, a total of 47 enriched pathways were obtained, and the top ten were Tuberculosis

10.3389/fimmu.2024.1423194

(NES=3.11,p.value=6.73E-10) in order, Leishmaniasis (NES=3.01, p.value=3.03E-09), Staphylococcus aureus infection (NES=3.01,p.value=7.05E-09), Th17 cell differentiation (NES=2.90, p.value=4.69E-08), Th1 and Th2 cell differentiation (NES=2.82, p.value=1.13E-07), Hematopoietic cell lineage (NES=2.72, p.value=5.33E-07), Influenza A (NES=2.71,p.value=4.87E-07), Systemic lupus erythematosus (NES=2.60,p.value=1.83E-06), Phagosome (NES=2.66,p.value=2.21E-06) and Neutrophil

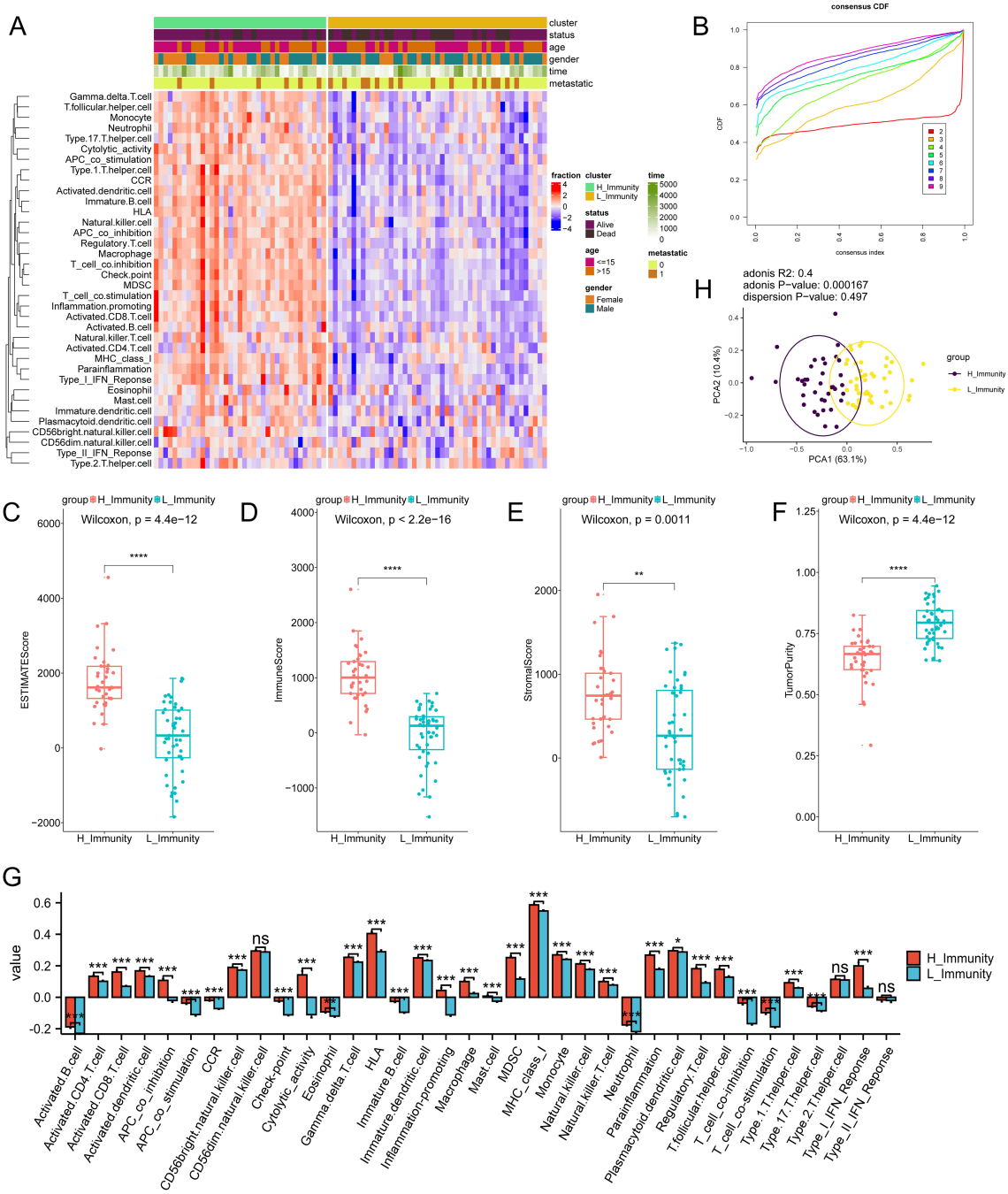

FIGURE 2
Immune subtype identification and comparative analysis. The symbols * represent p-values less than 0.05, ** represent p-values less than 0.01, *** represent p-values less than 0.001, **** represent p-values less than 0.0001. **(A)** ssGSEA analyses of 84 samples, divided into two groups based on 30 ssGSEA scores per sample. **(B)** Unsupervised clustering of the samples based on their immunological characteristics, where the number of clusters with the highest average within-group agreement is 2. **(C–F)** shows, in order, the differences in ESTIMATEScore, ImmuneScore, StromalScore, and TumorPurity between the high and low immunity groups. **(G)** A box plot is utilized to display the levels of immune cell infiltration in groups categorized as either having high or low immunity. In this visualization, the red boxes correspond to the high immunity group, while the blue boxes correspond to the low immunity group. **(H)** PCA analysis of the two immune subtypes, with purple and yellow dots representing the immunity–high and —low groups, respectively. "ns" stands for no statistical difference.

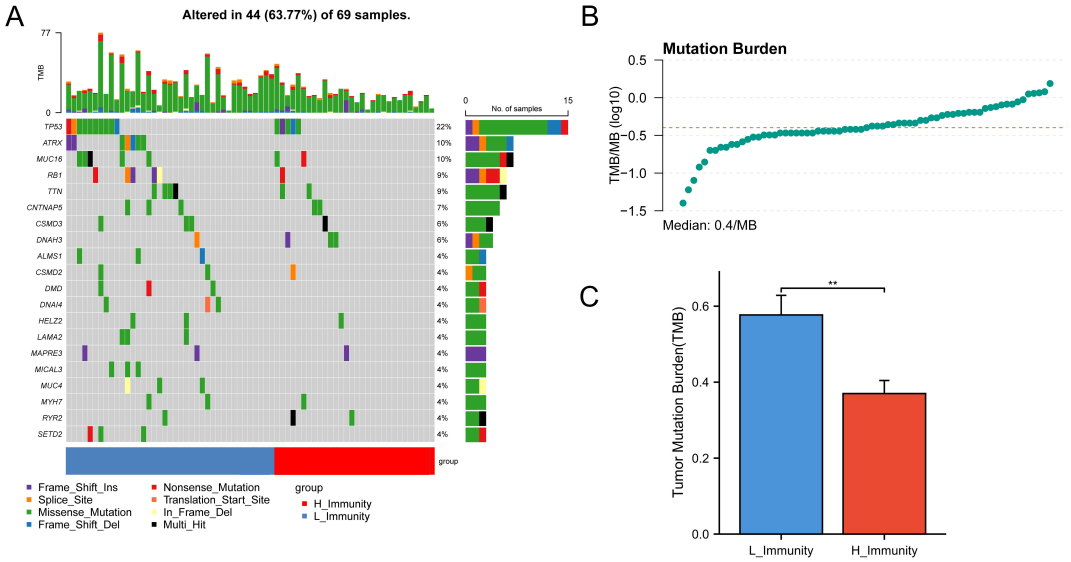

FIGURE 3
Mutations between high and low immunity groups. The symbols represent p-values less than 0.01. **(A)** Mutation status of genes in the high and low immunity groups. **(B)** TMB distribution of all samples. **(C)** Bar graph showing the difference in TMB between the high and low immunity groups. ** represent p-values less than 0.01.

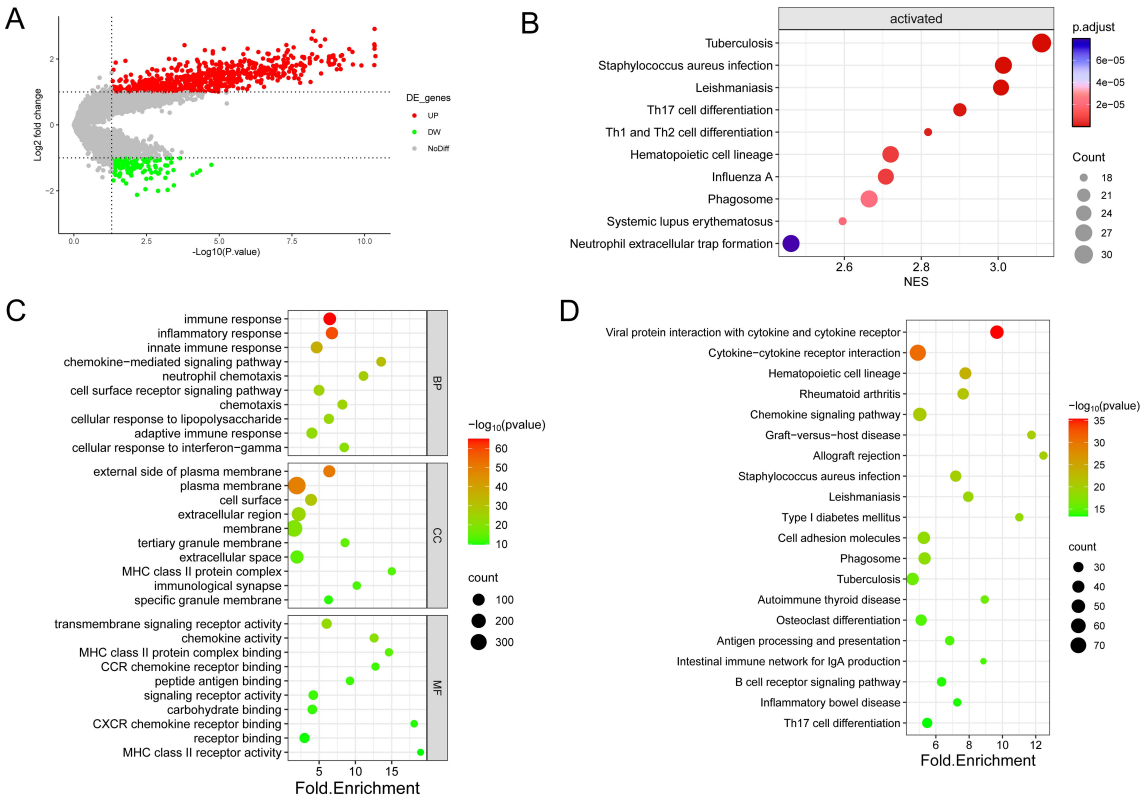

FIGURE 4
Enrichment analysis was conducted on the DEGs identified in the two immune subtypes. **(A)** Volcano diagram showing the regulation of DEG expression, with green, grey, and red dots representing down-regulation, unregulation, and up-regulation, respectively. **(B)** Bubble diagram showing the top ten pathways according to Gene Set Enrichment Analysis (GSEA). **(C)** Bubble plots showing the top 10 enriched GO BP, CC, and MF. **(D)** Bubble plots showing the top 20 enriched terms of the KEGG pathway, with the size of the dots representing the number of enrichments.

extracellular trap formation (NES=2.46,p.value=9.22E-06). These findings imply that the activation of the immune system in the tumor microenvironment is implicated in the development of osteosarcoma.

3.4 Screening and Evaluation of IR-DEGs

From the TIMER database, 1811 immune-related genes were obtained, and these genes intersected with DEGs to obtain 221 IR-DEGs (Figure 5A). The IR-DEGs were entered into the STRING online database to obtain the protein-protein interaction network (Figure 5B). The IR-DEGs were subjected to GO annotation and KEGG pathway enrichment analyses (Figures 5C, D), resulting in 418 BP, 57 CC, 57 MF, and 69 KEGG pathways. These IR-DEGs were mainly enriched in biological pathways such as immune response, inflammatory response, and adaptive immune response. Among KEGG-enriched pathways, the top five were Cytokine-cytokine receptor interaction, Viral protein interaction with cytokine and cytokine receptor, Rheumatoid arthritis, Chemokine signaling pathway and Graft-versus-host disease. GSEA enrichment analyses were also performed for IR-DEGs (Figure 5E). Their top

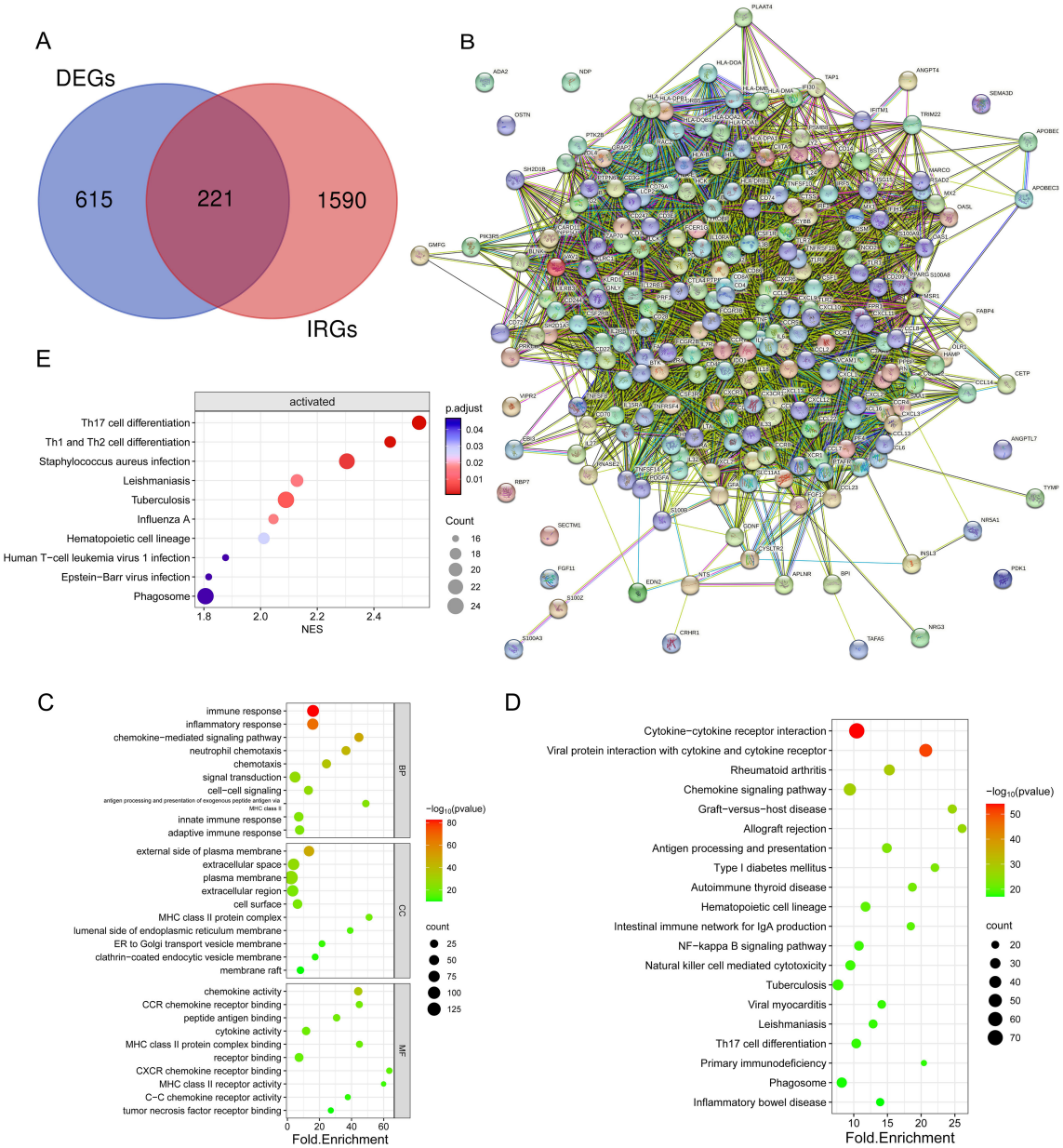

FIGURE 5
Identification and enrichment analysis of differentially expressed genes (DEGs) associated with the immune system. **(A)** Venn diagram showing 221 immune-associated DEGs overlapping 836 DEGs and 1811 IRGs. **(B)** Protein interaction network diagram of DEGs **(C)** Bubble plots showing the top 10 enriched GO BP, CC, and MF. **(D)** Bubble plots showing the top 20 enriched terms of the KEGG pathway, with the size of the dots representing the number of enrichments. **(E)** Bubble plots showing the top 20 enriched terms of the KEGG pathway, based on GSEA analyses of the top 10 pathways with the highest gene enrichment.

five were Th17 cell differentiation (NES=2.56, p.value=1.35E-05), Th1 and Th2 cell differentiation (NES=2.46,p.value=3.33E-05), Staphylococcus aureus infection (NES=2.30,p.value=0.0002), Tuberculosis (NES=2.09,p.value=0.0005), Leishmaniasis (NES=2.13,p.value=0.001). Similar to the above results. According to the results, it is clear that immune activation, especially T cells, is important for the development of osteosarcoma.

Following that, an examination of the connections and relationships among these IR-DEGs was carried out through the analysis of the protein-protein interaction network (Supplementary Table S8), and associations were found for a variety of IR-DEGs, with the most significant correlations between IL6, IL10, CD4, CD8A, IL1B, TNF, and CCL5 and the other immune IR-DEGs.

The interaction network is characterized by the presence of Interleukin (IL) family genes (including IL10, IL1B and IL6), T-Cell Surface Glycoprotein genes (including CD8A, CD86 and CD4), C-C Motif Chemokine Receptor genes (including CCR7 and CCR5) and C-C Motif Chemokine Ligand genes (including CCL2 and CCL5), which are among the hub nodes. Subsequently, the MCC algorithm was applied to obtain the top ten genes (Supplementary Table S9), and prognostic survival analysis and immune infiltration analysis were performed on these ten hub genes (Figures 6, 7).

The results showed that ten genes were closely associated with immune cells, and among all hub genes, Tumor Infiltrating Lymphocyte (TIL) infiltration levels were the highest, and mast cells and dendritic cell infiltration levels were lower. In the K-M survival analysis of the hub genes, CD4, CD8A, CCR5, and CCL5 were prognostically significant.

3.5 Risk modelling

Twenty-six genes were screened from 221 IR-DEGs using one-way COX analysis based on p<0.05, and then the 26 genes were further analyzed by applying the LASSO algorithm using ten-fold cross-validation when lambda.1se= 0.1745826 (Figures 8A, B), a risk model was developed using two candidate genes, namely PDK1 and PPARG. Utilizing the expression levels and coefficient values of the candidate genes, a risk score model was created through the application of the subsequent formula: risk score = (0.6839441 × PDK1 expression) + (-0.6420120 × PPARG expression). The risk score formula was utilized on all samples to calculate the risk score for each sample (Supplementary Table S10). Subsequently, The samples were divided into two cohorts at random, with no statistical distinction observed between the pair. The median risk scores of the original dataset, the training set, and the test set were used as thresholds (-0.279689391, -0.2077641135, and -0.3399543645), which were divided into a high-risk score group and a low-risk score group, respectively. To assess the accuracy of the risk scoring model constructed by PDK1 and PPARG on prognosis and to provide effective biomarkers for the prediction of osteosarcoma. K-M curve analysis and ROC curve analysis were then performed on the two cohorts and the original combined cohort (Figures 8C–H). ROC curves with area under the curve (AUC) values greater than 0.5 were considered statistically different. The results showed that the p-value of the K-M curve was less than 0.05 for the training set, the test set, and the merged set, so this feature was considered to have prognostic value. Whereas, in all three cohorts, the ROC curves indicated that the AUC values for 1-year, 3-year, and 5-year were above 0.5, and the feature had a higher predictive sensitivity for 3 and 5 years (AUC values were greater than 0.7 for both 3 and 5 years). In all three cohorts, a higher survival advantage was demonstrated for low-risk scores, and low-risk scores were strongly correlated with high survival.PDK1 and PPARG were analyzed according to the risk score grouping, and it was found that the expression of PDK1 was positively correlated with the risk score, while the expression of PPARG was inversely correlated with the risk score (Figure 8I). Then, the differences in TMB between the high and low-risk score groups were compared based on the previously calculated TMB values, and as expected, there was a difference between the two groups (P<0.05) (Figure 8J), with higher TMB values in the high-risk score group, which may be related to the poorer prognosis of the high-risk score group. Subsequently, we calculated the TIDE scores of the tumor samples (Figure 8K), which

FIGURE 6
Analysis of immune cell infiltration was conducted on the ten hub genes, visualized using lollipop charts.From left to right, the order is CCR5, TNF, IL10, IL6, CD8A, CD4, IL1B, CCR7, CCL5, and CCL2.

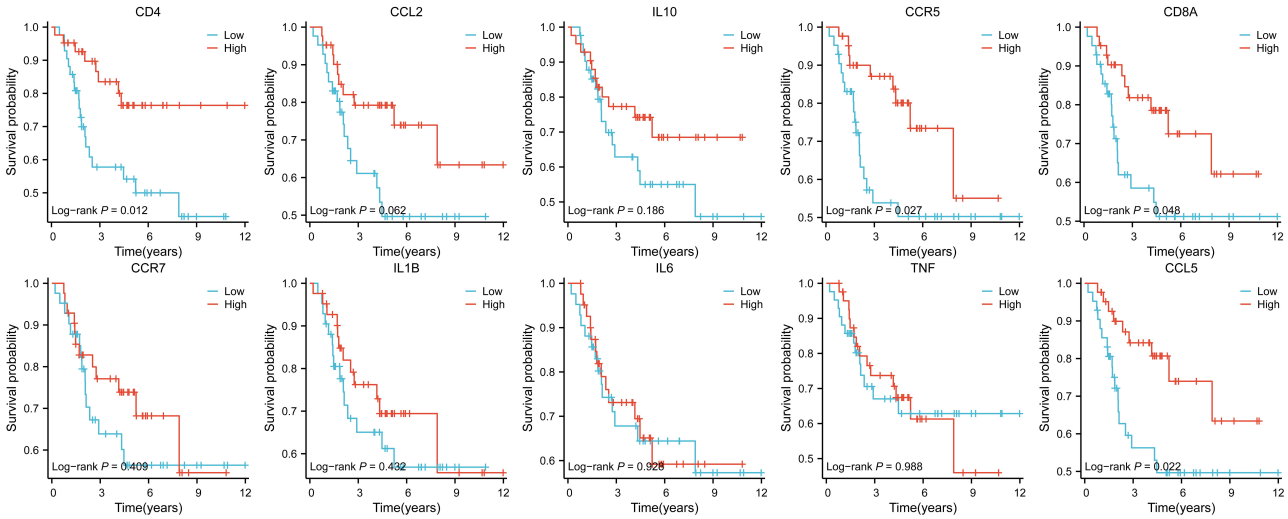

FIGURE 7
Ten hub genes were subjected to survival analysis.

were higher in the high-risk scoring group, suggesting that immune checkpoint blockade therapies were less effective in the high-risk scoring group. In contrast, the opposite was true for the low-risk scoring group. Finally, we used the third quartile of the TMB(0.62 muts/Mb) as a threshold to classify the TMB into two groups: high and low scores. The top 25% of patients were defined as the high TMB group, and the results, as shown in Figure 8L, showed that the high TMB group had a worse prognosis.

3.6 Performance of risk models

The samples were categorized based on the median risk score (-0.279689391), resulting in the formation of a high-risk group and a low-risk group. Subsequently, the variations in immune checkpoint-associated genes between these two groups were analyzed (Figure 9A). The results showed that most of the immune checkpoint-associated genes were differentially expressed, and of the genes that were differentially expressed, all had higher gene expression values in the low-risk score group. Differences in the expression of immune checkpoint-related genes in the high-risk scoring group and the low-risk scoring group are shown in Supplementary Table S11. Subsequently, to assess the correlation of immune checkpoint-associated genes with PDK1 and PPARG, the two candidate genes were grouped according to the median log2 (FPKM+1) value (PDK1: 1.24; PPARG: 1.75) into high and low expression groups, with differences in the expression of most of the genes (Figures 9B, C). High expression of PDK1 was positively correlated with low expression of immune-related genes, while high expression of PPARG was positively correlated with high expression of immune-related genes. The two candidate genes were shown to have opposite roles. Subsequently, CIBERSORT immune infiltration analysis was performed (Figure 9D), which showed differences in five immune cell subpopulations. Subsequently, the two candidate genes were still grouped according to median expression, and differential analysis of the five immune cell subpopulations obtained by CIBERSORT immune infiltration showed that high expression of PDK1 was positively correlated with high expression in Macrophages M0 and inversely correlated with high expression in Macrophages M2, and the opposite was true in PPARG (Figures 9E, F). Once again, the two candidate genes were shown to have opposite roles. Finally, the samples were analyzed using the xCell online website to obtain the MicroenvironmentScore (Supplementary Table S12), which was significantly different between the high-risk scoring and low-risk scoring groups and was higher in the low-risk scoring group (Figure 9G).

4 Discussion

Recent studies have shown that cancer development is influenced by the activation of the immune response (12). To delve deeper into the immune-related mechanisms of osteosarcoma, we explored the DEGs across two groups of immune characteristics. Furthermore, the majority of the IR-DEGs were found to be up-regulated in our study, exhibiting substantial enrichment in various immune-related biological pathways. Macrophages play a significant role in the tumor microenvironment, and in tumor development, tumor-associated macrophages can interact with other immune cells in the tumor to promote tumor development and progression. In addition, they can suppress tumor growth by promoting the phagocytosis of the cells (13). Furthermore, it has been shown that cytotoxicity of T cells can lead to tumor cell death (14). Tumor-infiltrating macrophages are plentiful within the tumor microenvironment and regulate the activity of T cells (15), tumor-associated macrophages and T cells play a key role in determining cancer prognosis and the efficacy of immunotherapies (16). Whereas macrophages and T cells were found to be statistically significant in the present study, therefore,

10.3389/fimmu.2024.1423194

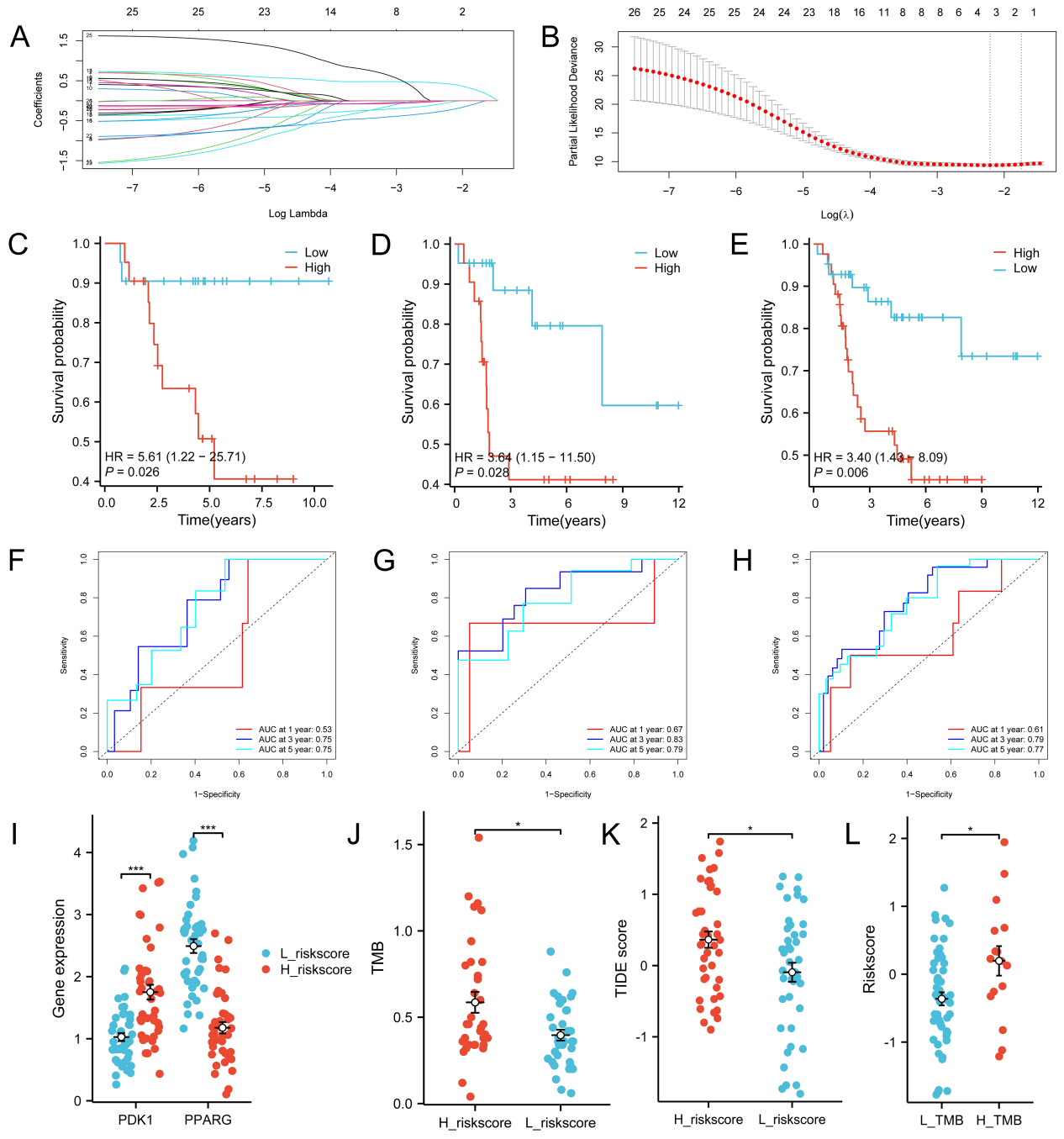

FIGURE 8
Construction of the total risk profile. The symbols * represent p-values less than 0.05, *** represent p-values less than 0.001. **(A, B)** Employing the LASSO method for the identification of key candidate genes. **(C–E)** Survival analysis K-M curves for the training cohort, validation cohort, and initial combined cohort, respectively. **(F–H)** ROC curves were generated to assess the prognostic significance of risk features in the training, validation, and original merged groups. **(I)** Differences in PDK1 and PPARG gene expression between high and low-risk score groups. **(J)** Differences in TMB between high and low-risk score groups. **(K)** Differences in TIDEscore in high and low-risk score groups. **(L)** Difference in risk scores between high and low TMB groups.

the immunological profile of TME in osteosarcoma is considered to have prognostic value.

The results showed that ImmuneScore had a significant correlation with prognosis, with higher ImmuneScore representing a higher level of immune infiltration, leading to higher survival. TumorPurity was inversely correlated, with high TumorPurity associated with low survival. Subsequently, we analyzed the correlation between the mutations and immunological features of the genes. The correlation between mutations in the TP53, ATRX, and RB1 genes and osteosarcoma has been extensively studied. TP53 prevents the transformation of bone marrow mesenchymal stem cells to osteosarcoma (17),

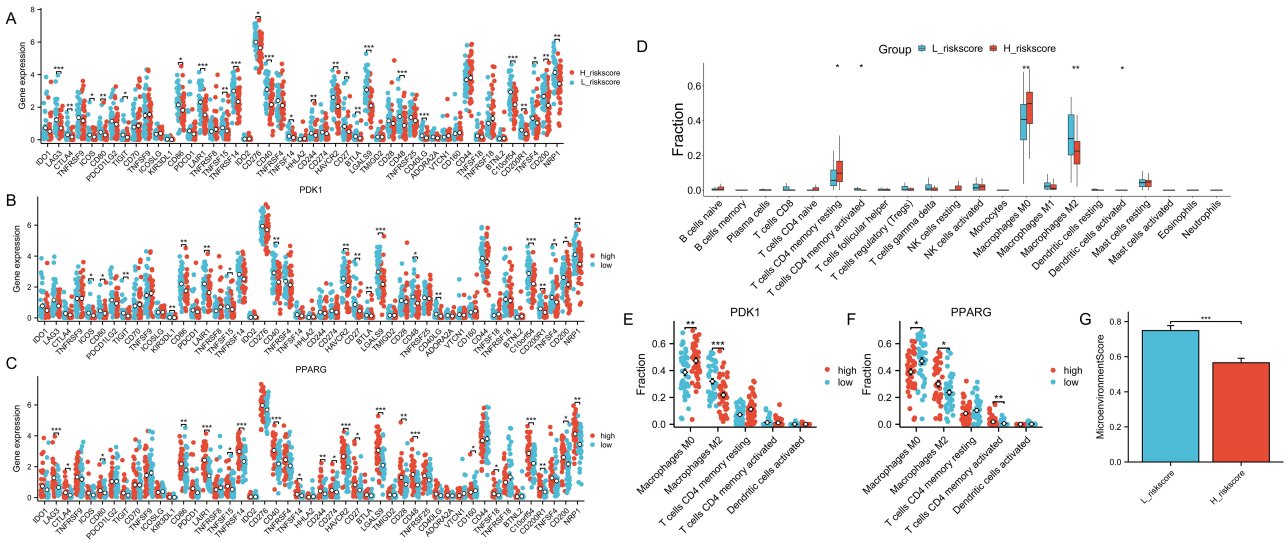

FIGURE 9
Role of risk models for immune checkpoints. The symbols * represent p-values less than 0.05, ** represent p-values less than 0.01, and *** represent p-values less than 0.001. **(A)** Comparison of the expression levels of immune checkpoint-related genes in the group with high-risk scores and the group with low-risk scores. **(B, C)** The expression levels of immune checkpoint-related genes between the two groups by dividing the gene expression of PDK1 and PPARG into high and low groups according to the median. **(D)** CIBERSORT immune infiltration analysis of all samples. **(E, F)** Infiltration abundance levels of some immune cells by dividing gene expression of PDK1 and PPARG into high and low groups by median. **(G)** MicroenvironmentScore in the high and low-risk scoring groups.

and Lang et al. showed that (18), in mice, mutation of TP53 promotes the development of osteosarcoma. Furthermore. Walkley et al. showed (19) that combined deletion of TP53 and RB1 in mouse osteoblasts leads to a high frequency of metastatic osteosarcoma, and that mutations in RB1 are a key driver of cancer (including osteosarcoma) (20). A meta-analysis (21) that included 491 patients with osteosarcoma showed that RB1 mutations were associated with a significantly reduced histological response to chemotherapy and a high risk of metastasis in osteosarcoma. ATRX plays an important tumor-suppressor role in OS, and deletion of this gene leads to tumor cell growth, migration, and invasion, and was one of the most commonly mutated genes in 288 osteosarcoma patients surveyed by the Genomics Evidence Neoplasia Information Exchange consortium in the USA (22). Taken together, mutations in the TP53, ATRX, and RB1 genes promote the development, invasion, and metastasis of osteosarcoma, and in Figure 3, the mutation frequency of these three genes is significantly higher in the low-immunity group than in the high-immunity group, indicating that the frequency of metastasis of osteosarcoma is also higher in the low-immunity group, which is in line with the results we obtained above.

Based on the findings from GO, KEGG, and GSEA enrichment analyses, numerous differentially expressed genes (DEGs) showed enrichment in pathways related to the immune system. Neutrophil chemotaxis was associated with more DEGs during BP in all GOs. Previous studies have shown that neutrophils are a major component of TME (23), which can exert a tumour-killing effect by affecting T cells (24, 25). In this study, two groups with high and low levels of immune activation were also studied in depth, and noticeable variances were observed in the extent of immune cell infiltration between the two groups, and the level of immune cell infiltration in the high-immunity group was significantly higher than that in the low-immunity group, which may be associated with the high survival rate of the high-immunity group. Ten pivotal genes were then identified, all of which are closely associated with neutrophils, macrophages, and T cells.

Following that, a univariate COX regression analysis and LASSO analysis were utilized to identify PDK1 and PPARG. A risk model was then established using these two factors, revealing a pronounced prognostic distinction between individuals in the high-risk and low-risk categories. Notably, the low-risk group exhibited a significantly superior prognostic survival rate. Pyruvate dehydrogenase kinase-1 (PDK1) is an enzyme involved in glycolysis that facilitates the transition from glucose oxidative metabolism to glycolytic metabolism in cancer cells by phosphorylating substrates (26) and also reduces the damage caused by reactive oxygen species (ROS) accumulation. In recent years, more and more evidence suggests that PDK1 is associated with tumor progression and metastasis (27–29), which provides a new idea for the development of targeting PDK1 for the treatment of osteosarcoma, as evidenced by Liu et al. who constructed a novel organoarsenic compound, Aa-Z2, which induces apoptosis of osteosarcoma by reprogramming metabolism through targeting PDK1 (30). Peroxisome proliferator-activated receptor-gamma (PPARG), a member of the nuclear receptor family, is a major regulator of adipocyte differentiation and function (31). PPARG has been shown to play a role in several cancers, and its association with cancer is primarily a result of the recording of PPARG in cancer cells and the tumor cell microenvironmental role (32). The role of PPARG is widely debated and it exerts inhibitory or promotional

effects on cancer growth depending on the tumor cell conditions and the pathways stimulated (33). In the literature, PPARG is an oncogene, which exerts anti-tumour effects by inhibiting cell proliferation, differentiation, cell growth, cell cycle, and inducing apoptosis. It has been shown that in human osteosarcoma, the pro-apoptotic effects exerted by Oridonin inhibition of the Nrf2 pathway require PPARG activation (34). PPARG can trigger cell apoptosis and suppress the growth of osteosarcoma cells by facilitating the terminal differentiation of osteoblasts (35).

When constructing the risk model, it was found that elevated levels of PDK1 were linked to the high-risk score group, which in turn was correlated with increased mortality rates. This implies that PDK1 may act as an oncogene. In contrast, high expression of PPARG was positively associated with the low-risk score group, which played the role of oncogene, which was consistent with the findings of previous scholars mentioned above, and further proved the accuracy of the risk model. While the high expression of PDK1 is proportional to the high expression of Macrophages M0 and inversely proportional to the high expression of Macrophages M2, the opposite is true in PPARG. Lin et al. Showed (36) that Nuanxinkang (NXK) reduced the transcript and protein levels of HIF-1α and PDK1 *in vivo*. NXK inhibited macrophage M1 and significantly increased macrophage M2 via the HIF-1α/PDK1 axis, and PDK1 and macrophage M2 levels *in vivo* were negatively correlated, which is in line with the findings of this study. Consistent with the findings of this study. Macrophage M1 is biased towards glycolytic metabolic processes, whereas macrophage M2 is more biased towards oxidative phosphorylation (OXPHOS) metabolic processes, and under the stimulation of lipopolysaccharides, the macrophage shifts from OXPHOS metabolism to glycolytic metabolism, PDK1 is a glycolytic enzyme, and when PDK1 is inhibited, glycolytic metabolism is inhibited, and the oxidative phosphorylation metabolic process is also strengthened, thus promoting the macrophage M2. PPARG agonists promote macrophage M2 polarisation (37). When PPARG signaling is inhibited, it promotes the macrophage transition from M2 to M1 (38), suggesting a positive correlation between PPARG levels and macrophage M2 levels, validating the accuracy of the findings of this study. Tumor-associated macrophages (TAM) are populations of macrophages that infiltrate into tumor tissue, including the M1 and M2 cell populations. TAM is closely associated with tumors, with M1 acting as an anti-tumor agent and M2 inhibiting T cell-mediated anti-tumor effects and promoting tumor formation (39, 40). TAMs are derived from monocytes in the bone marrow, and a variety of cytokines and chemokines can direct the migration of monocytes to the tumor site (41), the growth of tumors can also result in the transformation of CCR2+ monocytes into TAMs (42). TAMs can modulate the cytotoxicity of T cells and NK cells towards tumor cells. TAM can suppress the proliferation of CD8 T cells by nitrogen species, iNOS, and oxygen radicals (43–45). In addition, TAM can further inhibit the antitumor effects produced by T cells by recruiting Treg cells via CCL22 (46). Chen et al.'s study (47) showed that TAM promotes tumor growth by generating inflammatory Th subpopulations to stimulate an inflammatory response in tumors. TAM is also regulated by other immune cells, and Treg cells function to inhibit the release of IFN-γ from CD8 T cells (48), which is the main cytokine responsible for macrophage M2 inhibition; thus, Treg indirectly and selectively maintains metabolic fitness and survival of M2-like TAM. A study by Kumar et al. (49) showed that myeloid-derived suppressor cells (MDSC) could regulate TAM differentiation by down-regulating STAT3, promoting tumor proliferation. In addition, B cells can also induce macrophage M2 polarisation in tumors and inhibit T cells and macrophage M1 from promoting tumor proliferation (50). The role of Macrophages M0 for osteosarcoma is currently unclear (51). Therefore, immunotherapy targeting macrophage transformation may become a promising therapeutic strategy for the treatment of osteosarcoma.

In recent years, immunotherapy has been a widely researched therapeutic approach that has achieved excellent results in the treatment of many types of cancer. Immune checkpoint inhibitors (ICIs) are a form of immunotherapy that works by stimulating the body's immune system to combat cancer. This is achieved through the inhibition of immune checkpoint molecules like programmed cell death-1 (PD-1) and programmed cell death ligand-1 (PD-L1), which play crucial roles in regulating the immune response. programmed cell death ligand-1 (PD-L1) to activate the body's immune response to fight cancer. The results have been satisfactory in the treatment of many cancers. Nevertheless, targeted PD-1/PD-L1 therapy yields unsatisfactory outcomes in osteosarcoma (52), possibly attributed to the distinct PD-1/PD-L1 regulation in the tumor, commonly known as a "cold tumor" (53). Numerous studies have indicated a relationship between elevated levels of PD-L1 and unfavorable outcomes in osteosarcoma patients, yet the precise role of PD-L1 in osteosarcoma pathogenesis remains ambiguous. It can be seen from this study that most of the immune checkpoint-related genes have higher gene expression in the low-risk scoring group and lower gene expression in the high-risk scoring group, which suggests that the risk model obtained in this study has significance for the gene regulation of immune checkpoints. High expression of these immune checkpoint-associated genes was associated with better prognosis, whereas PDK1 was highly expressed in the high-risk scores and was associated with poorer prognosis, so PDK1 was negatively correlated with the expression of immune checkpoint-associated genes, whereas PPARG was highly expressed in the low-risk scores group, and, in contrast to PDK1, PPARG was positively correlated with the expression of immune checkpoint-associated genes. This may be because the tumor microenvironment in the low-risk group was more amenable to immune cell infiltration and activation, resulting in increased expression of immune checkpoint molecules, reflecting good immune surveillance of the tumor. High expression of immune checkpoint genes is associated with a better clinical prognosis, and we speculate that this may be because the immune system of osteosarcoma patients can efficiently recognize the tumor and develop an immune response, and because highly mutated genes in osteosarcoma does not produce sufficient neoantigens that can elicit an immune response so that targeted inhibition of PD-1/PD-L1 therapy in osteosarcoma is unsatisfactory. Therefore, PDK1 and

PPARG may become prognostic genes in osteosarcoma and may be targets for subsequent regulation of ICI-related genes for osteosarcoma treatment.

As we said above, mutations in TP53, RB1, and ATRX genes can promote the growth, invasion, and metastasis of osteosarcoma, which is a kind of 'cold tumor', and the microenvironment of osteosarcoma can monitor the tumor well, and it is less responsive to immune checkpoint blockade, which is confirmed by the calculation of the TIDE score, so the effect of high TMB on osteosarcoma is more inclined to promote the development of osteosarcoma, resulting in a poorer prognosis of osteosarcoma patients with high TMB.

In this study, the majority of IR-DEGs were found to be overrepresented in T lymphocytes. It has been well-documented in previous research that the infiltration and activation of T cells are crucial in the therapeutic management of osteosarcoma, and that adoptive T-cell therapy (ACT) has a promising future for the treatment of osteosarcoma, whereas ICI activates the immune system, ACT directly "tells" the T-cells the characteristics of the tumor, and then attacks the tumor in a targeted manner. Based on prior studies, it has been recognized that there are three primary categories of penicillin combination treatments: chimeric antigen receptor (CAR)-modified T cells, T cell receptor (TCR)-modified T cells, and tumor-infiltrating lymphocytes (TILs) (54). Our research findings indicate that there was a notable difference in the extent of immune cell infiltration between the hyperimmune and hyperimmune groups, with a marked increase in the hyperimmune group. This heightened immune response was correlated with a better survival outcome in the hyperimmune group. Ten hub genes were obtained in this study, which were significantly correlated with TILs and therefore they are highly specific for targeting tumors. Combining ICI with TIL T-cells may also be an effective option for individual therapy, and recent findings by Wang et al. showed that TILs in combination with anti-PD1 therapy demonstrated significant clinical efficacy in patients with metastatic osteosarcoma compared to anti-PD1 therapy applied alone. The objective remission rate of this combination regimen was almost five times higher than that of single anti-PD1 therapy, while intermediate progression-free survival and intermediate overall survival were also significantly prolonged (55).

More and more studies are being conducted, and the present study fully considers the effect of immune infiltration on osteosarcoma and uses it for risk modeling, demonstrating excellent prognostic specificity and providing a novel and valuable tool for future research.

5 Strengths and limitations

The strength of this study is the use of bioinformatics to investigate osteosarcoma from the perspective of immune infiltration, which revealed that higher immune infiltration has a better prognosis, and then concluded that two important genes, PDK1 and PPARG, whose high or low expression is associated with the prognosis of osteosarcoma, and whose effect on Macrophages M0 and Macrophages M2 regulation also has a crucial impact and can even regulate immune checkpoint-related genes. Subsequently, a risk model was constructed using PDK1 and PPARG, and the risk model provided a good prognosis prediction.

This study has some limitations. This study only used computers and their related software to analyze the data, and it still lacks relevant experimental validation. In our future work, we will further expand the clinical samples and conduct animal or human experiments to improve the study's accuracy and lay a more solid foundation for treating osteosarcoma.

6 Conclusions

From the above description of this study, it can be concluded that a high Immune score is associated with a better prognosis in osteosarcoma. Subsequently, several analyses were performed to verify the effect of immune infiltration on osteosarcoma, firstly, the samples were immuno-infiltrated using ssGSEA, and the samples were divided into two groups based on the immune score, with the group with high immune activation having a significant survival advantage over the other group. Then, using a univariate COX regression analysis and LASSO analyses, two genes, PDK1 and PPARG, were obtained, and a risk model was constructed based on the derived genes, in which PDK1 was positively correlated with the risk score, and PPARG was negatively correlated with the risk score, and through further analyses, we found that PDK1 was negatively correlated with macrophage M2, and the opposite was true for PPARG, and that the group with a high-risk score had a more high TMB and their prognosis was poorer. We also analyzed immune checkpoint-related genes, which were negatively correlated with risk scores, suggesting that the osteosarcoma microenvironment has good tumor surveillance and responds poorly to ICB treatment. Finally, we also analyzed the TMB of the samples. We found that high TMB was associated with low immune infiltration and that an increased mutation rate increased the risk of osteosarcoma. Therefore, the prognostic model obtained in this study is suitable for further optimization and eventual clinical application.

Data availability statement

The original contributions presented in the study are included in the article/Supplementary Files, further inquiries can be directed to the corresponding author/s.

Author contributions

AW: Conceptualization, Data curation, Investigation, Methodology, Project administration, Resources, Software, Supervision, Validation, Visualization, Writing – original draft, Writing – review & editing. PK: Conceptualization, Data curation, Formal analysis, Funding acquisition, Writing – original draft,

Writing – review & editing. PY: Conceptualization, Data curation, Investigation, Methodology, Software, Supervision, Writing – original draft. Z-KY: Conceptualization, Data curation, Investigation, Methodology, Software, Writing – original draft. Y-TL: Investigation, Software, Supervision, Validation, Writing – original draft. J-LX: Investigation, Resources, Software, Validation, Visualization, Writing – original draft. S-SB: Conceptualization, Formal analysis, Funding acquisition, Investigation, Project administration, Resources, Software, Validation, Visualization, Writing – original draft, Writing – review & editing. J-WT: Conceptualization, Data curation, Investigation, Methodology, Software, Supervision, Validation, Writing – original draft, Writing – review & editing.

Funding

The author(s) declare that financial support was received for the research, authorship, and/or publication of this article. This study was supported by the Natural Science Foundation of Shandong Province (ZR2020MH359) and the Natural Science Foundation of Shandong Province (ZR2023MH225).

Conflict of interest

The authors declare that the research was conducted in the absence of any commercial or financial relationships that could be construed as a potential conflict of interest.

Publisher's note

Supplementary material

The Supplementary Material for this article can be found online at: https://www.frontiersin.org/articles/10.3389/fimmu.2024.1423194/full#supplementary-material

References

1. Lingerih T, Yeshiwas S, Mohamedsaid A, Arega G. Patterns and treatment outcomes of primary bone tumors in children treated at tertiary referral hospital, Ethiopia. *BMC Cancer*. (2024) 24:394. doi: 10.1186/s12885-024-12169-x

2. Chen L, He L, Liu B, Zhou Y, Lv L, Wang Z. Intelligent structure prediction and visualization analysis of non-coding RNA in osteosarcoma research. *Front Oncol*. (2024) 14:1255061. doi: 10.3389/fonc.2024.1255061

3. Zhang Y, Wang F, Wang L, Zhang Q. MiR-363 suppresses cell migration, invasion, and epithelial-mesenchymal transition of osteosarcoma by binding to NOB1. *World J Surg Oncol*. (2020) 18:83. doi: 10.1186/s12957-020-01859-y

4. Lipson EJ, Drake CG. Ipilimumab: an anti-CTLA-4 antibody for metastatic melanoma. *Clin Cancer Res*. (2011) 17:6958–62. doi: 10.1158/1078-0432.CCR-11-1595

5. Paddock LE, Lu SE, Bandera EV, Rhoads GG, Fine J, Paine S, et al. Skin self-examination and long-term melanoma survival. *Melanoma Res*. (2016) 26:401–8. doi: 10.1097/CMR.0000000000000255

6. Sharon E, Streicher H, Goncalves P, Chen HX. Immune checkpoint inhibitors in clinical trials. *Chin J Cancer*. (2014) 33:434–44. doi: 10.5732/cjc.014.10122

7. Petitprez F, de Reyniès A, Keung EZ, Chen TW, Sun CM, Calderaro J, et al. B cells are associated with survival and immunotherapy response in sarcoma. *Nature*. (2020) 577:556–60. doi: 10.1038/s41586-019-1906-8

8. Oike N, Kawashima H, Ogose A, Hotta T, Hatano H, Ariizumi T, et al. Prognostic impact of the tumor immune microenvironment in synovial sarcoma. *Cancer Sci*. (2018) 109:3043–54. doi: 10.1111/cas.13769

9. Xiong K, Fang Y, Qiu B, Chen C, Huang N, Liang F, et al. Investigation of cellular communication and signaling pathways in tumor microenvironment for high TP53-expressing osteosarcoma cells through single-cell RNA sequencing. *Med Oncol*. (2024) 41:93. doi: 10.1007/s12032-024-02318-4

10. Yoshihara K, Shahmoradgoli M, Martínez E, Vegesna R, Kim H, Torres-Garcia W, et al. Inferring tumour purity and stromal and immune cell admixture from expression data. *Nat Commun*. (2013) 4:2612. doi: 10.1038/ncomms3612

11. Hanzelmann S, Castelo R, Guinney J. GSVA: gene set variation analysis for microarray and RNA-seq data. *BMC Bioinf*. (2013) 14:7. doi: 10.1186/1471-2105-14-7

12. Tahkola K, Mecklin JP, Wirta EV, Ahtiainen M, Helminen O, Böhm J, et al. High immune cell score predicts improved survival in pancreatic cancer. *Virchows Arch*. (2018) 472:653–65. doi: 10.1007/s00428-018-2297-1

13. Zhou L, Zhao T, Zhang R, Chen C, Li J. New insights into the role of macrophages in cancer immunotherapy. *Front Immunol*. (2024) 15:1381225. doi: 10.3389/fimmu.2024.1381225

14. Yuan Y, Li J, Chen J, Han L, Wang L, Yue Y, et al. Characterization of a novel T cell-engaging bispecific antibody for elimination of L1CAM-positive tumors. *BioMed Pharmacother*. (2024) 174:116565. doi: 10.1016/j.biopha.2024.116565

15. Zheng C, Wang J, Zhou Y, Duan Y, Zheng R, Xie Y, et al. IFNα-induced BST2+ tumor-associated macrophages facilitate immunosuppression and tumor growth in pancreatic cancer by ERK-CXCL7 signaling. *Cell Rep*. (2024) 43:114088. doi: 10.1016/j.celrep.2024.114088

16. Li Y, Wang Z, Lu F, Miao Y, Feng Q, Zhu W, et al. Novel T cell exhaustion gene signature to predict prognosis and immunotherapy response in thyroid carcinoma from integrated RNA-sequencing analysis. *Sci Rep*. (2024) 14:8375. doi: 10.1038/s41598-024-58419-7

17. Thoenen E, Curl A, Iwakuma T. TP53 in bone and soft tissue sarcomas. *Pharmacol Ther*. (2019) 202:149–64. doi: 10.1016/j.pharmthera.2019.06.010

18. Lang GA, Iwakuma T, Suh YA, Liu G, Rao VA, Parant JM, et al. Gain of function of a p53 hot spot mutation in a mouse model of Li-Fraumeni syndrome. *Cell*. (2004) 119:861–72. doi: 10.1016/j.cell.2004.11.006

19. Walkley CR, Qudsi R, Sankaran VG, Perry JA, Gostissa M, Roth SI, et al. Conditional mouse osteosarcoma, dependent on p53 loss and potentiated by loss of Rb, mimics the human disease. *Genes Dev*. (2008) 22:1662–76. doi: 10.1101/gad.1656808

20. Zoumpoulidou G, Alvarez-Mendoza C, Mancusi C, Ahmed RM, Denman M, Steele CD, et al. Therapeutic vulnerability to PARP1,2 inhibition in RB1-mutant osteosarcoma. *Nat Commun*. (2021) 12:7064. doi: 10.1038/s41467-021-27291-8

21. Ren W, Gu G. Prognostic implications of RB1 tumour suppressor gene alterations in the clinical outcome of human osteosarcoma: a meta-analysis. *Eur J Cancer Care (Engl)*. (2017) 26(1). doi: 10.1111/ecc.12401

22. Bartholf DeWitt S, Hoskinson Plumlee S, Brighton HE, Sivaraj D, Martz EJ, Zand M, et al. Loss of ATRX promotes aggressive features of osteosarcoma with increased NF-κB signaling and integrin binding. *JCI Insight*. (2022) 7:e151583. doi: 10.1172/jci.insight.151583

23. Awasthi D, Sarode A. Neutrophils at the crossroads: unraveling the multifaceted role in the tumor microenvironment. *Int J Mol Sci*. (2024) 25:2929. doi: 10.3390/ijms25052929

24. Mishalian I, Bayuh R, Eruslanov E, Michaeli J, Levy L, Zolotarov L, et al. Neutrophils recruit regulatory T-cells into tumors via secretion of CCL17–a new mechanism of impaired antitumor immunity. *Int J Cancer*. (2014) 135:1178–86. doi: 10.1002/ijc.28770

25. Zhou SL, Zhou ZJ, Hu ZQ, Huang XW, Wang Z, Chen EB, et al. Tumor-associated neutrophils recruit macrophages and T-regulatory cells to promote progression of hepatocellular carcinoma and resistance to sorafenib. *Gastroenterology*. (2016) 150:1646–1658.e17. doi: 10.1053/j.gastro.2016.02.040

26. Kwak CH, Lee JH, Kim EY, Han CW, Kim KJ, Lee H, et al. Huzhangoside A suppresses tumor growth through inhibition of pyruvate dehydrogenase kinase activity. *Cancers (Basel)*. (2019) 11:712. doi: 10.3390/cancers11050712

27. Siu MKY, Jiang YX, Wang JJ, Leung THY, Ngu SF, Cheung ANY, et al. PDK1 promotes ovarian cancer metastasis by modulating tumor-mesothelial adhesion, invasion, and angiogenesis via α5β1 integrin and JNK/IL-8 signaling. *Oncogenesis*. (2020) 9:24. doi: 10.1038/s41389-020-0209-0

28. Bai X, Li P, Xie Y, Guo C, Sun Y, Xu Q, et al. Overexpression of 3-phosphoinositide-dependent protein kinase-1 is associated with prognosis of gastric carcinoma. *Tumour Biol*. (2016) 37:2333–9. doi: 10.1007/s13277-015-4024-8

29. Scortegagna M, Ruller C, Feng Y, Lazova R, Kluger H, Li JL, et al. Genetic inactivation or pharmacological inhibition of Pdk1 delays development and inhibits metastasis of Braf(V600E)::Pten(-/-) melanoma. *Oncogene*. (2014) 33:4330–9. doi: 10.1038/onc.2013.383

30. Liu Y, She W, Li Y, Wang M, Liu Y, Ning B, et al. Aa-Z2 triggers ROS-induced apoptosis of osteosarcoma by targeting PDK-1. *J Transl Med*. (2023) 21:7. doi: 10.1186/s12967-022-03862-1

31. Xu X, Charrier A, Congrove S, Ockunzzi J, Buchner DA. Cell-state dependent regulation of PPAR γ signaling by ZBTB9 in adipocytes. *bioRxiv*. (2024) 6:107985. doi: 10.1101/2024.03.04.583402

32. Hernandez-Quiles M, Broekema MF, Kalkhoven E. PPARgamma in metabolism, immunity, and cancer: unified and diverse mechanisms of action. *Front Endocrinol (Lausanne)*. (2021) 12:624112. doi: 10.3389/fendo.2021.624112

33. Grygiel-Górniak B. Peroxisome proliferator-activated receptors and their ligands: nutritional and clinical implications–a review. *Nutr J*. (2014) 13:17. doi: 10.1186/1475-2891-13-17

34. Lu Y, Sun Y, Zhu J, Yu L, Jiang X, Zhang J, et al. Oridonin exerts anticancer effect on osteosarcoma by activating PPAR-γ and inhibiting Nrf2 pathway. *Cell Death Dis*. (2018) 9:15. doi: 10.1038/s41419-017-0031-6

35. He BC, Chen L, Zuo GW, Zhang W, Bi Y, Huang J, et al. Synergistic antitumor effect of the activated PPARgamma and retinoid receptors on human osteosarcoma. *Clin Cancer Res*. (2010) 16:2235–45. doi: 10.1158/1078-0432.CCR-09-2499

36. Lin ZJ, Dong X, He H, Jiang JL, Guan ZJ, Li X, et al. A simplified herbal decoction attenuates myocardial infarction by regulating macrophage metabolic reprogramming and phenotypic differentiation via modulation of the HIF-1α/PDK1 axis. *Chin Med*. (2024) 19:75. doi: 10.1186/s13020-024-00933-x

37. Zhang YA, Li FW, Dong YX, Xie WJ, Wang HB. PPAR-γ regulates the polarization of M2 macrophages to improve the microenvironment for autologous fat grafting. *FASEB J*. (2024) 38:e23613. doi: 10.1096/fj.202400126R

38. Wang Z, Luo W, Zhao C, Yu M, Li H, Zhou F, et al. FoxO1-modulated macrophage polarization regulates osteogenesis via PPAR-γ signaling. *Biochim Biophys Acta Mol Basis Dis*. (2024) 1870:167333. doi: 10.1016/j.bbadis.2024.167333

39. Pan Y, Yu Y, Wang X, Zhang T. Tumor-associated macrophages in tumor immunity. *Front Immunol*. (2020) 11:583084. doi: 10.3389/fimmu.2020.583084

40. Shao XJ, Xiang SF, Chen YQ, Zhang N, Cao J, Zhu H, et al. Inhibition of M2-like macrophages by all-trans retinoic acid prevents cancer initiation and stemness in osteosarcoma cells. *Acta Pharmacol Sin*. (2019) 40:1343–50. doi: 10.1038/s41401-019-0262-4

41. Mantovani A, Allavena P, Sica A, Balkwill F. Cancer-related inflammation. *Nature*. (2008) 454:436–44. doi: 10.1038/nature07205

42. Franklin RA, Liao W, Sarkar A, Kim MV, Bivona MR, Liu K, et al. The cellular and molecular origin of tumor-associated macrophages. *Science*. (2014) 344:921–5. doi: 10.1126/science.1252510

43. Movahedi K, Laoui D, Gysemans C, Baeten M, Stangé G, Van den Bossche J, et al. Different tumor microenvironments contain functionally distinct subsets of macrophages derived from Ly6C(high) monocytes. *Cancer Res*. (2010) 70:5728–39. doi: 10.1158/0008-5472.CAN-09-4672

44. Molon B, Ugel S, Del Pozzo F, Soldani C, Zilio S, Avella D, et al. Chemokine nitration prevents intratumoral infiltration of antigen-specific T cells. *J Exp Med*. (2011) 208:1949–62. doi: 10.1084/jem.20101956

45. Lu T, Ramakrishnan R, Altiok S, Youn JI, Cheng P, Celis E, et al. Tumor-infiltrating myeloid cells induce tumor cell resistance to cytotoxic T cells in mice. *J Clin Invest*. (2011) 121:4015–29. doi: 10.1172/JCI45862

46. Curiel TJ, Coukos G, Zou L, Alvarez X, Cheng P, Mottram P, et al. Specific recruitment of regulatory T cells in ovarian carcinoma fosters immune privilege and predicts reduced survival. *Nat Med*. (2004) 10:942–9. doi: 10.1038/nm1093

47. Chen MM, Xiao X, Lao XM, Wei Y, Liu RX, Zeng QH, et al. Polarization of tissue-resident TFH-like cells in human hepatoma bridges innate monocyte inflammation and M2b macrophage polarization. *Cancer Discovery*. (2016) 6:1182–95. doi: 10.1158/2159-8290.CD-16-0329

48. Liu C, Chikina M, Deshpande R, Menk AV, Wang T, Tabib T, et al. Treg cells promote the SREBP1-dependent metabolic fitness of tumor-promoting macrophages via repression of CD8+ T cell-derived interferon-γ. *Immunity*. (2019) 51:381–397.e6. doi: 10.1016/j.immuni.2019.06.017

49. Kumar V, Cheng P, Condamine T, Mony S, Languino LR, McCaffrey JC, et al. CD45 phosphatase inhibits STAT3 transcription factor activity in myeloid cells and promotes tumor-associated macrophage differentiation. *Immunity*. (2016) 44:303–15. doi: 10.1016/j.immuni.2016.01.014

50. Roghanian A, Fraser C, Kleyman M, Chen J. B cells promote pancreatic tumorigenesis. *Cancer Discovery*. (2016) 6:230–2. doi: 10.1158/2159-8290.CD-16-0100

51. Gong L, Sun X, Jia M. New gene signature from the dominant infiltration immune cell type in osteosarcoma predicts overall survival. *Sci Rep*. (2023) 13:18271. doi: 10.1038/s41598-023-45566-6

52. Heymann MF, Schiavone K, Heymann D. Bone sarcomas in the immunotherapy era. *Br J Pharmacol*. (2021) 178:1955–72. doi: 10.1111/bph.14999

53. Tian H, Cao J, Li B, Nice EC, Mao H, Zhang Y, et al. Managing the immune microenvironment of osteosarcoma: the outlook for osteosarcoma treatment. *Bone Res*. (2023) 11:11. doi: 10.1038/s41413-023-00246-z

54. Raes L, De Smedt SC, Raemdonck K, Braeckmans K. Non-viral transfection technologies for next-generation therapeutic T cell engineering. *Biotechnol Adv*. (2021) 49:107760. doi: 10.1016/j.bioteChadv.2021.107760

55. Wang C, Li M, Wei R, Wu J. Adoptive transfer of TILs plus anti-PD1 therapy: An alternative combination therapy for treating metastatic osteosarcoma. *J Bone Oncol*. (2020) 25:100332. doi: 10.1016/j.jbo.2020.100332

frontiers | Frontiers in Immunology

TYPE Original Research
PUBLISHED 06 December 2024
DOI 10.3389/fimmu.2024.1425687

OPEN ACCESS

EDITED BY
Chih-Hao Chang,
Jackson Laboratory, United States

REVIEWED BY
Shuheng Bai,
The First Affiliated Hospital of Xi'an Jiaotong University, China
Rupa Kumari,
University at Buffalo, United States

*CORRESPONDENCE
Kaixiong Tao
kaixiongtao@hust.edu.cn
Wei Li
liwei7962@hust.edu.cn

†These authors have contributed equally to this work and share first authorship

RECEIVED 30 April 2024
ACCEPTED 18 November 2024
PUBLISHED 06 December 2024

CITATION
Zhang R, Gao Y, Li C, Tao R, Mao G, Song T, Nie W, Liu S, Tao K and Li W (2024) Hypoxia reconstructed colorectal tumor microenvironment weakening anti-tumor immunity: construction of a new prognosis predicting model through transcriptome analysis.
Front. Immunol. 15:1425687.
doi: 10.3389/fimmu.2024.1425687

Hypoxia reconstructed colorectal tumor microenvironment weakening anti-tumor immunity: construction of a new prognosis predicting model through transcriptome analysis

Ruizhi Zhang[1†], Yisong Gao[1†], Chong Li[1], Ruikang Tao[2], Gan Mao[1], Tianyu Song[1], Wenxiang Nie[1], Suao Liu[1], Kaixiong Tao[1*] and Wei Li[1*]

[1]Department of Gastrointestinal Surgery, Union Hospital, Tongji Medical College, Huazhong University of Science and Technology, Wuhan, China, [2]Center for Biomolecular Science and Engineering, University of California Santa Cruz, Santa Cruz, CA, United States

Background: Hypoxia in the tumor microenvironment (TME) plays a pivotal role in the progression and prognosis of colorectal cancer (CRC). However, effective methods for assessing TME hypoxia remain lacking. This study aims to develop a novel hypoxia-related prognostic score (HPS) based on hypoxia-associated genes to improve CRC prognostication and inform treatment strategies.

Methods: Transcriptomic data from CRC patients were analyzed using Lasso regression to identify hypoxia-associated genes with the strongest prognostic significance. The identified genes were validated *in vitro* by assessing their expression under normoxic and hypoxic conditions in normal intestinal epithelial cells and CRC tumor cell lines. Functional relevance was explored through differential gene expression analysis, Gene Ontology (GO) and Kyoto Encyclopedia of Genes and Genomes (KEGG) enrichment analyses, and protein-protein interaction (PPI) network construction. The association of HPS with extracellular matrix (ECM) composition, immune cell infiltration, and immune suppression was also investigated.

Results: Seven hypoxia-associated signature genes were identified, each demonstrating a strong correlation with CRC prognosis. The hypoxia-related prognostic score (HPS), derived from these genes, was significantly linked to changes in the TME. Specifically, HPS values were associated with alterations in ECM composition and distinct immune cell infiltration patterns. Higher HPS values corresponded to increased infiltration of immune-suppressive cells and reduced presence of anti-tumor immune cells. This imbalance promoted an immune-suppressive TME, facilitating tumor progression and immune evasion.

Conclusions: The hypoxia-related prognostic score (HPS) captures the regulatory influence of TME hypoxia on immune responses, offering valuable insights into its role in tumor progression. HPS holds promise as a prognostic tool and a guide for developing personalized treatment strategies in CRC.

KEYWORDS

hypoxia, colorectal cancer, tumor microenvironment immunity, extracellular matrix, WGCNA

1 Introduction

Hypoxia, a critical component of the tumor microenvironment, is a result of imbalance between increased oxygen usage and insufficient oxygen supply drove by rapid and unlimited growth of tumor cells and lack of blood supply (1). This reciprocal interplay affects patient outcomes across various tumor types, significantly influencing tumor prognosis (2). Microenvironmental hypoxia is a factor that affects the prognosis of patients with various malignancies, including colorectal cancer (CRC) (3–5).

Hypoxia plays a pivotal role in driving tumor progression, orchestrating the growth and differentiation of tumor cells through various molecular mechanisms. Proliferation, invasion, and epithelial-mesenchymal transition of cancer cell are all associated with hypoxia and are closely linked to local tumor progression and distant metastasis (6–8). Moreover, hypoxia is involved in regulating different forms of tumor cell death, including apoptosis (9). Hypoxic cancer cells exhibit decreased levels of apoptosis and ferroptosis while autophagy levels increase, promoting their adaptation to the hypoxic TME (10–12).

Beyond its influence on cancer cells, hypoxia exerts significant effects on various other cells within the TME, including interstitial and immune cells. Hypoxia suppresses both the infiltration and functionality of immune cells, thereby critically influencing the tumor immune within the tumor microenvironment (13, 14). Furthermore, hypoxia can alter the matrix composition within the TME, leading to its remodeling (3).

Despite the critical role of TME hypoxia in tumor progression, detection techniques remain relatively inadequate (4). Surgical specimens are evaluated for hypoxia using immunohistochemistry or immunofluorescence to detect HIF1α expression (15). Although pimonidazole staining is utilized in animal experiments for hypoxia assessment, its clinical application remains limited (16). In our study, to enhance the assessment of hypoxia within the TME, obtain more precise tumor molecular classifications, and subsequently optimize the treatment of CRC patients, LASSO regression was employed. This method allowed us to screen for prognosis-associated genes, integrating clinicopathological characteristics to predict patient outcomes. Furthermore, we explored the mechanistic underpinnings of these genes through functional analysis.

2 Materials and methods

2.1 Data collection and preprocessing

Expression profiles of the GSE17536 and GSE14333 datasets were downloaded from the Gene Expression Omnibus database (GEO). The GEO dataset GSE17536 included 177 CRC samples, and the other GEO dataset GSE14333 included 290 CRC samples. TCGA-COAD and GTEx transcriptome cohort data were downloaded from the UCSC Xena website (https://xenabrowser.net/datapages/). The TCGA dataset included 616 CRC samples, and the GTEx dataset included 686 non-diseased colon tissue samples. All raw data were normalized and standardized using the R software packages including "limma" and "DESeq2".

2.2 Single sample gene set enrichment analysis

The R package "GSVA" facilitated single-sample gene set enrichment analysis (ssGSEA) to investigate tumor-related pathway enrichment and immune cell infiltration within the GSE17536 dataset. We sourced tumor-related datasets from the hallmark gene sets in the MSigDB database [https://www.gsea-msigdb.org/gsea/msigdb].

2.3 Weighted gene co-expression networks analysis

The weighted gene co-expression network analysis (WGCNA) was constructed using the GSE17536 dataset. Among all the soft threshold values, we selected the β value with the highest mean connectivity (β = 13). The minimum number of genes was set at 30 to ensure the high reliability of the results. All genes were then divided into modules, each named by a different color. For further quantification of hypoxia-related genes and modules, only genes with a p-value of less than 0.001 were retained for subsequent analysis.

2.4 Establishment and validation of a colorectal cancer prognostic predictive signature

Univariate Cox regression analysis identified cancer hallmarks related to disease-specific survival (DSS) and overall survival (OS). We applied Lasso penalized Cox regression analysis to select hypoxia-related genes associated with prognosis. Subsequently, we used the LASSO Cox regression model to identify genes highly correlated with hypoxia and to construct the hypoxia-related prognosis score (HPS). We calculated the HPS score for each patient using the formula: HPS score =Σ(coefficient × mRNA expression).

2.5 Construction of nomogram for colorectal cancer prognosis prediction

Hypoxia score and relevant clinical parameters were used to construct a nomogram, using the "survival" and the "rms" package of R. The nomogram was constructed to estimate 1-, 3-, and 5-year survival probabilities. The model's performance was evaluated by using the calibration curve and C-index to assess the survival probabilities.

2.6 Gene set enrichment analysis

The function of hypoxia-related genes was explored using gene set enrichment analysis (GSEA). Differential gene expression profiles in the training and validation cohorts were analyzed using the R software package "clusterProfiler" (17). P-values < 0.05 and FDR p-values < 0.25 were considered significant. Permission must be obtained for use of copyrighted material from other sources (including the web). Please note that it is compulsory to follow figure instructions.

2.7 Differential expression of genes and protein-protein interaction analyses

We performed DEG analysis using the "limma" R package on the GSE17536, GSE14333, TCGA-COAD, and GTEx cohorts. Genes with an adjusted P-value < 0.05 and an absolute log2 fold change (FC) > 0.5 were identified as DEGs.

Protein-coding genes in the DEG were used to construct a PPI network using common transcripts, employing STRING with all parameters set to their default values (https://cn.string-db.org/). Subsequent Gene Ontology (GO) and Kyoto Encyclopedia of Genes and Genomes (KEGG) analyses were also performed through STRING using the DEGs.

2.8 Stromal and immune cells infiltration

The ESTIMATE algorithm was employed to identify the tumor microenvironment, and the ESTIMATE, immune, and stroma scores were calculated using the R software package "estimate" (18). The cellular composition of stromal and immune cells in the tumor within the GSE17536 dataset was estimated using the R software package "xCell" (19). Scores for immune and stromal cells were calculated for each sample. Additionally, the CIBERSORTx online platform (https://cibersortx.stanford.edu/) was utilized to assess the infiltration of 22 immune cell types in each sample (20).

2.9 Cell lines, antibodies, and chemicals

All cell lines were obtained from the Cell Bank of Shanghai, Institutes for Biological Sciences, China, and tested negative for mycoplasma infection. These cells were cultured in DMEM medium or RPMI 1640 medium (Thermo Fisher Scientific, Waltham, MA, USA), supplemented with 10% fetal bovine serum (Thermo Fisher Scientific, Waltham, MA, USA), at 37°C in a humidified atmosphere containing 5% CO2. 5% O2 hypoxic cell culture was performed by incubating cells in a sealed container with a Mitsubishi AnaeroPack™ anaerobic gas generator (Mitsubishi Gas Chemical Co., Tokyo, Japan). Hypoxic conditions were verified with the use of a Mitsubishi RT Anaero-Indicator (Mitsubishi Gas Chemical Co., Tokyo, Japan).

Antibodies against HIF1α and β-actin were purchased from Cell Signaling Technology (Danvers, MA, USA). Antibodies against ACTA2, ACTN1, CAVIN3, CEP170, LTBP1 and POSTN were purchased from Proteintech Group (Rosemont, IL, USA), Antibody against PCSK5 was purchased from CUSABIO (Wuhan, Hubei, China). Antibodies were diluted according to manufacture instructions.

2.10 Protein extraction and western blotting

The cells were washed with PBS and trypsinized, neutralization with serum-supplemented media, washed with PBS, and resuspended in RIPA buffer (Sigma-Aldrich, St. Louis, MO, USA). A 1% protease inhibitor cocktail (Halt™ Protease Inhibitor Cocktail, EDTA-Free, Thermo Fisher Scientific) was added to the mixture. The lysate was collected by centrifugation at 12,000 rpm at 4°C for 15 minutes. The supernatant was transferred to a new tube, and its concentration was determined using the BCA protein quantification assay. The supernatant was mixed with loading buffer (Sigma-Aldrich, St. Louis, MO, USA) and denatured by boiling at 95 °C.

Samples were subjected to SDS-PAGE gel electrophoresis, and proteins were subsequently transferred to PVDF membranes. The membranes were blocked with 5% non-fat milk in TBST and then incubated with specific antibodies overnight at 4°C with gentle agitation. Following washing, the membranes were incubated with HRP-conjugated secondary antibodies. Protein bands were visualized using chemiluminescent substrates.

2.11 Total RNA extraction and quantitative real-time PCR

Total RNA was extracted from cells using TRIzol Reagent (Takara, Kusatsu, Japan) following the manufacturer's instructions. After assessing quality and quantity, samples were then stored at –80°C.

The extracted RNA was reverse-transcribed into cDNA using PrimeScript™ RT Master Mix (Takara, Kusatsu, Japan). The resulting cDNA was stored at −20°C for further analysis.

Gene expression levels were quantified using qRT-PCR with gene-specific primers and the One Step SYBR PrimeScript RT-PCR Kit II (Takara, Kusatsu, Japan). The qRT-PCR reaction conditions followed the manufacturer's instructions. Expression levels were normalized to β-actin, and relative quantification was performed using the 2^-ΔΔCt method.

2.12 siRNA-mediated RNA interference

Two siRNAs for each targeting human PCSK5 and POSTN (designated as si-PCSK5_1, si-PCSK5_2, si-POSTN_1, and si-POSTN_2) and a nontargeting control siRNA were purchased from RiboBio (Guangzhou, Guangdong, China). The siRNA target sequences were as follows: si-PCSK5_1: GCAAGTACG GATTCATCAA, si-PCSK5_2: CGGGACATTTGAACGCTAA, si-POSTN_1: GCACTTGTAAGAACTGGTA, and si-POSTN_2: GCTCAGAGTCTTCGTATAT. For transfection, Lipofectamine 3000 (Invitrogen, Carlsbad, CA, USA) was used according to the manufacturer's instructions. After 48 hours, some of the cells were harvested for Western blot analysis to assess the effects of siRNA inhibition.

2.13 *In vitro* migration assay

Cell migration was assessed using Transwell chambers (Corning, NY, USA). Suspensions of 10 × 10^4 cells in 200 μL of serum-free medium were added to the upper chamber, while the lower chamber contained medium with 10% FBS. After 16–24 hours, the cells were washed with PBS and fixed in 4% paraformaldehyde. The cells on the upper polycarbonate membranes were gently wiped with cotton swabs. The migrating cells were stained with crystal violet and then counted in four random fields under a light microscope.

2.14 Statistical analysis

Statistical analysis was conducted using R software. Forest plots were generated using univariate or multivariate Cox proportional hazard regression to calculate the hazard ratio (HR). The Kaplan-Meier method was employed for survival analysis. The Wilcoxon test was used to assess differences between groups. Statistically significant differences were indicated as follows: *p < 0.05; **p <0.01; ***p < 0.001; NS indicates not significant.

3 Results

3.1 Hypoxia is an important prognostic factor in patients with colorectal cancer

RNA-seq data from the GSE17536 dataset were utilized to calculate the ssGSEA scores for cancer hallmark pathways. Significant associations with prognosis were observed for hypoxia (HR: 6.14, 95% CI: 2.13–17.67, p = 0.001), TGF-β pathway (HR: 3.98, 95% CI: 1.32–12.01, p = 0.014), KRAS upregulation pathway (HR: 3.73, 95% CI: 1.26–11.03, p = 0.017), and PI3K-AKT mTOR pathway (HR: 0.25, 95% CI: 0.08–0.76, p = 0.014) (Figure 1A). Patients were categorized into two groups based on their prognosis. Those with a worse prognosis exhibited higher hypoxia scores (p < 0.001) (Figure 1B). Subsequently, patients were stratified into high-risk and low-risk groups using the median hypoxia score as the threshold. The high-risk group demonstrated significantly poorer survival (p = 0.011) (Figure 1C).

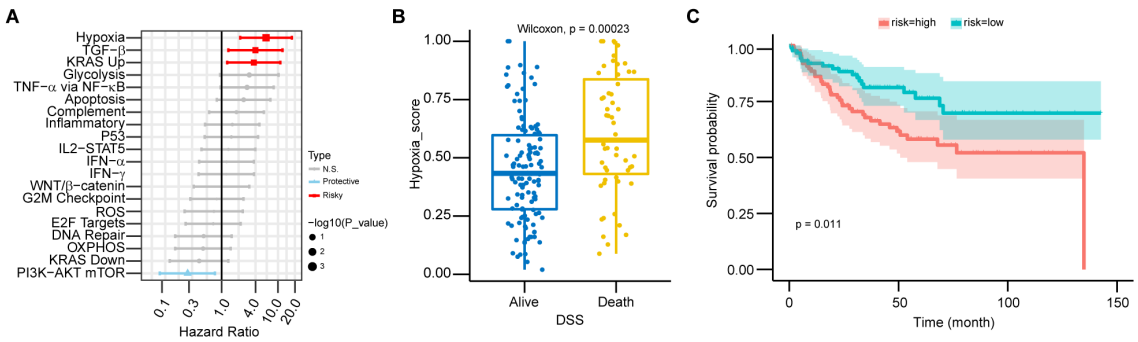

FIGURE 1
Hypoxia as a major prognostic factor in CRC patients. **(A)** Forest plot showing hazard ratios (HR) from univariate Cox regression for 20 cancer hallmark pathways in CRC patients. HRs and 95% confidence intervals (CIs) were calculated, with statistical significance assessed by the Wald test (p-value). Pathways with p > 0.05 are labeled "N.S." (not significant), HR > 1 as "Risky," and HR < 1 as "Protective." Error bars represent 95% CIs. **(B)** The boxplot shows the distribution of risk scores across DSS groups in CRC patients, including median values and interquartile ranges (IQR). Statistical significance was assessed using the Wilcoxon test (p < 0.01), with higher hypoxia scores associated with worse survival outcomes. **(C)** Kaplan-Meier survival curves for high-risk and low-risk CRC patients, stratified by risk score. Statistical significance was assessed by the log-rank test (p < 0.05), with higher hypoxia scores associated with poorer prognosis.

10.3389/fimmu.2024.1425687

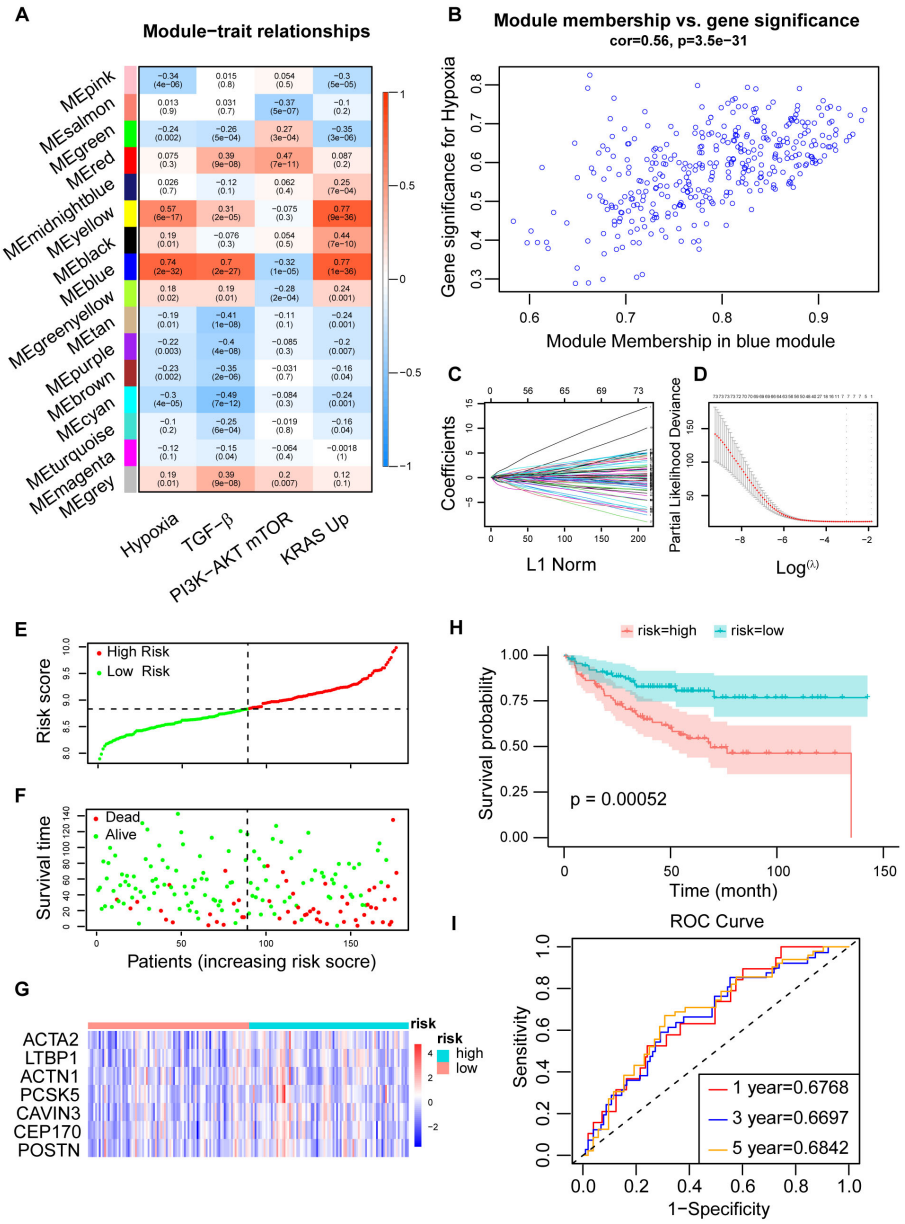

FIGURE 2
Construction of CRC prognosis prediction model using LASSO regression. **(A)** Determination of the correlation between modules and prognostic cancer hallmarks, including hypoxia, using module-trait correlation analysis. Correlations between module eigengenes (MEs) and cancer hallmarks were visualized using a heatmap. Pearson correlation coefficients were calculated between MEs and cancer hallmarks, and the corresponding p-values were obtained using the Student's t-test. **(B)** Correlations between genes in the blue module and hypoxia, with gene module membership (GMM) and gene trait significance (GTS) calculated for hypoxia-related traits. **(C)** LASSO coefficient profiles for hypoxia-related prognostic differential expressed genes. The coefficient values for the selected genes were plotted against the penalty parameter (lambda). **(D)** Cross-validation curve for the LASSO regression model, used to determine the optimal penalty parameter (lambda) for prognostic gene selection. **(E, F)** Distribution of the Hypoxia-related Prognostic Score (HPS) which was calculated based on the expression of seven hypoxia-related signature genes across CRC patients, along with their survival status and survival time showing worse prognosis following higher HPS. **(G)** Expression profiles of the seven signature genes in high- and low-risk patient groups, stratified by their HPS and visualized using a heatmap. **(H)** Kaplan-Meier survival curve for CRC patients stratified into high-risk and low-risk groups based on their HPS. Statistical significance was assessed by the log-rank test ($p < 0.01$). **(I)** Time-dependent ROC curves for the HPS at 1-, 3-, and 5-year time points in the training dataset (GSE17536). The area under the curve (AUC) values indicated the prognostic performance of the HPS.

3.2 Construction of a hypoxia-related score using WGCNA clustering and LASSO regression model to predict the prognosis of colorectal cancer patients

Using WGCNA, genes were categorized into 16 modules based on their correlation, with the blue module exhibiting the strongest association with hypoxia (Figures 2A, B; Supplementary Figures 1A, B). Univariate Cox analysis identified genes linked to patient prognosis, and LASSO regression analysis subsequently pinpointed 7 genes of interest (ACTA2, ACTN1, CAVIN3, CEP170, LTBP1, PCSK5, and POSTN). Based on the expression levels of these genes, we developed a novel hypoxia-related prognostic score (HPS) (Figures 2C, D). Patients were stratified into two groups using the median HPS, revealing significant differences in prognosis ($p < 0.001$), with the high-risk group faring worse. The distribution of HPS also varied significantly among patients with different prognoses ($p < 0.001$) (Figures 2E–H; Supplementary Figure 1C). Analysis of the 7 HPS signature gene expressions in colorectal cancer tumors versus normal tissues, using TCGA and GTEx databases, showed a marked difference (Supplementary Figure 1D). The ROC curves for 1-, 3-, and 5-

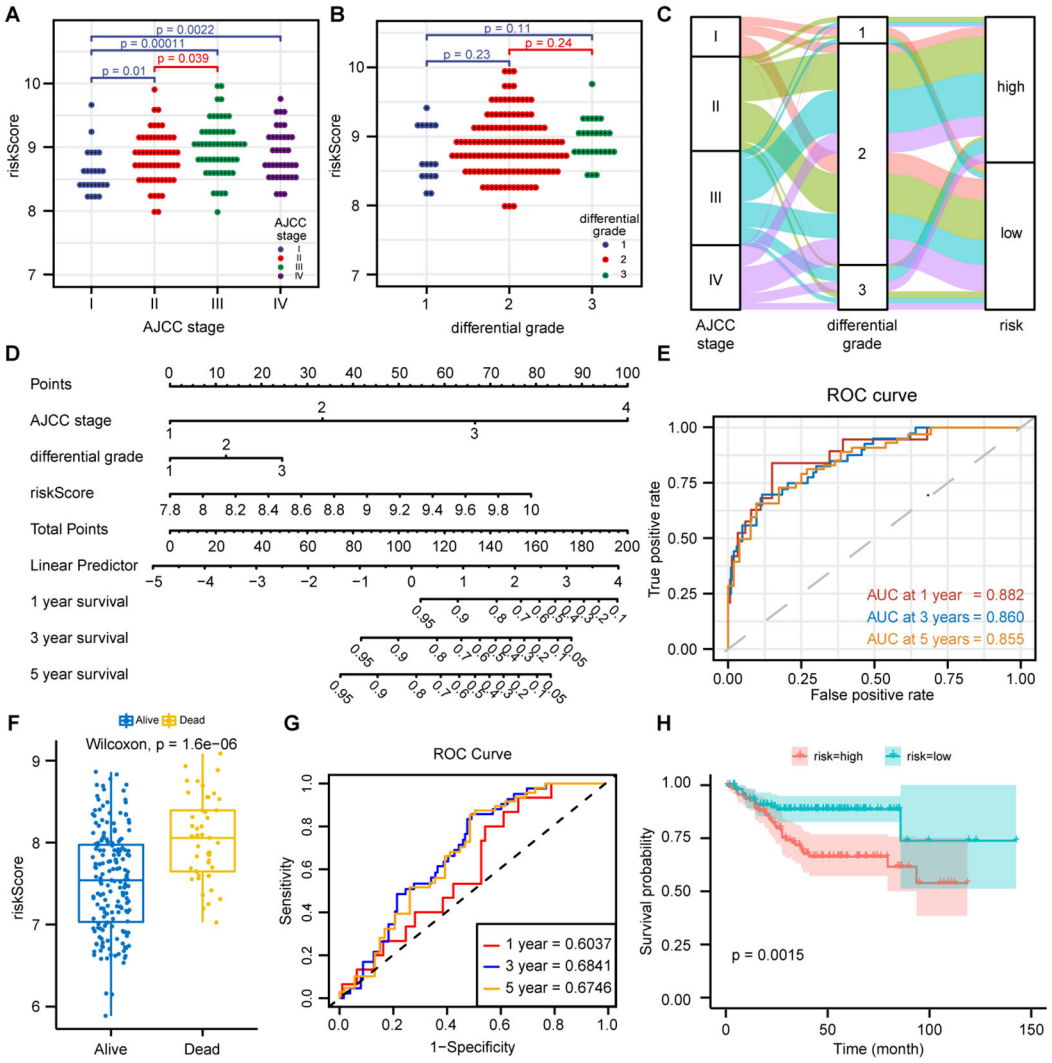

FIGURE 3
Prediction of CRC prognosis by combining clinicopathological features with HPS. **(A)** Distribution of Hypoxia-related Prognostic Score (HPS) across AJCC stages I-IV. Statistical analysis (Wilcoxon test, $p < 0.05$) revealed significantly higher HPS in advanced stages. **(B)** Distribution of HPS across different differentiation grades (well-differentiated, moderately differentiated, and poorly differentiated) in CRC patients. Data are presented as dot plots, with statistical significance assessed by the Wilcoxon test. **(C)** Alluvial diagram showing the relationships between AJCC stage, differentiation grade, and HPS risk group. **(D)** Nomogram integrating clinicopathological features and HPS for predicting 1-, 3-, and 5-year overall survival (OS) in CRC patients, based on a multivariate Cox regression model. **(E)** Time-dependent ROC curves of the nomogram at 1-, 3-, and 5-year time points in the GSE17536 training dataset, with AUC values indicating prognostic performance. **(F)** Boxplot of HPS distribution in different prognosis groups in the GSE14333 validation dataset. Wilcoxon test ($p < 0.01$) showed higher HPS in poor prognosis groups. **(G)** Time-dependent ROC curves of HPS at 1-, 3-, and 5-year time points in the GSE14333 dataset, with AUC values assessing HPS's prognostic accuracy. **(H)** Kaplan-Meier survival curves for high-risk and low-risk groups based on HPS in GSE14333. Log-rank test ($p < 0.01$) showed significantly worse survival in the high-risk group.

year overall survival (OS) based on HPS yielded areas under the curve of 0.6768, 0.6697, and 0.6842, respectively (Figure 2I).

3.3 Combining clinicopathological features with HPS to construct a nomogram predicting the prognosis of CRC patients

The distribution of HPS in CRC patients varied across different AJCC clinical stages, with later stages showing higher HPS (Figures 3A, B). The distribution of HPS in CRC patients with various clinicopathological characteristics is depicted in alluvium plots (Figure 3C). The study created a nomogram that integrates HPS with clinicopathological characteristics to predict prognosis (Figure 3D). The areas under the ROC curves for 1-, 3-, and 5-year OS of nomogram in CRC were 0.882, 0.860, and 0.855, respectively (Figure 3E). The nomogram predicted outcomes were largely consistent with the actual outcomes (Supplementary Figure 1E). To confirm the predictive capability of this score, the study applied HPS to forecast the prognosis of CRC patients in the validation set GSE14333. The distribution of HPS among patients with different prognoses was distinct ($p < 0.001$), and a statistically significant difference in prognosis was noted between the high- and low-risk HPS groups ($p = 0.0015$) (Figures 3F, H). The areas under the ROC for 1-, 3-, and 5-year OS of HPS were 0.6037, 0.6841, and 0.6746, respectively (Figure 3G).

3.4 Hypoxia changes HPS signature gene expression in normal intestinal epithelial cells and CRC cells in different patterns

To further investigate the molecular mechanisms of hypoxia regulation in the CRC TME, we treated human normal intestinal epithelial cells (FHC) and five human CRC epithelial cell lines (HCT116, HT-29, LOVO, SW480, and SW620) with hypoxia *in vitro*. We analyzed HIF1α protein expression via western blot to confirm the successful construction of the hypoxia model (Supplementary Figure 2A). Subsequently, we conducted qRT-PCR on the hypoxic cell lines to assess the expression of seven HPS signature genes (ACTA2, ACTN1, CAVIN3, CEP170, LTBP1, PCSK5 and POSTN). We observed that ACTN1 and CAVIN3 were slightly upregulated in FHC cells post-hypoxia, while the CRC cell lines exhibited varying degrees of upregulation, which was more pronounced than in FHC cells (Figure 4A). The marked disparity in gene expression changes between FHC and CRC cell lines following hypoxia indicates that the responses of normal intestinal epithelial cells and CRC cell lines to TME hypoxia are distinct (Supplementary Figure 2B). Further analysis of gene expression in both normal intestinal epithelial cell lines and tumor cell lines under normoxic conditions revealed significant differences in signature gene expression patterns between FHC and CRC cell lines (Figure 4B).

We conducted Western blot analysis to further explore the differences in protein expression between FHC and CRC cell lines under hypoxic conditions. The results indicated that the protein levels of all signature genes were altered following hypoxia, showing a high degree of consistency with our qRT-PCR findings (Figure 4C). Additionally, after knocking down POSTN and PCSK5 in CRC cell lines (HCT116 and LOVO) using siRNAs, our *in vitro* cell migration assays demonstrated that both genes are involved in the migration of CRC cells (Supplementary Figures 2C–E).

3.5 Functional enrichment analysis of differentially expressed genes identified by HPS risk model

After differential gene expression analysis between high- and low-risk groups and a GSEA enrichment analysis revealed that, in addition to the hypoxia pathway ($p < 0.001$), immune-related pathways such as inflammatory response ($p < 0.001$), interferon-γ response ($p < 0.001$), complement pathway ($p < 0.001$), and NF-κB-mediated TNF-α pathway ($p < 0.001$) were significantly enriched in the high-risk group (Figures 5A, B; Supplementary Figure 3A). Significant differences were observed in the expression patterns of genes related to immunotherapy among DEGs, although no significant differences were detected in the expression of the immune checkpoint inhibitor (ICI) genes CD274, PDCD1, and CTLA-4 (Figure 5C; Supplementary Figure 3B).Furthermore, the protein-protein interaction (PPI) analysis and GO enrichment analysis of protein-coding genes with the most significant changes in DEGs indicated that pathways were primarily enriched in the migration and chemotaxis of immune cells and the composition and structure of extracellular matrix (Figures 5D, E; Supplementary Figure 3C), suggesting that hypoxia has an influence on immune cell migration, thereby affecting the TME.

3.6 HPS risk is negatively related with immune response in TME

To discover how HPS risk is correlated with tumor immune, we performed xCell analysis to assess the infiltration of non-cancer cells in the TME, and its correlation with HPS was examined. In the analysis of different cell subsets, HPS showed a positive correlation with myeloid-derived immune cells (Supplementary Figure 4A) and a negative correlation with lymphoid-derived immune cells (Figure 6A). HPS was also positively correlated with most stromal cells and associated with other stem cells and some other cell types (Supplementary Figures 4B, C, D). The distribution of myeloid-derived immune cells, lymphoid-derived immune cells, and stromal cells between the high- and low-risk groups were further analyzed, revealing fewer myeloid-derived immune cells and stromal cells in the low-risk group, while lymphoid-derived immune cells were more abundant (Figure 6B, Supplementary Figures 4E, F). Additional analysis of immune cell infiltration using CIBERSORT indicated that macrophage infiltration predominated in the microenvironment (Supplementary Figures 5A, B). Notably, infiltration by undifferentiated macrophages and M2 macrophages significantly decreased in the low-risk group (Figure 6C, Supplementary Figure 5C). The linear correlation analysis

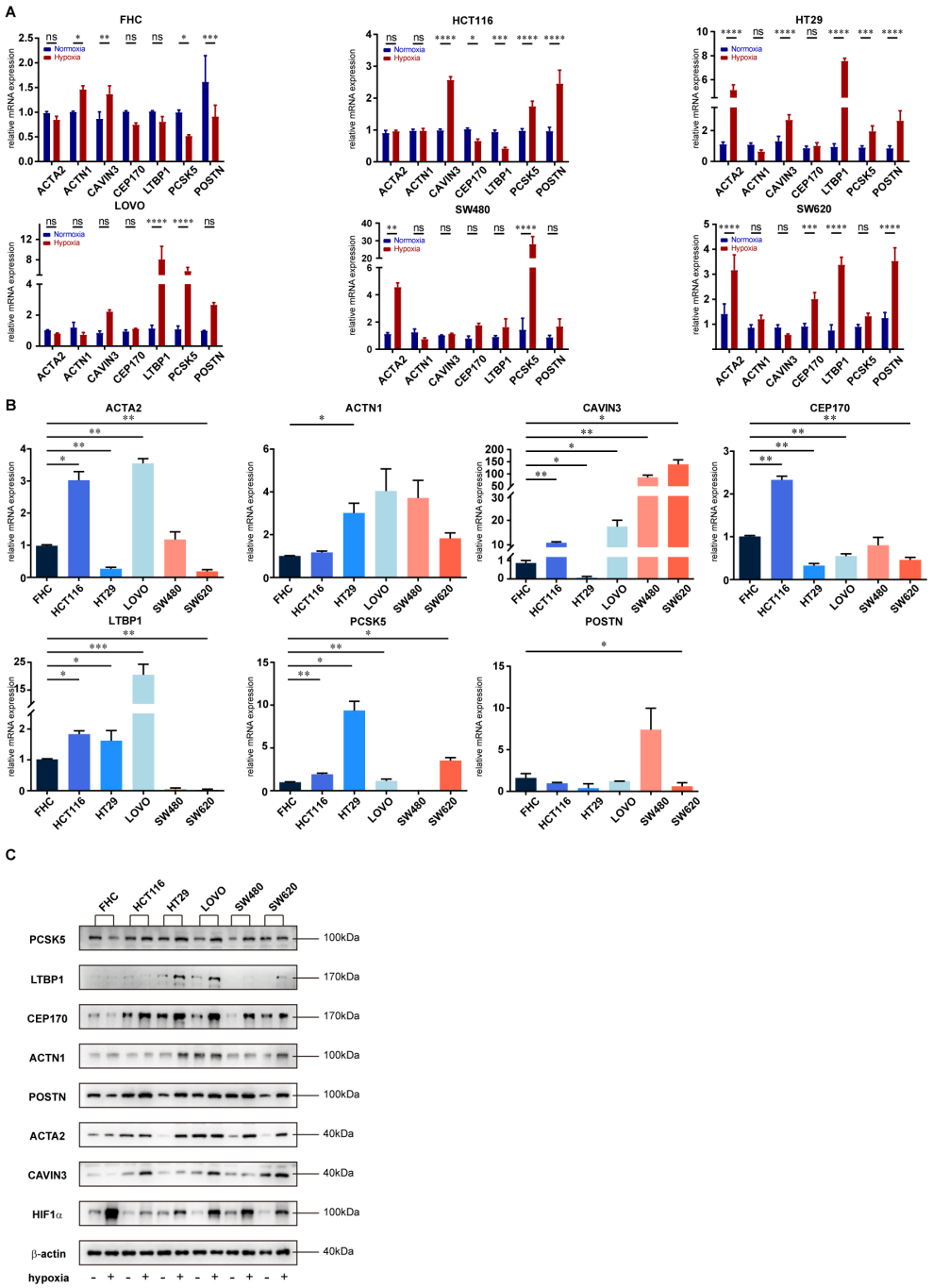

FIGURE 4
Different impacts of hypoxia on the expression of HPS signature genes in normal intestinal epithelial and CRC cells. **(A)** RT-PCR analysis of mRNA expression changes in HPS signature genes under hypoxic conditions in FHC normal intestinal epithelial cells and five colorectal cancer (CRC) cell lines (HCT116, HT29, LOVO, SW480, SW620). Total RNA was extracted from cells exposed to hypoxia. Data are presented as mean with error bars representing standard deviation (SD) from three biological replicates. Statistical significance was assessed using ANOVA, with *$p < 0.05$; **$p < 0.01$; ***$p < 0.001$; ****$p < 0.0001$; ns, not significant. **(B)** Expression profiles of HPS signature genes in FHC and CRC cell lines (HCT116, HT29, LOVO, SW480, SW620) following hypoxia. Data are presented as mean with error bars representing SD from three biological replicates. Statistical significance was assessed using ANOVA, with *$p < 0.05$; **$p < 0.01$; ***$p < 0.001$ indicating significant differences between groups. **(C)** Western blot analysis of protein expression changes in HPS signature genes following hypoxia in FHC and CRC cell lines. Cells were exposed to hypoxia, and protein lysates were analyzed by western blotting.

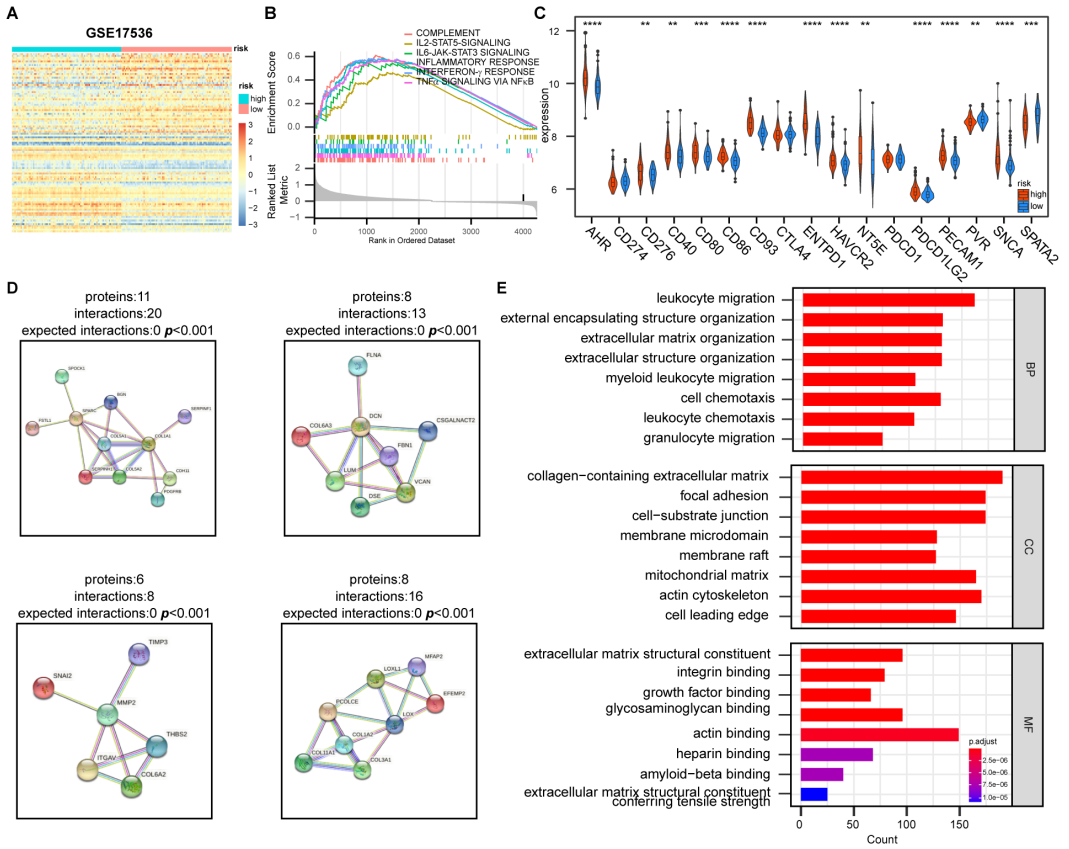

FIGURE 5
Effect of hypoxia on the expression of genes is related to tumor immune response and extracellular matrix construction. **(A)** Heatmap of differentially expressed genes between high- and low-risk groups based on HPS. Genes were selected based on fold change and statistical significance. **(B)** Gene Set Enrichment Analysis (GSEA) of immune-related pathways in high- and low-risk groups, showing significantly enriched pathways. **(C)** Differential expression of immunotherapy-related genes between high- and low-risk groups. Statistical significance was assessed using the t-test with FDR adjustment (**p < 0.01, ***, p < 0.001, ****, p < 0.0001). **(D)** The four most significantly altered protein-protein interaction (PPI) networks, identified using STRING database (https://cn.string-db.org/), highlighting key interactions between differentially expressed genes. **(E)** Gene Ontology (GO) functional enrichment analysis of the PPI network, showing the most enriched biological processes, molecular functions, and cellular components.

between HPS and immune cell infiltration demonstrated that the hypoxia score was significantly positively correlated with undifferentiated macrophages but negatively correlated with the infiltration of cytotoxic CD8 + T cells and plasma cells (Figure 6D).

4 Discussion

Tumors require significant amounts of oxygen and nutrients to support their rapid proliferation. However, due to insufficient tumor blood vessel density and dysfunctional vascular structure, tumor cells are often in a hypoxia state. To progress, tumor cells evolve various mechanisms to adapt to hypoxic environments, involving alterations in metabolic pathways, regulation of gene expression, as well as interactions with other cells or tissues (2, 21–24). In this study, through a series of bioinformatics analyses, we found seven hypoxia-associated signature genes with the most significant prognostic impact on colorectal cancer patients and established a hypoxia-related prognosis score (HPS) for CRC based on this signature gene set. *In vitro*, we observed significant differences in the signature gene expression among normal and cancer cell lines under hypoxia condition, which confirmed the malignant predictive value of this HPS model.

TME hypoxia could mediate immune evasion of cancer cells via multiple mechanisms. Hypoxia has been shown to modulate the expression of cytokines and effector molecules of immune cells, inhibiting their cytotoxic function (13, 14, 21, 25). In this study, HPS was showed to be associated with immune cytokine pathways in tumor microenvironment. However, the current study found no significant difference in the expression of immunotherapy-related molecules PD-1/PD-L1 or CTLA-4 between the low HPS and high HPS group, which suggested that high HPS might not directly promote immunosuppression by altering expression of ICI-related molecules. Hypoxia may mediate the infiltration and distribution of immune cells in the TME by affecting their migration and chemotaxis and there is an inverse relationship between the degree of hypoxia

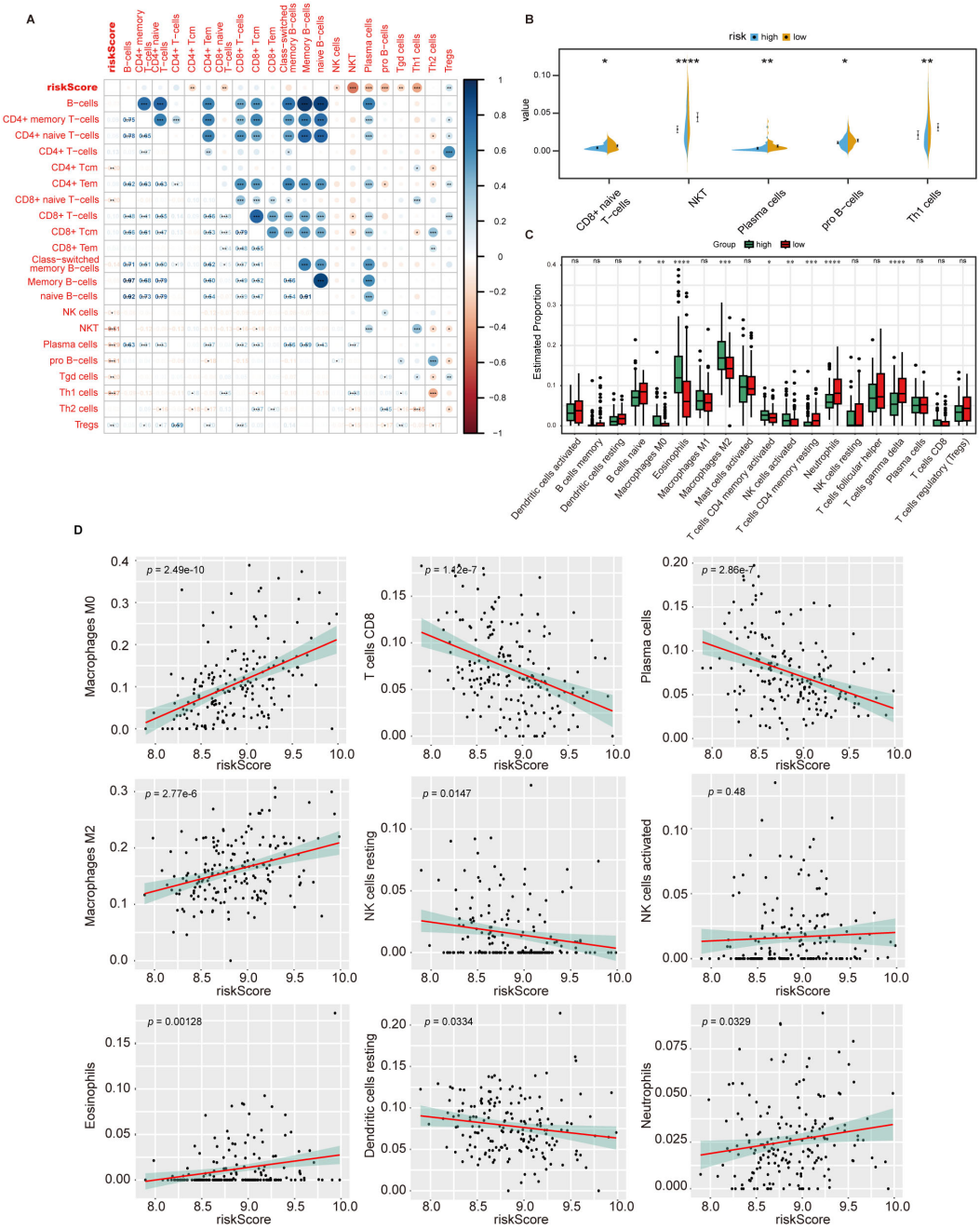

FIGURE 6
HPS is correlated with TME components. **(A)** Correlation between HPS and the infiltration of lymphoid-derived immune cells, assessed using the xCell algorithm. The correlation coefficients are shown, with statistical significance indicated by asterisks (*, p < 0.05, **, p < 0.01, ***, p < 0.001). **(B)** Infiltration of lymphoid-derived immune cells in high- and low-risk groups, analyzed using the t-test. Statistical significance is indicated by asterisks (*, p < 0.05, **, p < 0.01, ***, p < 0.001, ****, p < 0.0001). **(C)** Immune cell infiltration in high- and low-risk groups as determined by CIBERSORT. Statistical significance was assessed using the Kruskal-Wallis test, with p-values indicated as: *p < 0.05; **p < 0.01; ***p < 0.001; ****p < 0.0001; ns, not significant. Error bars represent the interquartile range (IQR). **(D)** Linear correlation between HPS and immune cell infiltration levels in the tumor microenvironment as determined by CIBERSORT. Statistical significance was assessed using Pearson's correlation test, with p-values indicating the strength of the correlation.

and CD8+ T cell infiltration (16). In our study, HPS was found positively correlated to MDSCs and negatively correlated to NK cells and tumor killing T cells, suggesting that different HPS groups might have different immune cell infiltration thereby leading to an immune suppression environment. Further CIBERSORT infiltration analysis showed that high HPS group exhibited higher overall immune cell infiltration and this increase was predominantly observed in suppressive immune cell subsets such as Treg cells and MDSCs. Meanwhile, the infiltration of tumor killing immune cells such as NK cells and γδT cells was found decreased. All these findings emphase our hypoxia-related prognosis score denoted an immunosuppressive microenvironment for tumor.

Hypoxia may also indirectly alter immune cell infiltration by regulating the composition of the extracellular matrix (25, 26). Our PPI data revealed significant differences in collagen gene expression across different HPS groups, which supported the role of hypoxia in matrix regulation. Previous studies have discovered that macrophage infiltration contributes to the remodeling of the extracellular matrix (27). Through CIBERSORT analysis, we found increase macrophage infiltration in high HPS group compared to low HPS group, suggesting the immunosuppressive microenvironment in high HPS group might be related to extracellular matrix modification. In addition, both our findings and earlier researches support that alterations in the extracellular matrix composition could affect T-cell entrapment and function leading to immunosuppression (27).

Our study confirmed the significant impact of hypoxia on CRC outcomes via transcriptomic analysis. Notably, it suggested that the unique effects of hypoxia on the extracellular matrix and immune cell infiltration might lead to varying patient prognoses. Revealing the importance that hypoxia in the TME might contribute to a potential targeted approach, such as hyperbaric oxygen, to reverse tumor favoring TME. When combined with immunotherapy, reversing hypoxia could enhance outcomes for CRC patients.

Data availability statement

The datasets presented in this study can be found in online repositories. The names of the repository/repositories and accession number(s) can be found in the article/Supplementary Material.

Ethics statement

Ethical approval was not required for the studies on humans in accordance with the local legislation and institutional requirements because only commercially available established cell lines were used.

Author contributions

RZ: Investigation, Writing – original draft. YG: Validation, Writing – original draft. CL: Visualization, Writing – review & editing. RT: Methodology, Writing – review & editing. GM: Writing – review & editing. TS: Writing – review & editing. WN: Formal analysis, Writing – review & editing. SL: Formal analysis, Writing – review & editing. KT: Conceptualization, Writing – review & editing. WL: Conceptualization, Writing – review & editing.

Funding

The author(s) declare financial support was received for the research, authorship, and/or publication of this article. This study was supported by the National Nature Science Foundation of China (No.81902703, 82072736, 82273319, 82322052).

Acknowledgments

We thank the authors of the GSE17536, GSE14333, datasets for their contribution.

Conflict of interest

The authors declare that the research was conducted in the absence of any commercial or financial relationships that could be construed as a potential conflict of interest.

Publisher's note

Supplementary material

The Supplementary Material for this article can be found online at: https://www.frontiersin.org/articles/10.3389/fimmu.2024.1425687/full#supplementary-material

References

1. Jing X, Yang F, Shao C, Wei K, Xie M, Shen H, et al. Role of hypoxia in cancer therapy by regulating the tumor microenvironment. *Mol Cancer*. (2019) 18:157. doi: 10.1186/s12943-019-1089-9

2. Chen Z, Han F, Du Y, Shi H, Zhou W. Hypoxic microenvironment in cancer: molecular mechanisms and therapeutic interventions. *Signal Transduct Target Ther*. (2023) 8:70. doi: 10.1038/s41392-023-01332-8

3. Cowman SJ, Fuja DG, Liu XD, Tidwell RSS, Kandula N, Sirohi D, et al. Macrophage HIF-1α Is an independent prognostic indicator in kidney cancer. *Clin Cancer Res Off J Am Assoc Cancer Res*. (2020) 26:4970–82. doi: 10.1158/1078-0432.CCR-19-3890

4. Yoshimura H, Dhar DK, Kohno H, Kubota H, Fujii T, Ueda S, et al. Prognostic impact of hypoxia-inducible factors 1alpha and 2alpha in colorectal cancer patients: correlation with tumor angiogenesis and cyclooxygenase-2 expression. *Clin Cancer Res Off J Am Assoc Cancer Res*. (2004) 10:8554–60. doi: 10.1158/1078-0432.CCR-0946-03

5. Sumiyoshi Y, Kakeji Y, Egashira A, Mizokami K, Orita H, Maehara Y. Overexpression of hypoxia-inducible factor 1alpha and p53 is a marker for an unfavorable prognosis in gastric cancer. *Clin Cancer Res Off J Am Assoc Cancer Res*. (2006) 12:5112–7. doi: 10.1158/1078-0432.CCR-05-2382

6. Depner C, Zum Buttel H, Böğürcü N, Cuesta AM, Aburto MR, Seidel S, et al. EphrinB2 repression through ZEB2 mediates tumour invasion and anti-angiogenic resistance. *Nat Commun*. (2016) 7:12329. doi: 10.1038/ncomms12329

7. Ju S, Wang F, Wang Y, Ju S. CSN8 is a key regulator in hypoxia-induced epithelial-mesenchymal transition and dormancy of colorectal cancer cells. *Mol Cancer*. (2020) 19:168. doi: 10.1186/s12943-020-01285-4

8. Romero-Ramirez L, Cao H, Nelson D, Hammond E, Lee AH, Yoshida H, et al. XBP1 is essential for survival under hypoxic conditions and is required for tumor growth. *Cancer Res*. (2004) 64:5943–7. doi: 10.1158/0008-5472.CAN-04-1606

9. Chen X, Zeh HJ, Kang R, Kroemer G, Tang D. Cell death in pancreatic cancer: from pathogenesis to therapy. *Nat Rev Gastroenterol Hepatol*. (2021) 18:804–23. doi: 10.1038/s41575-021-00486-6

10. Li J, Zhang T, Ren T, Liao X, Hao Y, Lim JS, et al. Oxygen-sensitive methylation of ULK1 is required for hypoxia-induced autophagy. *Nat Commun*. (2022) 13:1172. doi: 10.1038/s41467-022-28831-6

11. Liu J, Dong S, Gai S, Dong Y, Liu B, Zhao Z, et al. Design and mechanism insight of monodispersed auCuPt alloy nanozyme with antitumor activity. *ACS Nano*. (2023) 17:20402–23. doi: 10.1021/acsnano.3c06833

12. Okami J, Simeone DM, Logsdon CD. Silencing of the hypoxia-inducible cell death protein BNIP3 in pancreatic cancer. *Cancer Res*. (2004) 64:5338–46. doi: 10.1158/0008-5472.CAN-04-0089

13. Noman MZ, Desantis G, Janji B, Hasmim M, Karray S, Dessen P, et al. PD-L1 is a novel direct target of HIF-1α, and its blockade under hypoxia enhanced MDSC-mediated T cell activation. *J Exp Med*. (2014) 211:781–90. doi: 10.1084/jem.20131916

14. Mahiddine K, Blaisdell A, Ma S, Créquer-Grandhomme A, Lowell CA, Erlebacher A. Relief of tumor hypoxia unleashes the tumoricidal potential of neutrophils. *J Clin Invest*. (2020) 130:389–403. doi: 10.1172/JCI130952

15. Yang MH, Wu MZ, Chiou SH, Chen PM, Chang SY, Liu CJ, et al. Direct regulation of TWIST by HIF-1alpha promotes metastasis. *Nat Cell Biol*. (2008) 10:295–305. doi: 10.1038/ncb1691

16. de Almeida PE, Mak J, Hernandez G, Jesudason R, Herault A, Javinal V, et al. Anti-VEGF treatment enhances CD8+ T-cell antitumor activity by amplifying hypoxia. *Cancer Immunol Res*. (2020) 8:806–18. doi: 10.1158/2326-6066.CIR-19-0360

17. Wu T, Hu E, Xu S, Chen M, Guo P, Dai Z, et al. clusterProfiler 4.0: A universal enrichment tool for interpreting omics data. *Innov Camb Mass*. (2021) 2:100141. doi: 10.1016/j.xinn.2021.100141

18. Yoshihara K, Shahmoradgoli M, Martínez E, Vegesna R, Kim H, Torres-Garcia W, et al. Inferring tumour purity and stromal and immune cell admixture from expression data. *Nat Commun*. (2013) 4:2612. doi: 10.1038/ncomms3612

19. Aran D, Hu Z, Butte AJ. xCell: digitally portraying the tissue cellular heterogeneity landscape. *Genome Biol*. (2017) 18:220. doi: 10.1186/s13059-017-1349-1

20. Newman AM, Liu CL, Green MR, Gentles AJ, Feng W, Xu Y, et al. Robust enumeration of cell subsets from tissue expression profiles. *Nat Methods*. (2015) 12:453–7. doi: 10.1038/nmeth.3337

21. Vignali PDA, DePeaux K, Watson MJ, Ye C, Ford BR, Lontos K, et al. Hypoxia drives CD39-dependent suppressor function in exhausted T cells to limit antitumor immunity. *Nat Immunol*. (2023) 24:267–79. doi: 10.1038/s41590-022-01379-9

22. Suthen S, Lim CJ, Nguyen PHD, Dutertre CA, Lai HLH, Wasser M, et al. Hypoxia-driven immunosuppression by Treg and type-2 conventional dendritic cells in HCC. *Hepatol Baltim Md*. (2022) 76:1329–44. doi: 10.1002/hep.32419

23. Sattiraju A, Kang S, Giotti B, Chen Z, Marallano VJ, Brusco C, et al. Hypoxic niches attract and sequester tumor-associated macrophages and cytotoxic T cells and reprogram them for immunosuppression. *Immunity*. (2023) 56:1825–1843.e6. doi: 10.1016/j.immuni.2023.06.017

24. Kumagai S, Koyama S, Itahashi K, Tanegashima T, Lin YT, Togashi Y, et al. Lactic acid promotes PD-1 expression in regulatory T cells in highly glycolytic tumor microenvironments. *Cancer Cell*. (2022) 40:201–218.e9. doi: 10.1016/j.ccell.2022.01.001

25. Miar A, Arnaiz E, Bridges E, Beedie S, Cribbs AP, Downes DJ, et al. Hypoxia induces transcriptional and translational downregulation of the type I IFN pathway in multiple cancer cell types. *Cancer Res*. (2020) 80:5245–56. doi: 10.1158/0008-5472.CAN-19-2306

26. Park JH, Richards CH, McMillan DC, Horgan PG, Roxburgh CSD. The relationship between tumour stroma percentage, the tumour microenvironment and survival in patients with primary operable colorectal cancer. *Ann Oncol Off J Eur Soc Med Oncol*. (2014) 25:644–51. doi: 10.1093/annonc/mdt593

27. Schwörer S, Cimino FV, Ros M, Tsanov KM, Ng C, Lowe SW, et al. Hypoxia potentiates the inflammatory fibroblast phenotype promoted by pancreatic cancer cell-derived cytokines. *Cancer Res*. (2023) 83:1596–610. doi: 10.1158/0008-5472.CAN-22-2316

Frontiers in Immunology

Explores novel approaches and diagnoses to treat immune disorders.

The official journal of the International Union of Immunological Societies (IUIS) and the most cited in its field, leading the way for research across basic, translational and clinical immunology.

Discover the latest Research Topics

See more →

Frontiers

Avenue du Tribunal-Fédéral 34
1005 Lausanne, Switzerland
frontiersin.org

Contact us

+41 (0)21 510 17 00
frontiersin.org/about/contact